Interaction of sound with vorticity

Interaction of Sound with Vorticity

Deepesh Kumar Singh

Cover art: D. K. Singh

A catalogue record is available from the Eindhoven University of Technology Library

ISBN: 978-90-386-4135-5

Interaction of Sound with Vorticity

PROEFSCHRIFT

ter verkrijging van de graad van doctor aan de
Technische Universiteit Eindhoven, op gezag van de
rector magnificus prof.dr.ir. F.P.T. Baaijens, voor een
commissie aangewezen door het College voor
Promoties, in het openbaar te verdedigen
op donderdag 29 september 2016 om 16:00 uur

door

Deepesh Kumar Singh

geboren te Hathras, India

Dit proefschrift is goedgekeurd door de promotoren en de samenstelling van de promotiecommissie is als volgt:

voorzitter:	prof.dr. J. de Vlieg
1^{e} promotor:	prof.dr. J.J.M. Slot
2^{e} promotor:	dr. S. W. Rienstra
leden:	prof.dr. N. Peake (University of Cambridge)
	prof.dr.ir. A. Hirschberg
	prof.dr. W. Polifke (TU München)
	dr. Y. Aurégan (CNRS)
	prof.dr.ir. B. Koren
	prof.dr.ir. G.J.F. van Heijst

Het onderzoek of ontwerp dat in dit proefschrift wordt beschreven is uitgevoerd in overeenstemming met de TU/e Gedragscode Wetenschapsbeoefening.

Contents

1 Introduction **1**

1.1 Aircraft and industrial noise 2

1.2 Noise absorbing devices - liners 4

1.2.1 Locally reacting liners 4

1.2.2 Non locally reacting liners 5

1.3 Hard wall - soft wall discontinuities and liner repairs 6

1.4 Outline of the thesis 7

1.4.1 Non linear impedance modelling of the Helmholtz resonator liner 7

1.4.2 Vorticity scattering at hard - soft wall transition 8

1.4.3 Vorticity scattering at soft - hard wall transition 9

1.4.4 Experimental observation of hydrodynamic wave in a flow duct with porous walls 10

2 Derivation of the basic equations **11**

2.1 Conservation laws and constitutive equations 11

2.1.1 Viscous stress tensor $\boldsymbol{\tau}$ and heat flux vector $\boldsymbol{q}$, constitutive equations 12

2.2 Acoustic approximations 13

2.2.1 Non viscous and isentropic 14

2.2.2 Perturbations of a mean flow 15

2.2.3 Incompressible limit 16

2.2.4 Time harmonic perturbations and mean flow in 2D 16

2.3 Wave equation and acoustic compactness 16

3 Systematic non linear impedance model for a Helmholtz resonator liner **19**

3.1 Introduction 19

3.2 Mathematical formulation 21

3.3 Asymptotic analysis 24

3.3.1 Non resonant case 24

3.3.2 Resonant case 25

3.4 Time-domain solution 28

3.4.1 Comparison in time-domain with a fully numerical solution . . 30
3.5 Impedance calculation . . . 31
3.5.1 Non resonant impedance . . . 31
3.5.2 Resonant impedance . . . 32
3.5.3 Comparison with Motsinger and Kraft . . . 32
3.5.4 Comparison with Hersh et al. measurements . . . 34
3.5.5 Comparison with Ingard and Ising . . . 34
3.5.6 Comparison with Melling . . . 34
3.5.7 Comparison of impedances based on y_0 and $y_0 + \varepsilon y_1$ approximations . . . 35
3.5.8 Another asymptotic form . . . 36
3.6 Extension to the N wave source . . . 37
3.6.1 Impedance calculation . . . 40
3.6.2 Results . . . 40
3.7 Conclusions . . . 41

4 Impedance model for non linear Helmholtz resonator of finite depth 43
4.1 Introduction . . . 43
4.2 Mathematical formulation . . . 44
4.3 Scaling . . . 47
4.4 Asymptotic solution away from resonance $\omega \neq \omega_0$ . . . 48
4.5 Asymptotic solution close to resonance $\omega \approx \omega_0$ . . . 49
4.6 Impedance calculation . . . 55
4.6.1 Non resonant impedance . . . 55
4.6.2 Resonant impedance . . . 56
4.7 Comparison with Motsinger and Kraft . . . 58
4.8 Conclusions . . . 59

5 Vorticity scattering at hard wall - pressure release wall transition in shear flows 61
5.1 Introduction . . . 61
5.2 Model . . . 63
5.3 Mathematical formulation . . . 65
5.4 Wiener-Hopf procedure . . . 67
5.5 Analytical solution . . . 71
5.5.1 Solutions in the form of integrals . . . 71
5.5.2 Explicit evaluation of the integrals . . . 73
5.5.3 Far field behaviour of the incompressible solution . . . 76
5.6 Far field of inner solution – outside shear layer . . . 78
5.6.1 Low shear . . . 80
5.6.2 High shear . . . 80
5.7 Acoustic outer field and asymptotic matching . . . 81
5.7.1 Low shear case matching . . . 82

5.7.2 High shear case matching 83
5.8 Conclusion 83

6 Vorticity scattering at hard wall - soft wall transition in shear flows 85
6.1 Introduction 85
6.2 Model 86
6.3 Mathematical formulation 87
6.4 Wiener-Hopf procedure 88
6.5 Hydrodynamic solution 92
6.5.1 Solution of velocities u and v 93
6.5.2 Solution of pressure p 93
6.5.3 Far field of inner solution p – inside shear layer 96
6.5.4 Far field of inner solution – outside shear layer 97
6.6 Outer solution and asymptotic matching (low shear case only) 99
6.6.1 Far field sound, low shear case 100
6.7 Conclusions 101

7 Vorticity scattering at soft wall - hard wall transition in shear flows 103
7.1 Mathematical formulation 104
7.2 Wiener-Hopf procedure 106
7.3 Hydrodynamic solution 109
7.3.1 Solution of velocities u and v 109
7.3.2 Solution of pressure p 110
7.3.3 Far field of inner solution p – inside shear layer 111
7.3.4 Far field of pressure release wall solution - inside shear layer . . 113
7.4 Outer solution and asymptotic matching - (low shear case only) 115
7.4.1 Far field sound - impedance wall 116
7.4.2 Far field sound - pressure release wall 116
7.5 Conclusions 117

8 Experimental observation of hydrodynamic modes in flow duct with porous lining 119
8.1 Introduction 120
8.2 Set up description 121
8.3 Experimental results for transmission and reflection coefficients 122
8.4 Extraction of the hydrodynamic wave characteristics 125
8.5 Microphone measurements on the wall opposite to the porous material 130
8.6 Pressure drop along the porous material 131
8.7 Conclusion 132

9 Conclusion 133
9.1 Helmholtz resonator type impedance modeling 133
9.2 Vorticity scattering problem 134
9.3 Experimental observation of hydrodynamic wave over porous surface . 135

Appendix **137**

A Appendix to Chapter 3 **137**
A.1 Stability of stationary solution 137

B Appendix to Chapter 4 **139**
B.1 Solution of homogeneous problem 139
B.2 Solution of inhomogeneous problem 140
B.3 Order ε^2 equation 141

C Appendix to Chapter 5 **143**
C.1 Properties of half range Fourier transforms 143
C.2 Behaviour near the edge 145
C.3 Evaluation of the entire function E 146
C.4 Evaluation of the split functions 147
C.4.1 Low-shear case $\sigma < \omega$ 147
C.4.2 High-shear case $\sigma > \omega$ 148
C.5 Contour integrals 150
C.6 Incomplete Γ function 152

D Appendix to Chapter 6 **155**
D.1 Regularising Wiener-Hopf kernel K 155
D.2 Analytical evaluation of the split integral 156
D.3 Asymptotic analysis of the split integral I for k near 0 159
D.3.1 High shear case 159
D.3.2 Low shear case 161
D.3.3 Asymptotic analysis for k large 162
D.4 Evaluation of the entire function E 162
D.5 Regularisation of the diverging integral 163

E Appendix to Chapter 7 **165**
E.1 Wiener-Hopf formulation of pressure release wall 165
E.2 Analytic split functions and their asymptotic behaviour 166
E.2.1 Asymptotic behaviour of the split functions for k near 0 166
E.2.2 High shear case 166
E.2.3 Low shear case 167
E.3 Evaluation of the entire function E 167
E.4 Regularisation of the diverging integral 168

Bibliography **179**

Chapter 1

Introduction

Most of us are used to the sounds we hear in everyday life, for example music, television, people talking on their phone, the traffic and industrial noise. All of these sounds have become a part of the urban culture/lifestyle and rarely disturb us. However, when the noise emission level exceeds a certain limit called Exposure Action Value, EAV (about 85dB) like aircraft takeoff/landing, it turns into noise pollution. The United States department of labour has made mandatory regulations to limit the noise level that the employees can be exposed to in working conditions considering the occupational safety and health standards [62]. For most of us, the concept of pollution is limited to nature and resources like water, air *etc.* However, noise that tends to disrupt the natural rhythm of life makes up for one important pollutant. By definition, noise pollution takes place when there is either excessive or unpleasant sound that causes temporary disruption in the natural balance and distract the surrounding fauna. A few general causes of the noise pollution are industrialization, poor urban planning, social events, transportation, construction activities, excessive crowd and household chores like microwave, air conditioning, fan etc. While this form of pollution may seem harmless, it has, in fact far reaching consequences. The adverse effects of an excessively noisy environment on human health are quite severe. Noise can cause hearing impairment by long-term exposure above the Exposure Action Value limit, and it also acts as a causal factor for stress and raises systolic blood pressure. Long - terms exposure can also cause health issues such as sleeping disorders, cardiovascular disease *etc.* Those who are exposed to noise for longer duration of time, like those who work in an industrial environment or live close to the airport, tend to have severe health issues. Apart from the health problems, the environment is submitted to natural disorder with excessive sound emission and the overall behaviour of surrounding changes. In order to revert this, one must first understand the sources of sound, the way it propagates and economic methods to absorb it.

1.1 Aircraft and industrial noise

Out of all the noise sources mentioned above, the sound emissions from aircraft engines, ventilation ducts and manufacturing industries are of concern for the current work. The industrial power machines produce sound that is generally passed to the environment through ducted outlets. Same is the case with aircraft engines where the sound propagates through the inlet or outlet ducts in to the environment. Aircraft noise has long been a major concern to residents around airports. The severity of regulations on community noise near airports, and the imposed heavy penalty if the regulations are not met, have ensured that the reduction of noise generated by aircraft at take-off and approach conditions remains an essential consideration in the design of new commercial aircrafts.

The scale of the challenge that is faced by the aviation industry is alarming. In the United Kingdom, air traffic has increased five times in the last 30 years. Half the population enjoy air travel once a year and crowd flux passing through airports doubles every ten years. Such statistics will be eclipsed in the coming decades by the expansion of civil aviation. If these benefits continue to be enjoyed in a sustainable environment, expansion in aircraft size, seat capacity and aircraft movements must be accompanied by a commensurate reduction in the environmental cost. If this is to be achieved, it will require innovative technology solutions for noise and emissions.

The environmental impact of commercial aircraft noise is a local problem because it arises at take off and landing and affects populated areas close to airports, but it is not generally an issue at cruise. Especially with the emerging economies like India and China, the aerospace sector has to expand accordingly so that the benefits and comfort of the air travel is enjoyed by the emerging economies at the cost of low fuel consumption and hence carbon emission. Thus the paradigm of aviation sector has moved from the jet engines in the past to the turbo fan engines in the present because of the fuel efficiency gain. In a broader context, the environmental impact of air transport as a whole poses a major threat to its continued expansion. The reduction of noise and emissions is now critical to the continued prosperity of the aerospace sector and an essential prerequisite for the successful development of new aircraft.

The popularity of turbofan engines for civil aviation, due to low operational cost, has changed the prominent source of emitted sound to fan noise rather than jet noise. The current work pertains more to the civil aircraft engines rather than the military aircrafts because the latter are build to have maneuverability at the cost of fuel efficiency to some extent and hence, the jet propulsion system is used widely.

Characterizing the noise emission by an aircraft for certification and regulatory purposes became necessary afterwards 1960 as the use of commercial jet aircraft became widespread and contributed to a growing noise pollution near airports. The US Federal Aviation Administration issued a noise certification regulation, Federal Air Regulation, part 36 [1], mostly known as FAR36. The International Civil Aviation Organisation (ICAO) subsequently issued an annex (Annex 16) [64] about the noise

regulations to the Convention on International Civil Aviation. Annex 16 and FAR36 were essentially equivalent and remain so although both have been modified from time to time to make the requirements even more stringent. In FAR36 and Annex16, the metric used to measure public annoyance response to aircraft noise is the Effective Perceived Noise Level (EPNL) measured in decibels (0.1 bel) dB. This is determined by the spectral frequency content and duration of emission of the noise in addition to overall sound pressure level. The EPNL for an aircraft entering service is calculated from sound pressure recordings taken at three certification points known as take off, sideline and approach conditions. An EPNL figure is obtained at each of these three points and rated against prescribed maximum values which vary with takeoff weight *i.e.* the size of aircraft or seat capacity and number of engines.

More often, the sound emitted in the considered cases has a sharp spectrum such that one (or several) prominent frequencies can be identified. Such prominent frequencies are then tried to be attenuated with the sound absorbing devices called liners. Shown in Fig. 1.1 is the layout of a typical modern turbofan aircraft engine. On broader scale, the total noise recorded at the 3 points mentioned before can be divided into fan noise and jet noise. For high bypass ratio engines, the jet speed is relatively low and, the overall noiseness is dominated by fan noise. The fan noise can again be classified into the following categories owing to the regulations

- Rotor - alone tones
- Rotor - stator interaction tones
- Buzz saw tones
- Broadband noise.

The rotor alone tones sound field arises because of the rotating field associated with the fan hence is emitted over the range of frequency that are integral multiples of the shaft passing frequency and travel upstream of the fan and pass to the environment through the inlet duct [51]. Buzz saw noise arises at take off when the engines operate at high speed and the blade tip Mach number enters the supersonic regime and produces shock waves that travel upstream and interact with each other and produce a field in the form of N wave [50]. Since shock waves move with the blade tip speed, the buzz saw sound is produced at integral multiple of the blade passing frequency BPF. The rotor-stator interaction tones, also called Fan-OGV (outlet guide vanes) tones [89] are produced when the wakes from the fan impinge on the stator and produce a dipole source of sound at OGV surface. Again, the emitted sound frequency is an integral multiple of the BPF and the noise field passes through the by pass duct. The remaining broadband noise [97, 42] is caused by the random turbulence and installation effects and is emitted at all frequencies of the spectrum, more concentrated at the BPFs. The first three sources of sound always propagate through the duct, whether the intake or bypass duct, hence a meticulous design of the duct wall has a strong impact on the overall environmental noise generated by the engine.

Similarly, the industrial noise is more often emitted at the characteristic frequency of the power units and is taken outside to the open atmosphere through duct walls.

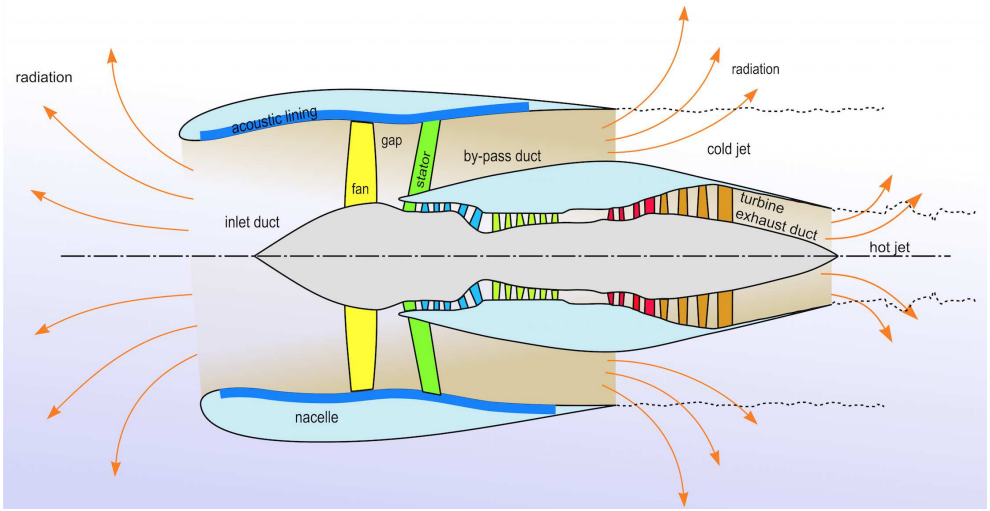

Figure 1.1: Layout of modern turbofan engine [81].

1.2 Noise absorbing devices - liners

The walls of the ducts through which the unpleasant sound propagates are often lined with sound absorbing material, called liners. Depending upon their structure and conditioning in which they are used, there are mainly two kinds of liners, known as locally reacting and non locally reacting liners, shown in Fig. 1.2. Typically, the duct has a long radius compared to the typical acoustic wavelength and hence, a 2D modelling approach is appropriate to describe the behaviour of the acoustic lining. Moreover, the presence of a high Mach number flow in the duct forces one to include the Doppler effect due to convection of the wave and the models including the mean flow have been introduced [37]. The mean flow in the inlet and bypass duct is almost uniform with a thick boundary layer hence, a linear shear model could be appropriate to understand the lining behaviour.

1.2.1 Locally reacting liners

This type of liner is very common in aircraft engines [37], industry power buildings, roof wall and theatres. Such type of acoustic liner for aero-engine inlet and exhaust ducts constitutes of a honeycomb array of small cells called Helmholtz resonators. The Helmholtz resonator is a cavity filled with air having a small opening called the neck. When excited with a fluctuating external sound pressure, the mass of air plug inside the neck moves against the large volume of compressible air inside the cavity, which acts as a spring, while viscous forces and vortex shedding generate dissipation of energy. Altogether this establishes a mass-spring-damper system. The damping is normally relatively small such that a resonance frequency can be identified. At and near resonance, the dissipation is largest and so narrow band sound absorption is

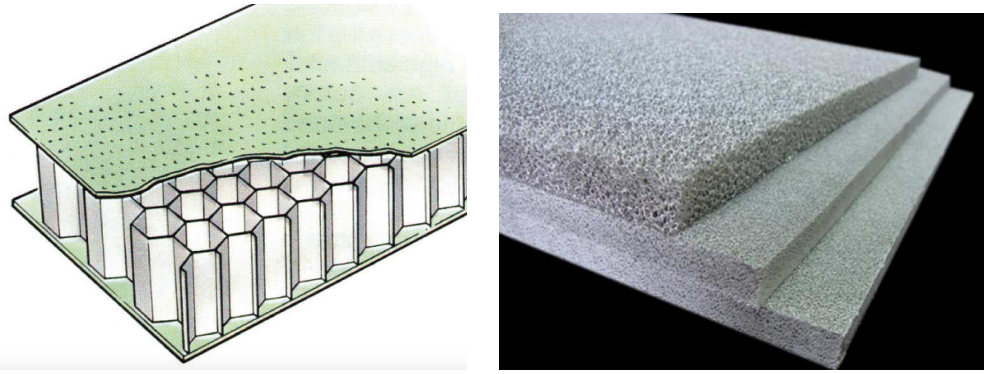

Figure 1.2: General locally reacting and non locally reacting liners respectively.

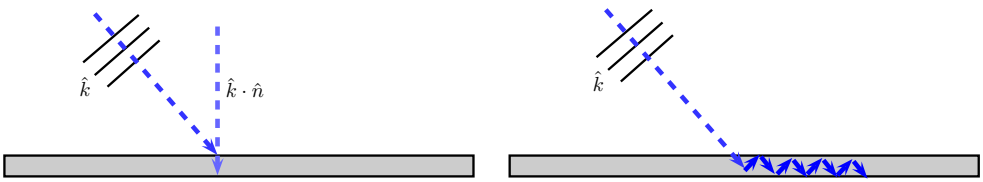

Figure 1.3: Locally reacting and non locally reacting liners respectively.

achieved for frequencies close to resonance. This process is the basic design criterion for the liners, shown in Fig. 1.2 *left*. The depth L and diameter of individual cavity of these honey comb structures are of the order of a few centimetres and one centimetre respectively and the efficiency is maximum close to the frequency with wavelength $4L$. The name is derived from the fact that these liners react locally to the external sound field. Suppose a wave vector $\hat{k}$ is hitting the liner at an angle as shown in Fig. 1.3, only the normal component $\hat{k} \cdot \hat{n}$ of the wave amplitude is allowed to interact with the resonator cavity and there is no interaction between the individual cells. Hence, the liner can be modelled with a single point value called impedance Z which is a complex number that denote the negative of the ratio of acoustic pressure and velocity at the particular frequency.

The above liners are very effective when acted upon a sound field that has a sharp frequency content [37]. However, if the noise is emitted over a wider spectrum, another type of liner, usually made of porous material, shown in Fig. 1.2, is useful.

1.2.2 Non locally reacting liners

Porous absorbers fall into this category of liners and are made up of metallic foam or porous materials, Fig. 1.2 *right* and are used in many situations to achieve the absorption of sound, e.g., in ventilation ducts, in power plants, and in the exhaust systems of cars and trucks. As shown in Fig. 1.3 *right*, the wave is allowed to enter the surface at any angle it chooses and propagates inside the layer. Hence the surface

does not interact locally. Because of the fluctuating wave amplitude, the air inside the surface moves against the solid foam and energy is dissipated in the form of heat that leads to the attenuation of the wave. Since the minute spaces inside the foam vary over a wider length scale, the surface is efficient to attenuate a wider spectrum of the noise. However, the porous material can not be used in aircraft engines because of it's weight and the constraint that the atmospheric humidity can fill the pores and make the liner ineffective. So the choice of liner that can be used to absorb particular sound is determined by the external factors like the weight and operating conditions.

Since the wave is permitted to travel in the direction parallel to the wall of the liner, the acoustic field inside and outside the liner are coupled [72] and hence the liner can not be classified with a single point number impedance. The usual way to model these liners is to solve the convective (if mean flow is present outside the liner) wave equation and wave equation outside and inside the liner respectively and applying the continuity of pressure and velocity at the lining wall. The density of the air inside the liner is a function of foam parameters and small vibrations in the minute foam structures could affect the sound attenuation. Hence, the mathematical modelling of these liners is more challenging and we have to rely more on the experiments in order to understand the behaviour of these surfaces.

1.3 Hard wall - soft wall discontinuities and liner repairs

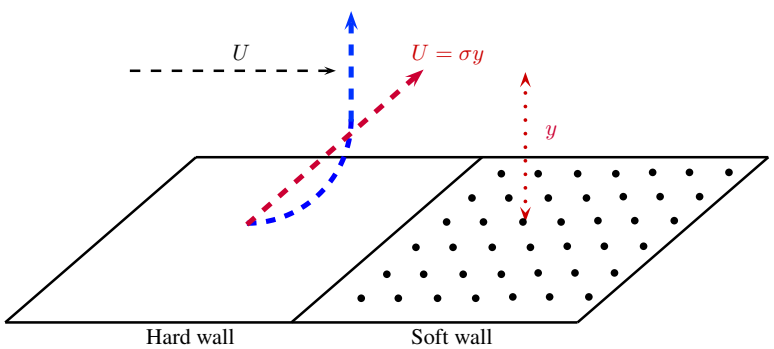

Figure 1.4: The hard soft discontinuties at liner repairs.

The acoustic liners used in aircraft engines are made in the form of rectangular sheets which are folded and carved at the inner surface of the duct with the help of splices [10, 52]. The splices generally have hard surfaces because they have to support the liner. The other components of the aircraft engines like spool and vanes also need support and hence the liners can not have a continuous porosity and there are always some regions where the wall is completely hard. Also during the operation for a larger period of time, some part of the liner is inevitably damaged leaving behind hard wall

patches. These hard wall patches that are present between the continuous soft lining are called liner repairs. The liner repairs introduce hard - soft or soft - hard transition points. Such non uniformity of the duct surface introduces modal scattering. Modal scattering is particularly relevant when a cut off wave mode scatters into other modes that are cut on. This behaviour makes the lining inevitably less efficient. The modal scattering is out of the scope of the current work.

The flow inside the duct has a boundary layer, Fig. 1.4, of thickness that may vary between very thin and several wavelengths. Within the boundary layer, the turbulence is prominent. In 2D, the turbulence can be represented as layers of vorticity. Such vortices decay exponentially away from their position and do not radiate any sound. However, because of the presence of the wall discontinuity, the vortices can use it and radiate sound and could become an important source of radiated noise [4]. Therefore, a discontinuity in the boundary may act as a "wave number converter" to produce the scattered far field noise. So the main production of sound due to vortex scattering concentrates at discontinuities of the boundary . This was confirmed by Crighton [27] who studied in detail the radiation from the flow over 2 semi-infinite planes that differ in their inertia and elastic properties with vortex near the edges. He formulated set of equations which are sufficient to find the radiated sound field entirely in terms of Lighthill's quadrupole strength and then argued about the scattered sound field based upon dimensional reasoning. Thus, the influence of boundaries, in particular soft or flexible boundaries, on the aerodynamic noise generated by turbulent flows in general and vortical perturbations in particular have been a noise problem which has been studied for decades. Some more examples are given in [38, 27, 24, 28, 96, 95]. That is why there is a need for canonical model problems that allow analytically exact solutions of vorticity in shear flow scattering at hard-soft transitions of a liner wall and this is one of the main topics in the current work. This behavior may also be relevant for the case of non locally reacting liners but this appears more difficult to model mathematically.

1.4 Outline of the thesis

In this section, we will go through the outline of the work presented in the current document in chronological order. In a broader context, we will study the interaction of sound and vorticity (or vice versa) at or along a liner, both mathematically and experimentally. After the introduction in the first Chapter 1, we will derive the basic governing equations in Chapter 2. The subsequent chapters are then grouped together for convenience and touched minutely in the next sections.

1.4.1 Non linear impedance modelling of the Helmholtz resonator liner

The Helmholtz type resonator shown in Fig. 1.2 *left*, as seen from the outside, is characterized by its impedance $Z = Z(\omega)$, relating (spatially averaged) pressure and

velocity at the wall. Ideally, Z is a wall property and independent of the acoustic field. However, in particular near resonance, when the frequency of the external sound field is close to the eigenfrequency of the cavity, Z is amplitude dependent for high but relevant amplitudes, for example, the buzz saw noise in a turbofan engine due to the shocks produced in front of the fan at take off and the blade tips operate in a supersonic regime [19, 3]. Since liners are designed to operate at resonance because of the highest achieved attenuation of the sound, it is important to know quantitatively and understand qualitatively such impedances Z with good precision. In Chapter 3, a systematic derivation of the asymptotic solution of the non linear Helmholtz resonator equation is performed to obtain an analytic expression of the impedance for near resonance frequencies. The obtained analytic expression is then compared with existing experimental data. In the modeling assumptions, the cavity length is considered to be smaller than to the acoustic wavelength so that the pressure inside is uniform and the exit velocity is given by the time derivative of the pressure. In this way, the cavity behaves like a spring, subjected to the external excitation.

This model is then improved in Chapter 4 to accommodate the waves inside the cavity, and is extended to resonators of large depth. The pressure inside the cavity is then no longer uniform and the relation between pressure and velocity is obtained by solving the wave equation inside the cavity. In this way, the model captures more physics of the problem and the results are indeed improved as we will see later. Also, in the limit of a low excitation frequency, the results converge to the previous model as expected.

1.4.2 Vorticity scattering at hard - soft wall transition

In the subsequent chapters, we study the vorticity scattering phenomenon introduced earlier at a hard - soft wall transition and vice versa. An artistic impression of the problem is shown in Fig. 1.5. The Reynolds number is large so that viscous effects are negligible. We consider a low Mach numbers to stay within the incompressible limit. Under these condition, the flow is governed by the linearised Euler's equations. The flow is modeled with a linear shear profile shown in Fig. 1.4 and 1.5 which enables us to obtain the exact analytic solution. The incident field (vorticity field) of perturbations

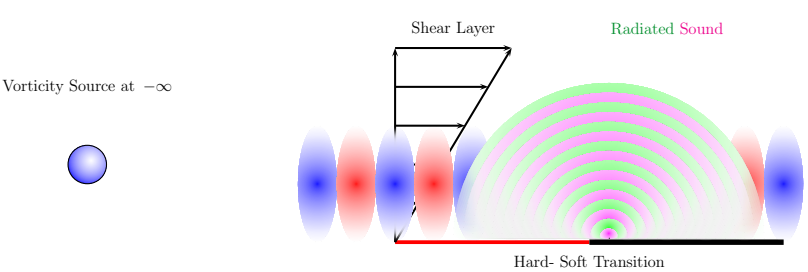

Figure 1.5: Artistic impression of the vorticity scattering problem.

in the case of linear shear may be considered as being produced by a monopole type mass source placed far upstream in the flow and is assumed to be vanishing at infinity. The initial field satisfies the hard wall boundary condition. The effect of the soft wall and hence the scattering is captured by the Wiener-Hopf method by exploiting analytic continuation properties of half range Fourier transform to obtain the solution in the form of Fourier integrals. This incompressible problem is a small part of a larger compressible problem and is referred as the inner solution. Next we derive the acoustic outer solution by solving the Helmholtz equation. In order to obtain the scattered sound field, we match the outer limit of our inner solution with the inner limit of our outer solution.

We start in Chapter 5 with a simplified case of pressure release wall which has zero impedance ($Z = 0$). The advantages of this limit are considerable. The inner solution that we obtain in the form of Fourier integrals is analytically integrable which yields valuable insight in to the problem. An explicit analytic expression of our solution and it's outer limit is easy to interpret and understand. In Chapter 6, we extend this analysis to a general wall impedance Z. Here we rely on the asymptotic limit of our inner solution integrals in the far field to match to the outer solution. This matching is validated against the explicit results of a pressure release wall. Based upon the frequency of the incoming wake ω and the shear parameter σ, the problem appears to split up into two different classes. In the low shear case when $\sigma < \omega$, the inner solution matches with the outer solution and we obtain the radiating acoustic pressure varying as $r^{-\frac{1}{2}}$ where r is the distance from the hard soft transition point. In the high shear case when $\sigma > \omega$, the radiating pressure behaves as a constant without possible matching with outerfield and the linear shear profile is found to be an inconsistent modeling assumption.

1.4.3 Vorticity scattering at soft - hard wall transition

We subsequently study the above problem when the transition is from soft to hard *i.e.* opposite to the previous chapters. Because of the presence of the shear, the problem is not symmetric and also, the initial field is different here because it satisfies the soft wall boundary condition rather than the hard wall condition of previous case. In particular, the Wiener-Hopf solution differs in a subtle way. In Chapter 7, we start with the $Z = 0$ limit again and conclude the analysis for the finite impedance case. For the low and high shear cases, the behavior of the outer sound field pressure is again found to be varying as $r^{-\frac{1}{2}}$ and as a constant respectively. Apart from the confirmation of the previous hard-soft analysis, the effect of boundary condition reversal is found to be insignificant to the scattering process. The radiated sound field differs only by a constant and has similar functional behaviour.

1.4.4 Experimental observation of hydrodynamic wave in a flow duct with porous walls

When the acoustic wave superimposed on a mean flow passes along any wall transition, it may excites a hydrodynamic instability or hydrodynamic mode. This instability can exchange energy with the sound field and can amplify the radiated noise. This behaviour was known in the case of locally reacting liners [75]. In Chapter 8, we will find experimental evidence of this wave along the porous material triggered by acoustic waves. A swept sound wave with frequency range varying from 100Hz to 3000Hz is superimposed on a fully developed mean flow in a rectangular channel. The amplitude and phase are acquired in front of the lining surface using the Agilent VXI 1432 hardware platform which drives the source excitation synchronously with the acoustic pressure signals recording. Using this data, the properties of the hydrodynamic wave are extracted. It is found that the excitation and properties of the instability are highly dependent on the Mach number in the channel, amplitude and frequency of the sound wave. The convection velocity of the hydrodynamic wave was found to be close to half of the mean flow speed. Otherwise, it is difficult to claim any firm conclusions about the amplitude growth rate of this mode because of the non linear behavior that indicates a saturation of this hydrodynamic wave.

The above experiments were conducted in Université du Maine, France under the supervision of Yves Aurégan and the work has been published in [13].

The individual Chapters 3, 4, 5, 6, 7 and 8 of the book are published as papers in [84, 83, 30], [85], [76], [77], [82] and [13] respectively.

The work reported in this book was funded by European Union through ITN-project *FlowAirS* (contract no. FP7-PEOPLE-2011-ITN-289352), with coordinator Yves Aurégan.

Chapter 2

Derivation of the basic equations

In this chapter, we will derive and understand the basic governing equations to be used later in this thesis. We will start from the basic governing conservation equations of mass, momentum and energy in compressible form. Coupled with two constitutive equations that result from the assumptions that local thermodynamic equilibrium holds in the fluid and that it behaves in viscous or Newtonian way, we obtain a set of five equations known as the Navier Stokes equations. Since the sound propagation is a fast process, the heat does not get enough time to conduct while the friction effects remain small. Hence, it is reasonable to assume the absence of friction and thermal conduction and the fluid being a perfect gas to have a possible acoustic model. Next, we will scale the variables in the equations to understand the relative importance of various terms under different modeling assumptions used in the current work so that we can determine the terms that can be neglected to obtain the simpler models. Such a trade-off is very common in applied analysis. The simpler models are easier to analyze mathematically and give more insight in the problem.

2.1 Conservation laws and constitutive equations

The laws of mass, momentum and energy conservation in terms of the flow variables pressure p, density ρ, velocity $\boldsymbol{v}$, viscous stress tensor $\boldsymbol{\tau}$, internal energy e and heat flux vector $\boldsymbol{q}$ are given by [81]

$$\frac{\partial \rho}{\partial t} + \nabla \cdot (\rho \boldsymbol{v}) = 0 \tag{2.1}$$

$$\frac{\partial (\rho \boldsymbol{v})}{\partial t} + \nabla \cdot (\rho \boldsymbol{v}\boldsymbol{v}) = -\nabla p + \nabla \cdot \boldsymbol{\tau} \tag{2.2}$$

$$\frac{\partial (\rho \boldsymbol{E})}{\partial t} + \nabla \cdot (\rho \boldsymbol{E}\boldsymbol{v}) = -\nabla \cdot \boldsymbol{q} - \nabla \cdot (p\boldsymbol{v}) + \nabla \cdot (\boldsymbol{\tau}\boldsymbol{v}) \tag{2.3}$$

with the specific total internal energy given as $E = e + \frac{1}{2}\boldsymbol{v}^2$, *i.e.* the summation of specific internal energy and specific kinetic energy.

Introducing the enthalpy function $h = e + \frac{p}{\rho}$, we have the fundamental law of thermodynamics for reversible processes as

$$T\mathrm{d}s = \mathrm{d}e + p\mathrm{d}\rho^{-1} = \mathrm{d}h - \rho^{-1}\mathrm{d}p \tag{2.4}$$

where T and s are temperature and entropy of the system, respectively. If we rewrite the above equation using convective derivative $\frac{\mathrm{d}}{\mathrm{d}t} = \frac{\partial}{\partial t} + \boldsymbol{v}\cdot\nabla$, we have

$$\frac{\mathrm{d}\rho}{\mathrm{d}t} = -\rho\nabla\cdot\boldsymbol{v} \tag{2.5}$$

$$\rho\frac{\mathrm{d}\boldsymbol{v}}{\mathrm{d}t} = -\nabla p + \nabla\cdot\boldsymbol{\tau} \tag{2.6}$$

$$\rho\frac{\mathrm{d}e}{\mathrm{d}t} = -\nabla\cdot\boldsymbol{q} - p\nabla\cdot\boldsymbol{v} + \boldsymbol{\tau}:\nabla\boldsymbol{v} \tag{2.7}$$

where $\boldsymbol{\tau}:\nabla\boldsymbol{v} = \nabla\cdot(\boldsymbol{\tau}\cdot\boldsymbol{v}) - \boldsymbol{v}\cdot(\nabla\cdot\boldsymbol{\tau})$ is the viscous dissipation term.

2.1.1 Viscous stress tensor $\boldsymbol{\tau}$ and heat flux vector $\boldsymbol{q}$, constitutive equations

In most of the applications, the viscous stress is neglected in the modelling assumptions. If this is not the case, a relation between $\boldsymbol{\tau}$ and the fluid deformation rate $(\nabla\boldsymbol{v} + (\nabla\boldsymbol{v})^T)$ is assumed because unlike solids, the stress is related to rate of strain in fluids rather than strain directly. When this relationship is linear, the fluids are called Newtonian fluids and the resulting equations are termed as Navier Stokes equations. Another simplification comes from the Stokes hypothesis that the fluid is in local thermodynamic equilibrium, hence the pressure p and the thermodynamic pressure are equivalent. In such case, we have

$$\boldsymbol{\tau} = \eta(\nabla\boldsymbol{v} + (\nabla\boldsymbol{v})^T) - \tfrac{2}{3}\eta(\nabla\cdot\boldsymbol{v})\boldsymbol{I} \tag{2.8}$$

where $\boldsymbol{I}$ is the unit tensor and the viscosity η is determined experimentally. Equation (2.8) is called a constitutive equation. The assumption of thermodynamic equilibrium fails partially at high frequencies and results in a dissipation related to the volume change $\nabla\cdot\boldsymbol{v}$ which is described with a volume viscosity parameter not simply related to η [67, 93] like in (2.8).

Another constitutive equation comes from the Fourier law which states a linear relationship between the heat flux vector $\boldsymbol{q}$ and the temperature gradient ∇T

$$q = -K\nabla T \tag{2.9}$$

where K is the thermal conductivity that depends on the pressure p and temperature

T. Using (2.4) and the equation for mechanical energy, obtained by taking the inner product of (2.2) with $\boldsymbol{v}$, we obtain the energy conservation law (2.3) written in two alternative forms

$$\rho\frac{\mathrm{d}h}{\mathrm{d}t} = \frac{\mathrm{d}p}{\mathrm{d}t} - \nabla\cdot q + \boldsymbol{\tau} : \nabla\boldsymbol{v} \tag{2.10}$$

$$\rho T\frac{\mathrm{d}s}{\mathrm{d}t} = -\nabla\cdot q + \boldsymbol{\tau} : \nabla\boldsymbol{v} \tag{2.11}$$

with (2.11) being the most convenient in acoustic applications because more often, the acoustic phenomena are isentropic since the right hand side of (2.11) is negligible.

For an ideal gas, we have the following relations

$$p = \rho RT, \qquad \mathrm{d}e = C_V\mathrm{d}T, \qquad \mathrm{d}h = C_P\mathrm{d}T \tag{2.12}$$

where C_P and C_V are the specific heat capacities at constant pressure and volume respectively that are functions of temperature only and R is the gas constant, $R = C_P - C_V$. The ratio $\gamma = C_P/C_V$ is called the specific heat ratio which is practically constant and independent of temperature for perfect gases. From (2.4), we have for ideal gases,

$$\mathrm{d}s = C_V\frac{\mathrm{d}p}{p} - C_P\frac{\mathrm{d}\rho}{\rho}. \tag{2.13}$$

The isentropic perturbations $\mathrm{d}s = 0$, like sound, propagates with the sound speed c given by

$$c^2 = \left(\frac{\partial p}{\partial \rho}\right)_s = \frac{\gamma p}{\rho} = \gamma RT. \tag{2.14}$$

In the incompressible limit, we see that the speed of sound approaches infinity.

2.2 Acoustic approximations

In this section, we will study the various acoustic modelling assumptions made in the current work. The modelling assumptions are taken based upon the knowledge of the 'importance' of the various terms in the compressible Navier Stokes equations determined after scaling. Suitable reference scales are needed to scale the variables and each scale is determined by the order of magnitude of the respective variable in the problem. For example, if the typical value of a variable y of a problem varies over a range y_0, we would scale it as $y = y_0 y'$, where $y' \sim O(1)$. Once we scale all the variables such that the resulting unknowns are $O(1)$ like y', we feed the variables back in the modeling equations and then determine the relative importance of various terms. That is how one generally approach to a suitable modeling assumption.

2.2.1 Non viscous and isentropic

In the considered cases, the viscous or turbulent shear stress terms will be assumed to play a role only in the aerodynamic source region while any perturbation is too fast to be affected by heat conduction. Hence, for the acoustic applications as we will see, the viscous shear stress term $\boldsymbol{\tau}$ and thermal heat conduction $\boldsymbol{q}$ are ignored. We conclude these assumptions as follows.

Suppose that we have a typical length L, velocity v_0, density ρ_0, temperature T_0 and temperature difference ΔT in the problem. In (2.4), (2.8) and (2.9), we introduce the following hydrodynamic scaling to make the variables dimensionless

$$
\begin{aligned}
x := Lx, \qquad \boldsymbol{v} := v_0\boldsymbol{v}, \qquad t := \frac{L}{v_0}t, \qquad \rho = \rho_0\rho, \\
\mathrm{d}p := \rho_0 v_0^2 \mathrm{d}p, \qquad \boldsymbol{\tau} := \frac{\mu v_0}{L}\boldsymbol{\tau}, \qquad \boldsymbol{q} = \frac{\kappa\Delta T}{L}\boldsymbol{q} \\
T := T_0 T, \qquad \mathrm{d}T = \Delta T \mathrm{d}T, \qquad \mathrm{d}s := \frac{C_P \Delta T}{T_0}\mathrm{d}s.
\end{aligned}
$$

This results in

$$
\begin{aligned}
\frac{\mathrm{d}\rho}{\mathrm{d}t} &= -\rho\nabla\cdot\boldsymbol{v} \\
\rho\frac{\mathrm{d}\boldsymbol{v}}{\mathrm{d}t} &= -\nabla p + \frac{1}{Re}\nabla\cdot\boldsymbol{\tau} \\
\rho T\frac{\mathrm{d}s}{\mathrm{d}t} &= -\frac{1}{Pe}\nabla\cdot\boldsymbol{q} + \frac{Ec}{Re}\boldsymbol{\tau} : \nabla\boldsymbol{v}
\end{aligned}
\tag{2.15}
$$

where $Re = \frac{\rho_0 v_0 L}{\mu}$, $Pe = \frac{\rho_0 C_P v_0 L}{\kappa}$ and $Ec = \frac{v_0^2}{C_P \Delta T}$ denote the Reynolds number, Peclet number and Eckert number respectively and κ is the heat conductivity per unit length. The Reynolds number and Peclet number are related by the relation $Pe = PrRe$ where the Prandtl number $Pr \sim O(1)$ for most fluids and gases. Hence if the Reynolds number approach to infinity, usually the Peclet number also does. If we assume that the Reynolds number is large enough so that the viscous and heat conduction terms are small compared to other terms and the Eckert number is not too large, we obtain

$$
\frac{\mathrm{d}\rho}{\mathrm{d}t} = -\rho\nabla\cdot\boldsymbol{v} \tag{2.16}
$$

$$
\rho\frac{\mathrm{d}\boldsymbol{v}}{\mathrm{d}t} = -\nabla p \tag{2.17}
$$

$$
\frac{\mathrm{d}s}{\mathrm{d}t} = 0 \tag{2.18}
$$

which means that the entropy is preserved along a streamline and hence from (2.4), $\mathrm{d}h = \rho^{-1}\mathrm{d}p$. If we assume that the gas is perfect (constant C_P and C_V), we have the following thermodynamic closure relationship in dimensional form

$$
C_V\frac{\mathrm{d}p}{p} - C_P\frac{\mathrm{d}\rho}{\rho} = 0, \qquad c^2 = \frac{\gamma p}{\rho}, \tag{2.19}
$$

where c appears to be the speed of sound. Substituting (2.19) into (2.18), we obtain the isentropic relation between pressure and density in dimensional form,

$$\frac{\mathrm{d}p}{\mathrm{d}t} = c^2 \frac{\mathrm{d}\rho}{\mathrm{d}t}. \tag{2.20}$$

If s is uniformly constant *i.e.* homentropic flow, $p = p(\rho)$ and so

$$p \propto \rho^{\gamma}. \tag{2.21}$$

2.2.2 Perturbations of a mean flow

When we have a stationary mean flow with instationary perturbations, given in dimensional form by

$$\boldsymbol{v} = \boldsymbol{v}_0 + \boldsymbol{v}', \qquad p = p_0 + p', \qquad \rho = \rho_0 + \rho', \qquad s = s_0 + s'$$

and linearize (2.16), (2.17) and (2.18) for small amplitude, we obtain for the mean flow

$$\begin{aligned} \nabla\cdot(\rho_0 \boldsymbol{v}_0) &= 0 \\ \rho_0(\boldsymbol{v}_0\cdot\nabla)\boldsymbol{v}_0 &= -\nabla p_0 \\ (\boldsymbol{v}_0\cdot\nabla)s_0 &= 0 \end{aligned}$$

while

$$\mathrm{d}s_0 = C_V \frac{\mathrm{d}p_0}{p_0} - C_P \frac{\mathrm{d}\rho_0}{\rho_0}, \qquad c_0^2 = \frac{\gamma p_0}{\rho_0}.$$

The perturbations satisfy the following relations

$$\begin{aligned} \frac{\partial \rho'}{\partial t} + \nabla\cdot(\boldsymbol{v}_0\rho' + \boldsymbol{v}'\rho_0) &= 0 \\ \rho_0\left(\frac{\partial}{\partial t} + \boldsymbol{v}_0\cdot\nabla\right)\boldsymbol{v}' + \rho_0(\boldsymbol{v}'\cdot\nabla)\boldsymbol{v}_0 + \rho'(\boldsymbol{v}_0\cdot\nabla)\boldsymbol{v}_0 &= -\nabla p' \\ \left(\frac{\partial}{\partial t} + \boldsymbol{v}_0\cdot\nabla\right)s' + \boldsymbol{v}'\cdot\nabla s_0 &= 0 \end{aligned} \tag{2.22}$$

while assuming the initial entropy perturbation $s'_{\mathrm{ini}} = 0$,

$$s' = \frac{C_V}{p_0}p' - \frac{C_P}{\rho_0}\rho' = \frac{C_V}{p_0}(p' - c_0^2\rho').$$

2.2.3 Incompressible limit

Introducing the 3 useful numbers in acoustic and fluid dynamics

$$\text{Mach number:} \qquad M = \frac{v_0}{c_0} \tag{2.23}$$

$$\text{Helmholtz number:} \qquad He = \frac{\omega L}{c_0} \tag{2.24}$$

$$\text{Strouhal number:} \qquad St = \frac{He}{M} = \frac{\omega L}{v_0}, \tag{2.25}$$

we see that in the incompressible limit, when the sound speed approaches to infinity, we may have the small Mach number M and Helmholtz number He such that the ratio being the Strouhal number St is $O(1)$. In such limit, waves such as sound waves can not be represented because the medium is incompressible and we see a uniform pressure of infinite wavelength in the system. However, such limits are quite useful when we perform a Matched Asymptotic Expansion MAE analysis for example. If an incompressible problem acts as an inner problem of an outer compressible problem and we obtain the solutions separately, MAE could be used to formulate a global solution that we might use later. Note that in the incompressible limit, the density perturbations in (2.22) vanish.

2.2.4 Time harmonic perturbations and mean flow in 2D

Suppose that we have an incompressible mean shear flow $(u_0 = U(y), v_0 = 0, \rho_0)$ in 2D as shown in Fig. 1.4 superimposed with time harmonic perturbations of the form $u = \mathrm{Re}(\hat{u}\,\mathrm{e}^{\mathrm{i}\omega t})$, $v = \mathrm{Re}(\hat{v}\,\mathrm{e}^{\mathrm{i}\omega t})$ and $p = \mathrm{Re}(\hat{p}\,\mathrm{e}^{\mathrm{i}\omega t})$. From (2.22), we obtain

$$\begin{aligned} \rho_0 \left(\frac{\partial \hat{u}}{\partial x} + \frac{\partial \hat{v}}{\partial y} \right) &= 0, \\ \rho_0 \left(\mathrm{i}\omega + U \frac{\partial}{\partial x} \right) \hat{u} + \rho_0 \frac{\mathrm{d}U}{\mathrm{d}y} \hat{v} + \frac{\partial \hat{p}}{\partial x} &= 0, \\ \rho_0 \left(\mathrm{i}\omega + U \frac{\partial}{\partial x} \right) \hat{v} + \frac{\partial \hat{p}}{\partial y} &= 0. \end{aligned} \tag{2.26}$$

This set (2.26) will be used later when we study the vortical perturbations in a linear shear flows.

2.3 Wave equation and acoustic compactness

By subtracting the time derivative of the linearised mass conservation (2.22) from the divergence of momentum conservation, neglecting the viscosity and having vanishing mean flow, we obtain the wave equation

$$\frac{1}{c^2} \frac{\partial^2 p}{\partial t^2} - \nabla^2 p = 0. \tag{2.27}$$

If we assume time harmonic perturbations as earlier, we obtain the Helmholtz equation

$$\nabla^2 p + \kappa^2 p = 0, \qquad \kappa = \omega/c. \tag{2.28}$$

The solution of (2.28) with point source in the origin in 2D polar coordinates consists of Bessel functions or combinations of Bessel functions called Hankel function. The Hankel functions $H_\nu^{(1)}(\kappa r)$ and $H_\nu^{(2)}(\kappa r)$ are used for incoming and outgoing wave solutions respectively with $\mathrm{e}^{\mathrm{i}\omega t}$ convention. In the low frequency limit (large wavelength), $\kappa \to 0$, we again enter in the incompressible regime and (2.28) reduces to Laplace equation

$$\nabla^2 p = 0. \tag{2.29}$$

The solution of (2.29) are harmonic functions. The solution for a point source in the origin that we are interested in is proportional to $\log r$, $r = \sqrt{x^2 + y^2}$.

For small values of argument (κr) *i.e.* in the innerfield, the Hankel function behaves like $\mathrm{e}^{\pm \mathrm{i}\kappa r} / \sqrt{r}$ that we need to match with the logarithm function in order to perform the asymptotic matching.

If we scale the space in (2.28) using a length parameter L , we have

$$\nabla^2 p + (He)^2 \, p = 0, \qquad He = \omega L/c. \tag{2.30}$$

If the Helmholtz number is small ($He \ll 1$), the wave would not see the details of any object of lengthscale less than L in the domain and we say that the domain is acoustically compact. This way, we can determine the lengthscale of the object that could potentially tamper with the properties of the waves.

Chapter 3

Systematic non linear impedance model for a Helmholtz resonator type liner

3.1 Introduction

An important type of acoustic liner for aero-engine inlet and exhaust ducts constitutes of a honeycomb array of small cells called Helmholtz resonators. The Helmholtz resonator is a cavity filled with air and having a small opening called the neck. When excited with a fluctuating external pressure, the mass of the air plug inside the neck moves against the large volume of compressible air inside the cavity, which acts as a spring, while viscous forces and vortex shedding cause dissipation of energy. Altogether this establishes a mass-spring-damper system. The damping is normally relatively small such that a resonance frequency can be identified. At and near resonance, the dissipation is largest and so narrow band sound absorption is achieved for frequencies close to resonance. This process is the basic design criterion for the liners. The resonator, as "seen" from outside, is characterized by its impedance $Z = Z(\omega)$, relating (spatially averaged) pressure and velocity at the wall. Ideally, Z is a wall property and independent of the acoustic field. However, in particular near resonance Z is amplitude dependent for high but relevant amplitudes, for example, the "buzz saw" noise in a turbofan engine due to the shocks produced in front of the fan at take off when the blade tips operate in a supersonic regime [19, 3]. Since liners are designed to operate at resonance, it is important to know quantitatively and understand qualitatively such impedances Z with good precision.

The non linear effects are mainly of hydrodynamical origin, due to the resistive

losses and vortex shedding at inflow/outflow from the opening. This is physically a process of great complexity [39, 81] which has indeed exacerbated the possibility to obtain the impedance with an accurate model based on first principles. Ingard and Labate [92] investigated the motion of air associated with sound waves at audio frequencies in the neighbourhood of an orifice and proved a quantitative connection with the non linearities of the impedance of orifices. Guess [6] developed a semi empirical method for calculating the parameters of a perforate in order to achieve a specified acoustic impedance for single-frequency excitation. Zinn [15] proposed a resistance formulation with the aid of conservation equations. Cummings and Eversman [2] demonstrated theoretically, with some approximations that the net acoustic energy dissipation can occur when sound waves interact with free shear layers and compared the predicted and measured net energy loss in the transmission of high amplitude impulsive acoustic waves. Hersh and Walker [36] proposed a non linear differential equation as a model for Helmholtz resonator response to a sound wave in the presence of a grazing mean flow and provided a semi empirical solution of the problem. The fundamental nature of their problem is the *very* high amplitude excitation of the resonator in the presence of a grazing flow and hence a differential equation (slightly) different from ours. Innes and Crighton [29] obtained a complete systematic solution to this model equation using matched asymptotic expansions.

In these examples, the non linear corrections of the impedance are based on physically inspired modelling assumptions, but otherwise do not aim to solve the equations of the non linear resonator [87, 35, 5]. In contrast, the properties of the Helmholtz resonator have been obtained from the full equations in [22, 23, 19, 20, 40, 21, 68], but these are all fully CFD (for example DNS or LES) simulations which do not give information for the simpler models.

The present work focuses on a systematic derivation of an asymptotic solution of a stand-alone non linear Helmholtz resonator equation from first principles. The extra complication of grazing flow along the liner wall will not be considered here. This effect is important if the mean flow boundary layer is thin enough and the resonator outflow velocity is comparable to or higher than the mean flow velocity.

We start with the classical modelling of the Helmholtz resonator and formulate a perturbation problem in terms of a small parameter ε which is based on the excitation amplitude of a given pressure of fixed frequency. The stationary solution of this problem is solved asymptotically up to second order. Secular effects of the external forcing are treated in the usual way by a suitable Lindstedt-Poincaré type transformation. A non standard problem was the presence of a modulus term $|u|$ involving the velocity. This prohibits a standard asymptotic expansion because the location of the zeros of u are a priori unknown. This problem has been tackled by adding an unknown shift of the origin, to be determined along with the construction of the solution, and using the fact that the stationary solution has the same periodicity as the driving force.

A more complete model that capture more physics of this damping phenomenon is derived in the next Chapter, 4.

3.2 Mathematical formulation

A sketch of the Helmholtz resonator considered is shown in Fig. 3.1. A simple and classic model (in various forms presented in the previously mentioned literature), that includes non linear separation effects for the air flow in and out the neck, is derived as follows. If the cross-sectional area S_b of the bottle is large compared to

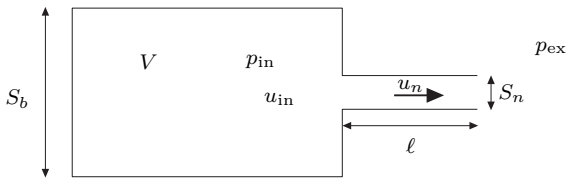

Figure 3.1: Helmholtz resonator

the cross sectional area S_n of the neck, the acoustic velocities in the bottle will be small compared to those in the neck. Hence we may assume that the pressure and density perturbations p_{in} and ρ_{in} in the bottle are uniform. It should be noted that the neck area S_n is to be interpreted as the effective cross section. In other words, the geometric cross section multiplied by a discharge coefficient, to include what is commonly known as the *vena contracta* effect (due to separation of the streamlines at the opening edge). This will normally be a weak function of the amplitude [88], but is assumed to be constant here.

If the cavity neck is acoustically compact, *i.e.* $k\ell \ll 1$ for a typical wave number $k = \omega/c_0$, we can neglect compressibility in the neck and determine the line integral of the momentum equation from (2.1), (2.2) and (2.8)

$$\rho_0\Big(\frac{\partial \boldsymbol{v}}{\partial t} + \boldsymbol{v}\cdot\nabla\boldsymbol{v}\Big) + \nabla p = \mu\nabla^2\boldsymbol{v}$$

along a typical streamline with velocity $\boldsymbol{v}$ from a point (just) inside to a point (just) outside the neck. We obtain the relation

$$\rho_0 \int_{\text{in}}^{\text{ex}} \frac{\partial \boldsymbol{v}}{\partial t}\cdot\mathbf{d}\boldsymbol{s} + \tfrac{1}{2}\rho_0(v_{\text{ex}}^2 - v_{\text{in}}^2) + (p_{\text{ex}} - p_{\text{in}}) = \int_{\text{in}}^{\text{ex}} \mu\nabla^2\boldsymbol{v}\cdot\mathbf{d}\boldsymbol{s}, \tag{3.1}$$

with $v = \|\boldsymbol{v}\|$ and μ denoting the viscosity. Following Melling [87] we average pressure and velocity along the neck's cross section, assume that the averaged squared velocity is approximately equal to the squared averaged velocity, and obtain

$$\rho_0 \int_{\text{in}}^{\text{ex}} \frac{\partial \bar{\boldsymbol{v}}}{\partial t}\cdot\mathbf{d}\boldsymbol{s} + \tfrac{1}{2}\rho_0(\bar{v}_{\text{ex}}^2 - \bar{v}_{\text{in}}^2) + (p_{\text{ex}} - p_{\text{in}}) = \int_{\text{in}}^{\text{ex}} \mu\overline{\nabla^2\boldsymbol{v}}\cdot\mathbf{d}\boldsymbol{s}. \tag{3.2}$$

Assuming that the streamline does not change in time, we have

$$\int_{\text{in}}^{\text{ex}} \frac{\partial \bar{\boldsymbol{v}}}{\partial t}\cdot\mathbf{d}\boldsymbol{s} = \frac{\mathrm{d}}{\mathrm{d}t}\int_{\text{in}}^{\text{ex}} \bar{\boldsymbol{v}}\cdot\mathbf{d}\boldsymbol{s}. \tag{3.3}$$

The velocity line integral evidently scales on a typical length times a typical velocity. If end effects are minor, we can use the neck flux velocity $\bar{\boldsymbol{v}} = u_n \boldsymbol{e}_x$ with a corresponding length being the neck length ℓ, added by a small end correction δ to take into account the inertia of the acoustic flow at both ends just outside the neck (inside and outside the resonator). Then we have

$$\int_{\text{in}}^{\text{ex}} \bar{\boldsymbol{v}} \cdot \mathbf{d}\boldsymbol{s} = (\ell + 2\delta) u_n. \tag{3.4}$$

End corrections δ for various geometries are given by Ingard [90]. For a circular orifice, for example, we may use

$$\delta = 0.85 \left(\frac{S_n}{\pi} \right)^{\frac{1}{2}}, \tag{3.5}$$

although one should be aware of the fact that this suggests an accuracy, totally incompatible with the modelling assumptions necessary for (3.4). Experiments show that δ weakly depends on the excitation amplitude [88], however, it is not a problem parameters for the current model.

For the stress term line integral we observe that, apart from u_n itself, it will depend on flow profile, Reynolds number, wall heat exchange, turbulence, separation from sharp edges, and maybe more. Following Melling [87], we will take these effects together in a resistance factor R, which will be assumed relatively small, in order to have resonance and a small decay per period to begin with. We thus have

$$\int_{\text{in}}^{\text{ex}} \mu \overline{\nabla^2 \boldsymbol{v}} \cdot \mathbf{d}\boldsymbol{s} = -R u_n. \tag{3.6}$$

(Note that this form is exact for a Poiseuille flow with parabolic profile). Due to separation from the outer exit, we have with outflow $\bar{v}_{\text{in}} \simeq 0$ with $\bar{v}_{\text{ex}} = u_n$ jetting out, while similarly during inflow, $\bar{v}_{\text{ex}} \simeq 0$ with $\bar{v}_{\text{in}} = u_n$ jetting into the cavity; see Fig. 3.2. The pressure in the jets, however, has to remain equal to the surrounding pressure (p_{ex} and p_{in} respectively) because the boundary of the jet cannot support a pressure difference. Therefore, we have altogether

$$\rho_0 (\ell + 2\delta) \frac{\mathrm{d}}{\mathrm{d}t} u_n + \tfrac{1}{2} \rho_0 u_n |u_n| + R u_n = p_{\text{in}} - p_{\text{ex}}. \tag{3.7}$$

The second equation between p_n and u_n is obtained by applying the integral mass conservation law on the volume V of the cavity. The change of mass must be equal to the flux through the cavity neck, which is in linearised form for the density perturbation ρ_{in}

$$V \frac{\mathrm{d}\rho_{\text{in}}}{\mathrm{d}t} = -\rho u_n S_n \approx -\rho_0 u_n S_n. \tag{3.8}$$

Assuming an adiabatic compression of the fluid in the cavity, we have $p_{\text{in}} = c_0^2 \rho_{\text{in}}$.

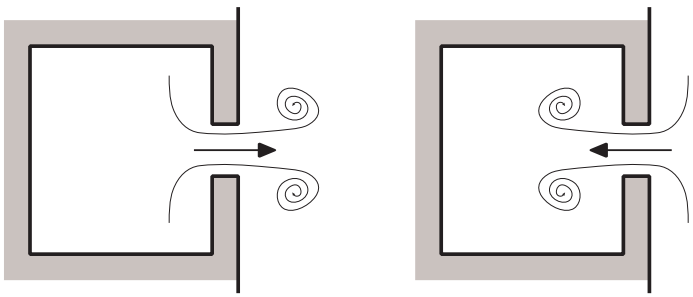

out-flow phase in-flow phase

Figure 3.2: Separation and vortex shedding during the out-flow and in-flow phase

Elimination of ρ_{in} and u_n from (3.7) by using (3.8) and redefining $(\ell + 2\delta) =: \ell$ yields the non linear Helmholtz resonator equation

$$\frac{\ell V}{c_0^2 S_n}\frac{\mathrm{d}^2 p_{\text{in}}}{\mathrm{d}t^2} + \frac{V^2}{2\rho_0 c_0^4 S_n^2}\frac{\mathrm{d}p_{\text{in}}}{\mathrm{d}t}\left|\frac{\mathrm{d}p_{\text{in}}}{\mathrm{d}t}\right| + \frac{RV}{\rho_0 c_0^2 S_n}\frac{\mathrm{d}p_{\text{in}}}{\mathrm{d}t} + p_{\text{in}} = p_{\text{ex}}. \tag{3.9}$$

For a proper analysis it is most clarifying to rewrite the equation into non dimensional variables. For this we need an inherent timescale and pressure level. For vanishing amplitudes and negligible dissipation the equation describes a harmonic oscillator, so the reciprocal of its angular frequency

$$\omega_0 = \frac{c_0}{\ell}\left(\frac{\ell S_n}{V}\right)^{1/2}$$

is a suitable timescale of the problem. By dividing the non linear damping term by the acceleration term we find the pressure level $2\rho_0 c_0^2 \ell S_n/V$ at which the non linear damping would be just as large as the other terms. So for a pressure that is a small fraction, say ε, of this level we have a problem with only little non linear damping. In addition we assume that the linear damping is small and of the same order of magnitude as the non linear damping (that is to say: near resonance. Away from resonance the non linear term will be relatively smaller). Also, the driving amplitude p_{ex} will be an order smaller than p_{in}. In order to make all this explicit we introduce a small parameter ε (via the external forcing amplitude), and make dimensionless

$$\tau = \omega_0 t, \quad p_{\text{in}} = 2\varepsilon\rho_0 c_0^2\Big(\frac{\ell S_n}{V}\Big)y, \quad p_{\text{ex}} = 2\varepsilon^2\rho_0 c_0^2\Big(\frac{\ell S_n}{V}\Big)F, \quad R = \varepsilon\rho_0 c_0\Big(\frac{\ell S_n}{V}\Big)^{1/2} r, \tag{3.10}$$

where $0 < \varepsilon \ll 1$ and $r, y, F = O(1)$.

Suppose that we excite the Helmholtz resonator harmonically, such that $p_{\text{ex}} = C\cos(\omega t) + H(t)$ consists of a time-harmonic component of frequency ω plus a small contribution of higher harmonics H due to the interaction with the resonator[1]. In

[1] H will play no role in the results, but appears from the liner application of section 3.5. Here,

the scaled variables τ and F this becomes

$$F = F_0 \cos(\Omega\tau) + \varepsilon^\nu h(\tau), \qquad \Omega = \frac{\omega}{\omega_0}, \tag{3.11}$$

where $\nu = 1$ in the resonant case and $\nu = 2$ in the non resonant case.

Note that ε is a bookkeeping parameter, meant to measure the "smallness" of the various parameters and variables. In practice it is determined by the external forcing p_{ex}, so in the simple case of a harmonic excitation we can take $F_0 = 1$, and this will be done in any example below. Hence we have, for a case with harmonic excitation at a pressure level given by *SPL* dB, an equivalent value of ε given by

$$\varepsilon = \left(\frac{2 \cdot 10^{-5} \cdot 10^{\frac{\text{SPL}}{20}}}{2\rho_0 c_0^2 \frac{\ell S_p}{V} \frac{1}{2}\sqrt{2}} \right)^{\frac{1}{2}}. \tag{3.12}$$

Finally we arrive at the weakly non linear forced oscillator as given by (3.13). The initial conditions are not important as we are interested only in the stationary state[2] of the oscillator synchronised with the forcing.

$$\frac{\mathrm{d}^2 y}{\mathrm{d}\tau^2} + \varepsilon \frac{\mathrm{d}y}{\mathrm{d}\tau} \left| \frac{\mathrm{d}y}{\mathrm{d}\tau} \right| + \varepsilon r \frac{\mathrm{d}y}{\mathrm{d}\tau} + y = \varepsilon F_0 \cos(\Omega\tau) + \varepsilon^{1+\nu} h(\tau). \tag{3.13}$$

We note in passing that the problem considered by Innes and Crighton[29] relates to ours if we replace $y'|y'|$ by $y'|y|$, assume $y = O(\varepsilon^{-2})$ and $F = O(\varepsilon^{-4})$, and neglect r.

3.3 Asymptotic analysis

3.3.1 Non resonant case

Away from resonance, when $1 - \Omega^2 = O(1)$, the perturbation problem is regular and relatively straightforward. We will include it here for reference.

We look for solutions of

$$y'' + \varepsilon y'|y'| + \varepsilon r y' + y = \varepsilon F_0 \cos(\Omega\tau) + \varepsilon^3 h(\tau) \tag{3.14}$$

that are only caused by the external forcing. Since this forcing term is $O(\varepsilon)$ and we are not near resonance, the response is of the same order of magnitude, and we transform $y = \varepsilon Y$, where $Y = O(1)$.

$$Y'' + \varepsilon^2 Y'|Y'| + \varepsilon r Y' + Y = F_0 \cos(\Omega\tau) + \varepsilon^2 h(\tau). \tag{3.15}$$

the external forcing field is a combination of incident and reflected waves, say $p_{\text{ex}} = f(t) + g(t)$ and $v_{\text{ex}} \propto f(t) - g(t)$. If incident part f is harmonic, reflected part g will be harmonic plus higher harmonics. We will see, however, that these higher harmonics are one or two orders of magnitude smaller, and therefore play no role in y_1, eq. (3.34), resp. Y_1, eq. (3.19).

[2] In the appendix it is proved that solutions of this equation (3.13) are stable, so the stationary solution exists.

After substituting the assumed expansion $Y(\tau;\varepsilon) = Y_0(\tau) + \varepsilon Y_1(\tau) + \varepsilon^2 Y_2(\tau) + \ldots$ and collecting the coefficients of $O(1)$, we have

$$Y_0'' + Y_0 = F_0 \cos(\Omega\tau). \tag{3.16}$$

The solution that follows the driving force is periodic with frequency Ω and so

$$Y_0 = \frac{F_0}{1-\Omega^2} \cos(\Omega\tau), \tag{3.17}$$

Next we collect the coefficients of $O(\varepsilon)$ to obtain

$$Y_1'' + Y_1 = -rY_0' = \frac{rF_0\Omega}{1-\Omega^2} \sin(\Omega\tau) \tag{3.18}$$

with solution

$$Y_1 = \frac{rF_0\Omega}{(1-\Omega^2)^2} \sin(\Omega\tau). \tag{3.19}$$

We may go on to $O(\varepsilon^2)$ and find the appearance of higher harmonics. Efficiently collecting terms together, we obtain for the full solution

$$y = \varepsilon F_0 \frac{(1-\Omega^2)\cos\Omega\tau + \varepsilon r\Omega \sin\Omega\tau}{(1-\Omega^2)^2 + \varepsilon^2 r^2 \Omega^2} + O(\varepsilon^3) \tag{3.20}$$

showing that the response is indeed $O(\varepsilon)$ and follows the excitation almost in phase ($1-\Omega^2 > 0$) or anti-phase ($1-\Omega^2 < 0$). This is not the case anymore near resonance when $1-\Omega^2 = O(\varepsilon)$.

3.3.2 Resonant case

Near resonance when $1-\Omega^2 = O(\varepsilon)$, it was assumed and indeed confirmed by (3.20) that the amplitude y rises to levels of $O(1)$, and the assumption that the non linear damping is negligible to leading orders is not correct. As the physics of the problem essentially change when $\Omega = 1+O(\varepsilon)$, we introduce a parameter $\sigma = O(1)$ and assume that

$$\Omega = 1 + \varepsilon\sigma. \tag{3.21}$$

However, posed in this form we obtain secular terms in the expansion $\cos(\tau+\varepsilon\sigma\tau) = \cos(\tau) - \varepsilon\sigma\tau\sin(\tau) + \ldots$ of the driving force, which prohibits a uniform approximation of y later [70, sec 15.3.2]. Therefore we remove the ε-dependence from the driving force by absorbing Ω into a new time coordinate.

Moreover, the asymptotic expansion of the modulus $|y'|$ introduces difficulties near the ε-dependent (and unknown) zeros of y'. This will be tackled by a translation of the origin by an amount $\theta(\varepsilon)$, such that the locations of the sign change of y' are fixed (as y is synchronised with the driving force) and independent of ε. (Of course, a certain amount of smoothness is anticipated such that y' has the same number of

zeros per period as the forcing term). So we introduce

$$\tilde{\tau} = \Omega\tau - \theta(\varepsilon)$$

to obtain

$$\Omega^2 \frac{\mathrm{d}^2 y}{\mathrm{d}\tilde{\tau}^2} + \varepsilon\Omega^2 \frac{\mathrm{d}y}{\mathrm{d}\tilde{\tau}} \left|\frac{\mathrm{d}y}{\mathrm{d}\tilde{\tau}}\right| + \varepsilon\Omega r \frac{\mathrm{d}y}{\mathrm{d}\tilde{\tau}} + y = \varepsilon F_0 \cos(\tilde{\tau} + \theta) + \varepsilon^2 h, \tag{3.22}$$

where θ is to be chosen such that $y'(\tilde{\tau}) = 0$ at $\tilde{\tau} = N\pi$. In other words, $\Omega\tau = \omega t = \theta$ corresponds with the phase lag of response p_{in} to excitation p_{ex}.

When we substitute the following (assumed uniform) asymptotic expansions for y and θ [69]

$$y(\tilde{\tau};\varepsilon) = y_0(\tilde{\tau}) + \varepsilon y_1(\tilde{\tau}) + \varepsilon^2 y_2(\tilde{\tau}) + \ldots, \quad \text{and} \quad \theta(\varepsilon) = \theta_0 + \varepsilon\theta_1 + \ldots,$$

and collect like powers of ε, we find for y_0

$$\frac{\mathrm{d}^2 y_0}{\mathrm{d}\tilde{\tau}^2} + y_0 = 0, \qquad y_0'(N\pi) = 0. \tag{3.23}$$

This has the general solution

$$y_0(\tilde{\tau}) = A_0 \cos(\tilde{\tau}), \tag{3.24}$$

with A_0 and θ_0 to be determined. Although y_0 is the result of driving force F, at this level we don't have any information about their relation yet, so we can't determine the integration constants A_0 and θ_0. Therefore, we continue with the next order y_1.

$$\begin{aligned}\frac{\mathrm{d}^2 y_1}{\mathrm{d}\tilde{\tau}^2} + y_1 &= F_0 \cos(\tilde{\tau} + \theta_0) - 2\sigma \frac{\mathrm{d}^2 y_0}{\mathrm{d}\tilde{\tau}^2} - \frac{\mathrm{d}y_0}{\mathrm{d}\tilde{\tau}} \left|\frac{\mathrm{d}y_0}{\mathrm{d}\tilde{\tau}}\right| - r\frac{\mathrm{d}y_0}{\mathrm{d}\tilde{\tau}} \\ &= F_0 \cos(\tilde{\tau} + \theta_0) + 2\sigma A_0 \cos(\tilde{\tau}) + A_0|A_0| \sin(\tilde{\tau})\,|\sin(\tilde{\tau})| + rA_0 \sin(\tilde{\tau})\end{aligned} \tag{3.25}$$

From the arguments that y is the stationary solution and its asymptotic expansion is uniform in $\tilde{\tau}$, it follows that no resonant excitation is allowed in the right hand side of the equation for y_1. This means that we should suppress the cos- and sin-terms, including the first term of the Fourier expansion of

$$\sin(\tilde{\tau})\,|\sin(\tilde{\tau})| = -\frac{1}{\pi} \sum_{n=0}^{\infty} \frac{\sin(2n+1)\tilde{\tau}}{(n^2 - \frac{1}{4})(n + \frac{3}{2})} = \tfrac{8}{3\pi} \sin\tilde{\tau} + \ldots \tag{3.26}$$

to obtain

$$F_0 \cos\theta_0 = -2\sigma A_0, \qquad F_0 \sin\theta_0 = \left(\tfrac{8}{3\pi}|A_0| + r\right) A_0 \tag{3.27}$$

or

$$\left[\left(\tfrac{8}{3\pi}|A_0| + r\right)^2 + (2\sigma)^2\right] A_0^2 = F_0^2, \qquad \tan(\theta_0) = -\frac{\frac{8}{3\pi}|A_0| + r}{2\sigma}. \tag{3.28}$$

In general, the equation for A_0 has to be solved numerically, from which θ_0 follows. There exist two (real) solutions, while if (A_0, θ_0) is a solution, then also $(-A_0, \theta_0 + \pi)$. So, if convenient, we could assume that A_0 is positive and maintain $|A_0| = A_0$, but this depends on θ_0.

The next order y_1 is then given by

$$y_1(\tilde{\tau}) = A_1 \cos\tilde{\tau} + B_1 \sin\tilde{\tau} + \frac{1}{4\pi} A_0|A_0| \sum_{n=1}^{\infty} \frac{\sin(2n+1)\tilde{\tau}}{n(n+1)(n^2-\frac{1}{4})(n+\frac{3}{2})} \tag{3.29}$$

with derivative

$$y_1'(\tilde{\tau}) = -A_1 \sin\tilde{\tau} + B_1 \cos\tilde{\tau} + \frac{1}{4\pi} A_0|A_0| \sum_{n=1}^{\infty} \frac{(2n+1)\cos(2n+1)\tilde{\tau}}{n(n+1)(n^2-\frac{1}{4})(n+\frac{3}{2})} \tag{3.30}$$

and so the boundary condition

$$\begin{aligned} y_1'(N\pi) &= -A_1 \sin(N\pi) + B_1 \cos(N\pi) \\ &\qquad + \frac{1}{4\pi} A_0|A_0| \sum_{n=1}^{\infty} \frac{(2n+1)\cos((2n+1)N\pi)}{n(n+1)(n^2-\frac{1}{4})(n+\frac{3}{2})} \\ &= (-1)^N B_1 + \frac{(-1)^N}{4\pi} A_0|A_0| \sum_{n=1}^{\infty} \frac{2n+1}{n(n+1)(n^2-\frac{1}{4})(n+\frac{3}{2})} \\ &= (-1)^N \left[B_1 + \tfrac{2}{9\pi} A_0|A_0|\right] = 0 \end{aligned} \tag{3.31}$$

is satisfied by

$$B_1 = -\frac{2}{9\pi} A_0|A_0|, \quad \text{because} \quad \sum_{n=1}^{\infty} \frac{2n+1}{n(n+1)(n^2-\frac{1}{4})(n+\frac{3}{2})} = \frac{8}{9}.$$

The sum of the telescoping series is easily found by partial fractions and noting the terms cancelling in pairs. Altogether we have

$$y_1(\tilde{\tau}) = A_1 \cos\tilde{\tau} - \frac{2}{9\pi} A_0|A_0| \sin\tilde{\tau} + \frac{1}{4\pi} A_0|A_0| \sum_{n=1}^{\infty} \frac{\sin(2n+1)\tilde{\tau}}{n(n+1)(n^2-\frac{1}{4})(n+\frac{3}{2})}. \tag{3.32}$$

The amplitude A_1 is to be determined in a similar way as with y_0 by suppressing resonant terms in y_2. The next order term y_2 is obtained from (3.22) when it is expanded to $O(\varepsilon^2)$ and terms of $O(\varepsilon^2)$ are collected

$$y_2'' + y_2 = -\sigma^2 y_0'' - 2\sigma y_1'' - 2\sigma y_0'|y_0'| - 2y_1'|y_0'| - r y_1' - r\sigma y_0' - \theta_1 F_0 \sin(\tilde{\tau} + \theta_0) + h. \tag{3.33}$$

After substituting y_0 and y_1, and considering only the terms on the right hand side

that are possibly in resonance with the left hand side, we obtain

$$\begin{aligned} y_2'' + y_2 =& \sigma^2 A_0 \cos\tilde\tau + 2\sigma A_1 \cos\tilde\tau - \tfrac{4}{9\pi}\sigma A_0|A_0|\sin\tilde\tau \\ &+ \left(2\sigma A_0 \sin\tilde\tau + 2A_1 \sin\tilde\tau + \tfrac{4}{9\pi}A_0|A_0|\cos\tilde\tau\right)|A_0\sin\tilde\tau| \\ &- \frac{1}{\pi}A_0|A_0|\sum_{n=1}^{\infty}\frac{\cos(2n+1)\tilde\tau}{n(n+1)(n-\frac{1}{2})(n+\frac{3}{2})}|A_0\sin\tilde\tau| \\ &+ rA_1\sin\tilde\tau + \tfrac{2}{9\pi}rA_0|A_0|\cos\tilde\tau + r\sigma A_0\sin\tilde\tau \\ &- \theta_1 F_0\cos\theta_0\sin\tilde\tau - \theta_1 F_0\sin\theta_0\cos\tilde\tau + \dots \end{aligned} \tag{3.34}$$

By Fourier expansion it can be found that

$$\cos\tilde\tau|\sin\tilde\tau| = \frac{4}{3\pi}\cos\tilde\tau + \dots, \quad \sum_{n=1}^{\infty}\frac{|\sin\tilde\tau|\cos(2n+1)\tilde\tau}{n(n+1)(n-\frac{1}{2})(n+\frac{3}{2})} = \frac{1}{\pi}\left(\frac{80}{27}-\frac{\pi^2}{3}\right)\cos\tilde\tau + \dots \tag{3.35}$$

and only higher harmonics otherwise. Suppressing the cos- and sin-terms of (3.34) thus results into

$$\begin{aligned} 2\sigma A_1 - \theta_1 F_0\sin\theta_0 &= -\sigma^2 A_0 - \left(\frac{1}{3}-\frac{64}{27\pi^2}\right)A_0^3 - \frac{2}{9\pi}rA_0|A_0| \\ \left(\frac{16}{3\pi}|A_0|+r\right)A_1 - \theta_1 F_0\cos\theta_0 &= -\left(\frac{44}{9\pi}|A_0|+r\right)\sigma A_0 \end{aligned} \tag{3.36}$$

By solving the linear system (3.36), we can obtain A_1 and θ_1.

3.4 Time-domain solution

The solution $y = y_0 + \varepsilon y_1 + O(\varepsilon^2)$ ascertains in principle (for small ε) a better approximation of y than the leading order approximation y_0, which would later provide a better approximation of the impedance. We have this full solution as

$$\begin{aligned} y(\tilde\tau;\varepsilon) = (A_0+\varepsilon A_1)\cos\tilde\tau &- \frac{2}{9\pi}\varepsilon A_0|A_0|\sin\tilde\tau \\ &+ \frac{1}{4\pi}\varepsilon A_0|A_0|\sum_{n=1}^{\infty}\frac{\sin(2n+1)\tilde\tau}{n(n+1)(n^2-\frac{1}{4})(n+\frac{3}{2})} + \dots. \end{aligned} \tag{3.37}$$

where $\tilde\tau = \omega t - \theta$ and $\theta = \theta_0 + \varepsilon\theta_1 + \dots$. The constants A_0, θ_0 and A_1, θ_1 can be determined from (3.27) and (3.36) respectively.

Consider first the leading order approximation. Equation (3.28) for A_0 has 2 real symmetric solutions (of which we normally need to consider only the positive one), but solving $A_0 = A_0(\sigma)$ is not straightforward. Therefore, it is useful to consider the

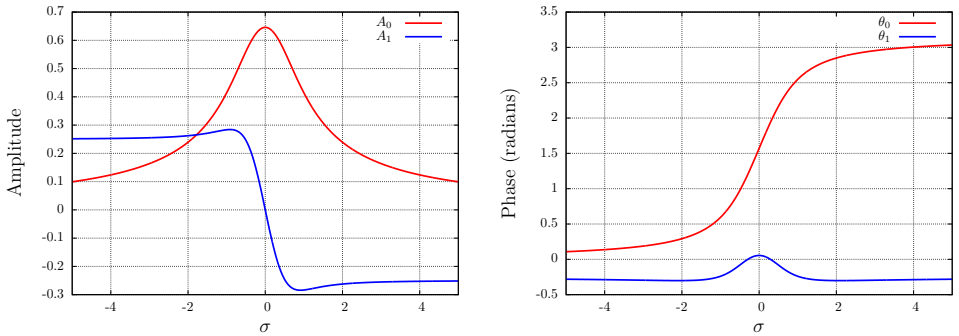

Figure 3.3: Solution of amplitude (A_0, A_1) and phase (θ_0 , θ_1) as a function of σ, while $r = F_0 = 1$

inverse, $\sigma = \sigma(A_0)$, given by

$$4\sigma^2 = \frac{F_0^2}{A_0^2} - \left(\frac{8}{3\pi}|A_0| + r\right)^2 \tag{3.38}$$

Since $\sigma^2 \geqslant 0$ we see immediately that solutions exists only for a finite interval in A_0, while $\sigma \to \infty$ only when $A_0 \to 0$. In particular, we have

$$A_0 \simeq \frac{F_0}{2|\sigma|}, \qquad \tan\theta_0 \simeq -\frac{r}{2\sigma} \quad \text{or} \quad \theta_0 \simeq -\frac{r}{2\sigma} + n\pi, \tag{3.39}$$

which is in exact agreement with the asymptotic behaviour for $\Omega = 1 + \varepsilon\sigma$, σ large, corresponding to the linear solution (3.17). In fact, by tracing the solution parametrically as a function of σ, we can see that if we start with $\theta_0 = 0$ for $\sigma \to -\infty$, we end with $\theta_0 = \pi$ for $\sigma \to \infty$. In this way, we have obtained the expression for A_0 and θ_0; see Fig. 3.3 for an example.

Substituting the obtained value of A_0 and θ_0 in (3.36), we can solve the linear algebraic system to obtain A_1 and θ_1. This way, we have determined all the coefficients in (3.37); hence, the solution y is known which, when used with (3.10), gives p_{in}

$$p_{\text{in}} = 2\varepsilon\rho_0 c_0^2 \frac{\ell S_n}{V}\Bigg[(A_0 + \varepsilon A_1)\cos(\omega t - \theta)$$
$$- \frac{2}{9\pi}\varepsilon A_0|A_0|\sin(\omega t - \theta) + \frac{1}{4\pi}\varepsilon A_0|A_0|\sum_{n=1}^{\infty}\frac{\sin(2n+1)(\omega t - \theta)}{n(n+1)(n^2 - \frac{1}{4})(n + \frac{3}{2})} + \dots\Bigg]. \tag{3.40}$$

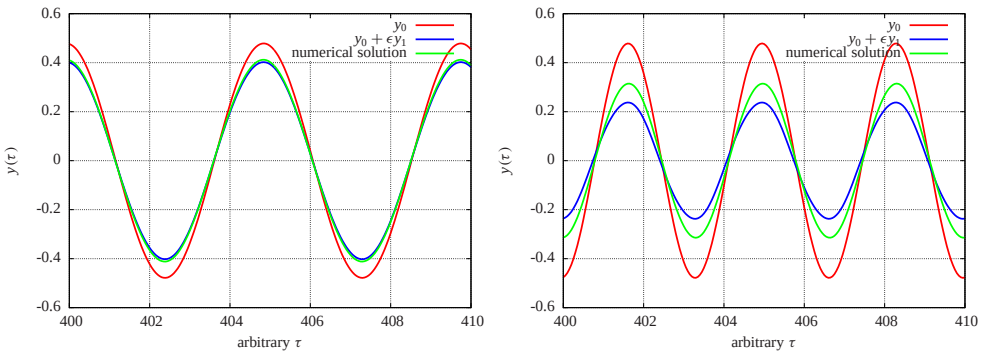

Figure 3.4: Comparison of solution y_0 and $y_0 + \varepsilon y_1$ for $r = 0.2$, $\sigma = 1$ and $\varepsilon = 0.28$ (left) and $\varepsilon = 0.88$ (right) with a fully numerical solution.

From this solution and (3.8) we may determine the neck velocity u_n

$$u_n = 2\varepsilon\omega\ell\Bigg[(A_0 + \varepsilon A_1)\sin(\omega t - \theta) + \frac{2}{9\pi}\varepsilon A_0|A_0|\cos(\omega t - \theta) - \frac{1}{4\pi}\varepsilon A_0|A_0|\sum_{n=1}^{\infty}\frac{(2n+1)\cos(2n+1)(\omega t - \theta)}{n(n+1)(n^2 - \frac{1}{4})(n + \frac{3}{2})} + \ldots\Bigg], \tag{3.41}$$

which will be used to obtain the impedance of the resonator in a later section.

3.4.1 Comparison in time-domain with a fully numerical solution

The solution (3.37), correct till $O(\varepsilon)$ (y_0) and $O(\varepsilon^2)$ ($y_0 + \varepsilon y_1$), are compared with a fully numerical solution of (3.13), obtained by Mathematica with a standard Runge-Kutta routine, see Fig. 3.4. In both cases $r = 0.2$, $\sigma = 1$, while $\varepsilon = 0.28$ in the left figure and $\varepsilon = 0.88$ in the right. Note that this last case is added to see how the solution behaves for values of ε that are really not small anymore. The one with $\varepsilon = 0.28$ is indeed remarkably accurate for $y_0 + \varepsilon y_1$, and we may observe an error of y_0 and $y_0 + \varepsilon y_1$ compared to y that follows indeed the predicted behaviour of $O(\varepsilon)$ and $O(\varepsilon^2)$. The one with $\varepsilon = 0.88$ cannot be expected to be really accurate, but surprisingly the results are still of the right order of magnitude.

We note, however, that there is always the assumption that $\sigma = O(1)$ and $1 - \Omega^2 = O(\varepsilon)$. In other words, the validity of the resonance solution is for an interval in frequency of $\omega = \omega_0(1 + O(\varepsilon))$. When we leave this interval, the non resonant solution (3.20) should gradually become applicable.

3.5 Impedance calculation

In order to obtain realistic numbers, we will consider the impedance Z as the effective impedance of an array of Helmholtz resonators, where the spatially averaged neck velocity is identified to the external acoustic velocity. Therefore, we add a porosity factor S_n/S_b to u_n and obtain

$$v_{\text{ex}} = \frac{S_n}{S_b} u_n. \tag{3.42}$$

Then we have to define what we mean with impedance for a sound field that is not entirely harmonic anymore. The natural choice is to define the impedance as the ratio of the Fourier transforms of the external pressure p_{ex} and (minus) the external velocity v_{ex} at excitation frequency ω.

$$Z(\eta) = \frac{\hat{p}_{\text{ex}}(\eta)}{-\hat{v}_{\text{ex}}(\eta)} = \frac{\frac{1}{2\pi}\int\limits_{-\infty}^{\infty} p_{\text{ex}}(t)\,\mathrm{e}^{-\mathrm{i}\eta t}\,\mathrm{d}t}{-\frac{1}{2\pi}\int\limits_{-\infty}^{\infty} v_{\text{ex}}(t)\,\mathrm{e}^{-\mathrm{i}\eta t}\,\mathrm{d}t} \quad (\eta = \omega). \tag{3.43}$$

3.5.1 Non resonant impedance

Taking the Fourier transforms of p_{ex} and v_{ex}, we have, from (3.14), (3.8), (3.10), for $\eta > 0$

$$\hat{p}_{\text{ex}}(\eta) = \frac{1}{2\pi}\int_{-\infty}^{\infty} p_{\text{ex}}(t)\,\mathrm{e}^{-\mathrm{i}\eta t}\,\mathrm{d}t = \frac{1}{2\pi}\varepsilon^2\rho_0 c_0^2 \frac{\ell S_n}{V} F_0 \delta(\eta-\omega) \tag{3.44}$$

and

$$\hat{v}_{\text{ex}}(\eta) = \frac{1}{2\pi}\int_{-\infty}^{\infty} v_{\text{ex}}(t)\,\mathrm{e}^{-\mathrm{i}\eta t}\,\mathrm{d}t = -\frac{1}{2\pi}\frac{S_n}{S_b}\varepsilon\omega\ell \times \left[-\varepsilon\frac{F_0}{1-\Omega^2}\frac{1}{\mathrm{i}}\delta(\eta-\omega) + \varepsilon^2\frac{rF_0\Omega}{(1-\Omega^2)^2}\delta(\eta-\omega)\right], \tag{3.45}$$

and so (with $V = LS_b$) we obtain

$$Z(\omega) = -\frac{\hat{p}_{\text{ex}}(\omega)}{\hat{v}_{\text{ex}}(\omega)} = \frac{\varepsilon\rho_0 c_0^2 F_0}{L\omega}\cdot\left(\frac{\varepsilon^2 r\Omega}{(1-\Omega^2)^2} + \mathrm{i}\frac{\varepsilon}{1-\Omega^2}\right)^{-1}. \tag{3.46}$$

To leading order in ε, we obtain the usual expression for the linear impedance of a mass spring damper type system as

$$Z(\omega) \simeq \frac{S_b}{S_n}\left(R + \mathrm{i}\rho_0\ell\omega_0\left(\frac{\omega}{\omega_0} - \frac{\omega_0}{\omega}\right)\right). \tag{3.47}$$

3.5.2 Resonant impedance

Taking the Fourier transforms of $p_{\rm ex}$ and $v_{\rm ex}$, we have for $\eta > 0$

$$\hat{p}_{\rm ex}(\eta) = \frac{1}{2\pi}\int_{-\infty}^{\infty} p_{\rm ex}(t)\,{\rm e}^{-{\rm i}\eta t}\,{\rm d}t = \frac{1}{2\pi}\varepsilon^2\rho_0 c_0^2\frac{\ell S_n}{V}F_0\delta(\eta-\omega) \tag{3.48}$$

and

$$\hat{v}_{\rm ex}(\eta) = \frac{1}{2\pi}\int_{-\infty}^{\infty} v_{\rm ex}(t)\,{\rm e}^{-{\rm i}\eta t}\,{\rm d}t = \frac{1}{2\pi}\frac{S_n}{S_b}\varepsilon\omega\ell\,{\rm e}^{-{\rm i}\theta}\Bigg[-{\rm i}(A_0+\varepsilon A_1)\delta(\eta-\omega)$$
$$+\frac{2}{9\pi}\varepsilon A_0|A_0|\delta(\eta-\omega) - \frac{1}{4\pi}\varepsilon A_0|A_0|\sum_{n=1}^{\infty}\frac{(2n+1)\delta(\eta-(2n+1)\omega)}{n(n+1)(n^2-\frac{1}{4})(n+\frac{3}{2})}+\dots\Bigg], \tag{3.49}$$

and so (with $V = LS_b$) we obtain

$$Z(\omega) = -\frac{\hat{p}_{\rm ex}(\omega)}{\hat{v}_{\rm ex}(\omega)} = \frac{\varepsilon\rho_0 c_0^2 F_0}{L\omega}\cdot\frac{-{\rm i}\,{\rm e}^{{\rm i}\theta}}{A_0+\varepsilon A_1+{\rm i}\frac{2}{9\pi}\varepsilon A_0|A_0|}. \tag{3.50}$$

It is interesting to consider Z to leading order in ε

$$Z(\omega) \simeq \frac{\varepsilon\rho_0 c_0^2 F_0}{L\omega}\,\frac{-{\rm i}\,{\rm e}^{{\rm i}\theta_0}}{A_0} = \rho_0 c_0\,\frac{c_0}{\omega L}\left(\frac{R}{\rho_0\omega_0\ell}+\frac{4}{3\pi}\frac{\|u_n\|}{\omega\ell}+2{\rm i}\frac{\omega-\omega_0}{\omega_0}\right) \tag{3.51}$$

(where $\|u_n\|$ denotes the amplitude of u_n) and observe that indeed ${\rm Re}(Z)$ is of the often assumed form $a+b\|u_n\|$. Although our a and b are no constants and depend on ω, this is a higher order effect because $\omega = \omega_0(1+O(\varepsilon))$. To leading order in ε they are constant. ${\rm Im}(Z)$ is independent of the excitation amplitude.

In order to illustrate formula (3.50), we have plotted in Fig. 3.5 resistance ${\rm Re}(Z)$ and reactance ${\rm Im}(Z)$ as a function of Ω, obtained for a typical geometry at different driving amplitudes, corresponding with ε varying from 0.05 to 0.28. As may be expected from (3.51), the main effect of the forcing amplitude is in the resistance. The reactance is practically independent of it. Typically, the resistance, being highest at or near the resonance frequency and decaying along both sides, increases everywhere with the amplitude, but more for frequencies less than resonance.

3.5.3 Comparison with Motsinger and Kraft

The behaviour in (3.50) may be compared in Fig. 3.6 with the measurements and predictions given by Motsinger and Kraft in [35]. Their predictions are (a.o.) based on a resistance of the form $R = \rho_0 c_0(a+b|v|)$ with suitably chosen a and b and $|v|$ corresponding to $\|u_n\|$ of our model. Unfortunately, only little experimental data for the higher amplitudes are available. The parameter values we used are based on $\omega_0/2\pi = 2200\,{\rm Hz}$, $\ell = 0.001\,{\rm m}$, $L = 0.035\,{\rm m}$, $S_n/S_b = 0.05$, $r = 0.1$.

The agreement is reasonable, taking into account that the ε's are not very small

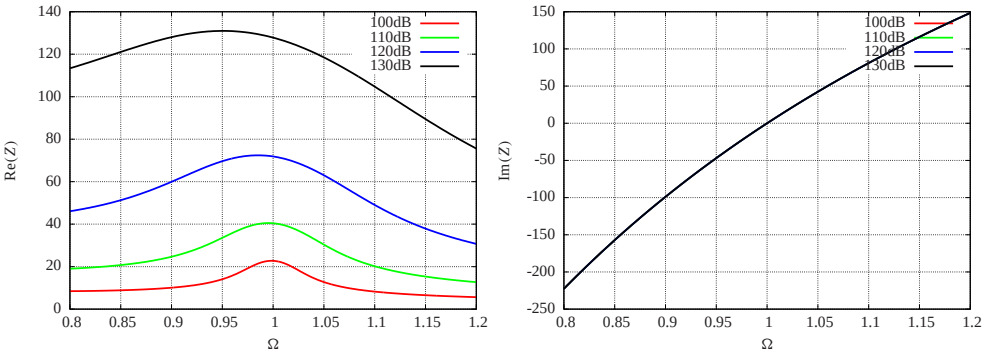

p_{ex} (dB)	100	110	120	130
ε	0.0497	0.0884	0.1572	0.2796

Figure 3.5: Real and imaginary parts of impedance Z for a Helmholtz resonator as a function of nondimensional frequency at different driving amplitudes. The realistic configuration that is chosen corresponds with $S_n/S_b = 0.05$, $r = 0.2$, $\omega_0/2\pi = 1447\,\text{Hz}$, $L = 0.035\,\text{m}$, $\ell = 0.002\,\text{m}$.

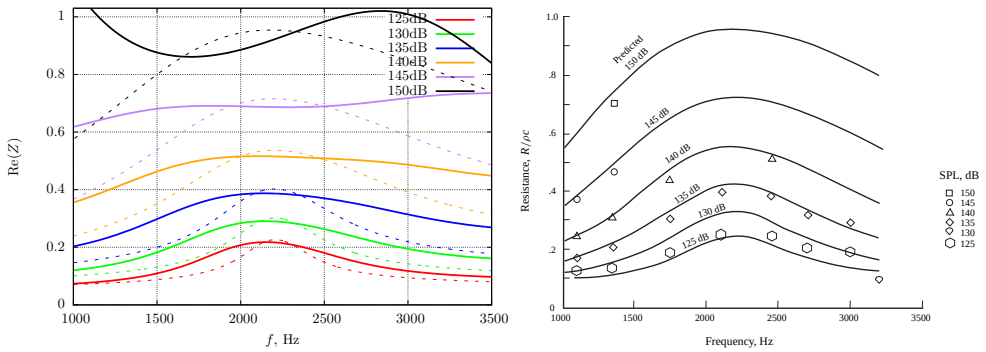

p_{ex} (dB)	125	130	135	140	145	150
ε	0.3125	0.4168	0.5558	0.7411	0.9883	1.3179

Figure 3.6: Comparison of (3.50) (solid line, *left*) with measurements and predictions of $\text{Re}(Z)/\rho_0 c_0$ given in [35], *right*. The markers in the right figure represent the measured values which were used, by adopting the relation $R = \rho_0 c_0(a + b|v|)$, to predict the resistance in solid curves. The dashed line, *left*, represents the resistance obtained from another asymptotic form (3.52) which is apparently more accurate.

and no experimental data are available in this frequency range for the higher amplitudes. Especially the increase of the maximum with the amplitude is confirmed. Only for the higher amplitudes (with value of $\varepsilon = 0.99$ or higher, that is far beyond what could be considered asymptotically "small") and frequencies well above resonance the decay suggested by [35] is not confirmed.

3.5.4 Comparison with Hersh et al. measurements

The Hersh et al. model [5] to predict the impedance is based on the experimental calibration of empirical parameters that were derived in the formulation. They introduced six assumptions, mostly inspired from measurements, to model the non linear terms. Shown in Fig. 3.7 is the comparison of our non resonant and resonant impedance values with 2 model configurations which have different value of ℓ. The maximum of 120dB curve was used for calibration and find r, and the same value of r was used for other amplitudes. The non linear curves asymptotically match with the linear curve and this transition is quite smooth for lower ϵ such that we can go from one model to the other. The resistance compares nicely at the near resonance frequencies when $\sigma = O(1)$ with ones amplitude fitted. Away from resonance ($\varepsilon\sigma = O(1)$) we see a considerable overprediction of the resistance. The reactance shows a good comparison across the range of frequencies. The same comparison was done with other experimental configurations from [5] and a reasonably good agreement is found for the near resonance frequencies.

3.5.5 Comparison with Ingard and Ising

Ingard and Ising [91] measured simultaneously fluctuating velocity and pressure, using hot wire measurements, followed by the exploitation of their phase relation to obtain the impedance at relatively high amplitudes. The chosen amplitudes were relatively high and in the domain of Innes and Crighton theoretical model [29]. The comparison shown in Fig. 3.8 is very accurate. This is a fortuitous result because we can not expect correct behaviour of the asymptotic analysis at such high $\varepsilon = O(1)$. It is a general observation that the predicted impedance in the close neighbourhood of resonance frequency is always agreeable even with higher values of ε.

3.5.6 Comparison with Melling

The measurements of Melling were used to further validate the model. Melling measured the impedance of a series of resonators constructed with multiple orifices backed by a cavity. Fig. 3.9 shows that the model predicted non linear resistance of a resonator constructed with an orifice diameter $(4S_n/\pi)^{\frac{1}{2}} = 0.127\,\text{cm}$, $\ell = 0.056\,\text{cm}$, $L = 7.5\,\text{cm}$ and $(S_b/\pi)^{\frac{1}{2}} = 3.46(S_n/\pi)^{\frac{1}{2}}\,\text{cm}$. The value of r is calibrated by its value giving the 143.5dB amplitude. The first 3 points of the measurements, being equal in magnitude, are apparently in the linear (non resonant) range. The model prediction is quite reasonable over the full amplitude regime.

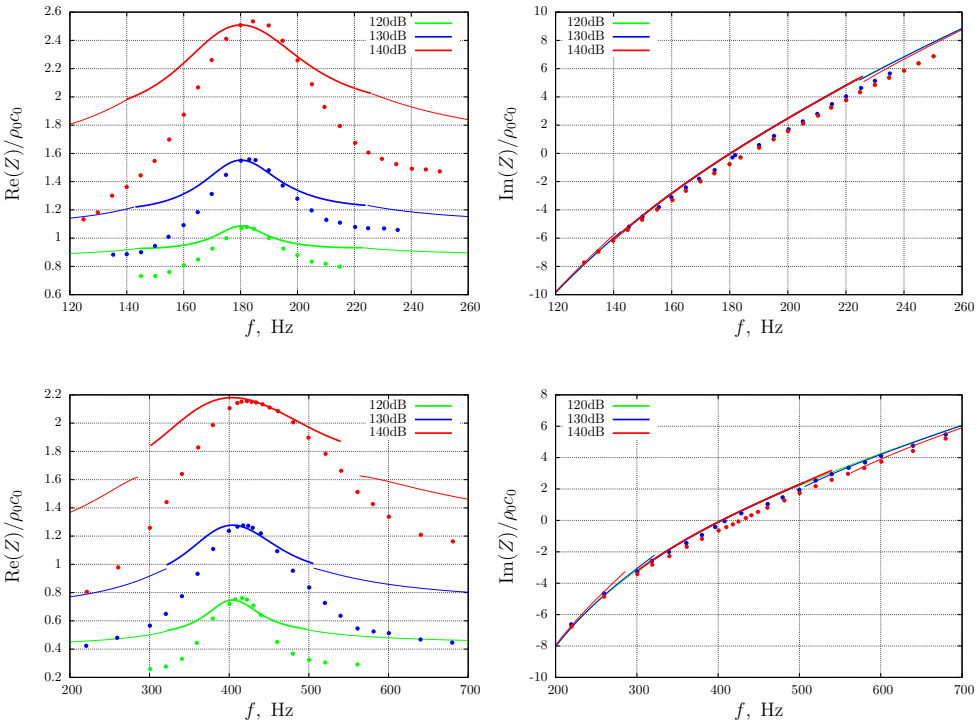

Figure 3.7: Comparison of the resonant (▬) and non resonant (──) resistance with Hersh and Walker measurements (•). *Configuration 1* (top): The cavity parameters are $\ell = 5.08\,\text{cm}$, $(4S_n/\pi)^{\frac{1}{2}} = 0.635\,\text{cm}$, $L = 2.54\,\text{cm}$ and $(4S_b/\pi)^{\frac{1}{2}} = 5.08$ cm. The desired resistance is obtained for $r = 0.65$. $\epsilon = 0.0455, 0.0809$ and 0.1439 respectively. *Configuration 2* (bottom): The cavity parameters are $\ell = 0.635\,\text{cm}$, $(4S_n/\pi)^{\frac{1}{2}} = 0.635\,\text{cm}$, $L = 2.54\,\text{cm}$ and $(4S_b/\pi)^{\frac{1}{2}} = 5.08$ cm. The desired resistance is obtained for $r = 1$. $\epsilon = 0.1021, 0.1815$ and 0.3228 respectively.

3.5.7 Comparison of impedances based on y_0 and $y_0 + \varepsilon y_1$ approximations

It is of interest to know when the driving amplitude becomes large enough to warrant the extra term εy_1 in the approximation of Z. Shown in Fig. 3.10 is the comparison of the impedance values obtained from y_0 and $y_0 + \varepsilon y_1$ approximations for different values of ε. Taking the same realistic geometry as above (Fig. 3.5), the value of ε varies from ~ 0.05 to 0.28 as the external driving amplitude is changed from 100 dB to 130 dB. We see that $O(\varepsilon)$ correction in the resulting resistance (the reactance is practically independent, especially near resonance) can be neglected for the lower amplitudes, but is indeed essential for the higher amplitudes.

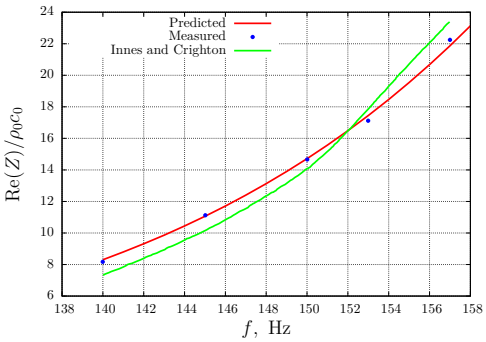

Figure 3.8: Comparison of the resistance with the measurements of Ingard and Ising. The cavity parameters are $\ell = 0.01$cm, $(4S_n/\pi)^{\frac{1}{2}} = 0.7$cm, $L = 7.5$cm and $(4S_b/\pi)^{\frac{1}{2}} = 9.5$ cm. The desired resistance is obtained for $r = 1$. $1.37541 < \varepsilon < 3.87643$

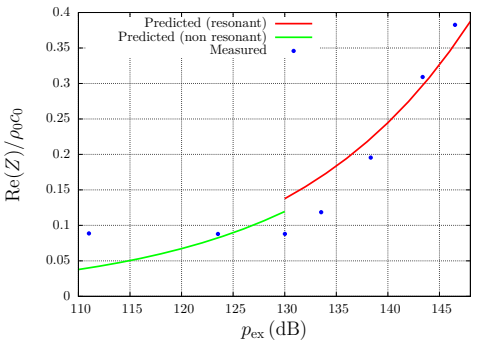

Figure 3.9: Comparison of the resistance with the measurements of Melling. The cavity parameters are $\ell = 0.056\,$cm, $(4S_n/\pi)^{\frac{1}{2}} = 0.127\,$cm, $L = 7.5\,$cm and $(S_b/\pi)^{\frac{1}{2}} = 3.46(S_n/\pi)^{\frac{1}{2}}\,$cm. The desired resistance is obtained for $r = 1$. $0.0705516 < \varepsilon < 0.705516$

3.5.8 Another asymptotic form

It is interesting to note that another asymptotic form of the impedance expression (3.50),

$$Z(\omega) = \frac{\varepsilon\rho_0 c_0^2 F_0}{L\omega_0} \frac{-\mathrm{i}\,\mathrm{e}^{\mathrm{i}\theta}}{A_0(1+\varepsilon\sigma) + \mathrm{i}\varepsilon\frac{2}{9\pi}A_0^2 + \varepsilon A_1} \tag{3.52}$$

by luck, produce better results for higher ε. We will derive and go through (3.52) in next chapter, where we improve the current model to capture more physics of the problem. For the time being, a comparison of the impedance obtained from (3.50) and (3.52) is shown in Fig. 3.11. Clearly, the asymptotic form (3.52) produces accurate predictions, especially at higher ε and decays away from resonance to match with the linear resistance. Comparison with the experimental data of [35], shown in Fig. 3.6

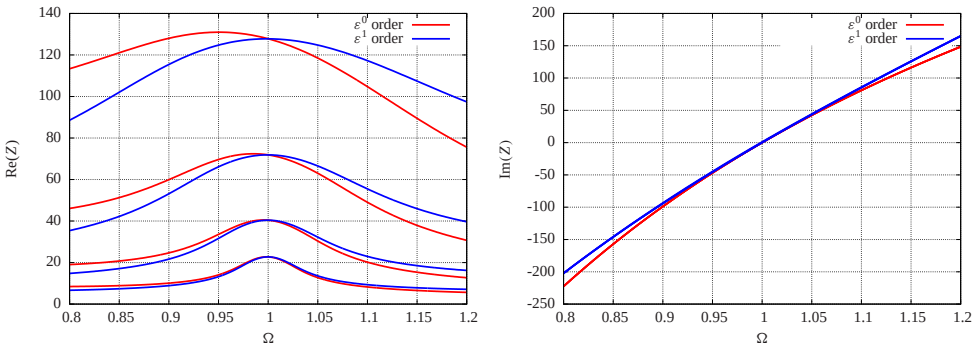

Figure 3.10: Comparison of the impedance obtained from the y_0 and $y_0 + \varepsilon y_1$ approximations for 100 dB, 110 dB, 120 dB and 130 dB. Same configuration as in Fig. 3.5

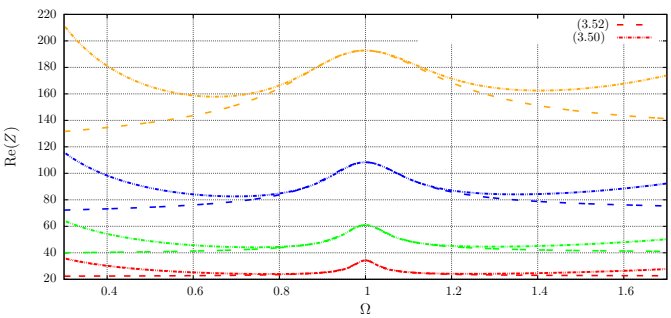

Figure 3.11: Comparison of resistance, Re(Z) based upon the two asymptotic form of our impedance expressions, (3.50) and (3.52) and external excitations, same as Fig. 3.5. The realistic configuration that is chosen corresponds with $\ell = 0.005\,\mathrm{m}$, $L = 0.035\,\mathrm{m}$ and $S_n/S_b = 0.05$ that gives $\kappa_0 = 0.55$ and $\omega_0 = 5367$ rad/sec, while $r = F_0 = 1$

reveals highly accurate predictions even at very high value of ε. Thus, the asymptotic form in (3.52) is more promising.

3.6 Extension to the N wave source

In this section, we will carry forward the impedance analysis when the resonator is driven by an N wave[3] type source, instead of harmonic source. Since the current

[3]The N wave sound also called as buzz-saw noise is very common in practise *e.g.* the current typical Dutch electronic dance music, EDM. Of particular interest and concern, is the buzz-saw sound produced by aircraft engine while take off when the blade tip Mach number exceeds unity that evolves a shock wave pattern at the blade leading edge close to the duct wall. Since the geometry of each blade is not ideally same, the shock waves are not parallel and interact with each other in the upstream of the intake duct. This interaction which is (highly) non linear in nature results in a sound field that is not only the first harmonic of the blade passing frequency but also contains

model does not permit to have the higher harmonics of wave inside the cavity, the resonator is not valid for the higher harmonics of resonance frequency and the model that we will study in next Chapter is more suitable for this analysis.

Typically, we can describe an N wave pressure field in time by the series

$$p_{\text{ex}} = p_{\text{ex}} = 2\varepsilon^2 \rho_0 c_0^2 \Big(\frac{\ell S_n}{V}\Big) F_0 \sum_{n=1}^{\infty} \frac{\sin(n\omega t)}{n} \tag{3.53}$$

where ω is the blade passing frequency, 1BPF and F_0 is the amplitude of nondimensional excitation. The liners are usually constructed in such a way that the resonance frequency corresponds to 1BPF to absorb the dominant sound spectrum and the impedance is usually obtained after ignoring the non linear effects. A time harmonic non linear model to predict the tone noise from the turbofan engine was constructed by [19]. In the frequency domain, the impedance information is vital to model the boundary condition. Hence a model which could describe the relationship between acoustic pressure and velocity is useful to maintain the understanding of the behavior of wall at the higher harmonics of N wave. In this section, we extend our model from harmonic source to N wave source and start the derivation from (3.22),

$$\Omega^2 \frac{\mathrm{d}^2 y}{\mathrm{d}\tilde{\tau}^2} + \varepsilon\Omega^2 \frac{\mathrm{d}y}{\mathrm{d}\tilde{\tau}} \left|\frac{\mathrm{d}y}{\mathrm{d}\tilde{\tau}}\right| + \varepsilon\Omega r \frac{\mathrm{d}y}{\mathrm{d}\tilde{\tau}} + y = \varepsilon F_0 \sum_{n=1}^{\infty} \frac{\sin n(\tilde{\tau}+\theta)}{n}. \tag{3.54}$$

where θ is to be chosen such that $y'(\tilde{\tau}) = 0$ at $\tilde{\tau} = (2N+1)\pi/2$. When we substitute the assumed Poincaré expansions $y(\tilde{\tau};\varepsilon) = y_0(\tilde{\tau}) + \varepsilon y_1(\tilde{\tau}) + \varepsilon^2 y_2(\tilde{\tau}) + \dots$ and $\theta(\varepsilon) = \theta_0 + \varepsilon\theta_1 + \dots$, and collect like powers of ε, we find for y_0

$$\frac{\mathrm{d}^2 y_0}{\mathrm{d}\tilde{\tau}^2} + y_0 = 0, \qquad y_0'(\frac{(N+1)\pi}{2}) = 0 \tag{3.55}$$

with general solution $y_0(\tilde{\tau}) = A_0 \sin(\tilde{\tau})$. The next order y_1 is

$$\begin{aligned}\frac{\mathrm{d}^2 y_1}{\mathrm{d}\tilde{\tau}^2} + y_1 &= F_0 \sum_{n=1}^{\infty} \frac{\sin n(\tilde{\tau}+\theta_0)}{n} - 2\sigma \frac{\mathrm{d}^2 y_0}{\mathrm{d}\tilde{\tau}^2} - \frac{\mathrm{d}y_0}{\mathrm{d}\tilde{\tau}} \left|\frac{\mathrm{d}y_0}{\mathrm{d}\tilde{\tau}}\right| - r\frac{\mathrm{d}y_0}{\mathrm{d}\tilde{\tau}} \\ &= F_0 \sum_{n=2}^{\infty} \frac{\sin n(\tilde{\tau}+\theta_0)}{n} + 2\sigma A_0 \sin(\tilde{\tau}) - A_0|A_0| \cos(\tilde{\tau})\,|\cos(\tilde{\tau})| - rA_0\cos(\tilde{\tau}).\end{aligned}$$

When we suppress the cos- and sin-terms, including the first term of the Fourier expansion of $\cos(\tilde{\tau})\,|\cos(\tilde{\tau})|$, we obtain the equation set (3.27) and (3.28), solving

several other harmonics [3]. The amplitude of each harmonic is inversely proportional to the it's frequency. Typically, there is a difference of about 6 dB between 1BPF and 2BPF and a difference of about 9.5 dB between 1BPF and 3BPF. Also, the shock interaction is much stronger in the upstream of the fan hence, the buzz-saw sound increases a bit when we move away from the fan and gains maturity at the shock interaction region and later starts to decrease.

which, we can determine A_0 and θ_0. The next order y_1 equation

$$\frac{\mathrm{d}^2 y_1}{\mathrm{d}\tilde{\tau}^2} + y_1 = \sum_{n=1}^{\infty}\left[F_0\frac{\sin(n+1)(\tilde{\tau}+\theta_0)}{(n+1)} + A_0|A_0|\frac{(-1)^n\cos(2n+1)\tilde{\tau}}{\pi(n^2-\frac{1}{4})(n+\frac{3}{2})}\right]$$

has the general solution

$$\begin{aligned} y_1(t) = {} & A_1\cos\tilde{\tau} + B_1\sin\tilde{\tau} \\ & - \sum_{n=1}^{\infty}\left[\frac{F_0\sin(n+1)(\tilde{\tau}+\theta_0)}{n(n+1)(n+2)} + \frac{A_0|A_0|}{4\pi}\frac{(-1)^n\cos(2n+1)\tilde{\tau}}{n(n+1)(n^2-\frac{1}{4})(n+\frac{3}{2})}\right]. \end{aligned} \tag{3.56}$$

With the condition that $y_1'(\frac{(2N+1)\pi}{2}) = 0$, the constant A_1 is determined. Next, we move to the next order asymptotic analysis from (3.54), collecting the like coefficients of ϵ^2, we have

$$\begin{aligned} y_2'' + y_2 = {} & \sigma^2 A_0\sin\tilde{\tau} + 2\sigma A_1\cos\tilde{\tau} + 2\sigma B_1\sin\tilde{\tau} + .. \\ & + \left[2\sigma A_0^2\cos^2\tilde{\tau} - 2A_0A_1\sin\tilde{\tau}\cos\tilde{\tau} + 2A_0B_1\cos^2\tilde{\tau}\right]\mathrm{sign}(A_0\cos\tilde{\tau}) \\ & + rA_1\sin\tilde{\tau} - rB_1\cos\tilde{\tau} - r\sigma A_0\cos\tilde{\tau} + \cdots + \theta_1 F_0(\cos\tilde{\tau}\cos\theta_0 - \sin\tilde{\tau}\sin\theta_0) \\ & - 2A_0F_0\sum_{n=1}^{\infty}\frac{\cos\tilde{\tau}\cos(n+1)(\tilde{\tau}+\theta_0)}{n(2n+1)}\,\mathrm{sign}(A_0\cos\tilde{\tau}) \\ & - \frac{2A_0^3}{4\pi}\sum_{n=1}^{\infty}\frac{(-1)^n(2n+1)\sin(2n+1)\tilde{\tau}\cos\tilde{\tau}}{n(n+1)(n^2-\frac{1}{4})(n+\frac{3}{2})}\,\mathrm{sign}(A_0\cos\tilde{\tau}). \end{aligned}$$

Suppressing the coefficients of the sine and cosine terms as done previously, we can obtain the value of B_1 and θ_1 from the linear equations

$$\begin{aligned} (16\frac{A_0}{3\pi} - r)B_1 + (F_0\cos\theta_0)\theta_1 = {} & -2\sigma A_1 - \frac{16\sigma A_0^2}{3\pi} + r\sigma A_0 \\ & - \frac{2A_0F_0}{\pi}\sum_{n=1}^{\infty}\frac{6\cos(\frac{n\pi}{2}) + 2\cos(\frac{3n\pi}{2})}{n(n^2-1)(n+3)}\cos(n+1)\theta_0 \\ (2\sigma)B_1 - (F_0\sin\theta_0)\theta_1 = {} & -\sigma^2 A_0 + \frac{8A_0A_1}{3\pi} - \frac{A_0^3}{27\pi^2}(80-9\pi^2) - rA_1 \\ & + \frac{2A_0F_0}{\pi}\sum_{n=1}^{\infty}\frac{3\cos(\frac{n\pi}{2}) + \cos(\frac{3n\pi}{2})}{n(n+1)(n^2-1)(n+3)}\sin(n+1)\theta_0. \end{aligned}$$

The series we see are truncated for a finite summation and can be evaluated numerically. This way, we know the asymptotic solution $y = y_0 + \varepsilon y_1$ correct till $O(\varepsilon)$. Next we formulate the impedance calculation.

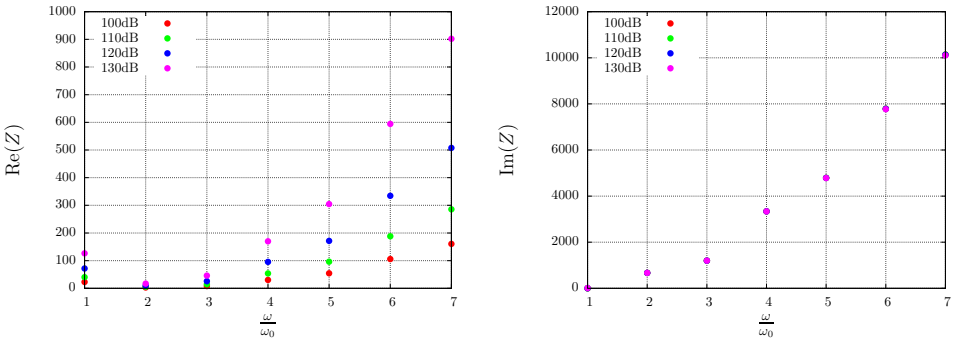

Figure 3.12: Impedance at observed frequency $\eta = n\omega$ and N wave excitation $\Omega = 1$. $\frac{S_n}{S_b} = 0.5$, $r = 0.2$, $\frac{\omega_0}{2\pi} = 1447Hz$, $L = 0.035$m and $\ell = 0.002$ m.

3.6.1 Impedance calculation

We define the impedance, same as in (3.43), as the negative of the ratio of the Fourier transform of the external pressure p_{ex} to the Fourier transform of the external velocity u_{ex}. The Fourier transform is taken over the frequency of interest, which happen to be the integral multiple of the resonance frequency ω_0 in our case *i.e.*

$$Z(\eta) = -\frac{\frac{1}{2\pi}\int_{-\infty}^{\infty} p_{\text{ex}} e^{-\mathrm{i}\eta t} dt}{\frac{1}{2\pi}\int_{-\infty}^{\infty} v_{\text{ex}} e^{-\mathrm{i}\eta t} dt}, \qquad (\eta = n\omega_0). \tag{3.57}$$

Defined in this way, the impedance gives an understanding of the behavior of the wall for different harmonics of the N wave. In other words, it is the response of the wall (acoustic velocity) to a particular pressure component of the source, characterized by its frequency. Of most importance are the first three harmonics of N wave because the later harmonics are practically cut off.

3.6.2 Results

The acoustic pressure and velocity are Fourier transformed to obtain the impedance, using (3.57), for a typical geometry with $S_n/S_b = 0.5$, $r = 0.2$, $\omega_0/2\pi = 1447\,\text{Hz}$, $L = 0.035\,\text{m}$ and $\ell = 0.002\,\text{m}$. Shown in Fig. 3.12 is the dimensional impedance for different harmonics of the resonant frequency calculated for different driving amplitudes. We notice that at $\omega = \omega_0$, the impedance has the same value as if the Helmholtz resonator is driven by the harmonic source and increases for higher harmonics. The resistance $\text{Re}(Z)$ term is strongly dependent on the driving amplitude and grows much higher for higher amplitudes. The reactance $\text{Im}(Z)$ term on the contrary, is practically independent of the driving amplitude. Essentially, the wall behaves like hard wall for very high harmonics of the resonant frequency ω_0.

3.7 Conclusions

A systematic approximation of the solution of the hydrodynamically non linear Helmholtz resonator equation is obtained, including the resulting impedance if the resonator is applied in an acoustic liner. To leading order, the usually assumed form of the resistance, $a + b|v|$, is recovered. The only unknown parameter that we need to adapt is resistance factor r, although in many cases the effective neck length ℓ is also unknown and has to be estimated. Comparisons with measurements prove that the model predicts the near resonance impedance at $\sigma = O(1)$ to a good accuracy.

Our approach, based on systematic use of asymptotic analysis, allows higher order corrections, which indeed are shown to be important and relevant for practical configurations involving high amplitudes.

The real part of the found impedance (the resistance) shows the usual characteristic behavior as a function of frequency, namely a maximum at or near the resonance frequency and a decay along both sides. All values increase with the amplitude, but slightly more for the frequencies less than resonance. The imaginary part of the impedance (the reactance) is linear in frequency in a way that it vanishes at resonance and is practically independent of the amplitude.

The current model is based upon the assumption that the pressure inside the cavity is uniform and the exit velocity is given by the time derivative of this uniform pressure. In reality, standing waves are developed inside the cavity and the relationship between velocity and pressure is given by the solution of the wave equation, inside the cavity. This is what we aim for, in the next Chapter, to capture more physics of the damping phenomenon.

Chapter 4

An asymptotic model for non linear Helmholtz resonator of finite depth

4.1 Introduction

The Helmholtz resonator equation which describes the neck region flow (Fig. 4.1) can be solved asymptotically with the boundary condition that relates the pressure and velocities inside the cavity (left of the neck in Fig. 4.1). This was done in the previous Chapter 3 and the formulated impedance was compared with the existing experimental data favourably. The considered cavity was acoustically compact, *i.e.* the length of the cavity considered was much smaller compared to the acoustic wavelength $L \ll \lambda$ so that the pressure inside was nearly uniform for simplicity and the neck velocity was simply given by the time derivative of the pressure. Hence the resonator acts like a spring to the external force. This modelling assumption could be improved and extended to cavities of large lengths by solving the wave equation inside the cavity to obtain a relationship between pressure and velocity that allows the waves to develop inside the cavity. In this way, we capture more physics of the problem and the fidelity of the model is improved.

We follow much of the derivation done in Chapter 3, and focus on a systematic derivation of an asymptotic solution of a stand-alone non linear Helmholtz resonator equation from first principles. Again, the extra complication of grazing flow along the liner wall will not be considered here. This effect is important if the mean flow boundary layer is thin enough and the resonator outflow velocity is comparable to (or higher than) the mean flow velocity.

We start with the classical modeling of the Helmholtz resonator and formulate a perturbation problem in terms of a small parameter ε which is based on the excitation amplitude of a given pressure of fixed frequency. The stationary solution of this

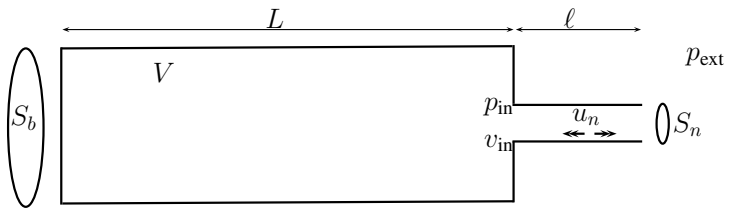

Figure 4.1: Organpipe resonator cavity and neck

problem is solved asymptotically. Secular effects of the external forcing are treated in the usual way by a suitable Lindstedt-Poincaré type approach. A non standard problem is the modulus term $|u|$ of the velocity. This prohibits a standard asymptotic expansion because the location of the zeros of u are a priori unknown. This problem has been tackled by adding an unknown shift of the origin, to be determined along with the construction of the solution, and using the fact that the stationary solution has the same periodicity as the driving force.

4.2 Mathematical formulation

The organ pipe type extended resonator considered is shown in Fig 4.1. The frequency of the external excitation is assumed to be low enough that crosswise higher order modes are cut off in the cavity region of length L and we have only plane waves inside. Considering that the cavity neck is acoustically compact *i.e.* $k\ell \ll 1$ for a typical wavenumber $k = \omega/c_0$, we can neglect compressibility in the neck and determine the line integral of the momentum equation, from (2.1), (2.2) and (2.8),

$$\rho_0\Big(\frac{\partial \boldsymbol{v}}{\partial t} + \boldsymbol{v}\cdot\nabla\boldsymbol{v}\Big) + \nabla p = \mu\nabla^2\boldsymbol{v}$$

along a streamline from a point inside to a point outside to obtain the relation

$$\rho_0 \int_{\text{in}}^{\text{ex}} \frac{\partial \boldsymbol{v}}{\partial t}\cdot\mathbf{d}\boldsymbol{s} + \tfrac{1}{2}\rho_0(v_{\text{ex}}^2 - v_{\text{in}}^2) + (p_{\text{ex}} - p_{\text{in}}) = \int_{\text{in}}^{\text{ex}} \mu\nabla^2\boldsymbol{v}\cdot\mathbf{d}\boldsymbol{s}, \tag{4.1}$$

with $v = \|\boldsymbol{v}\|$ and μ denoting the viscosity. Following Melling [87] we average pressure and velocity along the neck's cross section, assume that the averaged squared velocity is approximately equal to the squared averaged velocity, and obtain

$$\rho_0 \int_{\text{in}}^{\text{ex}} \frac{\partial \bar{\boldsymbol{v}}}{\partial t}\cdot\mathbf{d}\boldsymbol{s} + \tfrac{1}{2}\rho_0(\bar{v}_{\text{ex}}^2 - \bar{v}_{\text{in}}^2) + (p_{\text{ex}} - p_{\text{in}}) = \int_{\text{in}}^{\text{ex}} \mu\overline{\nabla^2\boldsymbol{v}}\cdot\mathbf{d}\boldsymbol{s}. \tag{4.2}$$

Assuming that the streamline does not change in time, we have

$$\int_{\text{in}}^{\text{ex}} \frac{\partial \bar{\boldsymbol{v}}}{\partial t}\cdot\mathbf{d}\boldsymbol{s} = \frac{\mathrm{d}}{\mathrm{d}t}\int_{\text{in}}^{\text{ex}} \bar{\boldsymbol{v}}\cdot\mathbf{d}\boldsymbol{s}. \tag{4.3}$$

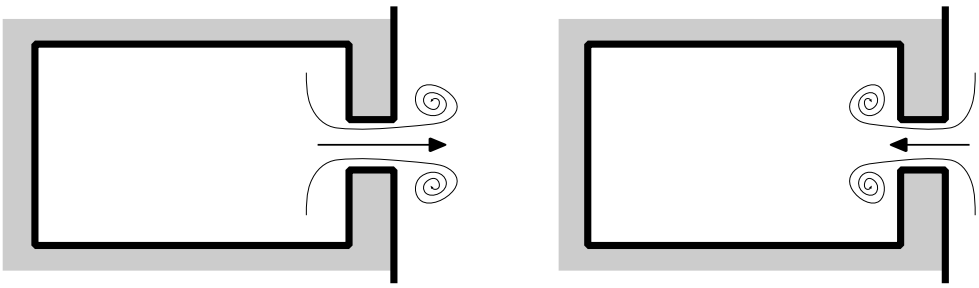

out-flow phase in-flow phase

Figure 4.2: Separation and vortex shedding during the out-flow and in-flow phase

The velocity line integral evidently scales on a typical length times a typical velocity. If end effects are minor, we can use the neck flux velocity $\bar{\boldsymbol{v}} = u_n \boldsymbol{e}_x$ with a corresponding length being the neck length ℓ, added by a small end correction δ to take into account the inertia of the acoustic flow at both ends just outside the neck (inside and outside the resonator). Then we have

$$\int_{\text{in}}^{\text{ex}} \bar{\boldsymbol{v}} \cdot \mathbf{d}\boldsymbol{s} = (\ell + 2\delta) u_n. \tag{4.4}$$

End corrections δ for various geometries are given by Ingard [90]. For a circular orifice, for example, we may use $\delta = 0.85(S_n/\pi)^{1/2}$.

For the stress term line integral we observe that, apart from u_n itself, it will depend on flow profile, Reynolds number, wall heat exchange, turbulence, separation from sharp edges, and maybe more. Following Melling [87], we will take these effects together in a resistance factor R, which will be assumed relatively small, in order to have resonance and a small decay per period to begin with. We thus have

$$\int_{\text{in}}^{\text{ex}} \mu \overline{\nabla^2 \boldsymbol{v}} \cdot \mathbf{d}\boldsymbol{s} = -R u_n \tag{4.5}$$

(Note that this form is exact for a Poiseuille flow with parabolic profile). Due to separation from the outer exit, we have with outflow $\bar{v}_{\text{in}} \simeq 0$ with $\bar{v}_{\text{ex}} = u_n$ jetting out, while similarly during inflow, $\bar{v}_{\text{ex}} \simeq 0$ with $\bar{v}_{\text{in}} = u_n$ jetting into the cavity; see Fig. 4.2. The pressure in the jets, however, has to remain equal to the surrounding pressure (p_{ex} and p_{in} respectively) because the boundary of the jet cannot support a pressure difference. Therefore, we have altogether (redefining $\ell + 2\delta =: \ell$)

$$\rho_0 \ell \frac{\mathrm{d}}{\mathrm{d}t} u_n + \tfrac{1}{2} \rho_0 u_n |u_n| + R u_n = p_{\text{in}} - p_{\text{ex}}. \tag{4.6}$$

The second equation between p_{in} and u_n is obtained by solving the wave equation in the attached cavity (organ pipe) of uniform cross section S_b and length L, varying along $-L \leqslant x \leqslant 0$ where $x = 0$ is the position where the cavity connects to the neck.

Inside the cavity, we have

$$\begin{aligned} \frac{\partial p}{\partial t} + \rho_0 c_0^2 \frac{\partial u}{\partial x} &= 0 \\ \rho_0 \frac{\partial u}{\partial t} + \frac{\partial p}{\partial x} &= 0, \end{aligned} \tag{4.7}$$

assuming an adiabatic compression of the fluid in the cavity $p = c_0^2 \rho$. The end conditions are then

$$\begin{aligned} u(-L,t) &= 0 \\ p(0,t) &= p_{\text{in}}(t) \\ S_b u(0,t) &= S_n u_n(t). \end{aligned} \tag{4.8}$$

Using d'Alembert's solution we can solve (4.7) to obtain

$$\begin{aligned} p(x,t) &= \rho_0 c_0^2 \big(f(c_0 t - x - L) + f(c_0 t + x + L)\big) \\ u(x,t) &= \quad c_0 \big(f(c_0 t - x - L) - f(c_0 t + x + L)\big) \end{aligned} \tag{4.9}$$

so

$$\begin{aligned} p_{\text{in}}(t) &= \rho_0 c_0^2 \big(f(c_0 t - L) + f(c_0 t + L)\big) \\ S_n u_n(t) &= S_b c_0 \big(f(c_0 t - L) - f(c_0 t + L)\big). \end{aligned} \tag{4.10}$$

After the Fourier transform of (4.7) using (4.8), we have

$$\begin{aligned} & \hat{u}(x) = A c_0 \sin(kx + kL) && \hat{p}(x) = \mathrm{i} A \rho_0 c_0^2 \cos(kx + kL), \\ \text{hence} \quad & S_n \hat{u}_n = S_b A c_0 \sin(kL) && \hat{p}_{\text{in}} = \mathrm{i} A \rho_0 c_0^2 \cos(kL). \end{aligned}$$

For the linear harmonic case, we have from (4.6)

$$\mathrm{i}\omega \rho_0 \ell \hat{u}_n + R \hat{u}_n = \hat{p}_{\text{in}} - \hat{p}_{\text{ex}}, \tag{4.11}$$

$$\hat{p}_{\text{ex}} = -\mathrm{i}\omega \rho_0 \ell \frac{S_b}{S_n} A c_0 \sin(kL) - R \frac{S_b}{S_n} A c_0 \sin(kL) + \mathrm{i} A \rho_0 c_0^2 \cos(kL). \tag{4.12}$$

The neck velocity $\hat{u}$ is averaged over the whole surface and can be multiplied by the porosity factor to obtain

$$\hat{u}_{\text{ex}} = \frac{S_n}{S_b} \hat{u}_n = \hat{u}(0) = A c_0 \sin(kL). \tag{4.13}$$

Combining (4.13) with (4.12), we obtain the standard expression of the linear imped-

ance [80]

$$\begin{aligned} Z &= \frac{\hat{p}_{\mathrm{ex}}}{-\hat{u}_{\mathrm{ex}}} \\ &= \frac{-\mathrm{i}\omega\rho_0\ell\frac{S_b}{S_n}Ac_0\sin(kL) - R\frac{S_b}{S_n}Ac_0\sin(kL) + \mathrm{i}A\rho_0c_0^2\cos(kL)}{Ac_0\sin(kL)} \\ &= \frac{S_b}{S_n}\big(R + \mathrm{i}\omega\rho_0\ell\big) - \mathrm{i}\rho_0c_0\cot(kL). \end{aligned} \tag{4.14}$$

The resistance R averaged over the surface becomes the resistance term of linear impedance. Close to resonance, the expression (4.14) is no longer valid because the non linear term in (4.6) is of same order of magnitude as the other terms, as the problem is formulated in that way. It will become more clear in the next section. In order to proceed further, it is important to scale the variables in (4.6) which we introduce in the next section.

4.3 Scaling

For a proper analysis, it is most clarifying to rewrite the equation into non dimensional variables. For this we need an inherent timescale and pressure level. The resonance frequency ω_0 for the linearised case and $R = 0$ is evidently given by the solution of

$$\kappa_0 \tan\kappa_0 = \frac{LS_n}{\ell S_b}, \quad \kappa_0 = \frac{\omega_0 L}{c_0}. \tag{4.15}$$

The reciprocal of this angular frequency is a suitable timescale of the problem. By dividing the non linear damping term by the acceleration term we find the pressure level at which the non linear damping would be just as large as the other terms. So for a pressure that is a small fraction, say ε, of this level we have a problem with only little non linear damping. In addition we assume that the linear damping is small and of the same order of magnitude as the non linear damping (that is to say: near resonance. Away from resonance the non linear term will be relatively smaller). Also, the driving amplitude p_{ex} will be an order smaller than p_{in}. In order to make all this explicit we introduce a small parameter ε (via the external forcing amplitude), and make dimensionless

$$\begin{aligned} &\tau = \omega_0 t && p_{\mathrm{in}}(t) = 2\varepsilon\rho_0c_0^2\left(\frac{\omega_0\ell}{c_0}\right)^2 y(\tau) && p_{\mathrm{ex}}(t) = 2\varepsilon^2\rho_0c_0^2\left(\frac{\omega_0\ell}{c_0}\right)^2 F(\tau) \\ &R = \varepsilon\rho_0c_0\left(\frac{\omega_0\ell}{c_0}\right)r && u_{\mathrm{n}}(t) = 2\varepsilon c_0\left(\frac{\omega_0\ell}{c_0}\right)v(\tau) && f(c_0t) = 2\varepsilon\left(\frac{\omega_0\ell}{c_0}\right)^2\phi(\tau). \end{aligned} \tag{4.16}$$

It should be noted that in practice the parameter R is usually a constant and not dependent of the excitation amplitude (ε). So the used scaling $\sim \varepsilon r$ should not be interpreted in that way, and is only meant to select out a certain class of problems with

a relatively small linear friction and similarly small non linear effects. If we consider a particular configuration for varying ε but otherwise fixed, we should preserve the product εr and adapt r, but never such that r is unacceptably large and we would enter a physically different regime.

Coupled with (4.6) and (4.9), we obtain the final non linear differential equation

$$\frac{\mathrm{d}v}{\mathrm{d}\tau} + \varepsilon v|v| + \varepsilon r v - y = -\varepsilon F \tag{4.17}$$

with conditions

$$\begin{aligned} \phi(\tau - \kappa_0) + \phi(\tau + \kappa_0) &= y(\tau) \\ \phi(\tau - \kappa_0) - \phi(\tau + \kappa_0) &= \tan\kappa_0\, v(\tau) \end{aligned} \tag{4.18}$$

that we need to solve asymptotically. Note that in case of small length L (the condition of Chapter 3), we have a small κ_0, and so

$$\kappa_0 \tan\kappa_0 \sim \kappa_0^2.$$

With (4.15), we obtain the same resonance frequency of the cavity used in Chapter 3. Also note that with positive ω_0, $\kappa_0 > 0$, and since the product $k_0 \tan\kappa_0 = LS_n/\ell S_b > 0$, we have $\tan\kappa_0 > 0$.

4.4 Asymptotic solution away from resonance $\omega \neq \omega_0$

Away from resonance $\omega \neq \omega_0$ and

$$F(\tau) = \cos(\Omega\tau), \quad \Omega = \frac{\omega}{\omega_0}, \tag{4.19}$$

our solution follows the external excitation in time, phase and order of magnitude. Hence we assume $y = O(\varepsilon)$ and expand the variables as

$$y = \varepsilon y_0 + \varepsilon^2 y_1 + \ldots, \qquad v = \varepsilon v_0 + \varepsilon^2 v_1 + \ldots, \qquad \phi = \varepsilon\phi_0 + \varepsilon^2\phi_1 + \ldots. \tag{4.20}$$

Collecting the like powers of ε, we obtain

$$\begin{aligned} \frac{\mathrm{d}v_0}{\mathrm{d}\tau} - y_0 &= -\cos(\Omega\tau) \\ \phi_0(\tau - \kappa_0) + \phi_0(\tau + \kappa_0) &= y_0(\tau) \\ \phi_0(\tau - \kappa_0) - \phi_0(\tau + \kappa_0) &= \tan\kappa_0\, v_0(\tau) \end{aligned} \tag{4.21}$$

and

$$\begin{aligned} \frac{\mathrm{d}v_1}{\mathrm{d}\tau} - y_1 &= -r v_0 \\ \phi_1(\tau - \kappa_0) + \phi_1(\tau + \kappa_0) &= y_1(\tau) \\ \phi_1(\tau - \kappa_0) - \phi_1(\tau + \kappa_0) &= \tan\kappa_0\, v_1(\tau). \end{aligned} \tag{4.22}$$

Assuming a slight amount of damping, the homogeneous solution of (4.21) and (4.22) given by appendix [B.1(B.1)] will dissipate for large time. The particular solution that remains, can be obtained as shown in appendix B.2. Using (B.9), we obtain

$$v = \varepsilon \frac{-\tan(\Omega\kappa_0)}{\Omega\tan(\Omega\kappa_0) - \tan\kappa_0}\sin(\Omega\tau) - \varepsilon^2 r\left[\frac{\tan(\Omega\kappa_0)}{\Omega\tan(\Omega\kappa_0) - \tan\kappa_0}\right]^2\cos(\Omega\tau). \quad (4.23)$$

which is asymptotically equivalent to the solution

$$v = -\varepsilon\tan(\Omega\kappa_0)\frac{(\Omega\tan(\Omega\kappa_0) - \tan\kappa_0)\sin(\Omega\tau) + \varepsilon r\tan(\Omega\kappa_0)\cos(\Omega\tau)}{(\Omega\tan(\Omega\kappa_0) - \tan\kappa_0)^2 + (\varepsilon r\tan(\Omega\kappa_0))^2} + O(\varepsilon^3). \quad (4.24)$$

We see that the response v is indeed $O(\varepsilon)$ and follows the excitation almost in phase ($\Omega\tan(\Omega\kappa_0) - \tan\kappa_0 > 0$) or antiphase $\Omega\tan(\Omega\kappa_0) - \tan\kappa_0 < 0$. Close to resonance when $\Omega = 1 + O(\varepsilon)$, the term $(\Omega\tan(\Omega\kappa_0) - \tan\kappa_0) = O(\varepsilon)$, so $v = O(1)$ and the assumption that the response v has the same order as the excitation $O(\epsilon)$ is not correct. Therefore the solution (4.24) is not valid close to resonance.

4.5 Asymptotic solution close to resonance $\omega \approx \omega_0$

Near resonance, the amplitude y in (4.17) rises to levels of $O(1)$ with $O(\varepsilon)$ forcing and the assumption that the non linear damping is negligible to leading orders is not correct. As the physics of the problem essentially change when $\Omega = 1 + O(\varepsilon)$, we introduce a parameter $\sigma = O(1)$ and assume that

$$\Omega = 1 + \varepsilon\sigma. \quad (4.25)$$

However, posed in this form we obtain secular terms in the expansion $\cos(\tau + \varepsilon\sigma\tau) = \cos(\tau) - \varepsilon\sigma\tau\sin(\tau) + \ldots$ of the driving force, which prohibits a uniform approximation of v later [70, sec15.3.2]. Therefore, we remove the ε-dependence from the driving force by absorbing Ω into a new time coordinate $\tilde{\tau} = \Omega\tau$. Moreover, the asymptotic expansion of the term $v|v|$ introduces difficulties near the ε-dependent (and unknown) zeros of v. This will be tackled by a translation of the origin by an amount $\theta(\varepsilon)$, such that the locations of the sign change of v are fixed (as v is synchronised with the driving force) and independent of ε. (Of course, a certain amount of smoothness is anticipated such that v has the same number of zeros per period as the forcing term). So we introduce

$$\tilde{\tau} = \Omega\tau - \theta(\varepsilon) \quad (4.26)$$

where θ is to be chosen such that the response v vanishes at integral multiples of π. This fixes the points along the time $\tilde{\tau}$ axis where v changes sign *i.e.*

$$v(\tilde{\tau}) = 0 \quad \text{at} \quad \tilde{\tau} = N\pi. \quad (4.27)$$

In other words, $\Omega\tau = \omega t = \theta$ corresponds with the phase lag of response v_{ex} to excitation p_{ex} like in Chapter 3.

Consider $\Omega = 1 + O(\varepsilon)$ and introduce the transformation

$$F = F_0 \cos(\tilde{\tau}+\theta),\ \Omega = 1+\varepsilon\sigma,\ \tilde{\tau} = \Omega\tau-\theta,\ y(\tau) = \tilde{y}(\tilde{\tau}),\ v(\tau) = \tilde{v}(\tilde{\tau}) \text{ and } \phi(\tau) = \tilde{\phi}(\tilde{\tau}), \tag{4.28}$$

to obtain the following set of equations

$$\Omega\frac{\mathrm{d}\tilde{v}}{\mathrm{d}\tilde{\tau}} + \varepsilon\tilde{v}|\tilde{v}| + \varepsilon r\tilde{v} - \tilde{y} = -\varepsilon F \tag{4.29}$$

with

$$\begin{aligned} \tilde{\phi}(\tilde{\tau} - \Omega\kappa_0) + \tilde{\phi}(\tilde{\tau} + \Omega\kappa_0) &= \tilde{y}(\tilde{\tau}) \\ \tilde{\phi}(\tilde{\tau} - \Omega\kappa_0) - \tilde{\phi}(\tilde{\tau} + \Omega\kappa_0) &= \tan\kappa_0\, \tilde{v}(\tilde{\tau}). \end{aligned} \tag{4.30}$$

Now we expand the variables as follows

$$\begin{aligned} &\tilde{y} = \tilde{y}_0 + \varepsilon\tilde{y}_1 + \ldots, \quad \tilde{v} = \tilde{v}_0 + \varepsilon\tilde{v}_1 + \ldots, \quad \tilde{\phi} = \tilde{\phi}_0 + \varepsilon\tilde{\phi}_1 + \ldots, \quad \theta = \theta_0 + \varepsilon\theta_1 + \ldots, \\ &\tilde{\phi}(\tilde{\tau} \pm \Omega\kappa_0) = \tilde{\phi}_0(\tilde{\tau} \pm \kappa_0) + \varepsilon\big[\tilde{\phi}_1(\tilde{\tau} \pm \kappa_0) \pm \sigma\kappa_0\tilde{\phi}_0'(\tilde{\tau} \pm \kappa_0)\big] \\ &\qquad + \varepsilon^2\left[\tilde{\phi}_2(\tilde{\tau} \pm \kappa_0) + \tfrac{1}{2}(\sigma\kappa_0)^2\tilde{\phi}_0''(\tilde{\tau} \pm \kappa_0) \pm \sigma\kappa_0\tilde{\phi}_1'(\tilde{\tau} \pm \kappa_0)+\right] + \ldots. \end{aligned} \tag{4.31}$$

Next we collect the terms of the same order of ε and construct our solution in the form of an asymptotic series.

Order ε^0 analysis:

Substituting (4.31) in (4.30) and afterwards in (4.29) and collecting the terms of $O(\varepsilon^0)$, we have

$$\begin{aligned} \frac{\mathrm{d}\tilde{v}_0}{\mathrm{d}\tilde{\tau}} - \tilde{y}_0 &= 0 \\ \tilde{\phi}_0(\tilde{\tau} - \kappa_0) + \tilde{\phi}_0(\tilde{\tau} + \kappa_0) &= \tilde{y}_0(\tilde{\tau}) \\ \tilde{\phi}_0(\tilde{\tau} - \kappa_0) - \tilde{\phi}_0(\tilde{\tau} + \kappa_0) &= \tan\kappa_0\, \tilde{v}_0(\tilde{\tau}). \end{aligned} \tag{4.32}$$

At large times, assuming a little damping, the cavity is driven by the external force in such a way that a steady state is reached and the initial conditions are not important. Hence from (B.1), we choose the steady solution and obtain, using (4.27),

$$\tilde{\phi}_0 = \tfrac{1}{2}A_0\cos\tilde{\tau}, \tag{4.33}$$

and hence

$$\tilde{y}_0 = A_0\cos\kappa_0\cos\tilde{\tau} \quad \text{and} \quad \tilde{v}_0 = A_0\cos\kappa_0\sin\tilde{\tau}, \tag{4.34}$$

where A_0 and θ_0 are to be determined from the regularity condition (absence of secular terms (B.10)) in the next order ε^1.

Order ε^1 analysis:

Collecting the terms of $O(\varepsilon)$ from (4.29), we obtain

$$\begin{aligned}
\frac{\mathrm{d}\tilde{v}_1}{\mathrm{d}\tilde{\tau}} - \tilde{y}_1 &= -\sigma\tilde{v}_0' - \tilde{v}_0|\tilde{v}_0| - r\tilde{v}_0 - F_0\cos(\tilde{\tau}+\theta_0)\\
\tilde{\phi}_1(\tilde{\tau}-\kappa_0) + \tilde{\phi}_1(\tilde{\tau}+\kappa_0) &= \sigma\kappa_0\tilde{\phi}_0'(\tilde{\tau}-\kappa_0) - \sigma\kappa_0\tilde{\phi}_0'(\tilde{\tau}+\kappa_0) + \tilde{y}_1(\tilde{\tau})\\
\tilde{\phi}_1(\tilde{\tau}-\kappa_0) - \tilde{\phi}_1(\tilde{\tau}+\kappa_0) &= \sigma\kappa_0\tilde{\phi}_0'(\tilde{\tau}-\kappa_0) + \sigma\kappa_0\tilde{\phi}_0'(\tilde{\tau}+\kappa_0) + \tan\kappa_0\,\tilde{v}_1(\tilde{\tau}).
\end{aligned} \tag{4.35}$$

From (4.33), (4.34) and (4.35), we have after eliminating $\tilde{y}_1$ and $\tilde{v}_1$

$$\begin{aligned}
&\frac{1}{\tan\kappa_0}\left[\tilde{\phi}_1'(\tilde{\tau}-\kappa_0) - \tilde{\phi}_1'(\tilde{\tau}+\kappa_0)\right] - \left[\tilde{\phi}_1(\tilde{\tau}-\kappa_0) + \tilde{\phi}_1(\tilde{\tau}+\kappa_0)\right] =\\
&\quad -\sigma\frac{\kappa_0}{\tan\kappa_0}A_0\cos\kappa_0\cos\tilde{\tau} + \sigma\kappa_0 A_0\sin\kappa_0\cos\tilde{\tau} - \sigma A_0\cos\kappa_0\cos\tilde{\tau}\\
&\quad - A_0|A_0|\cos^2\kappa_0\sin\tilde{\tau}|\sin\tilde{\tau}| - rA_0\cos\kappa_0\sin\tilde{\tau} - F_0\cos\tilde{\tau}\cos\theta_0 + F_0\sin\tilde{\tau}\sin\theta_0.
\end{aligned} \tag{4.36}$$

From the arguments that we just have the stationary solution and its asymptotic expansion is uniform in $\tilde{\tau}$, it follows that no resonant excitation is allowed in the right hand side of the equation (4.36). This means (see (B.10)) that we should suppress the cos- and sin-terms including those in the Fourier expansion of

$$\sin(x)|\sin(x)| \sim \frac{8}{3\pi}\sin(x) - \frac{8}{15\pi}\sin(3x) - \ldots.$$

Hence we obtain the algebraic equations

$$\begin{aligned}
F_0\cos\theta_0 &= -\sigma A_0\left[\frac{\kappa_0}{\tan\kappa_0}\cos\kappa_0 + \cos\kappa_0 - \kappa_0\sin\kappa_0\right]\\
F_0\sin\theta_0 &= \quad A_0\left[\frac{8}{3\pi}\cos^2\kappa_0|A_0| + r\cos\kappa_0\right].
\end{aligned} \tag{4.37}$$

In general, A_0 has to be solved numerically, from which θ_0 follows. There exist two (real) solutions, while if (A_0, θ_0) is a solution, then also $(-A_0, \theta_0+\pi)$. So, if convenient, we could assume that A_0 is positive and maintain $|A_0| = A_0$, but this depends on θ_0. Solving (4.37), we can obtain A_0 and θ_0 as plotted in Fig. 4.3. We notice that the amplitude rises to $O(1)$ at resonance and decays when $\sigma \to \pm\infty$.

If we take the low frequency limit ($\kappa_0 \to 0$) in (4.37), we obtain exactly the same equations as in Chapter 3 (3.27). Physically, in this limit, the cavity length L would be asymptotically smaller than the acoustic wavelength $2\pi c_0/\omega_0$ and hence the wave would feel a uniform pressure inside the cavity and thus the current modelling assumption converges to the one in Chapter 3.

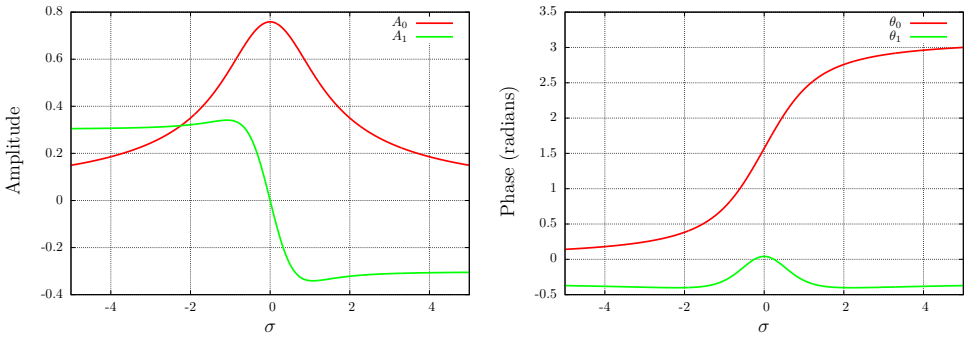

Figure 4.3: Solution of amplitude (A_0, A_1) and phase (θ_0, θ_1) as a function of σ, with $\kappa_0 = 0.55$, and $r = F_0 = 1$

From (4.36), we have

$$\frac{1}{\tan\kappa_0}\left[\tilde{\phi}_1'(\tilde{\tau}-\kappa_0) - \tilde{\phi}_1'(\tilde{\tau}+\kappa_0)\right] - \left[\tilde{\phi}_1(\tilde{\tau}-\kappa_0) + \tilde{\phi}_1(\tilde{\tau}+\kappa_0)\right] = \frac{A_0^2\cos^2(\kappa_0)}{\pi}\sum_{n=1}^{\infty}\frac{\sin(2n+1)\tilde{\tau}}{(n^2-\frac{1}{4})(n+\frac{3}{2})}$$

which can be solved term-wise using (B.1), similar to (4.33), to obtain

$$\tilde{\phi}_1(\tilde{\tau}) = \tfrac{1}{2}A_1\cos\tilde{\tau} + \tfrac{1}{2}B_1\sin\tilde{\tau} + \frac{A_0^2\cos^2\kappa_0\tan\kappa_0}{2\pi}\times \sum_{n=1}^{\infty}\frac{\sin(2n+1)\tilde{\tau}}{\cos(2n+1)\kappa_0\left[(2n+1)\tan(2n+1)\kappa_0 - \tan\kappa_0\right](n^2-\frac{1}{4})(n+\frac{3}{2})} \tag{4.38}$$

which upon substituting in (4.35) gives

$$\tilde{v}_1(\tilde{\tau}) = A_1\cos\kappa_0\sin\tilde{\tau} - B_1\cos\kappa_0\cos\tilde{\tau} + \sigma\kappa_0 A_0\frac{\cos\kappa_0}{\tan\kappa_0}\sin\tilde{\tau} - \frac{A_0^2\cos^2\kappa_0}{\pi}\sum_{n=1}^{\infty}\frac{\cos(2n+1)\tilde{\tau}}{\left[(2n+1)-\frac{\tan\kappa_0}{\tan(2n+1)\kappa_0}\right](n^2-\frac{1}{4})(n+\frac{3}{2})}. \tag{4.39}$$

Using the condition (4.27), *i.e.* $\tilde{v}_1(\tilde{\tau} = N\pi) = 0$, we find

$$B_1 = -\frac{A_0^2\cos^2\kappa_0}{\pi}\sum_{n=1}^{\infty}\frac{1}{\left[(2n+1)-\frac{\tan\kappa_0}{\tan(2n+1)\kappa_0}\right](n^2-\frac{1}{4})(n+\frac{3}{2})}. \tag{4.40}$$

Note that in the limit $\kappa_0 \to 0$, we have $B_1 = -\frac{2}{9\pi}A_0^2$, which is useful for later. The other two unknowns A_1 and θ_1 are to be determined from the regularity condition at next order (ε^2).

Order ε^2 analysis:

Collecting the terms of $O(\varepsilon^2)$ from (4.29), we obtain

$$\begin{aligned}
\tilde{v}_2' - \tilde{y}_2 =& -\sigma\tilde{v}_1' - 2\tilde{v}_1|\tilde{v}_0| - r\tilde{v}_1 + \theta_1\sin(\tilde{\tau}+\theta_0)\\
\tilde{\phi}_2(\tilde{\tau}-\kappa_0) + \tilde{\phi}_2(\tilde{\tau}+\kappa_0) =& -\tfrac{1}{2}(\sigma\kappa_0)^2\left[\tilde{\phi}_0''(\tilde{\tau}-\kappa_0) + \tilde{\phi}_0''(\tilde{\tau}+\kappa_0)\right]\\
&+\sigma\kappa_0\left[\tilde{\phi}_1'(\tilde{\tau}-\kappa_0) - \tilde{\phi}_1'(\tilde{\tau}+\kappa_0)\right] + \tilde{y}_2(\tilde{\tau})\\
\tilde{\phi}_2(\tilde{\tau}-\kappa_0) - \tilde{\phi}_2(\tilde{\tau}+\kappa_0) =& -\tfrac{1}{2}(\sigma\kappa_0)^2\left[\tilde{\phi}_0''(\tilde{\tau}-\kappa_0) - \tilde{\phi}_0''(\tilde{\tau}+\kappa_0)\right]\\
&+\sigma\kappa_0\left[\tilde{\phi}_1'(\tilde{\tau}-\kappa_0) + \tilde{\phi}_1'(\tilde{\tau}+\kappa_0)\right] + \tan\kappa_0\,\tilde{v}_2(\tilde{\tau}).
\end{aligned} \tag{4.41}$$

Substituting $\tilde{y}_2$ and $\tilde{v}_2$ in the first equation of (4.41), we obtain

$$\begin{aligned}
&\frac{1}{\tan\kappa_0}\left[\tilde{\phi}_2'(\tilde{\tau}-\kappa_0) - \tilde{\phi}_2'(\tilde{\tau}+\kappa_0)\right] - \left[\tilde{\phi}_2(\tilde{\tau}-\kappa_0) + \tilde{\phi}_2(\tilde{\tau}+\kappa_0)\right] =\\
&\quad\tfrac{1}{2}(\sigma\kappa_0)^2\left[\tilde{\phi}_0''(\tilde{\tau}-\kappa_0) + \tilde{\phi}_0''(\tilde{\tau}+\kappa_0)\right] - \frac{(\sigma\kappa_0)^2}{2\tan\kappa_0}\left[\tilde{\phi}_0'''(\tilde{\tau}-\kappa_0) - \tilde{\phi}_0'''(\tilde{\tau}+\kappa_0)\right]\\
&\qquad-\sigma\kappa_0\left[\tilde{\phi}_1'(\tilde{\tau}-\kappa_0) - \tilde{\phi}_1'(\tilde{\tau}+\kappa_0)\right] + \frac{\sigma\kappa_0}{\tan\kappa_0}\left[\tilde{\phi}_1''(\tilde{\tau}-\kappa_0) + \tilde{\phi}_1''(\tilde{\tau}+\kappa_0)\right]\\
&\qquad\qquad-\sigma\tilde{v}_1' - 2\tilde{v}_1|\tilde{v}_0| - r\tilde{v}_1 + \theta_1\sin(\tilde{\tau}+\theta_0),
\end{aligned} \tag{4.42}$$

in which we have to suppress the sine - cosine terms to obtain A_1 and θ_1. Using (4.33), (4.34), (4.38), (4.39) and (4.40) with (4.42), (see appendix [B.3]) and collecting the coefficients of cosine and sine terms and equating them to zero, we obtain a set of 2 linear equations with variables A_1 and θ_1

$$\begin{aligned}
&\left[\sigma\kappa_0\sin\kappa_0 + \frac{\sigma\kappa_0}{\tan\kappa_0}\cos\kappa_0 + \sigma\cos\kappa_0\right]A_1 - \theta_1\sin\theta_0 =\\
&\qquad\left(r\cos\kappa_0 + \frac{8}{3\pi}A_0\cos^2\kappa_0\right)B_1 - \sigma^2\kappa_0\frac{\cos\kappa_0}{\tan\kappa_0}A_0\\
&\qquad-\frac{2A_0^3\cos^3\kappa_0}{\pi^2}\sum_{n=1}^{\infty}\frac{1}{\left[(2n+1) - \frac{\tan\kappa_0}{\tan(2n+1)\kappa_0}\right](n^2-\frac{1}{4})(n+\frac{3}{2})(n-\frac{1}{2})(n+\frac{3}{2})}
\end{aligned}$$

$$\begin{aligned}
&\left[r\cos\kappa_0 + \frac{16}{3\pi}A_0\cos^2\kappa_0\right]A_1 - \theta_1\cos\theta_0 =\\
&-\left(\sigma\kappa_0\sin\kappa_0 + \frac{\sigma\kappa_0}{\tan\kappa_0}\cos\kappa_0 + \sigma\cos\kappa_0\right)B_1 - r\sigma\kappa_0\frac{\cos\kappa_0}{\tan\kappa_0}A_0 - \frac{16}{3\pi}\sigma\kappa_0\frac{\cos^2\kappa_0}{\tan\kappa_0}A_0^2.
\end{aligned} \tag{4.43}$$

Solving (4.43), we can determine A_1 and θ_1 as shown in Fig. 4.3. Hence we have the solution correct till $O(\varepsilon)$. In the limit $\kappa_0 \to 0$ and noting that

$$\sum_{n=1}^{\infty}\frac{(2n+1)}{4n(n+1)(n^2-\frac{1}{4})(n+\frac{3}{2})^2(n-\frac{1}{2})} = \frac{9\pi^2-80}{54},$$

we obtain from (4.43)

$$\begin{aligned} 2\sigma A_1 - \theta_1 \sin\theta_0 &= -\sigma^2 A_0 - \left[\frac{1}{3} - \frac{64}{27\pi^2}\right] A_0^3 - \frac{2}{9\pi} r A_0^2 \\ \left[\frac{16}{3\pi} A_0 + r\right] A_1 - \theta_1 \cos\theta_0 &= -r\sigma A_0 - \frac{44}{9\pi}\sigma A_0^2 \end{aligned} \tag{4.44}$$

which is exactly the equation set of Chapter 3 (3.36), as expected. This confirms the consistency of the current and previous solutions. Using (4.39), (4.31), (4.28) and (4.16), we finally obtain

$$\begin{aligned} u_n =& 2\varepsilon\ell\omega_0 \left[(A_0 \cos\kappa_0 + \varepsilon A_1 \cos\kappa_0 + \varepsilon\sigma\kappa_0 A_0 \frac{\cos\kappa_0}{\tan\kappa_0}) \sin(\omega t - \theta) \right] \\ & - 2\varepsilon\ell\omega_0 \left[\varepsilon B_1 \cos\kappa_0 \cos(\omega t - \theta) \right] \\ & - 2\varepsilon^2 \ell\omega_0 \frac{A_0^2 \cos^2\kappa_0}{\pi} \sum_{n=1}^{\infty} \frac{\cos(2n+1)(\omega t - \theta)}{\left[(2n+1) - \frac{\tan\kappa_0}{\tan(2n+1)\kappa_0}\right](n^2 - \frac{1}{4})(n + \frac{3}{2})}. \end{aligned} \tag{4.45}$$

The velocity in (4.45) after averaging over the surface (multiplying with S_n/S_b) can be used with the external excitation in (4.16) to obtain the impedance that we will derive in the next section. It is interesting to note that, to the leading orders,

$$u_n(t) = 2\varepsilon\ell\omega_0 A_0 \cos\kappa_0 \sin(\omega t - \theta_0). \tag{4.46}$$

If we expand the function $\tilde{\phi}(\tilde{\tau} - \Omega\kappa_0)$ about $\Omega\kappa_0$ in (4.30) assuming small κ_0, we obtain

$$\tilde{y}(\tilde{\tau}) = 2\tilde{\phi}(\tilde{\tau}) \qquad \text{and} \qquad \tilde{v}(\tilde{\tau}) = -2\Omega\tilde{\phi}'(\tilde{\tau}), \tag{4.47}$$

that can be substituted back in (4.29) to obtain

$$\Omega^2 \tilde{y}''(\tilde{\tau}) + \varepsilon\Omega^2 \tilde{y}'(\tilde{\tau})|\tilde{y}'(\tilde{\tau})| + \varepsilon\Omega r \tilde{y}'(\tilde{\tau}) + \tilde{y}(\tilde{\tau}) = \varepsilon F \tag{4.48}$$

which is exactly the equation analysed in Chapter 3 in the non linear regime with the condition that the pressure inside the cavity is uniform and the velocity inside is given by the time derivative of pressure *i.e.*

$$V \frac{\mathrm{d}p_{\mathrm{in}}}{\mathrm{d}t} = -\rho_0 c_0^2 u_n S_n \tag{4.49}$$

where $V = S_b L$ is the volume of the cavity. From (4.34) and (4.16), we obtain

$$p_{\mathrm{in}}(t) = 2\varepsilon\rho_0 \ell^2 \omega_0^2 A_0 \cos(\omega t - \theta_0) \tag{4.50}$$

which upon substituting in (4.49) gives

$$u_n(t) = 2\varepsilon\omega\ell A_0 \sin(\omega t - \theta_0). \tag{4.51}$$

The neck velocity $u_n(t)$ in (4.51) is exactly the one obtained in Chapter 3 (3.41) with the term ω instead of ω_0 like in (4.45). Note that close to resonance $\Omega = \omega/\omega_0 \approx 1$, ω and ω_0 are asymptotically equivalent. However, the two different approaches of cavity modeling produce different, but asymptotically equivalent forms of solutions.

4.6 Impedance calculation

In order to obtain realistic numbers, we will consider the impedance Z as the effective impedance of an array of Helmholtz resonators, where the spatially averaged neck velocity is identified to the external acoustic velocity. Therefore, we add a porosity factor S_n/S_b to u_n and obtain

$$v_{\rm ex} = \frac{S_n}{S_b} u_n. \tag{4.52}$$

Then we define the impedance as the ratio of the Fourier transforms of the external pressure $p_{\rm ex}$ and (minus) the external velocity $v_{\rm ex}$ at excitation frequency ω.

$$Z(\eta) = \frac{\hat{p}_{\rm ex}(\eta)}{-\hat{v}_{\rm ex}(\eta)} = \frac{\dfrac{1}{2\pi}\displaystyle\int_{-\infty}^{\infty} p_{\rm ex}(t)\,{\rm e}^{-{\rm i}\eta t}\,{\rm d}t}{-\dfrac{1}{2\pi}\displaystyle\int_{-\infty}^{\infty} v_{\rm ex}(t)\,{\rm e}^{-{\rm i}\eta t}\,{\rm d}t} \quad (\eta = \omega). \tag{4.53}$$

4.6.1 Non resonant impedance

Taking the Fourier transformation of $p_{\rm ex}(t)$ from (4.16) and Fourier transformation of $v_{\rm ex}(t) = (S_n/S_b)u_{\rm n}(t)$ from (4.24), we obtain for $\eta > 0$,

$$\begin{aligned}
\hat{p}_{\rm ex}(\eta) =& \frac{1}{2\pi}\int_{-\infty}^{\infty} p_{\rm ex}(t)\,{\rm e}^{-{\rm i}\eta t}\ {\rm d}t = \frac{1}{2\pi}\varepsilon^2\rho_0\ell^2\omega_0^2\,F_0\delta(\eta-\omega)\\
\hat{v}_{\rm ex}(\eta) =& \frac{1}{2\pi}\int_{-\infty}^{\infty} v_{\rm ex}(t)\,{\rm e}^{-{\rm i}\eta t}\ {\rm d}t\\
=& \frac{1}{2\pi}\frac{S_n}{S_b}\varepsilon^2\omega_0\ell\left[\frac{-\tan(\Omega\kappa_0)}{\Omega\tan(\Omega\kappa_0)-\tan\kappa_0}\frac{1}{\rm i} - \varepsilon r\left(\frac{\tan(\Omega\kappa_0)}{\Omega\tan(\Omega\kappa_0)-\tan\kappa_0}\right)^2\right]\delta(\eta-\omega)
\end{aligned} \tag{4.54}$$

with the negative of the ratio of above two in (4.54) being the impedance, given by

$$Z(\omega) = \frac{S_b}{S_n}\rho_0\ell\omega_0\left[\frac{\tan(\Omega\kappa_0)}{\Omega\tan(\Omega\kappa_0)-\tan\kappa_0}\frac{1}{\rm i} + \varepsilon r\left(\frac{\tan(\Omega\kappa_0)}{\Omega\tan(\Omega\kappa_0)-\tan\kappa_0}\right)^2\right]^{-1}. \tag{4.55}$$

To leading orders in ε, the impedance expression in (4.55) indeed becomes the one in (4.14) as expected.

4.6.2 Resonant impedance

Taking the Fourier transformation of $p_{\rm ex}$ from (4.16) and Fourier transformation of $v_{\rm ex}(t) = (S_n/S_b)u_{\rm n}(t)$ from (4.45), we have for $\eta > 0$

$$\hat{p}_{\rm ex}(\eta) = \frac{1}{2\pi}\int_{-\infty}^{\infty} p_{\rm ex}(t)\,{\rm e}^{-{\rm i}\eta t}\,{\rm d}t = \frac{1}{2\pi}\varepsilon^2\rho_0\ell^2\omega_0^2\,F_0\delta(\eta-\omega), \tag{4.56}$$

$$\begin{aligned}\hat{v}_{\rm ex}(\eta) &= \frac{1}{2\pi}\int_{-\infty}^{\infty} v_{\rm ex}(t)\,{\rm e}^{-{\rm i}\eta t}\,{\rm d}t \\ &= \frac{-{\rm i}}{2\pi}\frac{S_n}{S_b}\varepsilon\omega_0\ell\,{\rm e}^{-{\rm i}\theta}\left[A_0\cos\kappa_0 + \varepsilon A_1\cos\kappa_0 + \varepsilon\sigma\kappa_0 A_0\frac{\cos\kappa_0}{\tan\kappa_0} - {\rm i}\varepsilon B_1\cos\kappa_0\right]\delta(\eta-\omega).\end{aligned} \tag{4.57}$$

Substituting (4.56) and (4.57) in (4.53), we obtain

$$Z(\omega) = \varepsilon\rho_0\ell\omega_0\frac{S_b}{S_n}\frac{-{\rm i}\,{\rm e}^{{\rm i}\theta}\,F_0}{A_0\cos\kappa_0 + \varepsilon(A_1\cos\kappa_0 + \sigma A_0\cos\kappa_0\frac{\kappa_0}{\tan\kappa_0} - {\rm i}B_1\cos\kappa_0)}. \tag{4.58}$$

In order to illustrate formula (4.58), we have plotted in Fig. 4.4 resistance $\mathrm{Re}(Z)$ and reactance $\mathrm{Im}(Z)$ as a function of Ω, obtained for a typical geometry at different driving amplitudes, corresponding with ε varying from 0.03 to 0.19. As may be expected from (4.58), the main effect of the forcing amplitude is in the resistance. The reactance is practically independent of it. Typically, the resistance increases everywhere with the amplitude, being highest at or near the resonance frequency and decaying along both sides, but more for frequencies less than the resonance frequency. Away from the resonance, if we take the limit $\sigma \to \pm\infty$, in (4.58), we obtain the linear impedance described by (4.14). Hence, the non linear impedance matches asymptotically to the linear impedance which confirms the consistency of our non linear solution.

Effect of second order approximation and organ pipe cavity on the resistance

In order to understand the effect of the second order approximation on the resistance, the resistances obtained from the first ($\tilde{v}_0$) and second ($\tilde{v}_0+\varepsilon\tilde{v}_1$) order approximations are shown in Fig. 4.5 (*left)*. As we can see, for lower driving amplitudes, the second order correction is not necessary. It is, however, essential for higher amplitudes. In order to understand the effect of the organ pipe type cavity on the resistance term, we take the limit $\kappa_0 \to 0$ in (4.58) and obtain the expression

$$\begin{aligned}Z(\omega) &\sim \varepsilon\rho_0\ell\omega_0\frac{S_b}{S_n}\frac{-{\rm i}\,{\rm e}^{{\rm i}\theta}\,F_0}{(A_0 + \varepsilon A_1 + \varepsilon\sigma A_0 + {\rm i}\varepsilon\frac{2}{9\pi}A_0^2)} \\ &= \frac{\varepsilon\rho_0 c_0^2 F_0}{L\omega_0}\frac{-{\rm i}\,{\rm e}^{{\rm i}\theta}}{A_0(1+\varepsilon\sigma) + {\rm i}\varepsilon\frac{2}{9\pi}A_0^2 + \varepsilon A_1}.\end{aligned} \tag{4.59}$$

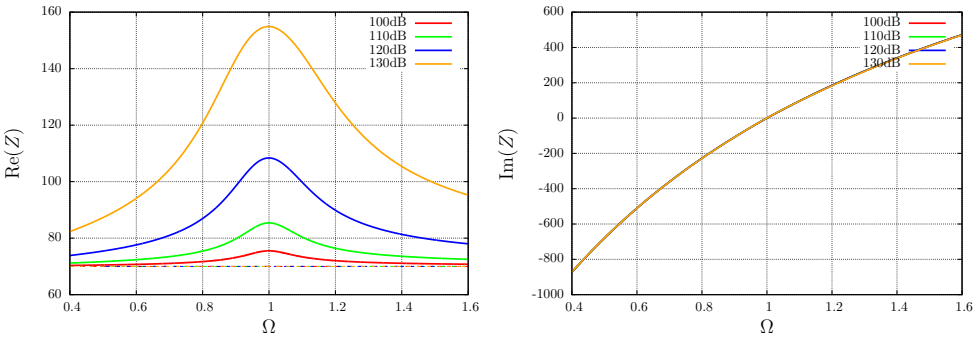

p_{ex} (dB)	100	110	120	130
ε	0.0337	0.0599	0.1065	0.1893

Figure 4.4: Real and imaginary parts of impedance Z for an extended Helmholtz resonator as a function of non dimensional frequency at different driving amplitudes. The realistic configuration that is chosen corresponds with $\ell = 0.005\,\text{m}$, $L = 0.035\,\text{m}$ and $S_n/S_b = 0.05$ that gives $\kappa_0 = 0.55$ and $\omega_0 = 5367$ rad/sec, while $F_0 = 1$. The dashed line represents the linear resistance which is obtained by multiplying $R = 3.5$ with porosity factor *i.e.* $(S_b/S_n)R = 70$. Note: r is adapted such that εr is kept fixed.

The plots of resistance obtained with finite κ_0 (4.58) and $\kappa_0 \to 0$ (4.59) are shown in Fig. 4.5 *(right)*. For very low amplitudes, this effect is minor, but it is quite essential for higher amplitudes. Also, we notice that a finite κ_0 resistance curve has a better behavior away from the resonance frequency when compared with the experimental data curve in Fig. 4.7 *(right)*.

Comparison with previous model, Chapter 3

The impedance expression found in Chapter 3 (3.50),

$$\begin{aligned} Z(\omega) &= \frac{\varepsilon\rho_0 c_0^2 F_0}{L\omega} \frac{-\mathrm{i}\,\mathrm{e}^{\mathrm{i}\theta}}{A_0 + \mathrm{i}\varepsilon\frac{2}{9\pi}A_0^2 + \varepsilon A_1} \\ &= \frac{\varepsilon\rho_0 c_0^2 F_0}{L\omega_0} \frac{-\mathrm{i}\,\mathrm{e}^{\mathrm{i}\theta}}{A_0(1+\varepsilon\sigma) + \mathrm{i}\varepsilon\frac{2}{9\pi}A_0^2 + \varepsilon A_1 + \varepsilon\sigma(\mathrm{i}\varepsilon\frac{2}{9\pi}A_0^2 + \varepsilon A_1)}, \end{aligned} \tag{4.60}$$

is asymptotically equivalent to (4.59) (note that $\omega = \omega_0(1+\varepsilon\sigma)$). Shown in Fig. 4.6 is the plot of the resistance obtained from (4.60), (4.58) and (4.59), for a typical geometry and external excitation, varying from 100dB to 130dB. The current model with finite κ_0 (4.58) indeed predicts the near resonance behavior to a better accuracy and decays away from the resonance to match with the linear resistance. The resistance predicted by the (4.59) follows the same. The near resonance behaviour of Chapter 3 is similar to previous ones, however, with higher ε and away from the resonance, the resistance does not decay. It turns out just by sheer luck that the asymptotic-

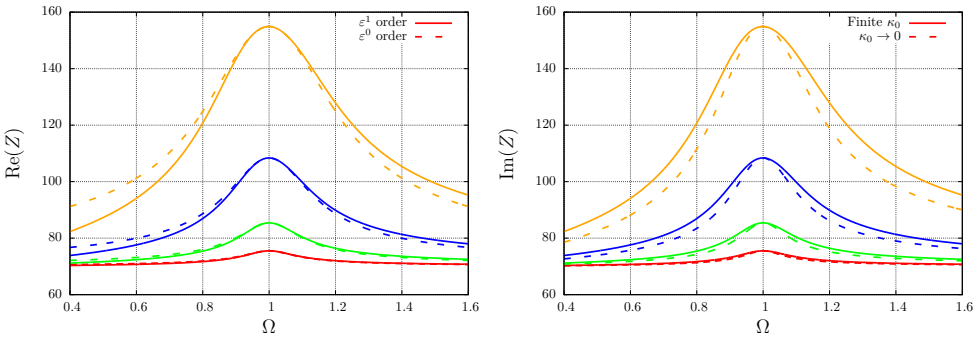

Figure 4.5: Resistance, Re(Z) as a function of non dimensional frequency at different driving amplitudes. The configuration of the resonator and driving amplitudes are the same as in Fig. 4.4.

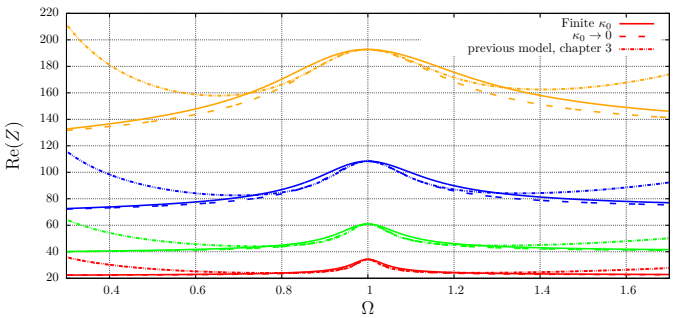

Figure 4.6: Comparison of resistance, Re(Z) based upon the current model and that of Chapter 3, as a function of non dimensional frequency at different driving amplitudes. The configuration of the resonator and deriving amplitudes are the same as in Fig. 4.4, except that $r = 1$ is kept constant.

ally equivalent form (4.59) of (4.60) gives good prediction at higher ε. There can be many asymptotically equivalent possible form of impedance solution, valid close to the resonance. However, (4.59) works better even away from the resonance. Hence, as a concluding remark, we suggest to use the asymptotically equivalent form (4.59) as the impedance expression derived in Chapter 3.

4.7 Comparison with Motsinger and Kraft

The behavior in (4.58) may be compared in Fig. 4.7 with the measurements and predictions given by Motsinger and Kraft in [35]. Their predictions are (a.o.) based on a resistance of the form $R = \rho_0 c_0(a + b|v|)$ with suitably chosen a and b while $|v|$ corresponds to $\|u_n\|$. The parameter values we used are based on $\omega_0/2\pi = 2209.1\,\text{Hz}$, $\ell = 0.002\,\text{m}$, $L = 0.014\,\text{m}$, $S_n/S_b = 0.05$, $r = 0.26$ and $\kappa_0 = 0.5715$. Unfortunately,

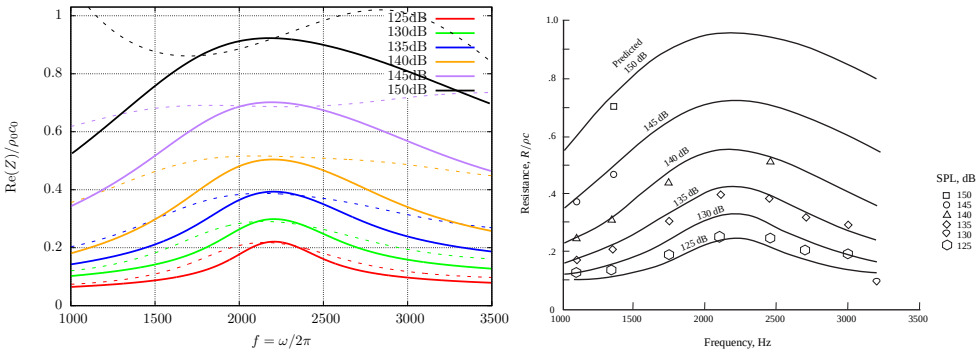

p_{ex} (dB)	125	130	135	140	145	150
ε	0.1373	0.1830	0.2441	0.3255	0.4340	0.5788

Figure 4.7: Comparison of (4.58) with measurements and predictions of $\mathrm{Re}(Z)/\rho_0 c_0$ given in [35]. The solid lines in the left corresponds to the resistance values produced by (4.58) while the dotted lines corresponds to the previous model, Chapter 3. The markers in the right figure represent the measured values which were used, by adopting the relation $R = \rho_0 c_0(a + b|v|)$, to predict the resistance in solid curves.

only little experimental data for the higher amplitudes are available. However, the agreement is remarkably good, even when ε is relatively large for higher amplitudes. The impedance for higher amplitude (ε) at and near resonance is predicted much more accurately compared to the previous model, which is plotted by dotted lines. So we conclude that the current model has indeed a better accuracy and could be used to predict the impedance for resonators of small or big lengths.

4.8 Conclusions

A systematic approximation of the hydrodynamically non linear Helmholtz resonator equation that includes higher order axial modes in the cavity is obtained, including the resulting impedance if the resonator as applied in an acoustic liner. The only unknown parameter that we need to adapt is resistance factor r, and sometimes the effective neck length ℓ is also unknown and has to be estimated. Comparisons with measurements show that the model predicts the near resonance impedance behaviour at $\sigma = O(1)$ to a good accuracy and a better resemblance is found (especially for higher excitation amplitudes) compared to the previous model of Chapter 3.

The real part of the found impedance (the resistance) shows the usual characteristic behavior as a function of frequency, namely a maximum at the resonance frequency and a decay along both sides. All values increase with the amplitude. The imaginary part of the impedance (the reactance) is linear in frequency in a way that it vanishes at resonance and is practically independent of the amplitude. The non linear solution asymptotically matches smoothly with the linear solution, which confirms the

consistency of our solution.

Chapter 5

Vorticity scattering at hard wall - pressure release wall transition in shear flows

An extensive analysis of the isolated Helmholtz resonator has been performed in the previous chapters. Locally reacting liners consist of many of such small tiny resonators and the lining surface acts as a sound absorbing device to the external sound field. As stated earlier in Chapter 1, the liners are characterized by their impedance Z and are manufactured in the form of rectangular sheets. When such liners are placed in the inlet or bypass duct of aircraft engines or in the ventilation ducts, there are always some hard wall surfaces where the acoustic lining treatment is not possible. Some other reasons why hard wall surfaces are often associated close to the acoustic lining are explained in Chapter 1. Due to the presence of such hard - soft or soft - hard discontinuities, the vorticity present in the flow is scattered and causes far field sound radiations. This scattering process will be studied in detail in the subsequent chapters.

5.1 Introduction

The theory of aerodynamic noise, first introduced by Lighthill [44] and based upon the equations of fluid motion, was devoted to the noise generated by incompressible turbulence, in the absence of boundaries behaving acoustically as compact sources of the quadrupole type. This lead to the celebrated Lighthill estimate of radiated acoustic intensity being $\sim M_0^8$, where M_0 is the typical flow Mach number. Curle [26] subsequently showed that (large) rigid boundaries increase the efficiency of the noise process by turning the neighbouring turbulent noise sources from quadrupole into dipole type, leading to a radiated intensity varying as $\sim M_0^6$. Ffowcs Williams and Hall [34] later on showed that turbulence passing an edge are even more efficient

sources of noise. The singularity of the scattering field near the edge creates an equivalent source distribution that leads to a radiated intensity $\sim M_0^5$.

Powell [4] formulated this process as follows. If the Mach number of the flow is small, the spectral component of the boundary layer pressure perturbations, *i.e.* the Fourier transform of pressure in the plane of boundary layer, have subsonic phase velocities which constitute a strong local field but decays exponentially with the distance from the flow and hence, can not propagate as sound. The presence of an infinite homogeneous boundary must facilitate some interaction with the flow in order to scatter the subsonic nearfield to far field sound. However, this boundary responding to the turbulent vibrations of small amplitude is inefficient and hence, the flow can not use such a boundary to improve its radiation and the sound field must be essentially that due to the inefficient quadrupole type turbulence sources. On the other hand, if there is a discontinuity in the boundary, the flow may use it as a "wave number converter" to amplify the scattered far field noise. So the main sound production of sound concentrates at discontinuities of the boundaries.

This was confirmed by Crighton who studied in detail the radiation from flow passing a transition of two semi-infinite planes that differ in their inertia and elastic properties [27] , and the passage of a 2D vortex along the edge of a semi-infinite plane [24]. More examples may be found in [38, 28, 96, 95].

Thus, the influence of discontinuities in boundaries on the aerodynamic noise generated by turbulent flows in general and vortical perturbations in particular have been shown to be relevant in aerodynamic noise. The available theory is limited to the scattering of vortices in vanishing or uniform mean flow. However, if the vorticity is convected by, and to a certain extent part of the mean flow, the role of shear may be essential, since the sound producing vorticity may be just perturbations of the mean shear [86]). This is the problem that we will address here, and in particular sheared mean flow along a wall that is partly solid and partly soft.

Such hard-soft wall transition points are common for example in lined flow ducts of aircraft engines, or ventilation ducts. Since little is known about any functional relationships of the radiated sound field, there is a need for canonical model problems that allow analytically exact solutions of vorticity in shear flow scattering at hard-soft transitions of a liner wall. In the current work, the scattering of 2D vorticity perturbations in an inviscid low Mach number shear flow (with vanishing velocity at the wall) passing over a hard to soft transition of this wall has been examined. The analysis is divided into two chapters. In the current Chapter, 4, the mathematical limit of impedance $Z = 0$ is considered which enables us to obtain the hydrodynamic solution analytically exactly and the explicit estimates of the radiated sound field. In Chapter 5, the extension of the analysis to a finite impedance Z wall is considered, while we use the insight obtained from the $Z = 0$-problem of this chapter.

The method we will employ is the Wiener-Hopf method combined with Fourier transformation in space. In acoustics this is a common approach, especially when we deal with configurations of semi-infinite geometries. The present problem of incompressible flow, however, is considerably different from the usual acoustic problems, and

the application of the Wiener-Hopf method is not straightforward. This is mainly due to the solutions diverging at infinity and not being standard Fourier transformable. Careful regularisation of the associated singularity in the origin of the Fourier domain are necessary.

5.2 Model

The incident field is assumed to be produced by a source far upstream, for example a mass source. Following [86], a 2D vorticity χ with mass source Q, satisfying

$$\rho\Big(\frac{\partial}{\partial t}+\boldsymbol{v}\cdot\nabla\Big)\Big(\frac{\chi}{\rho}\Big)=-\frac{\chi}{\rho}Q. \tag{5.1}$$

is considered. A non conservative force field f would also produce similar results [81]. If the source is small enough for linearisation, located in a bounded region $\mathcal{G}$, and induces harmonic isentropic perturbations of frequency $\omega>0$ to a parallel sheared flow U with otherwise constant density ρ_0 and sound speed c_0 given by

$$\boldsymbol{v}=U(y)\boldsymbol{e}_x+\hat{\boldsymbol{v}}\,\mathrm{e}^{\mathrm{i}\omega t},\quad \chi=-U'(y)+\hat{\chi}\,\mathrm{e}^{\mathrm{i}\omega t},\quad \rho=\rho_0+c_0^{-2}\hat{p}\,\mathrm{e}^{\mathrm{i}\omega t},\quad Q=\hat{q}\,\mathrm{e}^{\mathrm{i}\omega t}, \tag{5.2}$$

then we have after linearisation[1]

$$\rho_0\Big(\mathrm{i}\omega+U(y)\frac{\partial}{\partial x}\Big)\Big(\hat{\chi}+\frac{U'(y)}{\rho_0c_0^2}\hat{p}\Big)=\rho_0U''(y)\hat{v}+U'(y)\hat{q}. \tag{5.3}$$

For a linear profile $U(y)=\sigma y$, with $\sigma>0$, $U(y_0)=\sigma y_0=U_0$, $U'=\sigma$ and $U''=0$, we have

$$\rho_0\Big(\mathrm{i}\omega+U(y)\frac{\partial}{\partial x}\Big)\Big(\hat{\chi}+\frac{\sigma}{\rho_0c_0^2}\hat{p}\Big)=\sigma\hat{q}=\sigma\iint_{\mathcal{G}}\big[\hat{q}(x_0,y_0)\delta(x-x_0)\delta(y-y_0)\big]\,\mathrm{d}x_0\mathrm{d}y_0. \tag{5.4}$$

This has, under causal free field conditions (allowing only perturbations generated by the source) and $U_0>0$, the solution [86]

$$\hat{\chi}+\frac{\sigma}{\rho_0c_0^2}\hat{p}=\frac{\sigma}{\rho_0U_0}\iint_{\mathcal{G}}\Big[\hat{q}(x_0,y_0)H(x-x_0)\,\mathrm{e}^{-\mathrm{i}k_0(x-x_0)}\,\delta(y-y_0)\Big]\,\mathrm{d}x_0\mathrm{d}y_0,\quad k_0=\frac{\omega}{U_0}. \tag{5.5}$$

where $H(x)$ denotes Heaviside's function. Downstream the source we have just $H(x-x_0)=1$. Utilising linearity we will consider a single (x_0,y_0)-component with unit amplitude and phase factor $\mathrm{e}^{\mathrm{i}k_0x_0}=1$, in the incompressible limit, leading to the oscillatory vortex sheet

$$\hat{\chi}=\frac{\sigma}{\rho_0U_0}\,\mathrm{e}^{-\mathrm{i}k_0x}\,\delta(y-y_0). \tag{5.6}$$

[1] This corrects an unfortunate error in the introduction of [86], where in equation (1.7) the term $\rho_0U''\hat{v}$ is missing. The suggested generality of result (1.10) is therefore not correct. However, for the linear mean flow $U(y)=\sigma y$, assumed everywhere else, this missing term vanishes and all results remain valid.

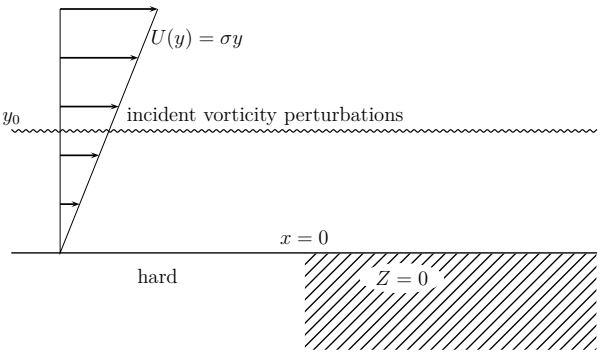

Figure 5.1: Sketch of the problem

With uniform boundary conditions along the wall $y = 0$, the velocity and pressure fields associated with this vortex sheet are easily determined. Technically speaking, this is not exactly the same as the downstream limit of the field from a point mass source [86, eqs. 3.18,19,24] due to the source associated logarithmic divergence of the pressure, inherent to two-dimensional incompressible flow. By postulating the source far enough away (in the acoustic outer field), it is justified to ignore this part of the field.

In summary, we consider the two-dimensional incompressible inviscid problem of perturbations of a linearly sheared mean flow $U(y) = \sigma y$, with harmonic time dependence ($\mathrm{e}^{\mathrm{i}\omega t}$) and a vortex sheet along $y = y_0$ in $y > 0$. The flow is along a wall at $y = 0$ which is hard for $x < 0$ and soft (a vanishing impedance) for $x > 0$; see Fig. 5.1. In this configuration we will have no contribution of a critical layer or an instability like in [33]. The linear flow profile is considered to be found at the bottom of a mean flow boundary layer, thick enough to neglect any finite thickness effects, but this assumption is not a trivial one. We will see that only under certain conditions the interaction with the top of the boundary layer can be ignored and a mean flow profile $U(y) = \sigma y$ is a consistent modelling assumption.

The associated field of the downstream travelling vorticity decays exponentially away from the line $y = y_0$ in the order $\sim \mathrm{e}^{-k_0|y-y_0|-\mathrm{i}k_0 x}$. When this field hits the hard-to-soft wall transition point $x = 0$, it is scattered into a local field that will radiate, at least for a part, as sound into the far field.

The flow in the domain shown in Fig. 5.1 is governed by the linearised incompressible Euler equations with mixed boundary conditions (a vanishing normal velocity for $x < 0$ and a vanishing pressure for $x > 0$), which makes the Wiener-Hopf technique [14, 28] a natural choice for obtaining the solution. Once this solution is obtained, we can try to determine the corresponding acoustic source strength and assess the produced sound. For this we will try to match the incompressible inner solution to a compressible (acoustic) outer solution.

It will appear that the analysis is segregated in two different branches depending upon the parameters σ and ω. For brevity, we use the term *low shear* case when $0 < \sigma < \omega$ and *high shear* case when $0 < \omega < \sigma$.

5.3 Mathematical formulation

The governing equation of mass and momentum conservation, written in frequency domain (and ignoring the hats) expressed in the variables introduced in (5.2), are

$$\begin{aligned} \rho_0 \left(\frac{\partial u}{\partial x} + \frac{\partial v}{\partial y} \right) &= 0, \\ \rho_0 \left(\mathrm{i}\omega + U \frac{\partial}{\partial x} \right) u + \rho_0 \frac{\mathrm{d}U}{\mathrm{d}y} v + \frac{\partial p}{\partial x} &= 0, \\ \rho_0 \left(\mathrm{i}\omega + U \frac{\partial}{\partial x} \right) v + \frac{\partial p}{\partial y} &= 0. \end{aligned} \tag{5.7}$$

For later reference we note that, analogous to equation (5.3), the perturbation vorticity $\chi = v_x - u_y$ satisfies

$$\rho_0 \Big(\mathrm{i}\omega + U(y) \frac{\partial}{\partial x} \Big) \chi = \rho_0 U''(y) v. \tag{5.8}$$

So vorticity is convected but remains the same as long as $U'' = 0$. For now, we will assume a mean flow $U = \sigma y$, with indeed $U'' = 0$. However, in the far field there is inevitably a region where the real U must be curtailed in order to have the postulated compressible (acoustic) field with small mean flow Mach number, and so there will be a transitional region where U'' is non zero.

Boundary conditions at half planes $y = 0$ are vanishing velocity and pressure respectively, *i.e.*

$$v = 0 \quad \text{if} \quad x < 0, \qquad p = 0 \quad \text{if} \quad x > 0 \tag{5.9}$$

and an edge condition of vanishing energy flux from $(0, 0)$. The far field boundary conditions will be of vanishing velocity, but maybe not of vanishing pressure. The incident field (of the undulating vortex sheet at $y = y_0 = U_0/\sigma$) is given by

$$\begin{aligned} u_{\mathrm{in}} = \quad & U_0 \, \mathrm{e}^{-\mathrm{i}k_0 x} \Big[\quad - \operatorname{sign}(y - y_0) \; \mathrm{e}^{-k_0 |y - y_0|} \; + \qquad\qquad \mathrm{e}^{-k_0 (y + y_0)} \Big], \\ v_{\mathrm{in}} = \quad & \mathrm{i} U_0 \, \mathrm{e}^{-\mathrm{i}k_0 x} \Big[\qquad\qquad\quad \mathrm{e}^{-k_0 |y - y_0|} \; - \qquad\qquad \mathrm{e}^{-k_0 (y + y_0)} \Big], \\ p_{\mathrm{in}} = \quad & \frac{\sigma}{\omega} \rho_0 U_0^2 \, \mathrm{e}^{-\mathrm{i}k_0 x} \Big[\quad (1 + k_0 |y - y_0|) \, \mathrm{e}^{-k_0 |y - y_0|} \; - \quad (1 + k_0 (y - y_0)) \, \mathrm{e}^{-k_0 (y + y_0)} \Big], \end{aligned} \tag{5.10}$$

with $k_0 = \omega / U_0$, $k_0 y_0 = \omega / \sigma$ and assumed to be scaled by a small amplitude. Note that along the wall,

$$u_{\mathrm{in}}(x, 0) = 2 U_0 \, \mathrm{e}^{-\mathrm{i}k_0 x - k_0 y_0}, \quad v_{\mathrm{in}}(x, 0) = 0, \quad p_{\mathrm{in}}(x, 0) = 2 \rho_0 U_0^2 \, \mathrm{e}^{-\mathrm{i}k_0 x - k_0 y_0}, \tag{5.11}$$

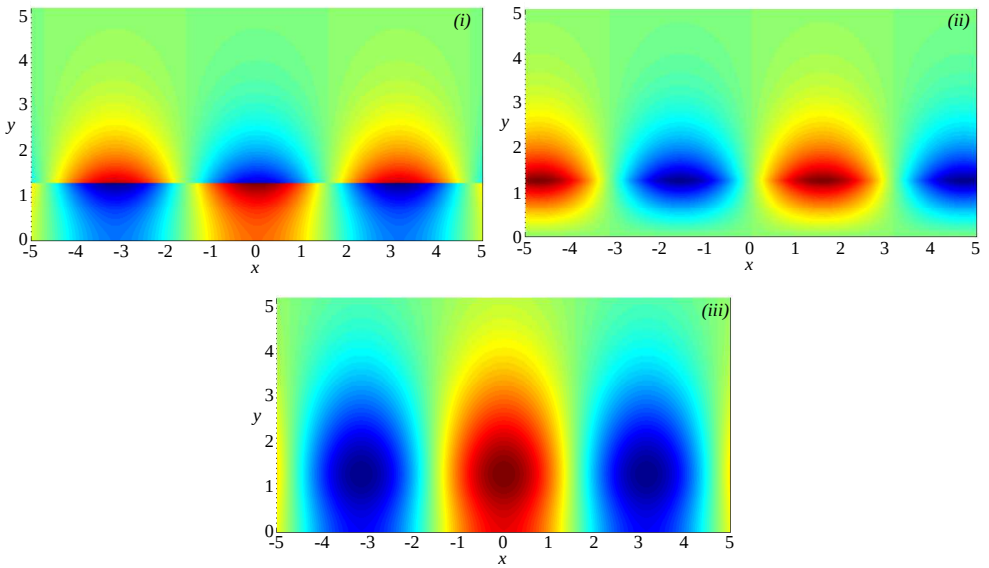

Figure 5.2: The initial field u_{in}, v_{in} and p_{in} respectively. $\omega = 5, \sigma = 4, U_0 = 5, k_0 = 1, y_0 = 1.25$, (hard wall).

so for any interaction between vorticity and wall to happen, $k_0 y_0$ should not be too large. Fig. 5.2 shows pressure and velocities of a typical case.

The triple $(u_{\text{in}}, v_{\text{in}}, p_{\text{in}})$ satisfies the differential equation, continuity of p_{in} and v_{in} across $y = y_0$, and the hard-wall boundary condition $v_{\text{in}} = 0$ at $y = 0$. The scattered perturbations are due to the non vanishing p_{in} along $y = 0, x > 0$.

We split up the field in the incident part and the scattered part as follows

$$u = u_{\text{in}} + \overline{u}, \quad v = v_{\text{in}} + \overline{v}, \quad p = p_{\text{in}} + \overline{p}. \tag{5.12}$$

After Fourier transformation in x (assuming, at least formally, the existence of the integrals)

$$\overline{p}(x, y) = \frac{1}{2\pi} \int_{-\infty}^{\infty} \tilde{p}(y, k)\, \mathrm{e}^{-\mathrm{i}kx}\, \mathrm{d}k, \tag{5.13}$$

the same for $\overline{u}$ and $\overline{v}$, we obtain the following set of equations

$$\rho_0(-\mathrm{i}k\tilde{u} + \tilde{v}') = 0, \qquad \mathrm{i}\rho_0\Omega\tilde{u} + \rho_0\sigma\tilde{v} - \mathrm{i}k\tilde{p} = 0, \qquad \mathrm{i}\rho_0\Omega\tilde{v} + \tilde{p}' = 0, \tag{5.14}$$

where $\Omega = \omega - kU$. The system of equations has two independent solutions, namely $\sim \mathrm{e}^{\pm ky}$ [45, 65]. The one, bounded for $y \to \infty$ (and a possible singularity at $k = 0$),

is then

$$\begin{aligned}\tilde{u}(y) &= kA(k)\,\mathrm{e}^{-|k|y},\\ \tilde{v}(y) &= -\mathrm{i}|k|A(k)\,\mathrm{e}^{-|k|y},\\ \tilde{p}(y) &= \rho_0(\Omega - \operatorname{sign}(\operatorname{Re} k)\sigma)A(k)\,\mathrm{e}^{-|k|y},\end{aligned} \tag{5.15}$$

where $A(k)$ is to be determined. $|k| = \sqrt{k^2}$ and $\operatorname{sign}(\operatorname{Re} k) = k/|k|$, where $\sqrt{\ }$ denotes the principal value square root. $|k|$ has thus branch cuts along the imaginary axis given by $(-\mathrm{i}\infty, 0)$ and $(0, \mathrm{i}\infty)$. This definition of $\operatorname{sign}(\operatorname{Re} k)$ will be maintained with the regularisation of $|k|$ later.

5.4 Wiener-Hopf procedure

The method of Wiener and Hopf [57] was initially devised to solve certain type of integral equations in complex the domain. By introducing suitable half range Fourier transforms, Jones [41] was able to apply the method to problems written as partial differential equations in domains with semi-infinite boundary conditions, which is typically the situation here. To facilitate the application of the Wiener-Hopf method in the complex k-plane of the Fourier transform introduced above, we introduce a regularising small positive parameter ε and have an upper and a lower half plane, and an overlapping strip as follows.

$$\mathbb{C}^+ = \{k \in \mathbb{C} \mid \operatorname{Im} k > -\varepsilon\},\ \mathbb{C}^- = \{k \in \mathbb{C} \mid \operatorname{Im} k < \varepsilon\},\ S = \{k \in \mathbb{C} \mid -\varepsilon < \operatorname{Im} k < \varepsilon\}.$$

The physical problem will be the limit $\varepsilon \to 0$ of a regularised problem with k_0 replaced by $\lambda_0 = k_0 - \mathrm{i}\varepsilon \notin \mathbb{C}^+$ (such that we have an incident field $\sim \mathrm{e}^{-\mathrm{i}\lambda_0 x} = \mathrm{e}^{-\mathrm{i}k_0 x - \varepsilon x}$ slightly decaying with x) and $|k|$ replaced by the smoother function

$$|k| \simeq \mu(k) = \sqrt{k^2 + \varepsilon^2},$$

with a principal value square root and branch cuts $(-\mathrm{i}\infty, -\mathrm{i}\varepsilon) \cup (\mathrm{i}\varepsilon, \mathrm{i}\infty)$ avoiding strip S (*cf.* [79]).

Introduce the half-range Fourier transforms

$$F_-(k) = \int_{-\infty}^{0} \overline{p}(x,0)\,\mathrm{e}^{\mathrm{i}kx}\,\mathrm{d}x, \quad G_+(k) = \int_0^{\infty} \overline{v}(x,0)\,\mathrm{e}^{\mathrm{i}kx}\,\mathrm{d}x, \tag{5.16}$$

that are assumed to be analytic in $\mathbb{C}^+$ and $\mathbb{C}^-$ respectively, as explained in appendix C.1. Then we have for G_+

$$G_+(k) = \int_0^{\infty} \overline{v}(x,0)\,\mathrm{e}^{\mathrm{i}kx}\,\mathrm{d}x = \int_{-\infty}^{\infty} \overline{v}(x,0)\,\mathrm{e}^{\mathrm{i}kx}\,\mathrm{d}x = -\mathrm{i}\mu A(k), \tag{5.17}$$

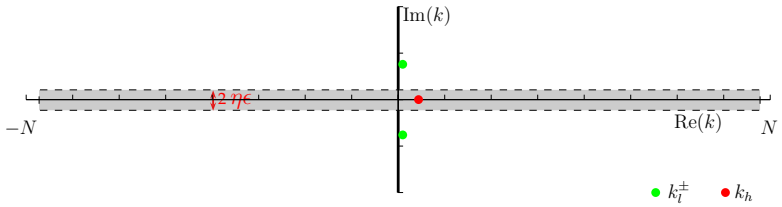

Figure 5.3: Contour $\mathcal{C}$ and zeros of $L(k)$.

and for F_-

$$F_-(k) = \int_{-\infty}^{0} \overline{p}(x,0)\,\mathrm{e}^{\mathrm{i}kx}\,\mathrm{d}x = \int_{-\infty}^{\infty} \overline{p}(x,0)\,\mathrm{e}^{\mathrm{i}kx}\,\mathrm{d}x + \int_{0}^{\infty} p_{\mathrm{in}}(x,0)\,\mathrm{e}^{\mathrm{i}kx}\,\mathrm{d}x$$
$$= \rho_0 A(k)\frac{\omega\mu - \sigma k}{\mu} + 2\mathrm{i}\rho_0 U_0^2 \frac{\mathrm{e}^{-\lambda_0 y_0}}{k-\lambda_0} = \rho_0 A(k)\mu L(k) + 2\mathrm{i}\rho_0 U_0^2 \frac{\mathrm{e}^{-\lambda_0 y_0}}{k-\lambda_0}, \quad (5.18)$$

with Wiener-Hopf kernel

$$L(k) = \frac{\omega\mu - \sigma k}{k^2+\varepsilon^2}, \quad K(k) = \lim_{\varepsilon\downarrow 0} L(k). \quad (5.19)$$

So the limit of $L(k)$ for $\varepsilon \downarrow 0$ will be indicated by $K(k)$. With $\varepsilon = 0$ and $\omega \neq \sigma$, $L(k) = K(k)$ is free from zeros outside $k = 0$, and singular at $k = 0$. However, for $\varepsilon > 0$ there are zero's, as indicated in Fig. 5.3, namely

$$k_l^{\pm} = +0 \pm \mathrm{i}\varepsilon\frac{\omega}{\sqrt{\omega^2-\sigma^2}} \qquad \text{if} \quad \sigma < \omega,$$
$$k_h = \varepsilon\frac{\omega}{\sqrt{\sigma^2-\omega^2}} \qquad \text{if} \quad \sigma > \omega.$$

In the low-shear case $\sigma < \omega$, $|k_h^{\pm}| > \varepsilon$, so the zeros are imaginary, outside S and located on the right side of the branchcuts of μ. In the high-shear case $\sigma > \omega$, on the other hand, there is only one zero. This zero is real and therefore always inside the strip. This is relevant when we construct splitfunctions (below) and this zero calls for a slight change in the procedure (Appendix C.4).

From (5.18), we arrive at the Wiener-Hopf equation

$$F_-(k) = \mathrm{i}\rho_0 G_+(k) L(k) + 2\mathrm{i}\rho_0 U_0^2 \frac{\mathrm{e}^{-\lambda_0 y_0}}{k-\lambda_0}, \quad (5.20)$$

which is to be solved in the standard way [14] by writing

$$L(k) = \frac{L_+(k)}{L_-(k)}, \quad (5.21)$$

where splitfunction L_+ is analytic and non zero in $\mathbb{C}^+$ and L_- is analytic and non

zero in $\mathbb{C}^-$.

If the function to be split is well behaved at infinity, free of zero's in the strip, and we can define its logarithm such that no branch cuts cross the strip, then the construction of the splitfunctions is classic [57, 14]. We consider $k \in S$ inside a large rectangular contour $\mathcal{C} \subset S$ between $k = -N - \mathrm{i}\eta\varepsilon$ and $k = N + \mathrm{i}\eta\varepsilon$, where η is small enough, as shown in Fig. 5.3. Then by Cauchy's integral representation theorem, limits taken for $N \to \infty$, and taking the upper and lower contour apart, we obtain (for a generic function $\mathcal{F}(k)$)

$$\log \mathcal{F}_\pm(k) = \frac{1}{2\pi\mathrm{i}} \int_{-\infty}^{\infty} \frac{\log \mathcal{F}(\xi \mp \mathrm{i}\eta\varepsilon)}{\xi \mp \mathrm{i}\eta\varepsilon - k} \,\mathrm{d}\xi, \quad k \in \mathbb{C}^\pm. \tag{5.22}$$

If $\varepsilon \to 0$, the representations of $\mathcal{F}_+$ and $\mathcal{F}_-$ become the same, in the sense that it is $\mathcal{F}_+$ if $k \in \mathbb{C}^+$ and $\mathcal{F}_-$ if $k \in \mathbb{C}^-$.

Since $L(k)$ may have a zero in the strip, and $L(k) \not\to 1$ at infinity, we cannot apply the above recipe directly, and we have to modify the procedure in a way similar to Noble [14, example 1.12, page 41-42]. This modification is essentially different for the low shear ($\sigma < \omega$) and the high shear ($\sigma > \omega$) cases and is explained in Appendix C.4. We find splitfunctions $L_\pm$, which are for $\varepsilon = 0$ indicated by $K_\pm$ and analytically exactly given by

$$\begin{aligned} &\sigma < \omega: \quad K_+(k) = (\omega - \sigma)(k)_+^{-\frac{1}{2} - \mathrm{i}\delta}, \quad K_-(k) = (k)_-^{\frac{1}{2} - \mathrm{i}\delta}, \\ &\sigma > \omega: \quad K_+(k) = (\omega - \sigma)(k)_+^{-\mathrm{i}\delta}, \qquad K_-(k) = (k)_-^{1 - \mathrm{i}\delta}, \end{aligned} \qquad \delta = \frac{1}{2\pi} \log\left|\frac{\omega + \sigma}{\omega - \sigma}\right|. \tag{5.23}$$

$(k)_+^\alpha$ denotes the complex power function k^α with $(1)_+^\alpha = 1$ and the branch cut along the negative imaginary axis, and is thus analytic in $\mathbb{C}^+$. $(k)_-^\alpha$ denotes the complex power function k^α with $(1)_-^\alpha = 1$ and the branch cut along the positive imaginary axis, and is thus analytic in $\mathbb{C}^-$. These exact splitfunctions will allow explicit solutions later. Once we have the split function $L_+(k)$ and $L_-(k)$, we can conclude that in S

$$\begin{aligned} L_-(k)F_-(k) - \mathrm{i}\rho_0 L_+(k)G_+(k) &= 2\mathrm{i}\rho_0 U_0^2 \,\mathrm{e}^{-\lambda_0 y_0} \frac{L_-(k)}{k - \lambda_0} \\ &= 2\mathrm{i}\rho_0 U_0^2 \,\mathrm{e}^{-\lambda_0 y_0} \frac{L_-(k) - L_-(k_0)}{k - \lambda_0} + 2\mathrm{i}\rho_0 U_0^2 \,\mathrm{e}^{-\lambda_0 y_0} \frac{L_-(k_0)}{k - \lambda_0}, \end{aligned} \tag{5.24}$$

where we isolated pole $\lambda_0 \in \mathbb{C}^-$ from L_-. The parts that are analytic in $\mathbb{C}^+$ and in $\mathbb{C}^-$ respectively, are via their equivalence in S each other's analytic continuations, and define an entire function $E(k)$

$$\begin{aligned} E(k) &= L_-(k)F_-(k) - 2\mathrm{i}\rho_0 U_0^2 \,\mathrm{e}^{-\lambda_0 y_0} \frac{L_-(k) - L_-(\lambda_0)}{k - \lambda_0} \\ &= \mathrm{i}\rho_0 L_+(k)G_+(k) + 2\mathrm{i}\rho_0 U_0^2 \,\mathrm{e}^{-\lambda_0 y_0} \frac{L_-(\lambda_0)}{k - \lambda_0}. \end{aligned} \tag{5.25}$$

E can be determined from the condition for $k \to \infty$, related to the edge condition for $(x, y) \to 0$. Following Appendix C.3, we conclude that $|G_+(k)| = O(k^{-\alpha})$ for some $\alpha > 0$, so that E is bounded and thus (according to Liouville's theorem) a constant which is for both low and high shear $E = 0$. Finally, for $\varepsilon \downarrow 0$ and λ_0 replaced by k_0 and $L_\pm$ by $K_\pm$, we can write from (5.18) and (5.25)

$$\begin{aligned} F_-(k) &= 2\mathrm{i}\rho_0 U_0^2 \,\mathrm{e}^{-k_0 y_0}\, \frac{K_-(k) - K_-(k_0)}{(k-k_0)K_-(k)}, \\ G_+(k) &= -2U_0^2 \,\mathrm{e}^{-k_0 y_0}\, \frac{K_-(k_0)}{(k-k_0)K_+(k)}, \\ A(k) &= -2\mathrm{i}U_0^2 \,\mathrm{e}^{-k_0 y_0}\, \frac{K_-(k_0)}{|k|(k-k_0)K_+(k)}. \end{aligned} \qquad (5.26)$$

$A(k)$ obtained from (5.26) can be substituted back into (5.15). This gives, with the inverse Fourier transform from (5.13) added to the initial field (5.10), the formal solution u, v and p

$$\begin{aligned} u &= u_{\mathrm{in}} + U_0^2 \,\mathrm{e}^{-k_0 y_0}\, K_-(k_0) \frac{1}{\pi\mathrm{i}} \fint_{-\infty}^{\infty} \frac{\operatorname{sign}(\operatorname{Re} k)}{(k-k_0)K_+(k)} \,\mathrm{e}^{-|k|y - \mathrm{i}kx}\, \mathrm{d}k, \\ v &= v_{\mathrm{in}} - U_0^2 \,\mathrm{e}^{-k_0 y_0}\, K_-(k_0) \frac{1}{\pi} \fint_{-\infty}^{\infty} \frac{1}{(k-k_0)K_+(k)} \,\mathrm{e}^{-|k|y - \mathrm{i}kx}\, \mathrm{d}k, \\ p &= p_{\mathrm{in}} + \rho_0 U_0^2 \,\mathrm{e}^{-k_0 y_0}\, K_-(k_0) \frac{1}{\pi\mathrm{i}} \fint_{-\infty}^{\infty} \frac{\Omega - \sigma \operatorname{sign}(\operatorname{Re} k)}{|k|(k-k_0)K_+(k)} \,\mathrm{e}^{-|k|y - \mathrm{i}kx}\, \mathrm{d}k. \end{aligned} \qquad (5.27)$$

where k_0 is captured from above, *i.e.* $k_0 \in \mathbb{C}^-$. The behaviour of the $K_+(k)$ function in (5.27) is different for the low shear (C.9) and high shear (C.10) cases, and hence the solution u, v, p differs likewise, as announced earlier. The Fourier integrals in (5.27) can be evaluated analytically. The process differs slightly whether $x \gtrless 0$ due to the existence of the pole $k = k_0$, which corresponds to trailing vorticity of the hard-soft discontinuity [86]. From (5.27) and (5.23), we have for the low shear case

$$\begin{aligned} \overline{u} &= \frac{U_0^2 \,\mathrm{e}^{-k_0 y_0}\, k_0^{\frac{1}{2}-\mathrm{i}\delta}}{(\omega-\sigma)\pi\mathrm{i}} \fint_{-\infty}^{\infty} \frac{\operatorname{sign}(\operatorname{Re} k)}{k-k_0} (k)_+^{\frac{1}{2}+\mathrm{i}\delta} \,\mathrm{e}^{-|k|y - \mathrm{i}kx}\, \mathrm{d}k, \\ \overline{v} &= -\frac{U_0^2 \,\mathrm{e}^{-k_0 y_0}\, k_0^{\frac{1}{2}-\mathrm{i}\delta}}{(\omega-\sigma)\pi} \fint_{-\infty}^{\infty} \frac{1}{k-k_0} (k)_+^{\frac{1}{2}+\mathrm{i}\delta} \,\mathrm{e}^{-|k|y - \mathrm{i}kx}\, \mathrm{d}k, \\ \overline{p} &= \frac{\rho_0 U_0^2 \,\mathrm{e}^{-k_0 y_0}\, k_0^{\frac{1}{2}-\mathrm{i}\delta}}{(\omega-\sigma)\pi\mathrm{i}} \fint_{-\infty}^{\infty} \frac{\Omega - \sigma \operatorname{sign}(\operatorname{Re} k)}{|k|(k-k_0)} (k)_+^{\frac{1}{2}+\mathrm{i}\delta} \,\mathrm{e}^{-|k|y - \mathrm{i}kx}\, \mathrm{d}k. \end{aligned} \qquad (5.28)$$

and for the high shear case

$$\begin{aligned}
\overline{u} &= \frac{U_0^2\,\mathrm{e}^{-k_0 y_0}\,k_0^{1-\mathrm{i}\delta}}{(\omega-\sigma)\pi\mathrm{i}} \int\!\!\!\!\!\!-_{-\infty}^{\infty} \frac{\operatorname{sign}(\operatorname{Re} k)}{k-k_0}(k)_+^{\mathrm{i}\delta}\,\mathrm{e}^{-|k|y-\mathrm{i}kx}\,\mathrm{d}k,\\
\overline{v} &= -\frac{U_0^2\,\mathrm{e}^{-k_0 y_0}\,k_0^{1-\mathrm{i}\delta}}{(\omega-\sigma)\pi} \int\!\!\!\!\!\!-_{-\infty}^{\infty} \frac{1}{k-k_0}(k)_+^{\mathrm{i}\delta}\,\mathrm{e}^{-|k|y-\mathrm{i}kx}\,\mathrm{d}k,\\
\overline{p} &= \frac{\rho_0 U_0^2\,\mathrm{e}^{-k_0 y_0}\,k_0^{1-\mathrm{i}\delta}}{(\omega-\sigma)\pi\mathrm{i}} \int\!\!\!\!\!\!-_{-\infty}^{\infty} \frac{\Omega-\sigma\operatorname{sign}(\operatorname{Re} k)}{|k|(k-k_0)}(k)_+^{\mathrm{i}\delta}\,\mathrm{e}^{-|k|y-\mathrm{i}kx}\,\mathrm{d}k.
\end{aligned} \tag{5.29}$$

From (5.28) and (5.29), we notice that the high shear case has a stronger singularity at $k=0$ than the low shear case and hence we may expect a stronger far field, because $k\to 0$ in Fourier domain relates to $r\to\infty$ in physical domain. In some sense this will indeed be the case and the consequences are important. The high shear solution will not decay fast enough to provide a matching with any proper outer field, leading to the conclusion that the present high shear solution is inconsistent with the modelling assumptions.

For the time being, we will not draw this conclusion yet, and continue with our derivation. In the next section, we will evaluate the integrals in (5.28) and (5.29) analytically.

5.5 Analytical solution

5.5.1 Solutions in the form of integrals

In contrast to the accompanying problem with a general impedance, the Fourier integral representations (5.28) and (5.29) of the present problem can be evaluated completely analytically. The evaluation is pursued by first transforming the integrals using $k=k_0\kappa$. For the low shear case this amounts to

$$\begin{aligned}
\overline{u} &= U_0\,\mathrm{e}^{-k_0 y_0}\,\frac{\omega}{\omega-\sigma}\frac{1}{\pi\mathrm{i}} \int\!\!\!\!\!\!-_{-\infty}^{\infty} \frac{\operatorname{sign}(\operatorname{Re}\kappa)}{\kappa-1}(\kappa)_+^{\frac{1}{2}+\mathrm{i}\delta}\,\mathrm{e}^{-|\kappa|k_0 y-\mathrm{i}\kappa k_0 x}\,\mathrm{d}\kappa,\\
\overline{v} &= -U_0\,\mathrm{e}^{-k_0 y_0}\,\frac{\omega}{\omega-\sigma}\frac{1}{\pi} \int\!\!\!\!\!\!-_{-\infty}^{\infty} \frac{1}{\kappa-1}(\kappa)_+^{\frac{1}{2}+\mathrm{i}\delta}\,\mathrm{e}^{-|\kappa|k_0 y-\mathrm{i}\kappa k_0 x}\,\mathrm{d}\kappa,\\
\overline{p} &= \rho_0 U_0^2\,\mathrm{e}^{-k_0 y_0}\,\frac{1}{\pi\mathrm{i}} \int\!\!\!\!\!\!-_{-\infty}^{\infty} \frac{\omega-\sigma\operatorname{sign}(\operatorname{Re}\kappa)-\kappa k_0\sigma y}{(\omega-\sigma)|\kappa|(\kappa-1)}(\kappa)_+^{\frac{1}{2}+\mathrm{i}\delta}\,\mathrm{e}^{-|\kappa|k_0 y-\mathrm{i}\kappa k_0 x}\,\mathrm{d}\kappa.
\end{aligned} \tag{5.30}$$

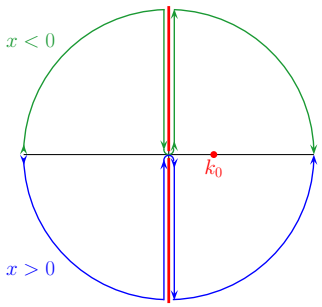

Figure 5.4: Deformed paths of the integration contour. The residue of k_0 is to be included if $x > 0$.

and for the high shear case,

$$\begin{aligned}
\overline{u} &= U_0\,\mathrm{e}^{-k_0 y_0}\,\frac{\omega}{\omega-\sigma}\,\frac{1}{\pi\mathrm{i}}\,\fint_{-\infty}^{\infty}\frac{\operatorname{sign}(\operatorname{Re}\kappa)}{\kappa-1}(\kappa)_+^{\mathrm{i}\delta}\,\mathrm{e}^{-|\kappa|k_0 y-\mathrm{i}\kappa k_0 x}\,\mathrm{d}\kappa,\\
\overline{v} &= -U_0\,\mathrm{e}^{-k_0 y_0}\,\frac{\omega}{\omega-\sigma}\,\frac{1}{\pi}\,\fint_{-\infty}^{\infty}\frac{1}{\kappa-1}(\kappa)_+^{\mathrm{i}\delta}\,\mathrm{e}^{-|\kappa|k_0 y-\mathrm{i}\kappa k_0 x}\,\mathrm{d}\kappa,\\
\overline{p} &= \rho_0 U_0^2\,\mathrm{e}^{-k_0 y_0}\,\frac{1}{\pi\mathrm{i}}\,\fint_{-\infty}^{\infty}\frac{\omega-\sigma\operatorname{sign}(\operatorname{Re}\kappa)-\kappa k_0\sigma y}{(\omega-\sigma)|\kappa|(\kappa-1)}(\kappa)_+^{\mathrm{i}\delta}\,\mathrm{e}^{-|\kappa|k_0 y-\mathrm{i}\kappa k_0 x}\,\mathrm{d}\kappa.
\end{aligned}\tag{5.31}$$

The integration contour along the real k axis can be folded around the lower and upper branch cut for $x > 0$ and $x < 0$ respectively (Fig. 5.4). The contribution of the real pole at $\kappa = 1$ should be included whenever $x > 0$. The integrals can be further evaluated as shown in Appendix C.5. For the low shear case we obtain the integrals (C.14) and (C.15) corresponding to $x > 0$ and $x < 0$ respectively. Similarly, for the high shear case we obtain the integrals (C.16) and (C.17) corresponding to $x > 0$ and $x < 0$, respectively.

Note that the solution is singular for $\omega = \sigma$, due to the factor $\omega - k\sigma y - \sigma = -k\sigma y$ which vanishes at $y = 0$.

The pressure integrals in (C.16) and (C.17) diverge at $k = 0$ in Fourier space. Due to their origin as Fourier transforms of non integrable functions, the singular integrals have to be considered in generalised sense by introducing the generalised derivative [86, 31, 47]

$$H(t)t^{-1+\mathrm{i}\delta} \overset{\text{def}}{=} \frac{\mathrm{d}}{\mathrm{d}t}\left(\frac{H(t)}{\mathrm{i}\delta}t^{\mathrm{i}\delta}\right).$$

When we consider the incompressible problem as an inner problem of a larger compressible problem, as in [28, 46, 81], this divergent behaviour should disappear and change into an outward radiating acoustic wave (this will be true for low shear, but not for high shear). In the next section, we will express the found expressions in terms of the regular and incomplete Gamma functions, $\Gamma(\alpha)$ and $\Gamma(\alpha, z)$ respectively [63].

5.5.2 Explicit evaluation of the integrals

We introduce the notation

$$z = x + \mathrm{i}y, \qquad z^* = x - \mathrm{i}y,$$

and use (C.14) , (C.18) and (C.15) , (C.19) for $x > 0$ and $x < 0$ respectively. This yields the following solution for low shear

$$\overline{u} = \frac{U_0}{\pi}\,\mathrm{e}^{-k_0 y_0}\,\Gamma(\tfrac{3}{2}+\mathrm{i}\delta)\Big(\frac{\omega+\sigma}{\omega-\sigma}\Big)^{\frac{1}{2}}\Big[\frac{\omega}{\omega+\sigma}\,\mathrm{e}^{-\mathrm{i}k_0 z}\,\Gamma(-\tfrac{1}{2}-\mathrm{i}\delta,-\mathrm{i}k_0 z)\;+ \\ \begin{cases}(x<0) & +\dfrac{\omega}{\omega+\sigma}\,\mathrm{e}^{-\mathrm{i}k_0 z^*}\,\Gamma(-\frac{1}{2}-\mathrm{i}\delta,-\mathrm{i}k_0 z^*)\Big] \\ (x>0) & -\dfrac{\omega}{\omega-\sigma}\,\mathrm{e}^{-\mathrm{i}k_0 z^*}\,\Gamma(-\frac{1}{2}-\mathrm{i}\delta,-\mathrm{i}k_0 z^*)\Big]\end{cases} - 2U_0\frac{\omega}{\omega-\sigma}\,\mathrm{e}^{-k_0 y_0-\mathrm{i}k_0 z^*} \tag{5.32}$$

$$\overline{v} = \mathrm{i}\frac{U_0}{\pi}\,\mathrm{e}^{-k_0 y_0}\,\Gamma(\tfrac{3}{2}+\mathrm{i}\delta)\Big(\frac{\omega+\sigma}{\omega-\sigma}\Big)^{\frac{1}{2}}\Big[\frac{\omega}{\omega+\sigma}\,\mathrm{e}^{-\mathrm{i}k_0 z}\,\Gamma(-\tfrac{1}{2}-\mathrm{i}\delta,-\mathrm{i}k_0 z)\;+ \\ \begin{cases}(x<0) & -\dfrac{\omega}{\omega+\sigma}\,\mathrm{e}^{-\mathrm{i}k_0 z^*}\,\Gamma(-\frac{1}{2}-\mathrm{i}\delta,-\mathrm{i}k_0 z^*)\Big] \\ (x>0) & +\dfrac{\omega}{\omega-\sigma}\,\mathrm{e}^{-\mathrm{i}k_0 z^*}\,\Gamma(-\frac{1}{2}-\mathrm{i}\delta,-\mathrm{i}k_0 z^*)\Big]\end{cases} + 2\mathrm{i}U_0\frac{\omega}{\omega-\sigma}\,\mathrm{e}^{-k_0 y_0-\mathrm{i}k_0 z^*} \tag{5.33}$$

$$\overline{p} = -\frac{\rho_0 U_0^2}{\pi}\,\mathrm{e}^{-k_0 y_0}\,\Gamma(\tfrac{1}{2}+\mathrm{i}\delta)\Big(\frac{\omega+\sigma}{\omega-\sigma}\Big)^{\frac{1}{2}}\Big[\\ \mathrm{e}^{-\mathrm{i}k_0 z}\,\Gamma(\tfrac{1}{2}-\mathrm{i}\delta,-\mathrm{i}k_0 z) + (\tfrac{1}{2}+\mathrm{i}\delta)\frac{k_0\sigma y}{\omega+\sigma}\,\mathrm{e}^{-\mathrm{i}k_0 z}\,\Gamma(-\tfrac{1}{2}-\mathrm{i}\delta,-\mathrm{i}k_0 z) \\ \begin{cases}(x<0) & +\dfrac{\omega-\sigma}{\omega+\sigma}\,\mathrm{e}^{-\mathrm{i}k_0 z^*}\,\Gamma(\frac{1}{2}-\mathrm{i}\delta,-\mathrm{i}k_0 z^*) \\ & \qquad +(\frac{1}{2}+\mathrm{i}\delta)\dfrac{k_0\sigma y}{\omega+\sigma}\,\mathrm{e}^{-\mathrm{i}k_0 z^*}\,\Gamma(-\frac{1}{2}-\mathrm{i}\delta,-\mathrm{i}k_0 z^*)\Big] \\ (x>0) & -\mathrm{e}^{-\mathrm{i}k_0 z^*}\,\Gamma(\frac{1}{2}-\mathrm{i}\delta,-\mathrm{i}k_0 z^*) - (\frac{1}{2}+\mathrm{i}\delta)\dfrac{k_0\sigma y}{\omega-\sigma}\,\mathrm{e}^{-\mathrm{i}k_0 z^*}\,\Gamma(-\frac{1}{2}-\mathrm{i}\delta,-\mathrm{i}k_0 z^*)\Big] \\ & \qquad -2\rho_0 U_0^2\Big(1-\dfrac{k_0\sigma y}{\omega-\sigma}\Big)\,\mathrm{e}^{-k_0 y_0-\mathrm{i}k_0 z^*}\,.\end{cases} \tag{5.34}$$

The behaviour near the edge $r = 0$ is indeed $\overline{p} = O(r^{\frac{1}{2}})$ and $\overline{u}, \overline{v} = O(r^{-\frac{1}{2}})$. Furthermore, the field is not discontinuous across the line $x = 0$, since we have to account for the jumps across the branch cuts of the various log, power and Gamma functions

(Appendix C.6).

Similarly, using (C.16), (C.18) and (C.17) and (C.19) , for $x > 0$ and $x < 0$ respectively, we obtain the following solution for high shear

$$\overline{u} = \mathrm{i}\frac{U_0}{\pi}\,\mathrm{e}^{-k_0 y_0}\,\Gamma(1+\mathrm{i}\delta)\Big(\frac{\sigma+\omega}{\sigma-\omega}\Big)^{\frac{1}{2}}\Bigg[\frac{\omega}{\sigma+\omega}\,\mathrm{e}^{-\mathrm{i}k_0 z}\,\Gamma(-\mathrm{i}\delta,-\mathrm{i}k_0 z) + \begin{cases}(x<0) & +\dfrac{\omega}{\sigma+\omega}\,\mathrm{e}^{-\mathrm{i}k_0 z^*}\,\Gamma(-\mathrm{i}\delta,-\mathrm{i}k_0 z^*)\Bigg] \\ (x>0) & +\dfrac{\omega}{\sigma-\omega}\,\mathrm{e}^{-\mathrm{i}k_0 z^*}\,\Gamma(-\mathrm{i}\delta,-\mathrm{i}k_0 z^*)\Bigg]\end{cases} + 2U_0\frac{\omega}{\sigma-\omega}\,\mathrm{e}^{-k_0 y_0-\mathrm{i}k_0 z^*} \tag{5.35}$$

$$\overline{v} = -\frac{U_0}{\pi}\,\mathrm{e}^{-k_0 y_0}\,\Gamma(1+\mathrm{i}\delta)\Big(\frac{\sigma+\omega}{\sigma-\omega}\Big)^{\frac{1}{2}}\Bigg[\frac{\omega}{\sigma+\omega}\,\mathrm{e}^{-\mathrm{i}k_0 z}\,\Gamma(-\mathrm{i}\delta,-\mathrm{i}k_0 z) + \begin{cases}(x<0) & -\dfrac{\omega}{\sigma+\omega}\,\mathrm{e}^{-\mathrm{i}k_0 z^*}\,\Gamma(-\mathrm{i}\delta,-\mathrm{i}k_0 z^*)\Bigg] \\ (x>0) & -\dfrac{\omega}{\sigma-\omega}\,\mathrm{e}^{-\mathrm{i}k_0 z^*}\,\Gamma(-\mathrm{i}\delta,-\mathrm{i}k_0 z^*)\Bigg]\end{cases} - 2\mathrm{i}U_0\frac{\omega}{\sigma-\omega}\,\mathrm{e}^{-k_0 y_0-\mathrm{i}k_0 z^*} \tag{5.36}$$

$$\overline{p} = -\mathrm{i}\frac{\rho_0 U_0^2}{\pi}\,\mathrm{e}^{-k_0 y_0}\,\Gamma(\mathrm{i}\delta)\Big(\frac{\sigma+\omega}{\sigma-\omega}\Big)^{\frac{1}{2}}\Bigg[\mathrm{e}^{-\mathrm{i}k_0 z}\,\Gamma(1-\mathrm{i}\delta,-\mathrm{i}k_0 z) + \mathrm{i}\delta\frac{k_0\sigma y}{\sigma+\omega}\,\mathrm{e}^{-\mathrm{i}k_0 z}\,\Gamma(-\mathrm{i}\delta,-\mathrm{i}k_0 z)$$
$$\begin{cases}(x<0) & -\dfrac{\sigma-\omega}{\sigma+\omega}\,\mathrm{e}^{-\mathrm{i}k_0 z^*}\,\Gamma(1-\mathrm{i}\delta,-\mathrm{i}k_0 z^*) + \mathrm{i}\delta\dfrac{k_0\sigma y}{\sigma+\omega}\,\mathrm{e}^{-\mathrm{i}k_0 z^*}\,\Gamma(-\mathrm{i}\delta,-\mathrm{i}k_0 z^*)\Bigg] \\ (x>0) & -\mathrm{e}^{-\mathrm{i}k_0 z^*}\,\Gamma(1-\mathrm{i}\delta,-\mathrm{i}k_0 z^*) + \mathrm{i}\delta\dfrac{k_0\sigma y}{\sigma-\omega}\,\mathrm{e}^{-\mathrm{i}k_0 z^*}\,\Gamma(-\mathrm{i}\delta,-\mathrm{i}k_0 z^*)\Bigg] \\ & -2\rho_0 U_0^2\Big(1+\dfrac{k_0\sigma y}{\sigma-\omega}\Big)\,\mathrm{e}^{-k_0 y_0-\mathrm{i}k_0 z^*}\,.\end{cases} \tag{5.37}$$

The behaviour near the edge $r = 0$ is indeed $\overline{p} = O(r)$ and $\overline{u}, \overline{v} = O(1)$ and the solutions are continuous across $x = 0$.

The expressions (5.32), (5.33), (5.34) added to the initial field (5.10) give the final solution of the low shear case shown in Fig. 5.5 (*left*). Similarly, the expressions (5.35), (5.36), (5.37) added to the initial field (5.10) gives the final solution of the high shear case shown in Fig. 5.5 (*right*).

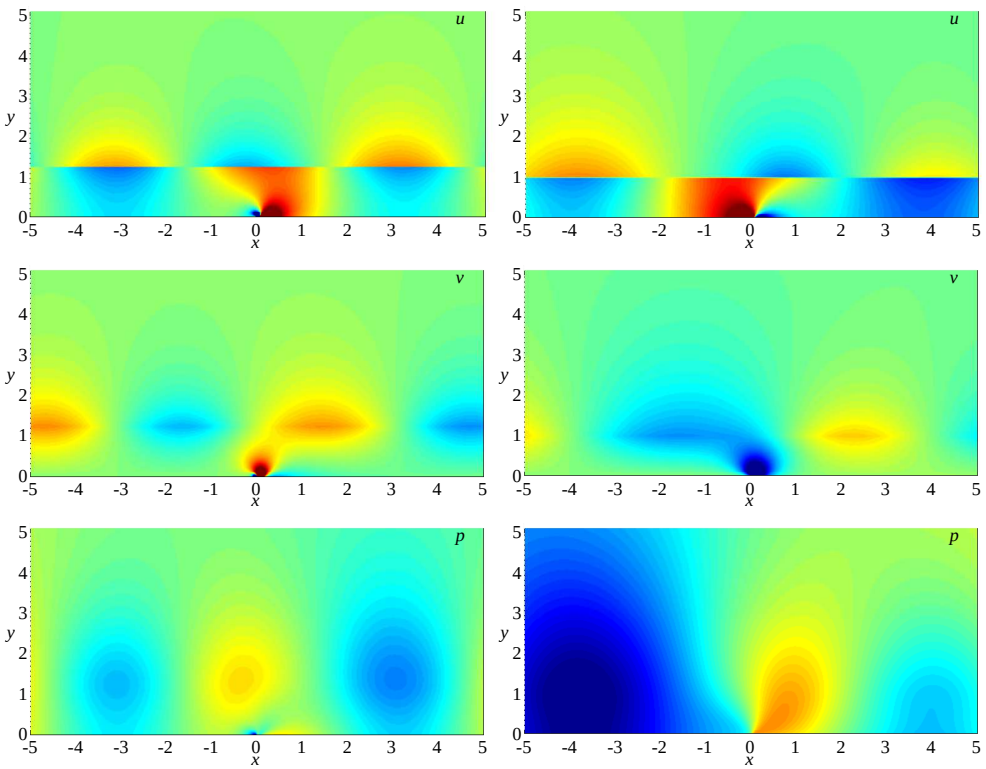

Figure 5.5: The solution fields u, v and p for low shear (*left*: $\sigma = 4 < \omega = 5, y_0 = 1.25, k_0 = 1$ and $U_0 = 5$) and high shear (*right*: $\sigma = 5 > \omega = 4, y_0 = 1, k_0 = 0.8$ and $U_0 = 5$)

5.5.3 Far field behaviour of the incompressible solution

When we are interested in the produced sound field it is necessary to consider the incompressible far field $|z| \to \infty$. Again we consider the low and high shear cases separately.

Low shear case

Using the asymptotic forms from (C.20), (C.21) in (5.32), (5.33), (5.34), we obtain single expressions for $|z| \to \infty$ (in particular, for $|x| \to \infty$ and $y \to \infty$)

$$\begin{aligned}
\overline{u} \sim\ & \mathrm{i}\frac{U_0}{\pi}\,\mathrm{e}^{-k_0 y_0}\,\mathrm{e}^{\frac{1}{4}\pi\mathrm{i}}\,\Gamma(\tfrac{3}{2}+\mathrm{i}\delta)\Big(\frac{\omega+\sigma}{\omega-\sigma}\Big)^{\frac{1}{4}}\Big[\frac{\omega}{\omega+\sigma}(k_0 z)^{-\frac{3}{2}-\mathrm{i}\delta} - \frac{\omega}{\omega-\sigma}(k_0 z^*)^{-\frac{3}{2}-\mathrm{i}\delta}\Big],\\
\overline{v} \sim\ & -\frac{U_0}{\pi}\,\mathrm{e}^{-k_0 y_0}\,\mathrm{e}^{\frac{1}{4}\pi\mathrm{i}}\,\Gamma(\tfrac{3}{2}+\mathrm{i}\delta)\Big(\frac{\omega+\sigma}{\omega-\sigma}\Big)^{\frac{1}{4}}\Big[\frac{\omega}{\omega+\sigma}(k_0 z)^{-\frac{3}{2}-\mathrm{i}\delta} + \frac{\omega}{\omega-\sigma}(k_0 z^*)^{-\frac{3}{2}-\mathrm{i}\delta}\Big],\\
\overline{p} \sim\ & -\frac{\rho_0 U_0^2}{\pi}\,\mathrm{e}^{-k_0 y_0}\,\mathrm{e}^{\frac{1}{4}\pi\mathrm{i}}\,\Gamma(\tfrac{1}{2}+\mathrm{i}\delta)\Big(\frac{\omega+\sigma}{\omega-\sigma}\Big)^{\frac{1}{4}}\Big[(k_0 z)^{-\frac{1}{2}-\mathrm{i}\delta} - (k_0 z^*)^{-\frac{1}{2}-\mathrm{i}\delta}\\
& \qquad + (\tfrac{1}{2}+\mathrm{i}\delta)\frac{\mathrm{i}k_0\sigma y}{\omega+\sigma}(k_0 z)^{-\frac{3}{2}-\mathrm{i}\delta} - (\tfrac{1}{2}+\mathrm{i}\delta)\frac{\mathrm{i}k_0\sigma y}{\omega-\sigma}(k_0 z^*)^{-\frac{3}{2}-\mathrm{i}\delta}\Big]
\end{aligned} \tag{5.38}$$

Note that both pressure and velocity decay, namely $\overline{p} = O(r^{-\frac{1}{2}})$ and $\overline{u}, \overline{v} = O(r^{-\frac{3}{2}})$, which will appear to be important for the consistency of the modelling assumption that $U = \sigma y$. In particular, any coupling (via reflection or any other back reaction) with an interface between the shear flow and a (uniform, or otherwise bounded) outerflow can be made as small as desired.

Being away from the incident vortices near $y = y_0$, there is no other cause for vorticity, and, in agreement with equation (5.8), the velocity far field is irrotational and has a potential $\overline{\phi}$ with $(\overline{u}, \overline{v}) = \nabla\overline{\phi}$, which is easily found to satisfy

$$\overline{\phi} \sim \frac{U_0^2}{\mathrm{i}\omega\pi}\,\mathrm{e}^{-k_0 y_0}\,\mathrm{e}^{\frac{1}{4}\pi\mathrm{i}}\,\Gamma(\tfrac{1}{2}+\mathrm{i}\delta)\Big(\frac{\omega+\sigma}{\omega-\sigma}\Big)^{\frac{1}{4}}\Big[\frac{\omega}{\omega+\sigma}(k_0 z)^{-\frac{1}{2}-\mathrm{i}\delta} - \frac{\omega}{\omega-\sigma}(k_0 z^*)^{-\frac{1}{2}-\mathrm{i}\delta}\Big]. \tag{5.39}$$

If we postulate a mean flow profile $U(y)$ which very slowly changes from linear σy to a constant U_∞, such that U'' remains small, and noting equation (5.8), it seems reasonable to assume that the voricity χ remains small, and the velocity potential $\overline{\phi}$ remains valid also where $U = U_\infty$. As a result we obtain for the pressure $\overline{p}$, satisfying

$$\overline{p} = -\rho_0\big(\mathrm{i}\omega + U\tfrac{\partial}{\partial x}\big)\phi \simeq -\mathrm{i}\rho_0\omega\phi, \tag{5.40}$$

the result

$$\overline{p} \sim -\frac{\rho_0 U_0^2}{\pi}\,\mathrm{e}^{-k_0 y_0}\,\mathrm{e}^{\frac{1}{4}\pi\mathrm{i}}\,\Gamma(\tfrac{1}{2}+\mathrm{i}\delta)\Big(\frac{\omega+\sigma}{\omega-\sigma}\Big)^{\frac{1}{4}}\Big[\frac{\omega}{\omega+\sigma}(k_0 z)^{-\frac{1}{2}-\mathrm{i}\delta} - \frac{\omega}{\omega-\sigma}(k_0 z^*)^{-\frac{1}{2}-\mathrm{i}\delta}\Big]. \tag{5.41}$$

Of course, the argument is heuristic and not very systematic, but we will see that it

is remarkably close to a more systematic result derived with an assumed piecewise continuous profile in the next section. Here, the mean flow will be taken equal to $U = \sigma y$ for $0 \leqslant y \leqslant h$ and $U = \sigma h = U_\infty$ for $y \geqslant h$, while h is big enough to assume that the back-interaction (reflection) from the interface to the wall is negligible. Furthermore, the resulting pressure can indeed be matched to an outward radiating sound field. For want of a strict proof, we will consider these evidences of consistency suffient argument to trust the physical relevance of expression (5.41).

High shear case

Using the asymptotic behaviour from (C.20), (C.21) in (5.35), (5.36), (5.37), we obtain a single expression for the high shear case continuous across $x = 0$

$$\begin{aligned}
\overline{u} \sim & -\frac{U_0}{\pi}\,\mathrm{e}^{-k_0 y_0}\,\Gamma(1+\mathrm{i}\delta)\Big(\frac{\sigma+\omega}{\sigma-\omega}\Big)^{\frac{1}{4}}\left[\frac{\omega}{\sigma+\omega}(k_0 z)^{-1-\mathrm{i}\delta}+\frac{\omega}{\sigma-\omega}(k_0 z^*)^{-1-\mathrm{i}\delta}\right]\\
\overline{v} \sim & -\mathrm{i}\frac{U_0}{\pi}\,\mathrm{e}^{-k_0 y_0}\,\Gamma(1+\mathrm{i}\delta)\Big(\frac{\sigma+\omega}{\sigma-\omega}\Big)^{\frac{1}{4}}\left[\frac{\omega}{\sigma+\omega}(k_0 z)^{-1-\mathrm{i}\delta}-\frac{\omega}{\sigma-\omega}(k_0 z^*)^{-1-\mathrm{i}\delta}\right]\\
\overline{p} \sim & -\mathrm{i}\frac{\rho_0 U_0^2}{\pi}\,\mathrm{e}^{-k_0 y_0}\,\Gamma(\mathrm{i}\delta)\Big(\frac{\sigma+\omega}{\sigma-\omega}\Big)^{\frac{1}{4}}\left[(k_0 z)^{-\mathrm{i}\delta}-(k_0 z^*)^{-\mathrm{i}\delta}\right.\\
& \left.-\delta\frac{k_0\sigma y}{\sigma+\omega}(k_0 z)^{-1-\mathrm{i}\delta}-\delta\frac{k_0\sigma y}{\sigma-\omega}(k_0 z^*)^{-1-\mathrm{i}\delta}\right]
\end{aligned} \tag{5.42}$$

Finally, like in the low shear case, we use the irrotational character of the velocity and define a potential function

$$\phi = \frac{U_0^2}{\omega\pi}\,\mathrm{e}^{-k_0 y_0}\,\Gamma(\mathrm{i}\delta)\Big(\frac{\sigma+\omega}{\sigma-\omega}\Big)^{\frac{1}{4}}\left[\frac{\omega}{\sigma+\omega}(k_0 z)^{-\mathrm{i}\delta}+\frac{\omega}{\sigma-\omega}(k_0 z^*)^{-\mathrm{i}\delta}\right] \tag{5.43}$$

and obtain (at least, that is what we aim for) the pressure in the uniform flow region as

$$\overline{p} \sim -\mathrm{i}\rho_0\omega\phi \sim -\mathrm{i}\frac{\rho_0 U_0^2}{\pi}\,\mathrm{e}^{-k_0 y_0}\,\Gamma(\mathrm{i}\delta)\Big(\frac{\sigma+\omega}{\sigma-\omega}\Big)^{\frac{1}{4}}\left[\frac{\omega}{\sigma+\omega}(k_0 z)^{-\mathrm{i}\delta}+\frac{\omega}{\sigma-\omega}(k_0 z^*)^{-\mathrm{i}\delta}\right] \tag{5.44}$$

This result is much less reliable, because the high-shear pressure – (5.42) as well as (5.44) – does not decay with distance. Hence, the coupling between the wall and any transition region between the linear shear flow and the uniform flow will be strong and cannot be neglected. We give the present result for the record, because up to now there was no reason to dismiss it. However, in the following we will see that the problem is serious. The high shear far field will not match with any outward radiating acoustic field. Therefore, equation (5.44), and by extension the whole high-shear solution, is most likely not correct, in the sense that with high shear a linear (*unbounded*) mean flow profile has to be considered as an inconsistent modelling assumption.

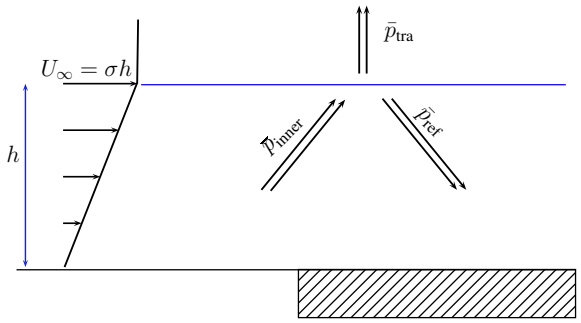

Figure 5.6: Inner pressure reflected and transmitted at interface $y = h$.

5.6 Far field of inner solution – outside shear layer

In order to approximate the solution outside the shear layer we assume a piecewise linear mean flow, with continuous transition of the shear layer at $y = h$ where it becomes straight as shown in Fig. 5.6, *i.e.*

$$\begin{aligned} U &= \sigma y, \qquad && y < h, \\ U &= U_\infty, \qquad && y \geqslant h. \end{aligned}$$

Assume that $k_0 h \gg k_0 y_0$, so that the incident vorticity does not interfere with the transition layer, and the above linear shear solution can be used as incident to the interface. This assumption is based on the physical understanding that incident field $p_{\rm in}$ is negligible near the interface, while the inner pressure field $\overline{p}$ is reflected back as $\overline{p}_{\rm ref}$ with negligible interaction with the wall, and transmitted as $\overline{p}_{\rm tra}$ into the uniform mean flow field. This scenario is justified for low shear, where $\overline{p} = O(r^{-\frac{1}{2}})$, but not for high shear with $\overline{p} = O(1)$.

We will find this transmitted field to differ only just a little from the approximation (5.44) based on a negigible vorticity. This confirms the conclusion that (5.44) is a reasonable representation to match with an outward radiating acoustic field.

In order to obtain $\overline{p}_{\rm tra}$, we apply the continuity of pressure $\overline{p}$ and $\overline{v}$ velocity at the boundary $y = h$. In the Fourier domain, we have for $y < h$ representation (5.27), which is for the Fourier transforms

$$\tilde{p}(k,y) = \rho_0 D\big(\Omega_\infty - \operatorname{sign}(\operatorname{Re} k)\sigma\big)\,\mathrm{e}^{-|k|(y-h)}, \quad \tilde{v}(k,y) = -\mathrm{i}D|k|\,\mathrm{e}^{-|k|(y-h)},$$
$$D = -\mathrm{i}2U_0^2 \frac{\mathrm{e}^{-k_0 y_0}}{k-k_0}\frac{K_-(k_0)}{|k|K_+(k)}\,\mathrm{e}^{-|k|h}, \quad \Omega_\infty = \omega - kU_\infty.$$

The reflected and transmitted variables are given as

$$\tilde{p}_{\rm ref}(k,y) = \rho_0 R(\Omega_\infty + \operatorname{sign}(\operatorname{Re} k)\sigma)\,\mathrm{e}^{|k|(y-h)}, \qquad \tilde{p}_{\rm tra}(k,y) = \rho_0 T\Omega_\infty\,\mathrm{e}^{-|k|(y-h)},$$
$$\tilde{v}_{\rm ref}(k,y) = \mathrm{i}R|k|\,\mathrm{e}^{|k|(y-h)}, \qquad \tilde{v}_{\rm tra}(k,y) = -\mathrm{i}T|k|\,\mathrm{e}^{-|k|(y-h)},$$

where reflection and transmission coefficients R and T are obtained from the conditions of continuity of pressure and velocity at $y = h$

$$\tilde{p}(k,h) + \tilde{p}_{\mathrm{ref}}(k,h) = \tilde{p}_{\mathrm{tra}}(k,h),$$
$$\tilde{v}(k,h) + \tilde{v}_{\mathrm{ref}}(k,h) = \tilde{v}_{\mathrm{tra}}(k,h).$$

The two linear equations in variables T and R

$$\begin{aligned} \rho_0 D\big(\Omega_\infty - \mathrm{sign}(\mathrm{Re}\, k)\sigma\big) + \rho_0 R(\Omega_\infty + \mathrm{sign}(\mathrm{Re}\, k)\sigma) &= \rho_0 T\Omega_\infty, \\ -\mathrm{i}D|k| \qquad\qquad + \quad \mathrm{i}R|k| &= -\mathrm{i}T|k|, \end{aligned}$$

can be solved to yield

$$T = D\frac{\Omega_\infty}{\Omega_\infty + \frac{1}{2}\,\mathrm{sign}(\mathrm{Re}\, k)\sigma}, \qquad R = D\frac{\frac{1}{2}\,\mathrm{sign}(\mathrm{Re}\, k)\sigma}{\Omega_\infty + \frac{1}{2}\,\mathrm{sign}(\mathrm{Re}\, k)\sigma}.$$

The inner variables $\overline{u}, \overline{v}$ and $\overline{p}$ transmitted outside the shear, *i.e.* for $y > h$, are then

$$\begin{aligned} \bar{u}_{\mathrm{tra}}(x,y) &= \int_{-\infty}^{\infty} -\mathrm{i}\frac{U_0^2}{\pi}\,\mathrm{e}^{-k_0 y_0}\,\frac{K_-(k_0)}{k-k_0}\cdot\frac{\Omega_\infty}{\Omega_\infty + \frac{1}{2}\,\mathrm{sign}(\mathrm{Re}\, k)\sigma}\cdot\frac{k\,\mathrm{e}^{-\mathrm{i}kx-|k|y}}{|k|K_+(k)}\,\mathrm{d}k \\ \bar{v}_{\mathrm{tra}}(x,y) &= \int_{-\infty}^{\infty} -\frac{U_0^2}{\pi}\,\mathrm{e}^{-k_0 y_0}\,\frac{K_-(k_0)}{k-k_0}\cdot\frac{\Omega_\infty}{\Omega_\infty + \frac{1}{2}\,\mathrm{sign}(\mathrm{Re}\, k)\sigma}\cdot\frac{\mathrm{e}^{-\mathrm{i}kx-|k|y}}{K_+(k)}\,\mathrm{d}k \\ \bar{p}_{\mathrm{tra}}(x,y) &= \int_{-\infty}^{\infty} -\mathrm{i}\frac{\rho_0 U_0^2}{\pi}\,\mathrm{e}^{-k_0 y_0}\,\frac{K_-(k_0)}{k-k_0}\cdot\frac{\Omega_\infty^2}{\Omega_\infty + \frac{1}{2}\,\mathrm{sign}(\mathrm{Re}\, k)\sigma}\cdot\frac{\mathrm{e}^{-\mathrm{i}kx-|k|y}}{|k|K_+(k)}\,\mathrm{d}k. \end{aligned} \tag{5.45}$$

In order to evaluate the above integrals, we define

$$q_1 = \frac{\omega - \frac{1}{2}\sigma}{U_\infty} \quad \text{and} \quad q_2 = \frac{\omega + \frac{1}{2}\sigma}{U_\infty}.$$

and break the integrals about $k = 0$ to obtain for $\bar{p}_{\mathrm{tra}}$ for example,

$$\begin{aligned} \bar{p}_{\mathrm{tra}}(x,y) = -\mathrm{i}\rho_0\frac{U_0^2}{\pi}\,\mathrm{e}^{-k_0 y_0}\,\frac{K_-(k_0)}{U_\infty} \\ \times\left[\frac{1}{q_1-k_0}\int_{-\infty}^{0}\frac{\Omega_\infty^2}{k-k_0}\cdot\frac{\mathrm{e}^{-\mathrm{i}kx-|k|y}}{|k|K_+(k)}\,\mathrm{d}k + \frac{1}{q_2-k_0}\int_0^{\infty}\frac{\Omega_\infty^2}{k-k_0}\cdot\frac{\mathrm{e}^{-\mathrm{i}kx-|k|y}}{|k|K_+(k)}\,\mathrm{d}k\right. \\ \left. -\frac{1}{q_1-k_0}\int_{-\infty}^{0}\frac{\Omega_\infty^2}{k-q_1}\cdot\frac{\mathrm{e}^{-\mathrm{i}kx-|k|y}}{|k|K_+(k)}\,\mathrm{d}k - \frac{1}{q_2-k_0}\int_0^{\infty}\frac{\Omega_\infty^2}{k-q_2}\cdot\frac{\mathrm{e}^{-\mathrm{i}kx-|k|y}}{|k|K_+(k)}\,\mathrm{d}k\right]. \end{aligned}$$

The poles in q_1 and q_2 relate to the production of vorticity at the interface (where U'' has the form of a delta-function in y and provides a source of vorticity). So they are, like k_0 to be considered as part of the lower half plane.

5.6.1 Low shear

The above integral can be evaluated in the same way as (5.27) with the limit h fixed and $z \to \infty$ to obtain the low shear case solution as

$$\begin{aligned}
\overline{u}_{\mathrm{tra}} &\sim \mathrm{i}\frac{U_0}{\pi}\,\mathrm{e}^{-k_0 y_0}\,\mathrm{e}^{\frac{1}{4}\pi\mathrm{i}}\,\Gamma(\tfrac{3}{2}+\mathrm{i}\delta)\Big(\frac{\omega+\sigma}{\omega-\sigma}\Big)^{\frac{1}{4}} \\
&\qquad\times\left[\frac{\omega}{\omega-\frac{1}{2}\sigma}\cdot\frac{\omega}{\omega+\sigma}(k_0 z)^{-\frac{3}{2}-\mathrm{i}\delta}-\frac{\omega}{\omega+\frac{1}{2}\sigma}\cdot\frac{\omega}{\omega-\sigma}(k_0 z^*)^{-\frac{3}{2}-\mathrm{i}\delta}\right] \\
\overline{v}_{\mathrm{tra}} &\sim -\frac{U_0}{\pi}\,\mathrm{e}^{-k_0 y_0}\,\mathrm{e}^{\frac{1}{4}\pi\mathrm{i}}\,\Gamma(\tfrac{3}{2}+\mathrm{i}\delta)\Big(\frac{\omega+\sigma}{\omega-\sigma}\Big)^{\frac{1}{4}} \\
&\qquad\times\left[\frac{\omega}{\omega-\frac{1}{2}\sigma}\cdot\frac{\omega}{\omega+\sigma}(k_0 z)^{-\frac{3}{2}-\mathrm{i}\delta}+\frac{\omega}{\omega+\frac{1}{2}\sigma}\cdot\frac{\omega}{\omega-\sigma}(k_0 z^*)^{-\frac{3}{2}-\mathrm{i}\delta}\right] \\
\overline{p}_{\mathrm{tra}} &\sim -\frac{\rho_0 U_0^2}{\pi}\,\mathrm{e}^{-k_0 y_0}\,\mathrm{e}^{\frac{1}{4}\pi\mathrm{i}}\,\Gamma(\tfrac{1}{2}+\mathrm{i}\delta)\Big(\frac{\omega+\sigma}{\omega-\sigma}\Big)^{\frac{1}{4}} \\
&\qquad\times\left[\frac{\omega}{\omega-\frac{1}{2}\sigma}\cdot\frac{\omega}{\omega+\sigma}(k_0 z)^{-\frac{1}{2}-\mathrm{i}\delta}-\frac{\omega}{\omega+\frac{1}{2}\sigma}\cdot\frac{\omega}{\omega-\sigma}(k_0 z^*)^{-\frac{1}{2}-\mathrm{i}\delta}\right].
\end{aligned} \tag{5.46}$$

The exponentially small contributions of the poles in k_0, q_1 and q_2 disappear for $y \to \infty$. Since $\omega > \sigma$, we have $\omega - \frac{1}{2}\sigma > 0$. The solution in (5.46) is remarkably similar to (5.41). In particular the functional relationship in x and y is entirely the same. Only the coefficients of $(k_0 z)^{-\frac{1}{2}-\mathrm{i}\delta}$ and $(k_0 z^*)^{-\frac{1}{2}-\mathrm{i}\delta}$ differ a little, but not in orders of magnitude. It confirms our previous arguments leading to expression (5.41).

5.6.2 High shear

A similar result can be constructed for the high shear case, namely

$$\begin{aligned}
\overline{p}_{\mathrm{tra}} \sim -\mathrm{i}\frac{\rho_0 U_0^2}{\pi}\,\mathrm{e}^{-k_0 y_0}\,\Gamma(\mathrm{i}\delta)\Big(\frac{\sigma+\omega}{\sigma-\omega}\Big)^{\frac{1}{4}}\left[\frac{\omega}{\omega-\frac{1}{2}\sigma}\cdot\frac{\omega}{\sigma+\omega}(k_0 z)^{-\mathrm{i}\delta}\right. \\
\left.-\frac{\omega}{\omega+\frac{1}{2}\sigma}\cdot\frac{\omega}{\sigma-\omega}(k_0 z^*)^{-\mathrm{i}\delta}\right].
\end{aligned} \tag{5.47}$$

This result, however, is inconsistent because the reflected field will not decay and therefore will not be negligible at the wall. The only systematic approach would be to include the interface and its reflected field right from the start. This complicates the Wiener-Hopf problem considerably and has not been done here. We will show later that, apart from this inconsistency, also the impossibility to match with an acoustic field adds to the conclusion that the high shear solution, and therefore the model, is not physically acceptable.

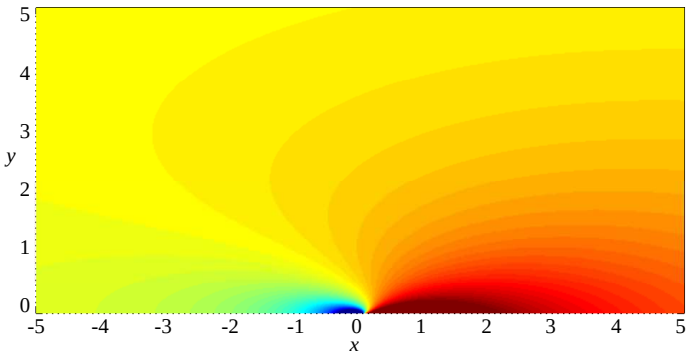

Figure 5.7: The acoustic pressure for low shear case when matched with $\overline{p}$ of (5.41). ($\sigma = 4 < \omega = 5, y_0 = 1.25, k_0 = 1$ and $U_0 = 5$).

5.7 Acoustic outer field and asymptotic matching

By assuming the mean flow Mach number small (the initially linear shear profile has evidently to be curtailed by a smooth transition to a uniform profile), as well as the local Helmholtz number (the ratio between the hydrodynamic wave number $k_0 = \omega/U_0$ and the acoustic wave number $\kappa = \omega/c_0$) U_0/c_0 being small, the hydrodynamic inner problem is incompressible. This inner field, however, produces an acoustic outer field, which is compressible but with negligible mean flow. Then we have the Helmholtz (= reduced wave) equation for $\overline{p}$ (or $\overline{u}$ or $\overline{v}$)

$$\nabla^2\overline{p} + \kappa^2\overline{p} = 0, \qquad \kappa = \frac{\omega}{c_0}. \tag{5.48}$$

With a point source in $x = y = 0$, assuming a certain symmetry in r and θ (where $x = r\cos\theta$ and $y = r\sin\theta$), we search for solutions of the form

$$\overline{p}(r,\theta) = B_0\gamma(r)\beta(\theta). \tag{5.49}$$

If we substitute this in the equations we find

$$\gamma'' + \frac{1}{r}\gamma' + \kappa^2\gamma - \frac{\nu^2}{r^2}\gamma = 0, \quad \beta'' + \nu^2\beta = 0, \tag{5.50}$$

such that $\beta(\theta) = B_1\,\mathrm{e}^{-\mathrm{i}\nu\theta} - B_2\,\mathrm{e}^{\mathrm{i}\nu\theta}$. Furthermore, due to the radiation condition,

$$\gamma(r) = mH_\nu^{(2)}(\kappa r) + nH_{-\nu}^{(2)}(\kappa r) = mH_\nu^{(2)}(\kappa r) + n\,\mathrm{e}^{-\nu\pi\mathrm{i}}\,H_\nu^{(2)}(\kappa r) = H_\nu^{(2)}(\kappa r), \tag{5.51}$$

with the relationship $H_{-\nu}^{(2)}(\kappa r) = \mathrm{e}^{-\mathrm{i}\nu\pi}\,H_\nu^{(2)}(\kappa r)$ [63]. Clearly, n can be taken zero and m equal to unity. The constants B_0, B_1, B_2 and ν are to be determined from the matching condition at $\kappa r \to 0$ where the Hankel function has the following asymptotic

behaviour [63]

$$H_\nu^{(2)}(\kappa r) \;\simeq\; \mathrm{i}\pi^{-1}\Gamma(\nu)(\tfrac{1}{2}\kappa r)^{-\nu} + \mathrm{i}^{1+2\nu}\pi^{-1}\Gamma(-\nu)(\tfrac{1}{2}\kappa r)^{\nu} = \alpha r^{-\nu} + \tilde{\alpha} r^{\nu}. \qquad (5.52)$$

The second term $\sim r^\nu$ can be ignored if $\mathrm{Re}(\nu) > 0$, but is essential if ν is imaginary. We aim to match our outer solution (5.49) with the inner solutions (5.41) or (5.46), and (5.44). This, however, is only possible for the low shear case.

5.7.1 Low shear case matching

From (5.52), (5.41) and (5.46), we have $\nu = \frac{1}{2} + \mathrm{i}\delta$, and

$$\begin{aligned}
B_0 &= \rho_0 U_0^2\, \mathrm{e}^{-k_0 y_0}\, \mathrm{e}^{\frac{3}{4}\pi\mathrm{i}} \Big(\frac{\omega+\sigma}{\omega-\sigma}\Big)^{\frac{1}{4}} \Big(\frac{U_0}{2c_0}\Big)^{\nu} \\
B_1 &= \frac{\omega}{\omega+\sigma} \qquad \text{and} \quad B_2 = \frac{\omega}{\omega-\sigma} \qquad\qquad \text{matched with } \overline{p}\ (5.41) \\
B_1 &= \frac{\omega}{\omega-\frac{1}{2}\sigma}\cdot\frac{\omega}{\omega+\sigma} \quad \text{and} \quad B_2 = \frac{\omega}{\omega+\frac{1}{2}\sigma}\cdot\frac{\omega}{\omega-\sigma} \quad \text{matched with } \overline{p}_{\mathrm{tra}}(5.46)
\end{aligned} \qquad (5.53)$$

and hence for pressure $\overline{p}$ and radial velocity $\overline{w}$

$$\begin{aligned}
\overline{p} &= B_0 H_\nu^{(2)}(\kappa r)\big(B_1\, \mathrm{e}^{-\mathrm{i}\nu\theta} - B_2\, \mathrm{e}^{\mathrm{i}\nu\theta}\big) \\
\overline{w} &= \frac{\mathrm{i}}{\rho_0 c_0} B_0 H_\nu^{(2)\prime}(\kappa r)\big(B_1\, \mathrm{e}^{-\mathrm{i}\nu\theta} - B_2\, \mathrm{e}^{\mathrm{i}\nu\theta}\big)
\end{aligned} \qquad (5.54)$$

Since the two different expressions of the constants B_1 and B_2 in (5.53) differ only slightly, we continue with the configuration that matches with (5.41). For example in Fig. 5.7 we have the acoustic pressure field for a model case.

From the far field behaviour

$$H_\nu^{(2)}(\kappa r) \sim \Big(\frac{2}{\pi\kappa r}\Big)^{\frac{1}{2}} \mathrm{e}^{-\mathrm{i}\kappa r + \frac{1}{2}\mathrm{i}\nu\pi + \frac{1}{4}\mathrm{i}\pi}, \quad H_\nu^{(2)\prime}(\kappa r) \sim -\mathrm{i}\Big(\frac{2}{\pi\kappa r}\Big)^{\frac{1}{2}} \mathrm{e}^{-\mathrm{i}\kappa r + \frac{1}{2}\mathrm{i}\nu\pi + \frac{1}{4}\mathrm{i}\pi} \qquad (5.55)$$

we obtain the time averaged radial acoustic intensity in the far field as

$$\tfrac{1}{2}\,\mathrm{Re}(\overline{p}\;\overline{w}^*) \simeq \frac{\rho_0\kappa}{2\pi r} U_0^5\, \mathrm{e}^{-2k_0 y_0} \left(\frac{\mathrm{e}^{2\delta\theta}}{(\omega+\sigma)^2} + \frac{\mathrm{e}^{-2\delta\theta}}{(\omega-\sigma)^2} - \frac{2\cos\theta}{\omega^2-\sigma^2} \right) \qquad (5.56)$$

Integrated over $0 < \theta < \pi$ we obtain an explicit expression of the radiated acoustic power

$$\int_0^\pi \tfrac{1}{2}\,\mathrm{Re}(\overline{p}\;\overline{w}^*) r\,\mathrm{d}\theta = \rho_0 c_0^3\, y_0 \Big(\frac{U_0}{c_0}\Big)^4 \frac{\mathrm{e}^{-2\omega/\sigma}}{\pi\delta} \Big(\frac{\omega}{\sigma} - \frac{\sigma}{\omega}\Big)^{-2}, \qquad (5.57)$$

to be multiplied by the square of the small dimensionless amplitude of the incident vorticity (5.10).

5.7.2 High shear case matching

The successful matching of the low shear case cannot be continued for the high shear case. As announced in (5.52), the acoustic field behaves like $\alpha r^{-\nu} + \tilde{\alpha} r^{\nu}$ when $\nu = \mathrm{i}\delta$ is now imaginary. The second term is essentially missing in our inner solution (5.44), where the pressure $\overline{p}$ behaves like $r^{-\mathrm{i}\delta}$ only.

5.8 Conclusion

A systematic and analytically exact solution is obtained by means of the Wiener-Hopf technique of the problem of vorticity, convected by a linearly sheared mean flow and scattered by a hard wall - pressure-release wall transition. A qualitatively different behaviour of the hydrodynamic and far field sound is found for low and high shear cases. A particular feature of the simplification $Z = 0$ is the fact that the Wiener-Hopf kernel can be split exactly and the solution integrals can be evaluated analytically exactly, which allows deeper insight into the problem. In particular, it enables us to find in detail the functional relationship of the hydrodynamic far field and hence the associated acoustic source strength.

If the mean shear is relatively weak ($\sigma < \omega$), the hydrodynamic far field varies as the inverse square root of the distance from the hard-soft edge. The radiated acoustic power is found to vary with U_0^4 where U_0 is the mean flow velocity at the source position. If the mean shear is relatively strong ($\sigma > \omega$), two features are striking. (i) The hydrodynamic far field tends (in modulus) to a constant, what implies a strong back reaction to the wall from any uniform or otherwise bounded part of the mean flow, and (ii) the hydrodynamic field can not be matched to an acoustic outer field.

This impossible matching and the (here not included) strong back reaction to the wall, leads to the conclusion that the unbounded linear mean shear flow is an inconsistent modeling assumption in the case of high shear.

In the next chapter, we will continue the analysis for a general impedance Z wall.

Chapter 6

Vorticity scattering at hard-wall - soft wall transition in shear flows

6.1 Introduction

In the previous chapter, we studied the vorticity scattering in shear flows at the hard wall - pressure release wall transition. In the current chapter, the analysis will be continued to the transition between a hard and a general impedance Z wall. In this case, the Wiener-Hopf solution in terms of Fourier integrals is too complex to be evaluated analytically and we have to rely upon the asymptotic behavior of the Fourier integrals in order to estimate the far field behavior of the solution. Such limits, although quite common in scattering problems are too complex to trust completely because of various regularizations involved in the Wiener-Hopf process. Such problems could be apprehended with the help of the pressure release wall solution of previous Chapter 5 where the solution is analytically integrable and could be used for further insight.

The initial field of the current problem is based upon the hard wall boundary condition and can be borrowed directly from the previous chapter (5.10). Similar to the previous chapter, we start with the formulation of the two auxiliary functions, that are analytic in the upper and lower half of the complex plane respectively with a finite strip S of overlap. Then we obtain the Wiener-Hopf equation and once we split the Wiener-Hopf kernel with the Cauchy integral theorem, we obtain eventually the inner solution. Later, this inner solution will be matched with the outer acoustic solution to know the far field sound behavior.

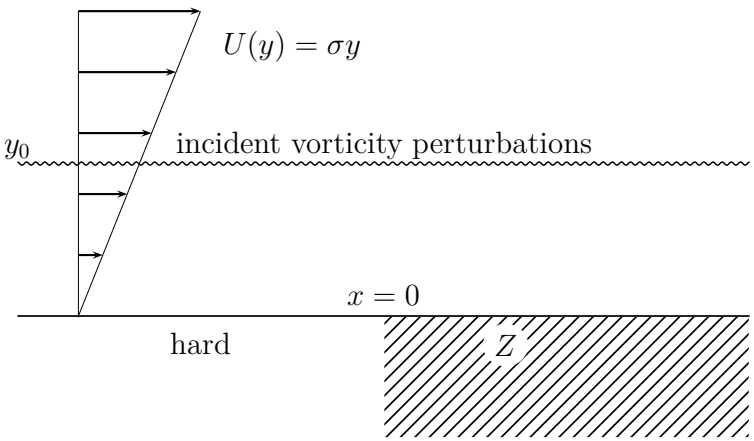

Figure 6.1: Sketch of the problem

6.2 Model

Consider the two-dimensional incompressible inviscid problem of perturbations of a linearly sheared mean flow with time dependent ($\mathrm{e}^{\mathrm{i}\omega t}$) vortex sheet along $y = y_0$ in $y > 0$ and a wall at $y = 0$ which is hard for $x < 0$ and soft (impedance) for $x > 0$ with $U(y) = \sigma y$; see Fig. 6.1. In this configuration we will have no contribution of a critical layer h_c or an instability like in [33].

As described above, we have a mass source placed at $x = x_0 \to -\infty$, $y = y_0$ which produce the downstream travelling vorticity that decays exponentially away from the line $y = y_0$ in the order $\sim \mathrm{e}^{-k_0|y-y_0|-\mathrm{i}k_0 x}$. When the convected vorticity field hits the hard-to-soft wall transition point $x = 0$, it is scattered into a local pressure field that will radiate as sound into the far field.

The flow in the domain shown in Fig. 6.1 is governed by the linearised Euler equations with mixed boundary conditions (hard for $x < 0$ and of impedance type for $x > 0$), which makes the Wiener-Hopf technique [14, 28] a natural choice for obtaining the solution. Once we obtained this (in the context of the acoustic field) inner solution, we can determine the source strength at the singularity $x = 0$. In order to assess the produced sound, the incompressible inner solution will be matched with a compressible (acoustic) outer solution. The artistic impression of this process is shown in Fig. 1.5.

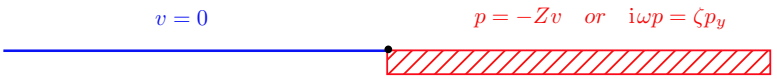

Figure 6.2: Boundary conditions at $x = 0$.

6.3 Mathematical formulation

The governing equations of mass and momentum conservation written in the frequency domain are (2.26),

$$\begin{aligned} \rho_0 \left(\frac{\partial u}{\partial x} + \frac{\partial v}{\partial y} \right) &= 0, \\ \rho_0 \left(\mathrm{i}\omega + U \frac{\partial}{\partial x} \right) u + \rho_0 \frac{\mathrm{d}U}{\mathrm{d}y} v + \frac{\partial p}{\partial x} &= 0, \\ \rho_0 \left(\mathrm{i}\omega + U \frac{\partial}{\partial x} \right) v + \frac{\partial p}{\partial y} &= 0. \end{aligned} \tag{6.1}$$

Boundary conditions at $y = 0$, Fig. 6.2, are

$$v = 0 \quad \text{if} \quad x < 0,$$

an edge condition of vanishing energy flux from $(0, 0)$, and a wall of impedance $Z = \rho_0 \zeta$ with

$$p = -Zv \quad \text{or} \quad \mathrm{i}\omega p = \zeta p_y \quad \text{if} \quad x > 0.$$

The far field boundary conditions will be of vanishing velocity, but maybe not of vanishing pressure. The incident field (of the undulating vortex sheet at $y = y_0 = U_0/\sigma$) is given by

$$\begin{aligned} u_{\mathrm{in}} = \quad & U_0 \, \mathrm{e}^{-\mathrm{i}k_0 x} \Big[\quad - \operatorname{sign}(y - y_0) \; \mathrm{e}^{-k_0 |y - y_0|} \; + \qquad\qquad \mathrm{e}^{-k_0 (y + y_0)} \Big], \\ v_{\mathrm{in}} = \quad & \mathrm{i} U_0 \, \mathrm{e}^{-\mathrm{i}k_0 x} \Big[\qquad\qquad \mathrm{e}^{-k_0 |y - y_0|} \; - \qquad\qquad \mathrm{e}^{-k_0 (y + y_0)} \Big], \\ p_{\mathrm{in}} = \quad & \frac{\sigma}{\omega} \rho_0 U_0^2 \, \mathrm{e}^{-\mathrm{i}k_0 x} \Big[\; (1 + k_0 |y - y_0|) \, \mathrm{e}^{-k_0 |y - y_0|} \; - \; (1 + k_0 (y - y_0)) \, \mathrm{e}^{-k_0 (y + y_0)} \Big], \end{aligned} \tag{6.2}$$

with $k_0 = \omega / U_0$, and so $k_0 y_0 = \omega / \sigma$. Fig. 5.2 shows pressure and velocities of a typical case. The triple $(u_{\mathrm{in}}, v_{\mathrm{in}}, p_{\mathrm{in}})$ in (6.2) satisfies the differential equation (6.1) , continuity of p_{in} and v_{in} across $y = y_0$ and the hard-wall boundary condition $v_{\mathrm{in}} = 0$ at $y = 0$. The scattered perturbations are due to the non vanishing $p_{\mathrm{in}} + Z v_{\mathrm{in}}$ along $y = 0, x > 0$ and are found through the Wiener-Hopf analysis.

We split up the field in the incident part and the scattered part as follows

$$u = u_{\mathrm{in}} + \overline{u}, \quad v = v_{\mathrm{in}} + \overline{v}, \quad p = p_{\mathrm{in}} + \overline{p}. \tag{6.3}$$

After Fourier transformation in x (formally assuming the convergence of the integrals)

$$\overline{p}(x,y) = \frac{1}{2\pi}\int_{-\infty}^{\infty} \tilde{p}(y,k)\,\mathrm{e}^{-\mathrm{i}kx}\,\mathrm{d}k, \tag{6.4}$$

(the same for $\overline{u}$ and $\overline{v}$) we obtain the following set of equations

$$\rho_0(-\mathrm{i}k\tilde{u} + \tilde{v}') = 0, \qquad \mathrm{i}\rho_0\Omega\tilde{u} + \rho_0\sigma\tilde{v} - \mathrm{i}k\tilde{p} = 0, \qquad \mathrm{i}\rho_0\Omega\tilde{v} + \tilde{p}' = 0, \tag{6.5}$$

where $\Omega = \omega - kU$. The system of equations has two independent solutions, namely $\sim \mathrm{e}^{\pm ky}$ [45, 65]. The one, bounded for $y \to \infty$, is then

$$\begin{aligned} \tilde{u}(y) &= kA(k)\,\mathrm{e}^{-|k|y}, \\ \tilde{v}(y) &= -\mathrm{i}|k|A(k)\,\mathrm{e}^{-|k|y}, \\ \tilde{p}(y) &= \rho_0(\Omega - \operatorname{sign}(\operatorname{Re}k)\sigma)A(k)\,\mathrm{e}^{-|k|y}, \end{aligned} \tag{6.6}$$

with amplitude $A(k)$ to be determined, and

$$|k| = \operatorname{sign}(\operatorname{Re}k)k = \sqrt{k^2}, \tag{6.7}$$

where $\sqrt{\ }$ denotes the principal value square root, and $|k|$ has thus branch cuts along the imaginary axis given by $(-\mathrm{i}\infty, 0)$ and $(0, \mathrm{i}\infty)$. The definition of $\operatorname{sign}(\operatorname{Re}(k))$ in (6.7) will be maintained throughout the work.

6.4 Wiener-Hopf procedure

To facilitate the following Wiener-Hopf procedure, we introduce a small positive parameter ε and have an upper and a lower half plane, and a strip of overlap

$$\mathbb{C}^+ = \{k \in \mathbb{C} \mid \operatorname{Im}k > -\varepsilon\}, \quad \mathbb{C}^- = \{k \in \mathbb{C} \mid \operatorname{Im}k < \varepsilon\}, \quad S = \{k \in \mathbb{C} \mid -\varepsilon < \operatorname{Im}k < \varepsilon\}.$$

The physical problem will be the limit $\varepsilon \to 0$ of a regularised problem with k_0 replaced by $k_0 - \mathrm{i}\varepsilon$ (an incident field $\sim \mathrm{e}^{-\mathrm{i}k_0x}$ slightly decaying with x) and $|k|$ replaced by the smoother function

$$|k| = \sqrt{k^2 + \varepsilon^2}$$

with branch cuts $(-\mathrm{i}\infty, -\mathrm{i}\varepsilon) \cup (\mathrm{i}\varepsilon, \mathrm{i}\infty)$ avoiding strip S (*cf.* [79]).

Introduce the auxiliary functions

$$F_-(k) = \int_{-\infty}^{0} \left[\overline{p}(x,0) + Z\overline{v}(x,0)\right]\mathrm{e}^{\mathrm{i}kx}\,\mathrm{d}x, \quad G_+(k) = \int_{0}^{\infty} \overline{v}(x,0)\,\mathrm{e}^{\mathrm{i}kx}\,\mathrm{d}x \tag{6.8}$$

which are analytic in $\operatorname{Im}(k) < 0$ and $\operatorname{Im}(k) > 0$ respectively, and assumed to be analytic in $\mathbb{C}^+$ and $\mathbb{C}^-$, as explained in appendix C.1 and shown in Fig. 6.3.

case	$\sigma-\omega$	$\operatorname{Im}\zeta$	$k_1=-a+b$	$k_2=-a-b$
1	+	+	$k=k_1\in I$	no solution
2	+	−	no solution	$k=k_2\in II$
3	−	+	no solution	no solution
4	−	−	$k=k_1\in IV$	$k=k_2\in II$

Table 6.1: Roots of non regularised WH kernel $K(k)$ in (6.11)

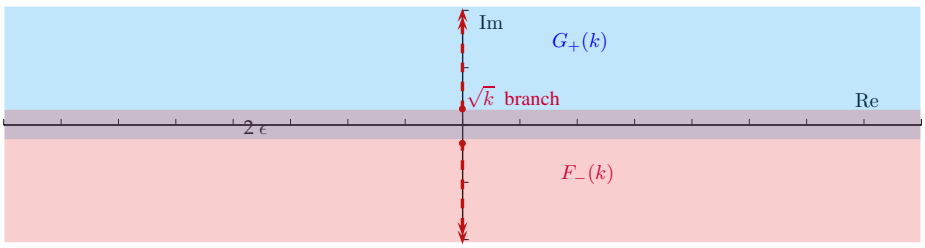

Figure 6.3: F_- and G_+ functions and their regions of analyticity

Then we have for G_+

$$G_+(k)=\int_0^\infty \overline{v}(x,0)\,\mathrm{e}^{\mathrm{i}kx}\,\mathrm{d}x=\int_{-\infty}^\infty \overline{v}(x,0)\,\mathrm{e}^{\mathrm{i}kx}\,\mathrm{d}x=-\mathrm{i}|k|A(k). \tag{6.9}$$

Furthermore, we have for F_-

$$\begin{aligned}
F_-(k)&=\int_{-\infty}^0 \left[\overline{p}(x,0)+Z\overline{v}(x,0)\right]\mathrm{e}^{\mathrm{i}kx}\,\mathrm{d}x\\
&=\int_{-\infty}^\infty \left[\overline{p}(x,0)+Z\overline{v}(x,0)\right]\mathrm{e}^{\mathrm{i}kx}\,\mathrm{d}x+\int_0^\infty p_{\mathrm{in}}(x,0)\,\mathrm{e}^{\mathrm{i}kx}\,\mathrm{d}x\\
&=-\rho_0 A(k)\operatorname{sign}(\operatorname{Re}k)\big(\mathrm{i}k\zeta+\sigma-\operatorname{sign}(\operatorname{Re}k)\omega\big)+2\mathrm{i}\rho_0U_0^2\frac{\mathrm{e}^{-k_0y_0}}{k-k_0}\\
&=-\mathrm{i}\rho_0\zeta A(k)|k|K(k)+2\mathrm{i}\rho_0U_0^2\frac{\mathrm{e}^{-k_0y_0}}{k-k_0}
\end{aligned} \tag{6.10}$$

with Wiener-Hopf kernel

$$K(k)=1+\frac{a}{k}-\frac{b}{|k|},\qquad a=\frac{\sigma}{\mathrm{i}\zeta},\quad b=\frac{\omega}{\mathrm{i}\zeta}. \tag{6.11}$$

With $\varepsilon=0$, $K(k)$ has 0, 1, or 2 zeros in the 1st, 2nd, or 4th quadrant, as shown in table 6.1, depending on the signs of $\sigma-\omega$ and $\operatorname{Im}\zeta$, and assuming that $\sigma,\omega,\operatorname{Re}\zeta>0$.

case	$\sigma-\omega$	$\operatorname{Im}\zeta$	$k_1 \simeq -a+b+\mathrm{i}\varepsilon\frac{a}{a-b}$	$k_2 \simeq -a-b+\mathrm{i}\varepsilon\frac{a}{a+b}$	$k_3 \simeq -\mathrm{i}\varepsilon\frac{a^2+b^2}{a^2-b^2}+\varepsilon^2\frac{8a^3b^2}{(a^2-b^2)^3}$
1	+	+	$k \simeq -a+b \in I$	no solution	no solution
2	+	−	no solution	$k \simeq -a-b \in II$	no solution
3	−	+	no solution	no solution	$k \simeq -\mathrm{i}\varepsilon\frac{a^2+b^2}{a^2-b^2}$
4	−	−	$k \simeq -a+b \in IV$	$k \simeq -a-b \in II$	$k \simeq -\mathrm{i}\varepsilon\frac{a^2+b^2}{a^2-b^2}$

Table 6.2: Roots of the regularised WH kernel $K(k)$ in (6.12)

The Kernel $K(k)$ should be free from all poles and zeros and since our $K(k)$ has a singularity in $k=0$, which is inside strip S, we follow D.1 and consider the regularised version

$$K(K) = 1 + \frac{a}{k-\mathrm{i}\varepsilon} - \frac{b}{\sqrt{k^2+\varepsilon^2}}. \tag{6.12}$$

The regularized $K(k)$ has 3 zeros, which for small ε are approximated as shown in table 6.2. So in general the zeros and singularities of K are not real and there is a neighbourhood of the real axis where $K(k)$ is analytic.

Hence from (6.4), we arrive at the Wiener-Hopf equation

$$F_-(k) = \rho_0\zeta G_+(k)K(k) + 2\mathrm{i}\rho_0 U_0^2 \frac{\mathrm{e}^{-k_0 y_0}}{k-k_0} \tag{6.13}$$

which is to be solved in the standard way [14] by writing

$$K(k) = \frac{K_+(k)}{K_-(k)} \tag{6.14}$$

where splitfunction K_+ is analytic in $\mathbb{C}^+$ and K_- is analytic in $\mathbb{C}^-$. These splitfunctions are constructed in the usual way [57] as follows.

Consider $k \in S$ inside a large rectangular contour $\mathcal{C} \subset S$ between $k = -L - \mathrm{i}\eta\varepsilon$ and $k = L + \mathrm{i}\eta\varepsilon$, where η is small enough that we remain within the strip of width 2ε as shown in Fig. 6.4. In general K has no zeros $k_{1,2,3}$ (if any) within $\mathcal{C}$ and we assume a definition of $\log K(k)$ with branch cuts not crossing S. As it happens, with the present choice of the regularised K, this is achieved by taking the principal value logarithm. Then by Cauchy's integral representation theorem,

$$\begin{aligned}\log K(k) &= \lim_{L\to\infty} \frac{1}{2\pi\mathrm{i}} \int_{\mathcal{C}} \frac{\log K(\xi)}{\xi-k}\,\mathrm{d}\xi \\ &= \frac{1}{2\pi\mathrm{i}} \int_{-\infty}^{\infty} \frac{\log K(\xi-\mathrm{i}\eta\varepsilon)}{\xi-\mathrm{i}\eta\varepsilon-k}\,\mathrm{d}\xi - \frac{1}{2\pi\mathrm{i}} \int_{-\infty}^{\infty} \frac{\log K(\xi+\mathrm{i}\eta\varepsilon)}{\xi+\mathrm{i}\eta\varepsilon-k}\,\mathrm{d}\xi,\end{aligned} \tag{6.15}$$

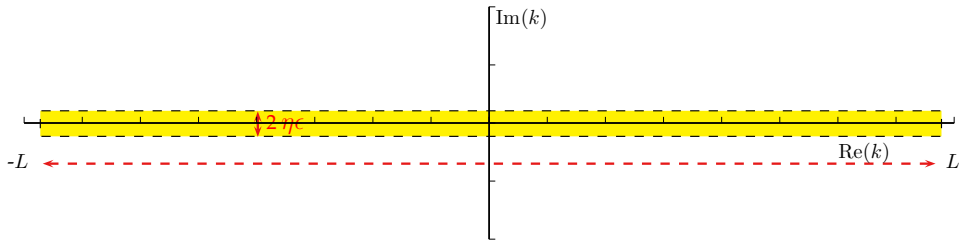

Figure 6.4: Contour $\mathcal{C}$

where it may be noted that the integrals converge at infinity since

$$\frac{\log K(\xi)}{\xi - k} = O(1/\xi^2) \quad (\xi \to \infty).$$

Considered as a function of k, the first integral can be analytically continued to $\mathbb{C}^+$, and the second integral can be analytically continued to $\mathbb{C}^-$. So we can identify

$$\log K_+(k) = \frac{1}{2\pi \mathrm{i}} \int_{-\infty}^{\infty} \frac{\log K(\xi - \mathrm{i}\eta\varepsilon)}{\xi - \mathrm{i}\eta\varepsilon - k} \,\mathrm{d}\xi, \quad k \in \mathbb{C}^+, \tag{6.16}$$

$$\log K_-(k) = \frac{1}{2\pi \mathrm{i}} \int_{-\infty}^{\infty} \frac{\log K(\xi + \mathrm{i}\eta\varepsilon)}{\xi + \mathrm{i}\eta\varepsilon - k} \,\mathrm{d}\xi, \quad k \in \mathbb{C}^-. \tag{6.17}$$

If $\varepsilon \to 0$, the representations of K_+ and K_- become the same, in the sense that it becomes K_+ if $k \in \mathbb{C}^+$ and K_- if $k \in \mathbb{C}^-$.

Although the splitfunctions for $\varepsilon > 0$ are only available numerically, it appears (see Appendix D.2) that for $\varepsilon = 0$ they can be given analytically exactly, by equation (D.3), albeit by using the somewhat unusual dilogarithm function. Furthermore, by extensive comparison with the numerical versions for very small but non zero ε, we could verify that the analytical splitfunctions as defined above are indeed the proper limit for $\varepsilon \to 0$. This remarkable result will be important later for the far field analysis of the physical solution represented by a Fourier integral.

Altogether, we can conclude from (6.13) that in S

$$\begin{aligned} F_-(k)K_-(k) - \rho_0\zeta G_+(k)K_+(k) &= 2\mathrm{i}\rho_0 U_0^2 \frac{\mathrm{e}^{-k_0 y_0}}{k - k_0} K_-(k) \\ &= 2\mathrm{i}\rho_0 U_0^2 \,\mathrm{e}^{-k_0 y_0} \,\frac{K_-(k) - K_-(k_0)}{k - k_0} + 2\mathrm{i}\rho_0 U_0^2 \frac{\mathrm{e}^{-k_0 y_0}}{k - k_0} K_-(k_0), \end{aligned} \tag{6.18}$$

where we isolated pole $k_0 \in \mathbb{C}^-$ from K_-. The parts that are analytic in $\mathbb{C}^+$ and in $\mathbb{C}^-$ respectively, are via their equivalence in S each other's analytic continuations,

and define an entire function E

$$\begin{aligned} E(k) &= F_-(k)K_-(k) - 2\mathrm{i}\,\rho_0 U_0^2\,\mathrm{e}^{-k_0 y_0}\,\frac{K_-(k)-K_-(k_0)}{k-k_0} \\ &= \rho_0\zeta G_+(k)K_+(k) + 2\mathrm{i}\,\rho_0 U_0^2\frac{\mathrm{e}^{-k_0 y_0}}{k-k_0}K_-(k_0). \end{aligned} \tag{6.19}$$

E can be determined from the condition at $k\to\infty$, related to the edge condition for $(x,y)\to 0$. Following Appendix D.4, we have $E\equiv 0$, consistent with the Part 1 pressure release wall. Hence we can write from (6.4) and (6.19)

$$\begin{aligned} F_-(k) &= 2\mathrm{i}\rho_0 U_0^2\,\mathrm{e}^{-k_0 y_0}\,\frac{K_-(k)-K_-(k_0)}{(k-k_0)K_-(k)}, \\ G_+(k) &= \frac{-2\mathrm{i}U_0^2}{\zeta}\frac{\mathrm{e}^{-k_0 y_0}}{k-k_0}\frac{K_-(k_0)}{K_+(k)}, \\ A(k) &= \frac{2U_0^2}{\zeta}\frac{\mathrm{e}^{-k_0 y_0}}{k-k_0}\frac{K_-(k_0)}{|k|K_+(k)}. \end{aligned} \tag{6.20}$$

$A(k)$ obtained from (6.20) can be substituted back into (6.6). This gives, with the inverse Fourier transform from (6.4) added to the initial field (6.2), the formal solution u, v and p of the problem.

$$\begin{aligned} u &= u_{\mathrm{in}} + \frac{1}{2\pi}\fint_{-\infty}^{\infty}\mathrm{sign}(\mathrm{Re}\,k)\frac{2U_0^2}{\zeta}\frac{\mathrm{e}^{-k_0 y_0}}{k-k_0}\frac{K_-(k_0)}{K_+(k)}\,\mathrm{e}^{-|k|y}\,\mathrm{e}^{-\mathrm{i}kx}\,\mathrm{d}k \\ v &= v_{\mathrm{in}} + \frac{1}{2\pi}\fint_{-\infty}^{\infty}-\mathrm{i}\frac{2U_0^2}{\zeta}\frac{\mathrm{e}^{-k_0 y_0}}{k-k_0}\frac{K_-(k_0)}{K_+(k)}\,\mathrm{e}^{-|k|y}\,\mathrm{e}^{-\mathrm{i}kx}\,\mathrm{d}k \\ p &= p_{\mathrm{in}} + \frac{1}{2\pi}\fint_{-\infty}^{\infty}\rho_0(\Omega-\mathrm{sign}(\mathrm{Re}\,k)\sigma)\frac{2U_0^2}{\zeta}\frac{\mathrm{e}^{-k_0 y_0}}{k-k_0}\frac{K_-(k_0)}{|k|K_+(k)}\,\mathrm{e}^{-|k|y}\,\mathrm{e}^{-\mathrm{i}kx}\,\mathrm{d}k. \end{aligned} \tag{6.21}$$

We notice that the expressions of u and v are integrable at $k=0$, while the pole $k=k_0$ is included if $x>0$. Indeed it corresponds to a trailing vorticity [86] of the hard-soft discontinuity. The singularity at $k=0$ is, unlike the one at $k=k_0$, not a pole and has a different origin. Due to this singularity, if not integrable, the Fourier transformation of the pressure in (6.21) becomes too singular to be interpreted normally and diverges, away from the edge, for $r\to\infty$. When we consider the incompressible problem as an inner problem of a larger compressible problem, as in [46, 28, 94, 81], this divergent behavior disappears as it changes into an outward radiating acoustic wave. The inverse Fourier transform for pressure p is then calculated by splitting off the singular part and interpreting the singular integral in generalized sense [31, 47, 86].

6.5 Hydrodynamic solution

The solution set u, v and p in (6.21) is the solution of incompressible inner problem of a larger compressible acoustic problem and is referred as inner solution that contains

the hydrodynamic characters of the problem. The hydrodynamic characters (inner solution) interacts with the acoustic characters (outer solution) and this information is passed through the asymptotic matching of the inner and outer solutions. This matching is accomplished by comparing term-wise the outer limit ($r \to \infty$) of the inner solution to the inner limit ($r \to 0$) of the outer solution.

The K_+ function in (D.3) if substituted back in (6.21) renders the integral function too difficult to evaluate analytically like in $Z = 0$, Chapter 5. However the integrals can be evaluated in the limit $k \to 0$ which corresponds to the limit $r \to \infty$ and that is exactly what we need. This way, the problem is curbed. The fidelity of this process is checked by comparing the behaviour of the solution with the $Z = 0$ analysis, Chapter 5, where the integrals were analytically integrable and it was precisely the reason to conduct the pressure release analysis in Chapter 5.

In order to evaluate the solutions, in the form of Fourier integrals (6.21), numerically or asymptotically in the far field, we need to know the behaviour of $K_+(k)$ at $k = 0$. The following asymptotic behaviour of $K_+(k \to 0)$ can be confirmed from D.3.1 and D.3.2

$$K_+(k) \simeq c_1 k^{-\frac{1}{2}-\mathrm{i}\delta} \quad \text{for} \quad \sigma < \omega \quad \text{and} \quad K_+(k) \simeq c_1 k^{-\mathrm{i}\delta} \quad \text{for} \quad \sigma > \omega, \tag{6.22}$$

where c_1 is a complex constant given by (D.5), (D.7) and $\delta = \frac{1}{2\pi} \log |\frac{\sigma+\omega}{\sigma-\omega}|$ is real positive. Since the behavior of the K_+ function in (6.22) differs essentially for $(\sigma < \omega)$ and $(\sigma > \omega)$, we shall refer to $(\sigma < \omega)$ and $(\sigma > \omega)$ as *low shear* and *high shear* case respectively. Please note that the $K_+(k)$ function in (D.3) assumes the asymptotic form in (6.22) which is practically equal to the K_+ (5.23) of the $Z = 0$, up to a constant which does not matter because the Wiener-Hopf kernel split functions are unique up to a constant [25].

6.5.1 Solution of velocities u and v

We see by combining (6.22) and (6.21) that in either case, the velocities u and v are integrable at $k = 0$. Shown in Fig. 6.6 (top and middle) are the numerical solutions of the velocity integrals (6.21) added to the initial field (6.2) to obtain the full solution (6.3) of velocities for a typical representative case. Apparently, the high mean shear intensifies the velocity field especially downstream the edge. The solution converges at infinity and behaves like $\sim r^{-\frac{3}{2}-\mathrm{i}\delta}$ and $\sim r^{-1-\mathrm{i}\delta}$ for the low and high shear cases respectively which is consistent with the $Z = 0$ analysis, Chapter 5. The difference in the low and high shear cases arises because of the different $K_+(k)$ function that results from the boundary conditions along $y = 0$ in combination with the edge condition at origin.

6.5.2 Solution of pressure p

As we have noticed, the behaviour of the singularity at $k = 0$ is different for the low and high shear which splits our problem into 2 different cases in terms of radiated

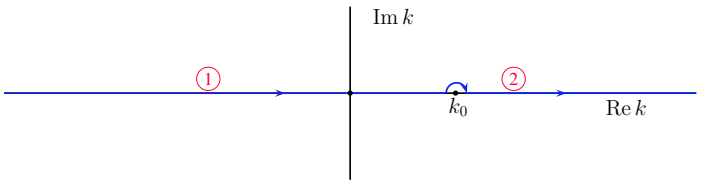

Figure 6.5: Integration contour

pressure. They are discussed in separate sections below.

Low shear

The low shear case corresponds with $\sigma < \omega$, *i.e.* $k_0 y_0 > 1$. The behaviour of $K_+ \sim k^{-\frac{1}{2}-\mathrm{i}\delta}$ in the limit $k \to 0$ weakens the non integrable singularity $|k|^{-1}$ to an integrable singularity $k^{-\frac{1}{2}+\mathrm{i}\delta}$ of the integrand in (6.21). Hence the pressure solution can be obtained by direct integration like the velocities. For a typical case, this is shown in Fig. 6.6 (bottom left). It can be predicted even at this stage that a weaker singularity at $k = 0$ produces a weaker far field sound.

High shear

The high shear case corresponds with $\sigma > \omega$, *i.e.* $k_0 y_0 < 1$. The behaviour of $K_+ \sim k^{-\mathrm{i}\delta}$ in the limit $k \to 0$ does not weaken the singularity in this case and the integral function behaves as $\sim |k|^{-1+\mathrm{i}\delta}$ as $k \to 0$ and hence diverges. The divergent behaviour at $k = 0$ in Fourier space suggests a strong far field at $r = \sqrt{x^2 + y^2} \to \infty$ in the physical plane. The Fourier representation of pressure is too singular to interpret and hence should be regularised, using generalised functions, by splitting off the singular part and the part which is integrable. From (6.21), we have

$$\begin{aligned}
\overline{p}(x,y) = {} & \frac{\rho_0 U_0^2}{\zeta\pi}\,\mathrm{e}^{-k_0 y_0}\,K_-(k_0)\int_{-\infty}^{0}\left(\frac{\Omega+\sigma}{(k-k_0)|k|K_+(k)}\right. \\
& \qquad\qquad \left. - \frac{\omega+\sigma}{-k_0|k|c_1 k^{-\mathrm{i}\delta}}\right)\mathrm{e}^{-\mathrm{i}kx-|k|y}\,\mathrm{d}k \\
& + \frac{\rho_0 U_0^2}{\zeta\pi}\,\mathrm{e}^{-k_0 y_0}\,K_-(k_0)\int_{0}^{\infty}\left(\frac{\Omega-\sigma}{(k-k_0)|k|K_+(k)}\right. \\
& \qquad\qquad \left. - \frac{\omega-\sigma}{-k_0|k|c_1 k^{-\mathrm{i}\delta}}\right)\mathrm{e}^{-\mathrm{i}kx-|k|y}\,\mathrm{d}k \\
& + \frac{\rho_0 U_0^2}{\zeta\pi}\,\mathrm{e}^{-k_0 y_0}\,\frac{K_-(k_0)}{-c_1 k_0}\left[\int_{-\infty}^{0}\frac{\omega+\sigma}{|k|k^{-\mathrm{i}\delta}}\,\mathrm{e}^{-\mathrm{i}kx-|k|y}\,\mathrm{d}k\right. \\
& \qquad\qquad \left. + \int_{0}^{\infty}\frac{\omega-\sigma}{|k|k^{-\mathrm{i}\delta}}\,\mathrm{e}^{-\mathrm{i}kx-|k|y}\,\mathrm{d}k\right]
\end{aligned} \tag{6.23}$$

The separated singularity renders the integrals of $\overline{p}(k,y)$ to be $O(1)$ at $k = 0$

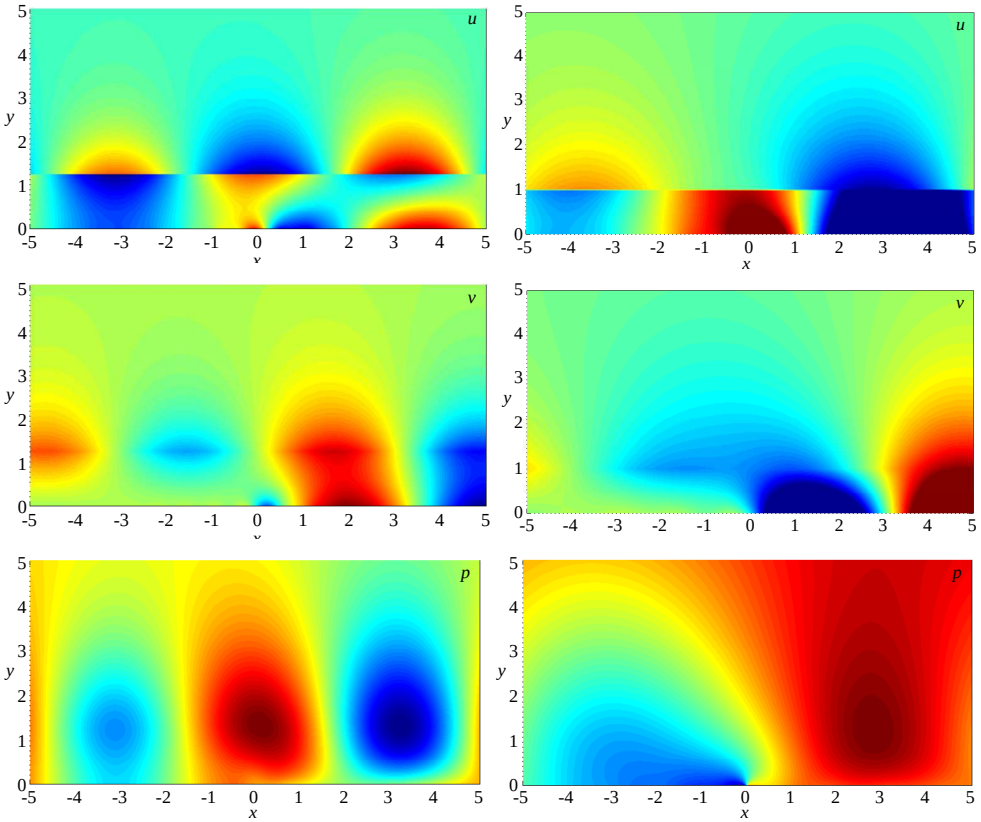

Figure 6.6: The solution fields u, v and p for low shear $\sigma = 4 < \omega = 5$, $y_0 = 1.25$ (left) and high shear $\sigma = 5 > \omega = 4$, $y_0 = 1$ (right), while $\zeta = \frac{1}{2}(1+\mathrm{i}), U_0 = 5$.

and hence integrable. In (6.23), the first 2 integrals have a finite limit at $k = 0$ and therefore can be evaluated along the integration contour 1 and 2 respectively, as shown in Fig. 6.5. The last integrals in (6.23) are those which carry the singularity and diverge at $k = 0$ which makes them difficult to interpret. They can be evaluated as generalised functions [31, 47]. With Appendix D.5, we have

$$\frac{\rho_0 U_0^2}{\zeta\pi c_1}\,\mathrm{e}^{-k_0 y_0}\,\frac{K_-(k_0)}{-k_0}\left[\int_{-\infty}^{0}\frac{\omega+\sigma}{|k|k^{-\mathrm{i}\delta}}\,\mathrm{e}^{-\mathrm{i}kx-|k|y}\,\mathrm{d}k+\int_{0}^{\infty}\frac{\omega-\sigma}{|k|k^{-\mathrm{i}\delta}}\,\mathrm{e}^{-\mathrm{i}kx-|k|y}\,\mathrm{d}k\right]$$
$$=\frac{\rho_0 U_0^2}{\zeta\pi c_1}\,\mathrm{e}^{-k_0 y_0}\,\frac{K_-(k_0)}{-k_0}\mathrm{i}^{-\mathrm{i}\delta}\Gamma(\mathrm{i}\delta)\left[(\omega+\sigma)z^{-\mathrm{i}\delta}+(\omega-\sigma)z^{*\,-\mathrm{i}\delta}\right], \quad (6.24)$$

where $z = x + \mathrm{i}y$ and $z^* = x - \mathrm{i}y$. The results from (6.24) used with the first two integrals in (6.23) added to the initial field p_{in} gives the final solution of the inner pressure p (6.21). Shown in Fig. 6.6 (bottom right) is the pressure for a typical case. The pressure field is clearly more intense for high shear than for low shear.

6.5.3 Far field of inner solution p – inside shear layer

In order to have an estimate of the far field radiated pressure, we need the asymptotic evaluation of the pressure integral (6.21) in the limit $k \to 0$ because small k in Fourier space relates to large $r = \sqrt{x^2 + y^2} \sim \infty$ in the physical plane.

(a) Low shear, $\sigma < \omega$:

From (6.21) and (6.22), we have in the limit $k \to 0$,

$$\begin{aligned}
&\overline{p}(x,y)_{\sigma<\omega} \sim \overline{p}_{\text{inner}\,(\sigma<\omega)} \\
&\simeq \frac{\rho_0 U_0^2}{\zeta\pi c_1}\,\mathrm{e}^{-k_0 y_0}\,\frac{K_-(k_0)}{-k_0}\left[(\omega+\sigma)\int_{-\infty}^{0}\frac{\mathrm{e}^{-\mathrm{i}kx-|k|y}}{|k|k^{-\frac{1}{2}-\mathrm{i}\delta}}\,\mathrm{d}k+(\omega-\sigma)\int_{0}^{\infty}\frac{\mathrm{e}^{-\mathrm{i}kx-|k|y}}{|k|k^{-\frac{1}{2}-\mathrm{i}\delta}}\,\mathrm{d}k\right] \\
&= \frac{\rho_0 U_0^2}{\zeta\pi c_1}\,\mathrm{e}^{-k_0 y_0}\,\frac{K_-(k_0)}{-k_0}\left[(-1)^{(\frac{1}{2}+\mathrm{i}\delta)}(\omega+\sigma)\int_{0}^{\infty}\frac{\mathrm{e}^{ikz}}{k^{\frac{1}{2}-\mathrm{i}\delta}}\,\mathrm{d}k+(\omega-\sigma)\int_{0}^{\infty}\frac{\mathrm{e}^{-ikz^*}}{k^{\frac{1}{2}-\mathrm{i}\delta}}\,\mathrm{d}k\right]
\end{aligned} \tag{6.25}$$

where $z = x + \mathrm{i}\,y$. The integrals converge, and can be evaluated like

$$\int_0^\infty \frac{\mathrm{e}^{ikz}}{k^{\frac{1}{2}-\mathrm{i}\delta}}\,\mathrm{d}k = \frac{\Gamma(\frac{1}{2}+\mathrm{i}\delta)}{(-\mathrm{i}\,z)^{\frac{1}{2}+\mathrm{i}\delta}}. \tag{6.26}$$

The net radiated innerfield pressure is then given by

$$\begin{aligned}
\overline{p}_{\text{inner}\,(\sigma<\omega)} \simeq \mathrm{i}^{-(\frac{1}{2}+\mathrm{i}\delta)}\Gamma(\tfrac{1}{2}+\mathrm{i}\delta)\frac{\rho_0 U_0^2}{\zeta\pi c_1}\,\mathrm{e}^{-k_0 y_0}\,\frac{K_-(k_0)}{-k_0}\times \\
\left((\omega+\sigma)z^{-\frac{1}{2}-\mathrm{i}\delta}+(\omega-\sigma){z^*}^{-\frac{1}{2}-\mathrm{i}\delta}\right)
\end{aligned} \tag{6.27}$$

with $z = r\,\mathrm{e}^{\mathrm{i}\theta}$ and $z^* = r\,\mathrm{e}^{-\mathrm{i}\theta}$. The pressure decays as $r^{-\frac{1}{2}}$, which thus limits its effective acoustic source strength. In the hard wall limit $\zeta \to \infty$, the radiated pressure disappears as expected. Also, the solution (6.27) resembles (5.41) and converges to the later in small k_0 limit.

(b) High shear, $\sigma > \omega$:

The singularity in this case is stronger than the one in the previous case, which enables us to assess that the radiated pressure $\overline{p}_{\text{inner}\,(\sigma>\omega)}$ field must be stronger. The asymptotic behaviour of the integral (6.21) at $k \to 0$ is essentially the singularity taken out from the integral in (6.23). Hence the outer limit $r \to \infty$ of the inner pressure field $\overline{p}$ (with $z = r\,\mathrm{e}^{\mathrm{i}\theta}$) is given by (6.24) as:

$$\overline{p}_{\text{inner}\,(\sigma>\omega)} \simeq \mathrm{i}^{-\mathrm{i}\delta}\Gamma(\mathrm{i}\delta)\frac{\rho_0 U_0^2}{\zeta\pi c_1}\,\mathrm{e}^{-k_0 y_0}\,\frac{K_-(k_0)}{-k_0}\left[(\omega+\sigma)z^{-\mathrm{i}\delta}+(\omega-\sigma){z^*}^{-\mathrm{i}\delta}\right]. \tag{6.28}$$

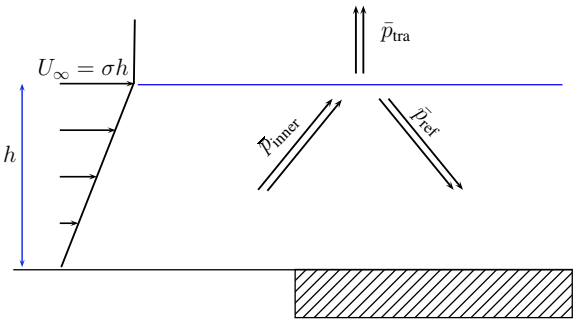

Figure 6.7: Inner pressure reflected and transmitted at interface $y = h$.

An important difference is that the modulus of the pressure field varies with r like $|r^{-\mathrm{i}\delta}| = 1$, *i.e.* remains constant rather than decaying, and is therefore much stronger than in the previous case. Physically, it means that there is a strong interaction between the edge and the interphase. In case of low shear, this interaction is weak so that the reflected waves are order of magnitude smaller than the transmitted waves. But in the case of high shear, this interaction is strong hence the acoustic energy is contained in the boundary layer. Hence we conclude that an infinite linear shear and unbounded flow profile is an inconsistent modelling assumption for the high shear case. In the hard wall limit $\zeta \to \infty$, the radiating pressure (6.28) disappears as expected. Also, the solution (6.28) resembles (5.44) and converges to the later, considering the small k_0 limit on $K_-(k_0)$.

The above far field limit is taken inside the uniform shear flow, which means that we have a diverging mean flow velocity $U = \sigma y \to \infty$ as $y \to \infty$ which is not very physical. Although both (6.27) and (6.28) *do* satisfy the prevailing equations, we just want to make sure that no unphysical artefacts are created. So we curtail the shear at height h and define the mean flow being a constant U_∞ beyond $y > h$. This is explained in the next section.

6.5.4 Far field of inner solution – outside shear layer

In order to approximate the solution outside the shear layer, we assume a piecewise smooth transition of the shear layer at $y = h$ where it becomes straight as shown in Fig. 6.7, *i.e.*

$$\begin{aligned} U &= \sigma y, \qquad y < h, \\ U &= U_\infty, \qquad y \geqslant h. \end{aligned}$$

Let us assume that $h \gg y_0$, so that the source does not interfere with the transition layer. The assumption is based on the physical understanding that the vortical field decays exponentially off the line $y = y_0$. Under this assumption, the incident field p_{in} is negligible near the interface, while the inner pressure field $\overline{p}_{\text{inner}}$ is reflected back

as $\overline{p}_{\rm ref}$ without further interaction with the wall, and transmitted as $\overline{p}_{\rm tra}$ into the far field. Hence, we may match the outer acoustic field to $\overline{p}_{\rm tra}$ in order to obtain a more realistic value of the far field sound. In order to obtain $\overline{p}_{\rm tra}$, we apply the continuity of pressure and $\overline{v}$ velocity at the boundary $y = h$. In the Fourier domain, we have for $y < h$ representation (6.21), which is for the Fourier transforms

$$\tilde{p}(k,y) = \rho_0 D\big(\Omega_\infty - \operatorname{sign}(\operatorname{Re} k)\sigma\big)\,\mathrm{e}^{-|k|(y-h)}, \quad \tilde{v}(k,y) = -\mathrm{i}D|k|\,\mathrm{e}^{-|k|(y-h)},$$
$$D = \frac{2U_0^2}{\zeta}\frac{\mathrm{e}^{-k_0 y_0}}{k-k_0}\frac{K_-(k_0)}{|k|K_+(k)}\,\mathrm{e}^{-|k|h}, \quad \Omega_\infty = \omega - kU_\infty.$$

The reflected and transmitted variables are given by

$$\tilde{p}_{\rm ref}(k,y) = \rho_0 R(\Omega_\infty + \operatorname{sign}(\operatorname{Re} k)\sigma)\,\mathrm{e}^{|k|(y-h)}, \qquad \tilde{p}_{\rm tra}(k,y) = \rho_0 T\Omega_\infty\,\mathrm{e}^{-|k|(y-h)}$$
$$\tilde{v}_{\rm ref}(k,y) = \mathrm{i}R|k|\,\mathrm{e}^{|k|(y-h)}, \qquad \tilde{v}_{\rm tra}(k,y) = -\mathrm{i}T|k|\,\mathrm{e}^{-|k|(y-h)}$$

where reflection and transmission coefficients R and T are obtained from the conditions of continuity of pressure and velocity at $y = h$

$$\tilde{p}(k,h) + \tilde{p}_{\rm ref}(k,h) = \tilde{p}_{\rm tra}(k,h)$$
$$\tilde{v}(k,h) + \tilde{v}_{\rm ref}(k,h) = \tilde{v}_{\rm tra}(k,h).$$

The two linear equations in variables T and R

$$\begin{aligned} \rho_0 D\big(\Omega_\infty - \operatorname{sign}(\operatorname{Re} k)\sigma\big) + \rho_0 R(\Omega_\infty + \operatorname{sign}(\operatorname{Re} k)\sigma) &= \rho_0 T\Omega_\infty, \\ -\mathrm{i}D|k| \qquad\qquad + \quad \mathrm{i}R|k| &= -\mathrm{i}T|k|, \end{aligned}$$

can be solved to yield

$$T = D\frac{\Omega_\infty}{\Omega_\infty + \frac{1}{2}\operatorname{sign}(\operatorname{Re} k)\sigma}, \qquad R = D\frac{\frac{1}{2}\operatorname{sign}(\operatorname{Re} k)\sigma}{\Omega_\infty + \frac{1}{2}\operatorname{sign}(\operatorname{Re} k)\sigma}.$$

The inner pressure transmitted outside the shear is then

$$\bar{p}_{\rm tra}(x,y) = \frac{1}{2\pi}\int_{-\infty}^{\infty} \frac{2\rho_0 U_0^2}{\zeta}\,\frac{\mathrm{e}^{-k_0 y_0}\,K_-(k_0)}{k-k_0}\left[\frac{\Omega_\infty^2}{\Omega_\infty + \frac{1}{2}\operatorname{sign}(\operatorname{Re} k)\sigma}\right]\frac{\mathrm{e}^{-\mathrm{i}kx-|k|y}}{|k|K_+(k)}\,\mathrm{d}k. \tag{6.29}$$

If we write $\Omega_\infty = \omega - k\sigma h$, the outer limit of the inner pressure can be obtained by the asymptotic evaluation of the integral (6.29) in the limit $k \to 0$,

$$\begin{aligned} \bar{p}_{\rm tra}(x,y) = \frac{\rho_0 U_0^2}{\pi\zeta}\frac{\mathrm{e}^{-k_0 y_0}}{-k_0}K_-(k_0)\Bigg(&\int_{-\infty}^{0}\left[\frac{\omega^2}{\omega - \frac{1}{2}\sigma}\right]\frac{\mathrm{e}^{-\mathrm{i}kx-|k|y}}{|k|K_+(k)}\,\mathrm{d}k \\ &+ \int_0^{\infty}\left[\frac{\omega^2}{\omega + \frac{1}{2}\sigma}\right]\frac{\mathrm{e}^{-\mathrm{i}kx-|k|y}}{|k|K_+(k)}\,\mathrm{d}k\Bigg). \end{aligned} \tag{6.30}$$

In the case of $\sigma < \omega$, using (6.22) and (6.26), we obtain

$$\bar{p}_{\mathrm{tra}\,(\sigma<\omega)} = \mathrm{i}^{-(\frac{1}{2}+\mathrm{i}\delta)}\Gamma(\tfrac{1}{2}+\mathrm{i}\delta)\frac{\rho_0 U_0^2}{\zeta\pi c_1}\,\mathrm{e}^{-k_0 y_0}\,\frac{K_-(k_0)}{-k_0}\left[\frac{\omega^2}{\omega-\frac{1}{2}\sigma}z^{-\frac{1}{2}-\mathrm{i}\delta} + \frac{\omega^2}{\omega+\frac{1}{2}\sigma}z^{*\,-\frac{1}{2}-\mathrm{i}\delta}\right]. \tag{6.31}$$

In the other case, *i.e.* $\sigma > \omega$, using (6.22) and (6.24), we have

$$\bar{p}_{\mathrm{tra}\,(\sigma>\omega)} = \mathrm{i}^{-\mathrm{i}\delta}\Gamma(\mathrm{i}\delta)\frac{\rho_0 U_0^2}{\zeta\pi c_1}\,\mathrm{e}^{-k_0 y_0}\,\frac{K_-(k_0)}{-k_0}\left[\frac{\omega^2}{\omega-\frac{1}{2}\sigma}z^{-\mathrm{i}\delta} + \frac{\omega^2}{\omega+\frac{1}{2}\sigma}z^{*\,-\mathrm{i}\delta}\right]. \tag{6.32}$$

where $z = r\,\mathrm{e}^{\mathrm{i}\theta}$. We conclude from (6.27), (6.28), (6.31) and (6.32) that the inclusion of the transition layer does not change the functional relationship of the sound radiated to far field and differ by only a constant. We will match the outerfield acoustic solution to both inner fields in the next section.

6.6 Outer solution and asymptotic matching (low shear case only)

Since the mean flow Mach number is small, the inner problem is incompressible. We assume the outer acoustic field, where the mean flow velocity profile changed from linear $U(y) = \sigma y$ to a constant, compressible but with negligible mean flow. Then we have the Helmholtz (= reduced wave) equation for $\overline{p}$ (or $\overline{u}$ or $\overline{v}$)

$$\nabla^2\overline{p} + \kappa^2\overline{p} = 0, \qquad \kappa = \frac{\omega}{c_0}. \tag{6.33}$$

With a point source in $x = y = 0$, assuming a certain symmetry in r and θ (where $x = r\cos\theta$ and $y = r\sin\theta$), we search for solutions of the form

$$\overline{p}(r,\theta) = B_0\gamma(r)\beta(\theta). \tag{6.34}$$

If we substitute this in the equations we find

$$\gamma'' + \frac{1}{r}\gamma' + \kappa^2\gamma - \frac{\nu^2}{r^2}\gamma = 0, \quad \beta'' + \nu^2\beta = 0,$$

such that $\beta(\theta) = B_1\,\mathrm{e}^{\mathrm{i}\nu\theta} + B_2\,\mathrm{e}^{-\mathrm{i}\nu\theta}$. Furthermore due to the radiation condition,

$$\gamma(r) = mH_\nu^{(2)}(\kappa r) + nH_{-\nu}^{(2)}(\kappa r) = mH_\nu^{(2)}(\kappa r) + n\,\mathrm{e}^{-\nu\pi\mathrm{i}}\,H_\nu^{(2)}(\kappa r) = H_\nu^{(2)}(\kappa r) \tag{6.35}$$

with the relationship $H_{-\nu}^{(2)}(\kappa r) = \mathrm{e}^{-\mathrm{i}\nu\pi}\,H_\nu^{(2)}(\kappa r)$ [63]. Clearly, n can be taken zero and m equal to unity. The constants B_0, B_1, B_2 and ν are to be determined from the matching condition at $r \to 0$ where the Hankel function has the following asymptotic

behaviour [63]

$$H_\nu^{(2)}(\kappa r) \;\simeq\; \mathrm{i}\pi^{-1}\Gamma(\nu)(\tfrac{1}{2}\kappa r)^{-\nu} + \mathrm{i}^{1+2\nu}\pi^{-1}\Gamma(-\nu)(\tfrac{1}{2}\kappa r)^{\nu} = \alpha r^{\nu} + \tilde{\alpha} r^{-\nu}, \qquad (6.36)$$

the second term of which can be ignored if $\mathrm{Re}(\nu) > 0$, but is essential if ν is imaginary. We wish to match (6.36) with the outer limit of the inner solution. This however, is possible only for the low shear case *i.e.* (6.27) and (6.31).

6.6.1 Far field sound, low shear case

The matching of (6.36) with (6.27) or (6.31) leads to

$$\nu = \tfrac{1}{2} + \mathrm{i}\delta, \qquad B_0 = \mathrm{i}^{-\frac{3}{2}-\mathrm{i}\delta}\frac{\rho_0 U_0^2}{\zeta c_1}\,\mathrm{e}^{-k_0 y_0}\,\frac{K_-(k_0)}{-k_0}\,\big(\tfrac{1}{2}\kappa\big)^{\frac{1}{2}+\mathrm{i}\delta}, \qquad (6.37)$$

while B_1 and B_2 represent the different matching with the inner pressure $\overline{p}_{\mathrm{inner}\,(\sigma<\omega)}$ inside, or $\bar{p}_{\mathrm{tra}\,(\sigma<\omega)}$ outside the shear layer.

$$\begin{aligned} &B_1 = \omega - \sigma \quad \text{and} \quad B_2 = \omega + \sigma \qquad \text{matched with} \quad \overline{p}_{\mathrm{inner}\,(\sigma<\omega)} \\ &B_1 = \frac{\omega^2}{\omega + \frac{1}{2}\sigma} \quad \text{and} \quad B_2 = \frac{\omega^2}{\omega - \frac{1}{2}\sigma} \qquad \text{matched with} \quad \bar{p}_{\mathrm{tra}\,(\sigma<\omega)} \end{aligned} \qquad (6.38)$$

and hence the acoustic pressure $\overline{p}$ and radial velocity $\overline{w}$ are given by

$$\begin{aligned} \overline{p} &= B_0 H_\nu^{(2)}(\kappa r)\big(B_1\,\mathrm{e}^{\mathrm{i}\nu\theta} + B_2\,\mathrm{e}^{-\mathrm{i}\nu\theta}\big) \\ \overline{w} &= \frac{\mathrm{i}}{\rho_0 c_0} B_0 H_\nu^{(2)\prime}(\kappa r)\big(B_1\,\mathrm{e}^{\mathrm{i}\nu\theta} + B_2\,\mathrm{e}^{-\mathrm{i}\nu\theta}\big) \end{aligned} \qquad (6.39)$$

This effect of the reflection at the transition layer is for the type of sound field of rather little concern. Eventually, the far field sound is given by

$$\begin{aligned} \overline{p}(r,\theta) = \mathrm{i}^{-\frac{3}{2}-\mathrm{i}\delta}\frac{\rho_0 U_0^2}{\zeta c_1}\,\mathrm{e}^{-k_0 y_0}\,\frac{K_-(k_0)}{-k_0}\big(\tfrac{1}{2}\kappa\big)^{(\frac{1}{2}+\mathrm{i}\delta)}\times \\ H_\nu^{(2)}(\kappa r)\left(\big(\omega+\sigma\big)\,\mathrm{e}^{-\mathrm{i}(\frac{1}{2}+\mathrm{i}\delta)\theta} + \big(\omega-\sigma\big)\,\mathrm{e}^{\mathrm{i}(\frac{1}{2}+\mathrm{i}\delta)\theta}\right) \end{aligned} \qquad (6.40)$$

when matched with the inner pressure $\overline{p}_{\mathrm{inner}\,(\sigma<\omega)}$ inside the shear layer, or

$$\begin{aligned} \overline{p}(r,\theta) = \mathrm{i}^{-\frac{3}{2}-\mathrm{i}\delta}\frac{\rho_0 U_0^2}{\zeta c_1}\,\mathrm{e}^{-k_0 y_0}\,\frac{K_-(k_0)}{-k_0}\big(\tfrac{1}{2}\kappa\big)^{(\frac{1}{2}+\mathrm{i}\delta)}\times \\ H_\nu^{(2)}(\kappa r)\left(\frac{\omega^2}{\omega-\frac{1}{2}\sigma}\,\mathrm{e}^{-\mathrm{i}(\frac{1}{2}+\mathrm{i}\delta)\theta} + \frac{\omega^2}{\omega+\frac{1}{2}\sigma}\,\mathrm{e}^{\mathrm{i}(\frac{1}{2}+\mathrm{i}\delta)\theta}\right) \end{aligned} \qquad (6.41)$$

when matched with the inner pressure $\bar{p}_{\mathrm{tra}\,(\sigma<\omega)}$ transmitted outside the layer. Shown in Fig. 6.8 is the far field sound obtained by above two different matchings. Since the two different matching differ slightly, we choose the first expression coupled with the

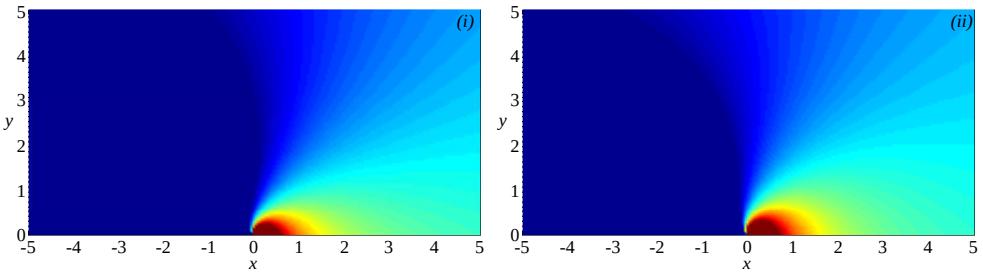

Figure 6.8: Far field sound obtained from (6.40) and (6.41) respectively. $\sigma = 4 < \omega = 5, \zeta = \frac{1}{2}(1+\mathrm{i}), U_0 = 5, k_0 = 1, y_0 = 1.25$.

far field behaviour

$$H_\nu^{(2)}(\kappa r) \sim \left(\frac{2}{\pi\kappa r}\right)^{\frac{1}{2}} \mathrm{e}^{-\mathrm{i}\kappa r + \frac{1}{2}\mathrm{i}\nu\pi + \frac{1}{4}\mathrm{i}\pi}, \qquad H_\nu^{(2)\prime}(\kappa r) \sim -\mathrm{i}\left(\frac{2}{\pi\kappa r}\right)^{\frac{1}{2}} \mathrm{e}^{-\mathrm{i}\kappa r + \frac{1}{2}\mathrm{i}\nu\pi + \frac{1}{4}\mathrm{i}\pi} \tag{6.42}$$

to obtain the time averaged radial acoustic intensity in the far field as

$$\begin{aligned} \tfrac{1}{2}\,\mathrm{Re}(\overline{p}\;\overline{w}^*) \simeq \frac{\rho_0 \kappa k_0}{2\pi c_1^2 \zeta^2 r} U_0^5\, \mathrm{e}^{-2k_0 y_0} \left(\frac{K_-(k_0)}{-k_0}\right)^2 \times \\ \left(\left(\frac{\omega+\sigma}{\omega}\right)^2 \mathrm{e}^{2\delta\theta} + \left(\frac{\omega-\sigma}{\omega}\right)^2 \mathrm{e}^{-2\delta\theta} - 2\left(\frac{\omega^2-\sigma^2}{\omega}\right)^2 \cos\theta\right) \end{aligned} \tag{6.43}$$

Integrated over $0 < \theta < \pi$ we obtain the interesting expression of the radiated acoustic power

$$\int_0^\pi \tfrac{1}{2}\,\mathrm{Re}(\overline{p}\;\overline{w}^*) r\,\mathrm{d}\theta = \rho_0 c_0^3 \left(\frac{U_0}{c_0}\right)^4 \frac{\mathrm{e}^{-2\omega/\sigma}}{\pi\delta c_1^2 \zeta^2} \left(\frac{K_-(k_0)}{k_0}\right)^2 \frac{\omega\sigma(\omega^2+\sigma^2)}{(\omega^2-\sigma^2)}, \tag{6.44}$$

to be multiplied by the square of the small dimensionless amplitude of the incident vorticity (6.2). In high shear case, the second term in (6.36) is essentially missing in the inner solution, hence the matching of the pressure is not possible. However, it is found that the outer solution does match with the velocities and integral of the pressure rather than pressure itself.

6.7 Conclusions

A systematic and analytically exact solution is obtained by means of the Wiener-Hopf technique of the problem of vorticity, convected by a linearly sheared mean flow, is scattered by the hard-soft transition of the wall. It is illustrated by numerical examples. A particular feature is the fact that the Wiener-Hopf kernel can be split

exactly. This enables us to find in rather detail the functional relationship of the hydrodynamic far field and hence the associated acoustic source strength.

The problem appears to be distinguished into two different classes, based upon the relative size of problem parameters σ (the mean flow shear U') and ω (the perturbation frequency), and not (for example) of the impedance of the wall. If the mean shear is relatively weak, *i.e.* if $\sigma < \omega$, the hydrodynamic far field varies as the inverse square root of the distance from the hard-soft singularity. If the mean shear is relatively strong, *i.e.* if $\sigma > \omega$, the hydrodynamic far field tends (in modulus) to a constant which confirms a strong interaction between the edge and the interphase that leads to the linear infinite shear as an inconsistent modelling assumption.

The far field and resulting sound field are based upon the asymptotic behaviour of the Fourier integrals and the reliability is confirmed by the limiting case $Z = 0$ where the solution is explicit.

Chapter 7

Vorticity scattering at soft wall - hard wall transition in shear flows

The scattering of 2D vorticity perturbations in an inviscid low Mach number shear flow with vanishing velocity at the wall passing over a hard to soft transition of this wall has been examined in previous two chapters 5 and 6. The current chapter extends the analysis to a soft to hard transition *i.e.* reversal of the boundary condition. Because of the presence of the shear layer, the problem is non symmetric and demands an analysis from scratch. The soft hard transition is as important as the hard soft transition and is very common in aircraft engines and ventilation ducts and hence, it is important to analyse the scattering process associated with such boundary condition reversal that is reported in this chapter. The Wiener-Hopf method in the incompressible limit poses some mathematical intricacies that are tackled with the help of the physical limit $Z = 0$. The solution confirms that a soft -hard singularity behaves as the hard soft singularity in low and high shear case and the resulting sound field is similar in behaviour.

The schematic scheme of the problem we consider is shown in Fig. 7.1. The modeling assumptions are similar to the previous chapters except that the boundary conditions are reversed. The initial field of the problem satisfies the soft wall boundary condition at $y = 0$ and is derived in a similar fashion as the previous initial field (5.10).

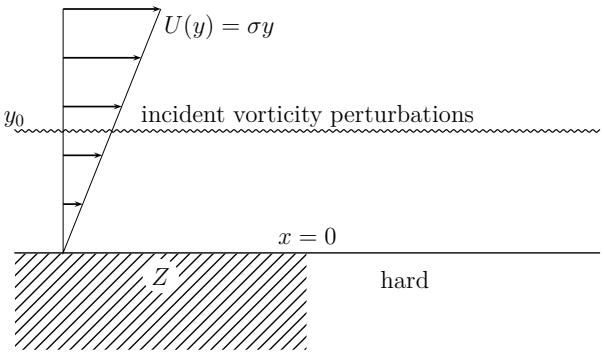

Figure 7.1: Sketch of the problem

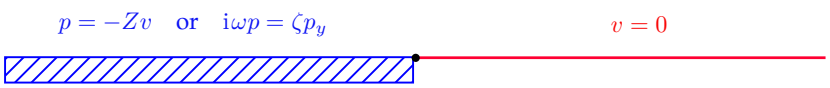

Figure 7.2: Boundary conditions at $y = 0$

7.1 Mathematical formulation

Like the previous formulations, we start from the governing equations of mass and momentum conservation in the frequency domain (2.26)

$$\begin{aligned} \rho_0 \left(\frac{\partial u}{\partial x} + \frac{\partial v}{\partial y} \right) &= 0, \\ \rho_0 \left(\mathrm{i}\omega + U \frac{\partial}{\partial x} \right) u + \rho_0 \frac{\mathrm{d}U}{\mathrm{d}y} v + \frac{\partial p}{\partial x} &= 0, \\ \rho_0 \left(\mathrm{i}\omega + U \frac{\partial}{\partial x} \right) v + \frac{\partial p}{\partial y} &= 0. \end{aligned} \tag{7.1}$$

Boundary conditions for finite impedance and hard wall at $y = 0$, as shown in Fig. 7.2, are

$$v = 0 \quad \text{if} \quad x > 0, \qquad p = -Zv \quad \text{or} \quad \mathrm{i}\omega p = \zeta p_y \quad \text{if} \quad x < 0. \tag{7.2}$$

Similarly, the boundary conditions for the pressure release and hard wall are

$$v = 0 \quad \text{if} \quad x > 0, \qquad p = 0 \quad \text{if} \quad x < 0. \tag{7.3}$$

Apart from (7.2) and (7.3), we have an edge condition of vanishing energy flux from $(0, 0)$. The far field boundary conditions will be of vanishing velocity, but maybe not of vanishing pressure. The incident field of the undulating vortex sheet at $y = y_0 = U_0/\sigma$ is determined by the soft wall boundary condition at $y = 0$.

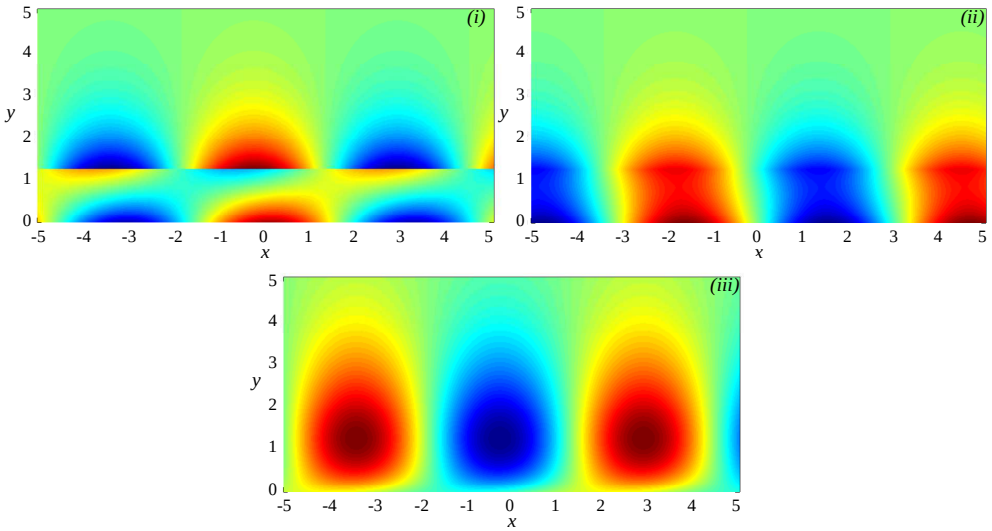

Figure 7.3: The initial field p_{in} and v_{in} respectively. $\omega = 5, \sigma = 4, U_0 = 5, k_0 = 1, y_0 = 1.25$.

Typically, there are infinitely many possible solutions. We choose the one with real k_0 and satisfying Myer's energy condition [48, 54, 56] and is given as

$$\begin{aligned}
u_{\text{in}} &= U_0\,\mathrm{e}^{-\mathrm{i}k_0x}\Big[\quad \lambda\,\mathrm{sign}(y-y_0)\;\mathrm{e}^{-k_0|y-y_0|} \;+\; \mathrm{e}^{-k_0(y+y_0)}\Big],\\
v_{\text{in}} &= \mathrm{i}U_0\,\mathrm{e}^{-\mathrm{i}k_0x}\Big[\quad -\lambda\,\mathrm{e}^{-k_0|y-y_0|} \;-\; \mathrm{e}^{-k_0(y+y_0)}\Big],\\
p_{\text{in}} &= \frac{\sigma}{\omega}\rho_0U_0^2\,\mathrm{e}^{-\mathrm{i}k_0x}\Big[-\lambda(1+k_0|y-y_0|)\,\mathrm{e}^{-k_0|y-y_0|} \;-\; (1+k_0(y-y_0))\,\mathrm{e}^{-k_0(y+y_0)}\Big],
\end{aligned} \tag{7.4}$$

with $k_0 = \omega/U_0$, and so $k_0y_0 = \omega/\sigma$. The effect of the soft wall is contained in dimensionless constant $\lambda = \lambda_-/\lambda_+$ where $\lambda_+ = (\omega+\sigma+\mathrm{i}k_0\zeta)$ and $\lambda_- = (\omega-\sigma-\mathrm{i}k_0\zeta)$ respectively. In the limit $\zeta \to \infty$, $\lambda = -1$, hence the initial field converges to the hard wall initial field in (6.2). In case of the pressure release wall, we have $\lambda_0 = (\omega-\sigma)/(\omega+\sigma)$. Fig. 7.3 shows the initial field for a typical case of low shear.

The triple $(u_{\text{in}}, v_{\text{in}}, p_{\text{in}})$ satisfies the differential equations (7.1), continuity of p_{in} and v_{in} across $y = y_0$, and the soft-wall boundary condition $p_{\text{in}} + Zv_{\text{in}}$ at $y = 0$. The scattered perturbations are due to the vanishing velocity $v_{\text{in}} = 0$ along $y = 0, x > 0$.

We split up the field in the incident part and the scattered part as follows

$$u = u_{\text{in}} + \overline{u}, \quad v = v_{\text{in}} + \overline{v}, \quad p = p_{\text{in}} + \overline{p}. \tag{7.5}$$

After Fourier transformation in x (formally assuming the convergence of the integrals)

$$\overline{p}(x,y) = \frac{1}{2\pi}\int_{-\infty}^{\infty} \tilde{p}(y,k)\,\mathrm{e}^{-\mathrm{i}kx}\,\mathrm{d}k, \tag{7.6}$$

(the same for $\overline{u}$ and $\overline{v}$) we obtain the following set of equations

$$\rho_0(-\mathrm{i}k\tilde{u} + \tilde{v}') = 0, \qquad \mathrm{i}\rho_0\Omega\tilde{u} + \rho_0\sigma\tilde{v} - \mathrm{i}k\tilde{p} = 0, \qquad \mathrm{i}\rho_0\Omega\tilde{v} + \tilde{p}' = 0, \tag{7.7}$$

where $\Omega = \omega - kU$. The system of equations has two independent solutions, namely $\sim \mathrm{e}^{\pm ky}$ [45, 65]. The one, bounded for $y \to \infty$, is then

$$\begin{aligned} \tilde{u}(y) &= kA(k)\,\mathrm{e}^{-|k|y}, \\ \tilde{v}(y) &= -\mathrm{i}|k|A(k)\,\mathrm{e}^{-|k|y}, \\ \tilde{p}(y) &= \rho_0(\Omega - \operatorname{sign}(\operatorname{Re} k)\sigma)A(k)\,\mathrm{e}^{-|k|y}, \end{aligned} \tag{7.8}$$

with amplitude $A(k)$ to be determined, and

$$|k| = \operatorname{sign}(\operatorname{Re} k)k = \sqrt{k^2}, \tag{7.9}$$

where $\sqrt{\ }$ denotes the principal value square root, and $|k|$ has thus branch cuts along the imaginary axis given by $(-\mathrm{i}\infty, 0)$ and $(0, \mathrm{i}\infty)$.

7.2 Wiener-Hopf procedure

To facilitate the following Wiener-Hopf procedure, we introduce a small positive parameter ε and have an upper and a lower half plane, and a strip of overlap

$$\mathbb{C}^+ = \{k \in \mathbb{C} \mid \operatorname{Im} k > -\varepsilon\}, \quad \mathbb{C}^- = \{k \in \mathbb{C} \mid \operatorname{Im} k < \varepsilon\}, \quad S = \{k \in \mathbb{C} \mid -\varepsilon < \operatorname{Im} k < \varepsilon\},$$

The physical problem will be the limit $\varepsilon \to 0$ of a regularised problem with k_0 replaced by $k_0 - \mathrm{i}\varepsilon$ (an incident field $\sim \mathrm{e}^{-\mathrm{i}k_0 x}$ slightly decaying with x) and $|k|$ replaced by the smoother function

$$|k| = \sqrt{k^2 + \varepsilon^2}$$

with branch cuts $(-\mathrm{i}\infty, -\mathrm{i}\varepsilon) \cup (\mathrm{i}\varepsilon, \mathrm{i}\infty)$ avoiding the strip S. In this way, we removed the branches of $|k|$ away from the strip (*cf.* [79]).

Introduce the auxiliary functions $F_-(k)$ and $G_+(k)$ that are analytic in lower $\operatorname{Im}(k) < \varepsilon$ and upper $\operatorname{Im}(k) > -\varepsilon$ half of the complex plane respectively, as shown in Fig. 6.3 and explained in appendix C.1.

$$F_-(k) = \int_{-\infty}^{0} \overline{v}(x,0)\,\mathrm{e}^{\mathrm{i}kx}\,\mathrm{d}x, \quad G_+(k) = \int_0^{\infty} \left[\overline{p}(x,0) + Z\overline{v}(x,0)\right]\mathrm{e}^{\mathrm{i}kx}\,\mathrm{d}x \tag{7.10}$$

$$\begin{aligned} F_-(k) &= \int_{-\infty}^{0} \overline{v}(x,0)\,\mathrm{e}^{\mathrm{i}kx}\,\mathrm{d}x \\ &= \int_{-\infty}^{0} [v_{\mathrm{in}}(x,0)+\overline{v}(x,0)]\,\mathrm{e}^{\mathrm{i}kx}\,\mathrm{d}x - \int_{-\infty}^{0} v_{\mathrm{in}}(x,0)\,\mathrm{e}^{\mathrm{i}kx}\,\mathrm{d}x \\ &= \int_{-\infty}^{\infty} [v_{\mathrm{in}}(x,0)+\overline{v}(x,0)]\,\mathrm{e}^{\mathrm{i}kx}\,\mathrm{d}x - \int_{-\infty}^{0} v_{\mathrm{in}}(x,0)\,\mathrm{e}^{\mathrm{i}kx}\,\mathrm{d}x \\ &= \int_{-\infty}^{\infty} \overline{v}(x,0)\,\mathrm{e}^{\mathrm{i}kx}\,\mathrm{d}x + \int_{0}^{\infty} v_{\mathrm{in}}(x,0)\,\mathrm{e}^{\mathrm{i}kx}\,\mathrm{d}x \\ &= -\mathrm{i}|k|A(k) + (\lambda+1)U_0\frac{\mathrm{e}^{-k_0y_0}}{(k-k_0)} \end{aligned} \tag{7.11}$$

Furthermore, we have

$$G_+(k) = \int_0^\infty \left[\overline{p}(x,0)+Z\overline{v}(x,0)\right]\mathrm{e}^{\mathrm{i}kx}\,\mathrm{d}x = \int_{-\infty}^\infty \left[\overline{p}(x,0)+Z\overline{v}(x,0)\right]\mathrm{e}^{\mathrm{i}kx}\,\mathrm{d}x$$
$$= -\mathrm{i}\rho_0\zeta|k|A(k)K(k) \tag{7.12}$$

with the previous Wiener-Hopf kernel of Chapter 6,

$$K(k) = 1 + \frac{a}{k} - \frac{b}{|k|}, \qquad a = \frac{\sigma}{\mathrm{i}\zeta}, \quad b = \frac{\omega}{\mathrm{i}\zeta}. \tag{7.13}$$

With $\varepsilon = 0$, $K(k)$ has 0, 1, or 2 zeros in the 1st, 2nd, or 4th quadrant, as shown in table 6.1, depending on the signs of $\sigma-\omega$ and $\operatorname{Im}\zeta$, and assuming that $\sigma, \omega, \operatorname{Re}\zeta > 0$. As $K(k)$ has a singularity in $k = 0$, which is inside strip S, we follow (6.12) and consider the regularized version

$$K(k) = 1 + \frac{a}{k-\mathrm{i}\varepsilon} - \frac{b}{\sqrt{k^2+\varepsilon^2}}. \tag{7.14}$$

This $K(k)$ has 3 zeros, which are for small ε approximated as shown in table 6.2. So in general the zeros and singularities of K are not real and there is a neighbourhood of the real axis where K is analytic.

Hence we arrive at the Wiener-Hopf equation

$$\begin{aligned} F_-(k) =& \frac{G_+(k)}{\rho_0\zeta}\frac{1}{K(k)} + (\lambda+1)U_0\frac{\mathrm{e}^{-k_0y_0}}{(k-k_0)}. \\ =& \frac{G_+(k)}{\rho_0\zeta}K'(k) + (\lambda+1)U_0\frac{\mathrm{e}^{-k_0y_0}}{(k-k_0)}. \end{aligned} \tag{7.15}$$

We notice from (7.15) that the new kernel $K'(k)$ is inverse of the previous kernel $K(k)$, (6.13), hence the poles and zeros of the previous kernel turn into the zeros and poles of the new kernel respectively. Since the strip S, after regularization, is

free from all poles are zeros, the inverse kernel follows the same. However, there is a subtle difference that we will encounter later in the high shear case. As stated in Chapter 5 that there is a real zero within the strip S in the high shear case that we regularized with an imaginary component to absorb it in the numerator of Wiener-Hopf equation. However, now that zero turns into a pole and can not be regularized in the denominator and must be multiplied out across the Wiener-Hopf equation, as we will see later. For now, we proceed with our derivation and define by writing

$$K(k) = \frac{K_+(k)}{K_-(k)} \tag{7.16}$$

where splitfunction K_+ is analytic in $\mathbb{C}^+$ and K_- is analytic in $\mathbb{C}^-$. Altogether, we conclude that in S,

$$\begin{aligned}\frac{F_-(k)}{K_-(k)} - \frac{G_+(k)}{\rho_0\zeta K_+(k)} &= (\lambda+1)U_0\frac{\mathrm{e}^{-k_0y_0}}{k-k_0}\frac{1}{K_-(k)} \\ &= (\lambda+1)U_0\frac{\mathrm{e}^{-k_0y_0}}{k-k_0}\left[\frac{1}{K_-(k)} - \frac{1}{K_-(k_0)}\right] + (\lambda+1)U_0\frac{\mathrm{e}^{-k_0y_0}}{k-k_0}\frac{1}{K_-(k_0)}\end{aligned} \tag{7.17}$$

where we have isolated the pole $k_0 \in \mathbb{C}^-$ from K_- and write

$$\begin{aligned}\frac{F_-(k)}{K_-(k)} - (\lambda+1)U_0\frac{\mathrm{e}^{-k_0y_0}}{k-k_0}\left[\frac{1}{K_-(k)} - \frac{1}{K_-(k_0)}\right] \\ = \frac{G_+(k)}{\rho_0\zeta K_+(k)} + (\lambda+1)U_0\frac{\mathrm{e}^{-k_0y_0}}{k-k_0}\frac{1}{K_-(k_0)}\end{aligned} \tag{7.18}$$

The left and right side of (7.18) that are analytic in $\mathbb{C}^+$ and in $\mathbb{C}^-$ respectively, are via their equivalence in S each other's analytic continuations, and define an entire function E

$$\begin{aligned}E(k) &= \frac{F_-(k)}{K_-(k)} - (\lambda+1)U_0\frac{\mathrm{e}^{-k_0y_0}}{k-k_0}\left[\frac{1}{K_-(k)} - \frac{1}{K_-(k_0)}\right] \\ &= \frac{G_+(k)}{\rho_0\zeta K_+(k)} + (\lambda+1)U_0\frac{\mathrm{e}^{-k_0y_0}}{k-k_0}\frac{1}{K_-(k_0)}.\end{aligned} \tag{7.19}$$

Following E.3, we have $E \equiv 0$, hence we can write from (7.12) and (7.19)

$$\begin{aligned}F_-(k) &= (\lambda+1)U_0\frac{\mathrm{e}^{-k_0y_0}}{k-k_0}\left[1 - \frac{K_-(k)}{K_-(k_0)}\right], \\ G_+(k) &= -(\lambda+1)\rho_0\zeta U_0\frac{\mathrm{e}^{-k_0y_0}}{K_-(k_0)}\frac{K_+(k)}{(k-k_0)}, \\ A(k) &= -\mathrm{i}(\lambda+1)U_0\frac{\mathrm{e}^{-k_0y_0}}{K_-(k_0)}\frac{K_-(k)}{|k|(k-k_0)}.\end{aligned} \tag{7.20}$$

$A(k)$ obtained from (7.20) can be substituted back into (7.8). This gives, with the inverse Fourier transform from (7.6) added to the initial field, the formal solution of the problem

$$
\begin{aligned}
u &= u_{\text{in}} - \frac{1}{2\pi} \fint_{-\infty}^{\infty} \mathrm{i}\,\mathrm{sign}(k)(\lambda+1)U_0 \frac{\mathrm{e}^{-k_0 y_0}}{K_-(k_0)} \frac{K_-(k)}{k-k_0}\, \mathrm{e}^{-|k|y}\, \mathrm{e}^{-\mathrm{i}kx}\, \mathrm{d}k \\
v &= v_{\text{in}} - \frac{1}{2\pi} \fint_{-\infty}^{\infty} (\lambda+1)U_0 \frac{\mathrm{e}^{-k_0 y_0}}{K_-(k_0)} \frac{K_-(k)}{k-k_0}\, \mathrm{e}^{-|k|y}\, \mathrm{e}^{-\mathrm{i}kx}\, \mathrm{d}k \\
p &= p_{\text{in}} - \frac{1}{2\pi} \fint_{-\infty}^{\infty} \mathrm{i}(\lambda+1)\rho_0 U_0 \frac{\mathrm{e}^{-k_0 y_0}}{K_-(k_0)} (\Omega - \mathrm{sign}(\mathrm{Re}\, k)\sigma) \frac{K_-(k)}{|k|(k-k_0)}\, \mathrm{e}^{-|k|y}\, \mathrm{e}^{-\mathrm{i}kx}\, \mathrm{d}k.
\end{aligned}
\tag{7.21}
$$

The pole $k = k_0$ is to be included when $x > 0$ and corresponds to the trailing vorticity. The other singularity at $k = 0$ is the one responsible for the far field sound. The integrals in (7.21) can be evaluated numerically and depend on the $K_-(k)$ function which is essentially different for the low and high shear cases. Please note that in the hard wall limit $\lambda \to -1$, the scattering field (7.21) will vanish as expected.

7.3 Hydrodynamic solution

The solution set u, v and p is the solution of incompressible inner problem of a larger compressible acoustic problem. Although a strict Matched Asymptotic Expansion analysis has not been laid out here in detail, we will refer to it as the inner solution. The outer limit of this inner solution $r = \sqrt{x^2 + y^2} \to \infty$ is used to match it with the inner limit of the outer compressible solution. In order to evaluate the solutions, in the form of Fourier integrals (7.21), numerically or asymptotically in the far field, we need to know the behaviour of $K_-(k)$ at $k = 0$. The following asymptotic behaviour of $K_-(k \to 0)$ can be confirmed from E.2.2 and E.2.3

$$
\begin{aligned}
K_-(k) &\simeq \frac{c_1}{a - \mathrm{sign}(\mathrm{Re}\, k)b} k^{\frac{1}{2} - \mathrm{i}\delta} \quad \text{for} \quad \sigma < \omega \\
K_-(k) &\simeq \frac{c_1}{a - \mathrm{sign}(\mathrm{Re}\, k)b} k^{-\mathrm{i}\delta} \quad \text{for} \quad \sigma > \omega,
\end{aligned}
\tag{7.22}
$$

where c_1 is a complex constant and $\delta = \frac{1}{2\pi} \log |\frac{\sigma+\omega}{\sigma-\omega}|$ is real positive.

7.3.1 Solution of velocities u and v

We see by combining (7.22) and (7.21) that in either case, the velocities u and v are integrable at $k = 0$. In the far field, the u and v solution behaves like $r^{-\frac{3}{2}+\mathrm{i}\delta}$ and $r^{-1+\mathrm{i}\delta}$ for low and high shear cases respectively. Shown in Fig. 7.5 (top and middle) are the solutions (total = incident + scattered) of velocities for a typical representative case. Apparently, the high mean shear weaken the velocity field especially downstream of the edge. In the hard-soft transition case, chapter 6, similar behaviour of the

velocities was found hence, the boundary condition reversal has no change on the behaviour of velocities except that the new δ is negative of the previous one.

7.3.2 Solution of pressure p

As we noticed, the behaviour of the singularity at $k = 0$ is different for the cases $\sigma < \omega$ and $\sigma > \omega$. Hence, the far field solution in pressure is different for these cases. This splits our problem into 2 different cases in terms of radiated pressure. We will discuss them in separate sections.

Low shear

The low shear case corresponds with $\sigma < \omega$, *i.e.* $k_0 y_0 > 1$. The behaviour of $K_-(k) \sim k^{\frac{1}{2}-\mathrm{i}\delta}$ in the limit $k \to 0$ weakens the non integrable singularity $|k|^{-1}$ to an integrable singularity $k^{-\frac{1}{2}-\mathrm{i}\delta}$ of the integrand in (7.21). Hence the pressure solution can be obtained by direct integration along the contour shown in Fig. 7.4, like the velocities. For a typical case, this is shown in Fig. 7.5 (bottom left). It can be predicted, for example by invoking a version of Watson's Lemma, even at this stage that a weaker singularity at $k = 0$ produces a weaker far field sound that decays like $r^{-\frac{1}{2}+\mathrm{i}\delta}$. Please note that we found similar behaviour in the case of hard-soft wall transition as well except that the new δ is negative of the previous one.

High shear

The high shear case corresponds with $\sigma > \omega$, *i.e.* $k_0 y_0 < 1$. The behaviour of $K_-(k) \sim k^{-\mathrm{i}\delta}$ in the limit $k \to 0$ does not weaken the singularity in this case and the integral function behaves as $\sim |k|^{-1-\mathrm{i}\delta}$ as $k \to 0$ and hence diverges. The divergent behaviour at $k = 0$ in Fourier space suggests a strong far field at $r = \sqrt{x^2 + y^2} \to \infty$ in the physical plane. The Fourier representation of pressure is too singular to interpret and hence should be regularised, using generalised functions, by splitting off the singular part and the part which is integrable. From (7.21) and (7.22) , we have

$$
\begin{aligned}
\overline{p}(x,y) = &-\mathrm{i}(\lambda+1)\frac{\rho_0 U_0}{2\pi}\frac{\mathrm{e}^{-k_0 y_0}}{K_-(k_0)}\int_{-\infty}^{0}\left(\frac{(\Omega+\sigma)K_-(k)}{(k-k_0)|k|}\right.\\
&\qquad\left.-\frac{c_1(\omega+\sigma)}{-(a+b)k_0|k|k^{\mathrm{i}\delta}}\right)\mathrm{e}^{-\mathrm{i}kx-|k|y}\,\mathrm{d}k\\
&-\mathrm{i}(\lambda+1)\frac{\rho_0 U_0}{2\pi}\frac{\mathrm{e}^{-k_0 y_0}}{K_-(k_0)}\int_{0}^{\infty}\left(\frac{(\Omega-\sigma)K_-(k)}{(k-k_0)|k|}\right.\\
&\qquad\left.-\frac{c_1(\omega-\sigma)}{-(a-b)k_0|k|k^{\mathrm{i}\delta}}\right)\mathrm{e}^{-\mathrm{i}kx-|k|y}\,\mathrm{d}k\\
&-\mathrm{i}(\lambda+1)\frac{\rho_0 U_0}{2\pi}\frac{c_1\,\mathrm{e}^{-k_0 y_0}}{-k_0 K_-(k_0)}\left[\int_{-\infty}^{0}\frac{\mathrm{i}\zeta}{|k|k^{\mathrm{i}\delta}}\,\mathrm{e}^{-\mathrm{i}kx-|k|y}\,\mathrm{d}k\right.\\
&\qquad\left.+\int_{0}^{\infty}\frac{-\mathrm{i}\zeta}{|k|k^{\mathrm{i}\delta}}\,\mathrm{e}^{-\mathrm{i}kx-|k|y}\,\mathrm{d}k\right]
\end{aligned}
\tag{7.23}
$$

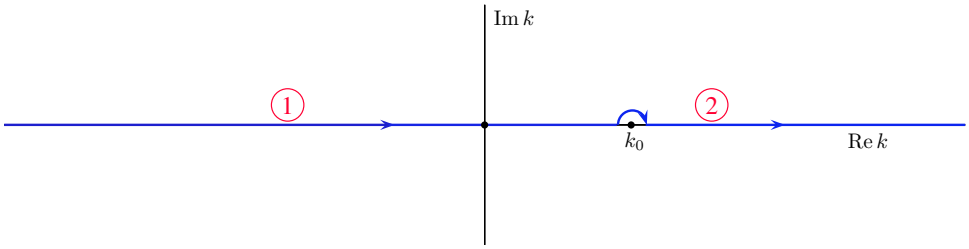

Figure 7.4: Integration contour

The separated singularity renders the pressure integral of $O(1)$ at $k = 0$ and hence integrable. In (7.23), the first two integrals have a finite limit at $k = 0$ and therefore can be evaluated along the integration contour 1 and 2 respectively, as shown in Fig. 7.4. The last integrals in (7.23) are those which carry the singularity and diverge at $k = 0$ which makes them difficult to interpret. They can be evaluated as generalised functions [31, 47]. With Appendix E.4, we have

$$-\mathrm{i}(\lambda+1)\frac{\rho_0 U_0}{2\pi}\frac{c_1\,\mathrm{e}^{-k_0 y_0}}{-k_0 K_-(k_0)}\left[\int_{-\infty}^{0}\frac{\omega+\sigma}{|k|k^{\mathrm{i}\delta}}\,\mathrm{e}^{-\mathrm{i}kx-|k|y}\,\mathrm{d}k+\int_{0}^{\infty}\frac{\omega-\sigma}{|k|k^{\mathrm{i}\delta}}\,\mathrm{e}^{-\mathrm{i}kx-|k|y}\,\mathrm{d}k\right]$$
$$=\mathrm{i}^{(1+\mathrm{i}\delta)}\Gamma(-\mathrm{i}\delta)\frac{\zeta c_1}{2\pi}(\lambda+1)\rho_0 U_0\frac{\mathrm{e}^{-k_0 y_0}}{-k_0 K_-(k_0)}\left(z^{\mathrm{i}\delta}-z^{*\,\mathrm{i}\delta}\right)\quad(7.24)$$

where $z = x + \mathrm{i}y$ and $z^* = x - \mathrm{i}y$. The results from (7.24) used with the first two integrals in (7.23) added to the initial field p_{in} gives the final solution of the inner pressure p (7.21). Shown in Fig. 7.5 (bottom right) is the pressure for a typical case. The pressure field is clearly more intense for high shear than for low shear. This behaviour was found similar in the hard-soft transition case where the singularity at $k = 0$ was behaving like $|k|^{-1+\mathrm{i}\delta}$ and hence the far field pressure was behaving as a constant in modulus $\sim r^{-\mathrm{i}\delta}$ (6.24).

7.3.3 Far field of inner solution p – inside shear layer

In order to have an estimate of the far field radiated pressure, we need the asymptotic evaluation of the pressure integral (7.21) in the limit $k \to 0$ because small k in Fourier space relates to large $r = \sqrt{x^2+y^2} \sim \infty$ in the physical plane.

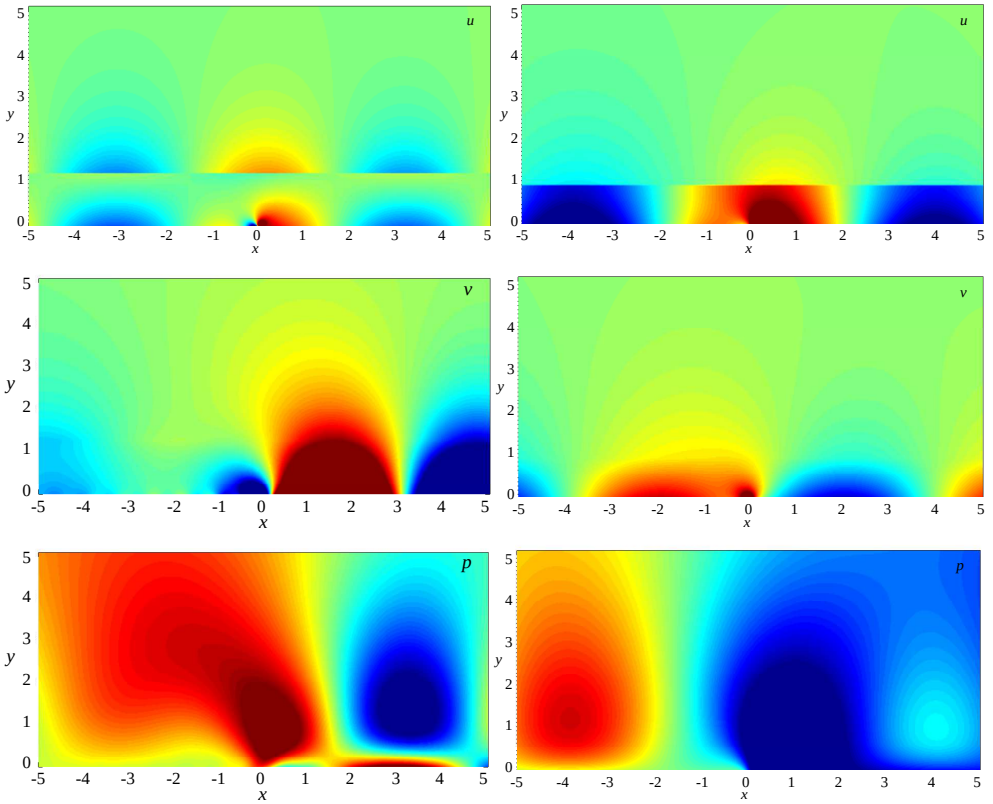

Figure 7.5: The solution fields u, v and p for low shear $\sigma = 4 < \omega = 5$, $y_0 = 1.25$ (left) and high shear $\sigma = 5 > \omega = 4$, $y_0 = 1$ (right), while $\zeta = \frac{1}{2}(1+\mathrm{i}), U_0 = 5$.

(a) Low shear, $\sigma < \omega$:

From (7.21) and (7.22), we have in the limit $k \to 0$,

$$\begin{aligned}\overline{p}(x,y)_{\sigma<\omega} &\sim \overline{p}_{\text{inner}\,(\sigma<\omega)} \\ &\simeq -\frac{1}{2\pi}\mathrm{i}(\lambda+1)\rho_0 U_0 \frac{\mathrm{e}^{-k_0 y_0}}{K_-(k_0)}\frac{1}{-k_0}\left[c_1\frac{\omega+\sigma}{a+b}\int_{-\infty}^{0}\frac{\mathrm{e}^{-\mathrm{i}kx-|k|y}}{|k|k^{-\frac{1}{2}+\mathrm{i}\delta}}\,\mathrm{d}k\right. \\ &\qquad\left. + \frac{\omega-\sigma}{a-b}\int_0^{\infty}\frac{\mathrm{e}^{-\mathrm{i}kx-|k|y}}{|k|k^{-\frac{1}{2}+\mathrm{i}\delta}}\,\mathrm{d}k\right] \\ &= \frac{\zeta c_1}{2\pi}(\lambda+1)\rho U_0\frac{\mathrm{e}^{-k_0 y_0}}{-k_0 K_-(k_0)}\left[(-1)^{(-\frac{1}{2}+\mathrm{i}\delta)}\int_0^{\infty}k^{-\frac{1}{2}-\mathrm{i}\delta}\,\mathrm{e}^{ikz}\,\mathrm{d}k\right.\end{aligned} \tag{7.25}$$

where $z = x + \mathrm{i}y$. The integrals converge, and can be evaluated like

$$\int_0^{\infty}\frac{\mathrm{e}^{ikz}}{k^{\frac{1}{2}+\mathrm{i}\delta}}\,\mathrm{d}k = \frac{\Gamma(\frac{1}{2}-\mathrm{i}\delta)}{(-\mathrm{i}z)^{\frac{1}{2}-\mathrm{i}\delta}}. \tag{7.26}$$

The net innerfield pressure is then given by

$$\overline{p}_{\text{inner}\,(\sigma<\omega)} \simeq \mathrm{i}^{-(\frac{1}{2}-\mathrm{i}\delta)}\Gamma(\tfrac{1}{2}-\mathrm{i}\delta)\frac{\zeta c_1}{2\pi}(\lambda+1)\rho_0 U_0 \frac{\mathrm{e}^{-k_0 y_0}}{-k_0 K_-(k_0)}\left(z^{-\frac{1}{2}+\mathrm{i}\delta} - {z^*}^{-\frac{1}{2}+\mathrm{i}\delta}\right) \tag{7.27}$$

with $z = r\,\mathrm{e}^{\mathrm{i}\theta}$ and $z^* = r\,\mathrm{e}^{-\mathrm{i}\theta}$. The pressure decays as $r^{-\frac{1}{2}}$, which thus limits its effective acoustic source strength.

(b) High shear, $\sigma > \omega$:

The singularity in this case is stronger than the one in the previous case, which enables us to assess that the radiated pressure $\overline{p}_{\text{inner}\,(\sigma>\omega)}$ field must be stronger. The asymptotic behaviour of the integral (7.21) at $k \to 0$ is essentially the singularity taken out from the integral in (7.23). Hence the outer limit $r \to \infty$ of the inner pressure field $\overline{p}$ (with $z = r\,\mathrm{e}^{\mathrm{i}\theta}$) is given by (7.24) as:

$$\overline{p}_{\text{inner}\,(\sigma>\omega)} \simeq \mathrm{i}^{(\mathrm{i}\delta)}\Gamma(-\mathrm{i}\delta)\frac{\zeta c_1}{2\pi}(\lambda+1)\rho_0 U_0 \frac{\mathrm{e}^{-k_0 y_0}}{-k_0 K_-(k_0)}\left(z^{\mathrm{i}\delta} - {z^*}^{\mathrm{i}\delta}\right). \tag{7.28}$$

An important difference is that the modulus of the pressure field varies with r like $|r^{-\mathrm{i}\delta}| = 1$, *i.e.* remains constant rather than decaying, and is therefore much stronger than in the previous case. Physically, it means that there is a strong interaction between the edge and the interphase. In case of low shear, this interaction is weak so that the reflected waves have small order of magnitude compared to the transmitted waves. But in the case of high shear, this interaction is strong hence the acoustic energy is contained in the boundary layer. Hence we conclude that an infinite linear shear profile model is an inconsistent modelling assumption for high shear case.

The above far field limit is taken inside the uniform shear flow, which means that we have a diverging mean flow velocity $U = \sigma y \to \infty$ as $y \to \infty$ which is not very physical. Although both (7.27) and (7.28) *do* satisfy the prevailing equations, we have to make sure that no unphysical artefacts are created. So we curtail the shear at height h and define the mean flow being a constant U_∞ beyond $y > h$. This is explained in the next section.

7.3.4 Far field of pressure release wall solution - inside shear layer

The solution set (7.21) is valid for the pressure release wall case as well and the integrals in (7.21) can be analytically evaluated like in C.5. Once the analytic evaluation is done, we can take the far field limit $z \to \infty$ as in C.6 and obtain the outer limit.

Low shear case

Substituting (E.6) into (7.21) coupled with the contour integral C.5 and far field limit C.6, we obtain the low shear case solution continuous across $x = 0$

$$\begin{aligned}
\overline{u} \sim\ & (\lambda+1)\frac{U_0}{2\pi}\,\mathrm{e}^{-k_0 y_0-\frac{1}{4}\pi\mathrm{i}}\,\Gamma(\tfrac{3}{2}-\mathrm{i}\delta)\Big(\frac{\omega-\sigma}{\omega+\sigma}\Big)^{\frac{1}{4}}\Big[(k_0 z)^{-\frac{3}{2}+\mathrm{i}\delta}+(k_0 z^*)^{-\frac{3}{2}+\mathrm{i}\delta}\Big],\\
\overline{v} \sim\ & \mathrm{i}(\lambda+1)\frac{U_0}{2\pi}\,\mathrm{e}^{-k_0 y_0-\frac{1}{4}\pi\mathrm{i}}\,\Gamma(\tfrac{3}{2}-\mathrm{i}\delta)\Big(\frac{\omega-\sigma}{\omega+\sigma}\Big)^{\frac{1}{4}}\Big[(k_0 z)^{-\frac{3}{2}+\mathrm{i}\delta}-(k_0 z^*)^{-\frac{3}{2}+\mathrm{i}\delta}\Big],\\
\overline{p} \sim & \mathrm{i}(\lambda+1)\frac{\rho_0 U_0^2}{2\pi\omega}\,\mathrm{e}^{-k_0 y_0-\frac{1}{4}\pi\mathrm{i}}\,\Gamma(\tfrac{1}{2}-\mathrm{i}\delta)\Big(\frac{\omega-\sigma}{\omega+\sigma}\Big)^{\frac{1}{4}}\Big[(\omega+\sigma)(k_0 z)^{-\frac{1}{2}+\mathrm{i}\delta}\\
& +(\omega-\sigma)(k_0 z^*)^{-\frac{1}{2}+\mathrm{i}\delta}+\mathrm{i}k_0\sigma y(\tfrac{1}{2}-\mathrm{i}\delta)\Big((k_0 z)^{-\frac{3}{2}+\mathrm{i}\delta}+(k_0 z^*)^{-\frac{3}{2}+\mathrm{i}\delta}\Big)\Big].
\end{aligned} \tag{7.29}$$

Also,

$$\begin{aligned}
\overline{p}(x<0,0)=0 &\Rightarrow p_{\mathrm{in}}(x<0,0)+\overline{p}(x<0,0)=0\\
\overline{v}(x>0,0)=\mathrm{i}(\lambda+1)U_0\,\mathrm{e}^{-k_0 y_0-\mathrm{i}k_0 x} &\Rightarrow v_{\mathrm{in}}(x>0,0)+\overline{v}(x>0,0)=0.
\end{aligned} \tag{7.30}$$

Hence, the *boundary conditions* are satisfied by the solution. The velocities $(\overline{u},\overline{v})$ and pressure $\overline{p}$ decays as $\sim r^{-\frac{3}{2}-\mathrm{i}\delta}$ and $\sim r^{-\frac{1}{2}-\mathrm{i}\delta}$ respectively similar to the finite impedance case. Similar to (5.40), consider the potential function with $(\overline{u},\overline{v})=\nabla\phi$ given by

$$\phi=-(\lambda+1)\frac{U_0^2}{2\pi\omega}\,\mathrm{e}^{-k_0 y_0}\,\mathrm{e}^{-\frac{1}{4}\pi\mathrm{i}}\,\Gamma(\tfrac{1}{2}-\mathrm{i}\delta)\Big(\frac{\omega-\sigma}{\omega+\sigma}\Big)^{\frac{1}{4}}\Big[(k_0 z)^{-\frac{1}{2}+\mathrm{i}\delta}+(k_0 z^*)^{-\frac{1}{2}+\mathrm{i}\delta}\Big]. \tag{7.31}$$

From (5.40) and (7.31), we have

$$\overline{p}=\mathrm{i}(\lambda+1)\frac{\rho_0 U_0^2}{2\pi}\,\mathrm{e}^{-k_0 y_0}\,\mathrm{e}^{-\frac{1}{4}\pi\mathrm{i}}\,\Gamma(\tfrac{1}{2}-\mathrm{i}\delta)\Big(\frac{\omega-\sigma}{\omega+\sigma}\Big)^{\frac{1}{4}}\Big[(k_0 z)^{-\frac{1}{2}+\mathrm{i}\delta}+(k_0 z^*)^{-\frac{1}{2}+\mathrm{i}\delta}\Big], \tag{7.32}$$

which is not exactly same as the $\overline{p}$ in (7.29) because in the far field with uniform flow, the linear velocity profile term σy in (7.29) will disappear and an expression similar to (7.32) is retrieved. The pressure release wall solution satisfies the boundary conditions and is analytically exact. It resembles with the finite impedance solution, (7.27) as well. Hence we conclude that the asymptotic limit $k \to 0$ of (7.21) is most reasonable to obtain the outer limit of the pressure solution and the regularizations so far, are correct.

High shear case

Similar to the previous case, substituting (C.10) into (7.21) coupled with the contour integral C.5 and far field limit C.6, we obtain the high shear case solution continuous across $x = 0$

$$\begin{aligned}
\overline{u} \sim \quad & (\lambda+1)\frac{U_0}{2\pi}\,\mathrm{e}^{-k_0 y_0}\,\Gamma(1-\mathrm{i}\delta)\Big(\frac{\sigma-\omega}{\sigma+\omega}\Big)^{\frac{1}{4}}\Big[(k_0 z)^{-1+\mathrm{i}\delta}+(k_0 z^*)^{-1+\mathrm{i}\delta}\Big],\\
\overline{v} \sim \quad & \mathrm{i}(\lambda+1)\frac{U_0}{2\pi}\,\mathrm{e}^{-k_0 y_0}\,\Gamma(1-\mathrm{i}\delta)\Big(\frac{\sigma-\omega}{\sigma+\omega}\Big)^{\frac{1}{4}}\Big[(k_0 z)^{-1+\mathrm{i}\delta}-(k_0 z^*)^{-1+\mathrm{i}\delta}\Big],\\
\overline{p} \sim & \mathrm{i}(\lambda+1)\frac{\rho_0 U_0^2}{2\pi\omega}\,\mathrm{e}^{-k_0 y_0}\,\Gamma(-\mathrm{i}\delta)\Big(\frac{\sigma-\omega}{\sigma+\omega}\Big)^{\frac{1}{4}}\Big[(\omega+\sigma)(k_0 z)^{\mathrm{i}\delta}\\
& \qquad +(\omega-\sigma)(k_0 z^*)^{\mathrm{i}\delta}+k_0\sigma y\delta\Big((k_0 z)^{-1+\mathrm{i}\delta}+(k_0 z^*)^{-1+\mathrm{i}\delta}\Big)\Big].
\end{aligned} \tag{7.33}$$

Also

$$\begin{aligned}
\overline{p}(x<0,0)=0 &\Rightarrow p_{\mathrm{in}}(x<0,0)+\overline{p}(x<0,0)=0\\
\overline{v}(x>0,0)=\mathrm{i}(\lambda+1)U_0\,\mathrm{e}^{-k_0 y_0-\mathrm{i}k_0 x} &\Rightarrow v_{\mathrm{in}}(x>0,0)+\overline{v}(x>0,0)=0.
\end{aligned} \tag{7.34}$$

Hence, the *boundary conditions* are satisfied by the solution. The velocities $(\overline{u},\overline{v})$ and pressure $\overline{p}$ decays as $\sim r^{-1+\mathrm{i}\delta}$ and $\sim r^{\mathrm{i}\delta}$ respectively, similar to the finite impedance wall. Finally, like the low shear case, we define a potential function and obtain the pressure in the uniform flow region as

$$\phi=-(\lambda+1)\frac{U_0^2}{2\pi\omega}\,\mathrm{e}^{-k_0 y_0}\,\Gamma(-\mathrm{i}\delta)\Big(\frac{\sigma-\omega}{\sigma+\omega}\Big)^{\frac{1}{4}}\Big[(k_0 z)^{\mathrm{i}\delta}+(k_0 z^*)^{\mathrm{i}\delta}\Big] \tag{7.35}$$

$$\overline{p}=\mathrm{i}(\lambda+1)\frac{\rho_0 U_0^2}{2\pi}\,\mathrm{e}^{-k_0 y_0}\,\Gamma(-\mathrm{i}\delta)\Big(\frac{\sigma-\omega}{\sigma+\omega}\Big)^{\frac{1}{4}}\Big[(k_0 z)^{\mathrm{i}\delta}+(k_0 z^*)^{\mathrm{i}\delta}\Big]. \tag{7.36}$$

The expression in (7.36) is similar to the finite impedance solution (7.28) and thus, we conclude that the limit $k \to 0$ in (7.21), in order to know the far field behaviour works precisely and the regularizations of poles and zeros so far, are correct.

7.4 Outer solution and asymptotic matching - (low shear case only)

The outer solution, derived in (6.34) is to be matched with the outer limit of our inner solution (7.27), (7.28), (7.32) and (7.36). This, however is possible only for low shear case, like chapters 5 and 6.

7.4.1 Far field sound - impedance wall

For low shear, $\sigma < \omega$, the asymptotic matching of (6.34) with (7.27) leads to the following expression of ν and B_0, given by

$$\nu = \tfrac{1}{2} - \mathrm{i}\delta, \qquad B_0 = \mathrm{i}^{-\frac{3}{2}+\mathrm{i}\delta}(\lambda+1)\frac{\zeta c_1}{2}\rho_0 U_0 \frac{\mathrm{e}^{-k_0 y_0}}{-k_0 K_-(k_0)}\left(\tfrac{1}{2}\kappa\right)^{\frac{1}{2}-\mathrm{i}\delta}, \tag{7.37}$$

while B_1 and B_2 are given as

$$B_1 = -1 \quad \text{and} \quad B_2 = 1. \tag{7.38}$$

Eventually, the far field sound is given by

$$p(r,\theta) = \mathrm{i}^{-\frac{3}{2}+\mathrm{i}\delta}(\lambda+1)\frac{\zeta c_1}{2}\rho_0 U_0 \frac{\mathrm{e}^{-k_0 y_0}}{-k_0 K_-(k_0)}\left(\tfrac{1}{2}\kappa\right)^{\frac{1}{2}-\mathrm{i}\delta} \times H_\nu^{(2)}(\kappa r)\left(-\mathrm{e}^{\mathrm{i}(\frac{1}{2}-\mathrm{i}\delta)\theta} + \mathrm{e}^{-\mathrm{i}(\frac{1}{2}-\mathrm{i}\delta)\theta}\right). \tag{7.39}$$

Shown in Fig. 7.6 *left* is the far field sound obtained for a typical representative case of low shear. The sound field behaves like $r^{-\frac{1}{2}+\mathrm{i}\delta}$ and is absolutely similar to the hard-soft case except that the δ becomes $-\delta$ now which is the effect of the boundary condition reversal.

7.4.2 Far field sound - pressure release wall

Similar to previous matching, the pressure release wall solution (7.29) can be also matched with (6.34) to obtain $\nu = \frac{1}{2} - \mathrm{i}\delta$, and

$$\begin{aligned} B_0 =& (\lambda+1)\frac{\rho_0 U_0^2}{2}\,\mathrm{e}^{-k_0 y_0 - \frac{1}{4}\pi\mathrm{i}}\left(\frac{\omega-\sigma}{\omega+\sigma}\right)^{\frac{1}{4}}\left(\frac{U_0}{2c_0}\right)^{\nu}, \\ B_1 =& 1 \qquad \text{and} \qquad B_2 = 1, \end{aligned} \tag{7.40}$$

and hence

$$\begin{aligned} \overline{p} &= B_0 H_\nu^{(2)}(\kappa r)\big(B_1\,\mathrm{e}^{\mathrm{i}\nu\theta} + B_2\,\mathrm{e}^{-\mathrm{i}\nu\theta}\big), \\ \overline{w} &= \frac{\mathrm{i}}{\rho_0 c_0} B_0 H_\nu^{(2)\prime}(\kappa r)\big(B_1\,\mathrm{e}^{\mathrm{i}\nu\theta} + B_2\,\mathrm{e}^{-\mathrm{i}\nu\theta}\big), \end{aligned} \tag{7.41}$$

$$H_\nu^{(2)}(\kappa r) \sim \left(\frac{2}{\pi\kappa r}\right)^{\frac{1}{2}} \mathrm{e}^{-\mathrm{i}\kappa r + \frac{1}{2}\mathrm{i}\nu\pi + \frac{1}{4}\mathrm{i}\pi}, \qquad H_\nu^{(2)\prime}(\kappa r) \sim -\mathrm{i}\left(\frac{2}{\pi\kappa r}\right)^{\frac{1}{2}} \mathrm{e}^{-\mathrm{i}\kappa r + \frac{1}{2}\mathrm{i}\nu\pi + \frac{1}{4}\mathrm{i}\pi}, \tag{7.42}$$

we can obtain the time averaged radial acoustic intensity in the far field as

$$\tfrac{1}{2}\,\mathrm{Re}(\overline{p}\;\overline{w}^*) \simeq \frac{(\lambda+1)^2\rho_0}{8\pi c_0^2 \kappa r} U_0^5\,\mathrm{e}^{-2k_0 y_0}\left(\mathrm{e}^{2\delta\theta} + \mathrm{e}^{-2\delta\theta} - 2\cos\theta\right). \tag{7.43}$$

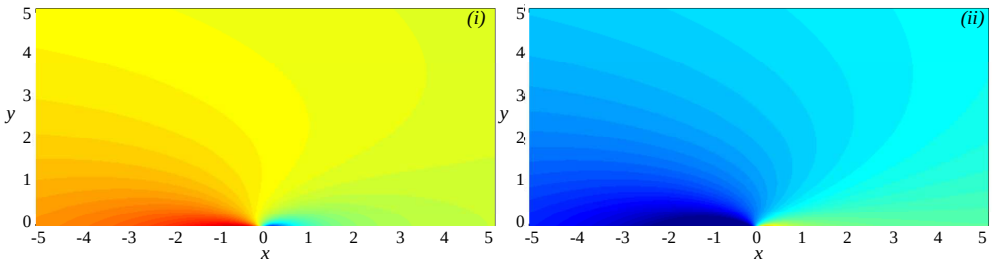

Figure 7.6: Far field sound obtained from (7.39) and (7.41) respectively. $\sigma = 4 < \omega = 5, U_0 = 5, k_0 = 1, y_0 = 1.25$. (i) $\zeta = \frac{1}{2}(1 + \mathrm{i})$, (ii) $\zeta = 0$.

Integrated over $0 < \theta < \pi$ we obtain the interesting expression of the radiated acoustic power

$$\int_0^\pi \tfrac{1}{2}\,\mathrm{Re}(\overline{p}\;\overline{w}^*) r\,\mathrm{d}\theta = \rho_0 c_0^3\, y_0 \Big(\frac{U_0}{c_0}\Big)^4 \frac{\mathrm{e}^{-2\omega/\sigma}}{2\pi\delta} \frac{\omega^2\sigma^2}{(\omega^2-\sigma^2)(\omega+\sigma)^2}, \tag{7.44}$$

to be multiplied by the square of the small dimensionless amplitude of the incident vorticity (7.4). The radiating acoustic power behaves as $\sim U_0^4$. Shown in Fig. 7.6 *right* the the sound field obtained for a typical representative case.

7.5 Conclusions

A systematic and analytically exact solution is obtained by means of the Wiener-Hopf technique of the problem of vorticity, convected by a linearly sheared mean flow, scattered by the soft-hard transition of the wall and the resulting sound field associated to the scattering process. It is illustrated by numerical examples. A particular feature is the fact that the Wiener-Hopf kernel can be split exactly. This enables us to find in rather detail the functional relationship of the hydrodynamic far field and hence the associated acoustic source strength. The far field and resulting sound field are based upon the asymptotic behaviour of the solution in terms of Fourier integrals and the reliability is confirmed by the limiting case $Z = 0$ where the solution is explicit and exact.

Like the hard-soft transition, The problem appears to be distinguished into two different classes, based upon the relative size of problem parameters σ (the mean flow shear U') and ω (the perturbation frequency), and not (for example) of the impedance of the wall. If the mean shear is relatively weak, *i.e.* if $\sigma < \omega$, the hydrodynamic far field varies as the inverse square root of the distance from the hard-soft singularity including U_0^4 relation for radiated acoustic power, consistent to the hard-soft transition, chapter 6. If the mean shear is relatively strong, *i.e.* if $\sigma > \omega$, the hydrodynamic far field tends (in modulus) to a constant which confirms a strong interaction between the edge and the interphase that leads to the linear infinite shear

as an inconsistent modelling assumption.

The functional relationship of the solution of soft - hard transition is similar to the hard - soft transition. The only difference is that the imaginary part of the powers $z^{-\mathrm{i}\delta}$ changes to $z^{\mathrm{i}\delta}$ and same follows for $z^{*\,-\mathrm{i}\delta}$. This evidently results from the boundary condition reversal. Consistent to the hard - soft transition, the high shear case is found to be inconclusive. A more realistic flow boundary layer profile could be useful to model this case.

Chapter 8

Experimental observation of hydrodynamic modes in flow duct with porous lining

So far, we have been investigating the interaction of vorticity with the wall transition from hard to soft or vice versa. Such interaction results in the scattering of the vorticity into acoustic waves which radiate away from the transition point. The soft wall in question was composed of a locally reacting liner that has fixed boundary condition at a point relating the acoustic pressure and velocity.

Acoustically treated ducts with flow are widely used to reduce noise emission. The calculation of the sound propagation in such devices is, however, difficult because of the complexity of the sound and flow interactions. The coupling between acoustics and flow vorticity can be especially important in the vicinity of a treated wall [12]. Very often, in existing models, the flow is simplified and the complexity due to the vortex sound interaction is only taken into account in the Myers condition at the wall [55]. In the case of a perfect fluid with Myers wall condition, it has been shown [73] that the modes in a flow duct can be classified into three different types:

- Infinite set of acoustic waves
- Two surface waves, with and without flow
- Two hydrodynamic surface waves, only with flow.

The first two surface waves exist only for specific values of the wall impedance. When the hydrodynamic surface waves exist, one of these waves is unstable. This instability can exchange energy with the acoustic waves. Over the locally reacting liners, the existence of this instability is studied widely and some mathematical models are made [74, 17] to understand the behaviour of this instability. Such instabilities are observed experimentally as well and their characteristic properties have been isolated

[11]. These experimental investigations demonstrate an increment in the acoustic transmission with flow, only in the vicinity of the liner resonance. The transmission coefficient can become larger than one *i.e.* sound amplification. This effect is associated with a variation of the static pressure drop leading to the possibility of a flow control by the acoustical waves.

In the current chapter, we will study this phenomenon, experimentally, for the case of non locally reacting liners. The mathematical modelling of this behaviour is indeed challenging because unlike the locally reacting liner, the boundary condition at the porous surface is not fixed at a point and the acoustic propagation inside the porous material and inside the duct/channel flow is coupled. We will first report the existence of hydrodynamic instability in case of porous absorbers with grazing flow inside a channel. Then the properties of this wave are extracted with a simple mathematical model.

8.1 Introduction

Porous absorbers are used in many situations to achieve the absorption of sound, e.g. in ventilation ducts, in power plants and in the exhaust systems of cars and trucks. To obtain the largest attenuation of sound in a duct by using an appropriate acoustic treatment is a problem of high practical concern.

A satisfactory understanding of the acoustic behavior of homogeneous porous materials, in term of fluid equivalent models, has been achieved by the current models [43, 8, 7]. The benefits of the porous materials on the sound attenuation can be masked and even destroyed by the presence of a grazing flow. The thin flow boundary layer along the material plays a crucial role as it is involved in the interface condition between the propagation in air and propagation in the porous material. Furthermore, this boundary layer may be unstable in the presence of a lined wall. This effect has been seen on locally-reacting liners [96] and optical measurements have shown that this instability is convective [49].

The current chapter gives the experimental evidence of the existence of a hydrodynamic instability along the porous material triggered by the acoustic waves. The hydrodynamic waves are those that are convected in the flow direction and are nearly incompressible. These waves can be unstable over a liner [73]. The presence of such hydrodynamic waves along a porous material has not been reported previously. This chapter only attends to demonstrate the existence of such waves. Further physical and mathematical investigations are needed to model this phenomena that can have important practical consequences by changing the transmission losses of porous absorbers.

This chapter describes the behavior of a porous material with a rigid frame (metallic foam) under grazing flow. After a short description of the setup (section 8.2), the experimental scattering coefficients in a flow duct are presented (section 8.3) which show that an unstable hydrodynamic mode is present. The accessible characteristics

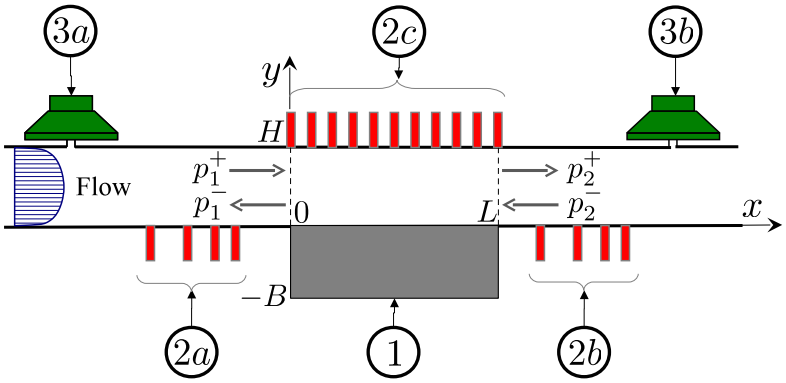

Figure 8.1: Schematic view of the experimental setup. 1: Porous material, 2a: 4 upstream microphones, 2b: 4 downstream microphones, 2c: array of 11 microphones, 3a: Upstream source, 3b: Downstream source.

of this hydrodynamic mode are extracted from the measurement of the scattering matrix (section 8.4). The characteristics are compared to the results of 11 microphones located in front of the porous material in section 8.5. Then the static pressure drop is measured with and without acoustical excitation of the material (section 8.6).

8.2 Set up description

The test facility is schematically depicted in Fig. 8.1. A complete description of this setup and of the used method have been reported previously [96, 71] and hence, only the key points are presented here.

The setup allows acoustic propagation in a rectangular duct (width A= 100 mm $\times$ height H = 15 mm) superimposed to a grazing flow over an acoustic liner. The turbulent flow is assumed to be fully developed in the liner test section. At each end of the duct, acoustic source and anechoic termination are found. According to the duct dimensions and to the position of the microphones (at mid-width), only the plane waves are considered in the rigid parts of the duct for the frequency range of interest (100 Hz to 3000 Hz).

The scattering matrix for the plane waves relates the scattered pressure amplitudes p_2^+ and p_1^- (see Fig. 1) to the incident pressure amplitudes p_1^+ and p_2^- by

$$\begin{pmatrix} p_2^+ \\ p_1^- \end{pmatrix} = \begin{bmatrix} T^+ & R^- \\ R^+ & T^- \end{bmatrix} \begin{pmatrix} p_1^+ \\ p_2^- \end{pmatrix}$$

where T^+ and T^- are the anechoic transmission coefficients, R^+ and R^- are the anechoic reflection coefficients. The superscript '+' refers to an incident wave in the flow direction and the superscript '−' to an incident wave against the flow. The scattering matrix is measured by means of 2×4 flush mounted microphones in the lower

hard wall downstream and upstream of the liner test section, respectively. It follows that the transmitted and reflected waves can be measured with over-determination in order to avoid inaccurate measurements when the acoustic wavelength is close to half the distance between two microphones. The two sources method is applied by conducting two measurements where the upstream and downstream sources are switched on successively.

On the other hand, an array of eleven flush mounted microphones is located in the wall in front of the porous material in order to measure the pressure evolution along the material. These microphones are evenly distributed along the x-axis spaced out by 2 cm. Please note that the presence of these 11 microphones can affect the propagation in the treated region. This effect is supposed to be small and thus, disregarded.

The acquisition of signals is performed by Agilent VXI 1432 hardware platform which drives the source excitation synchronously with the acoustic pressure signals recording. A swept-sine over the frequency range 100–3000 Hz is used with a frequency increment of 5 Hz. The amplitude of the excitation is automatically adapted to give a constant pressure, independently the frequency, on the microphone just in front of the transition hard duct/material (on the upstream side when the upstream source is on and on the downstream side when the downstream source is on).

Experiments were carried out on a metallic foam (RECEMAT, NC4753.05 Nickel-Chromium alloy). This material has been chosen to be as rigid as possible in order to avoid any skeleton vibrations and was supplied as plates ($L = 200\text{mm} \times A = 100\text{mm}$) of thickness 5 mm. Five of these plates have been assembled such that the total thickness of the material is $B = 25$ mm. The parameters of this foam used in the fluid equivalent model have been measured on another setup. The values are: porosity $\Phi = 0.99$, tortuosity $\alpha_\infty = 1.17$, viscous length $\Lambda = 1 \times 10^{-4}$ m, thermal length $\Lambda' = 2.45 \times 10^{-4}$ m, resistivity $\sigma = 6916$ kg m^{-3} s^{-1}. Although, it is not very relevant here, the normal impedance of this porous material sample with a rigid backing is given in Fig.8.2 for a comparison with locally reacting liners. This impedance can be computed using in the fluid equivalent model [7] by $Z_n = -\mathrm{i}(Z_{\mathrm{eq}}(f)/Z_c)/\tan(k_{\mathrm{eq}}(f)B)$ where $Z_{\mathrm{eq}}(f)$ is the equivalent characteristic impedance of the porous material, Z_c is the air characteristic impedance and $k_{\mathrm{eq}}(f)$ is the equivalent wavenumber in the porous material . Z_{eq} and k_{eq} are frequency dependent.

8.3 Experimental results for transmission and reflection coefficients

The experimental results for transmission (T^+ and T^-) and the reflection (R^+ and R^-) coefficients are given in Fig. 8.3 and Fig. 8.4 respectively. T^+ and T^- corresponds to the transmission coefficient for anechoic pipe terminations when the sound source is placed upstream and downstream respectively and same for R^+ and R^-. The curves in red circles represents the results without flow. Due the reciprocity principle

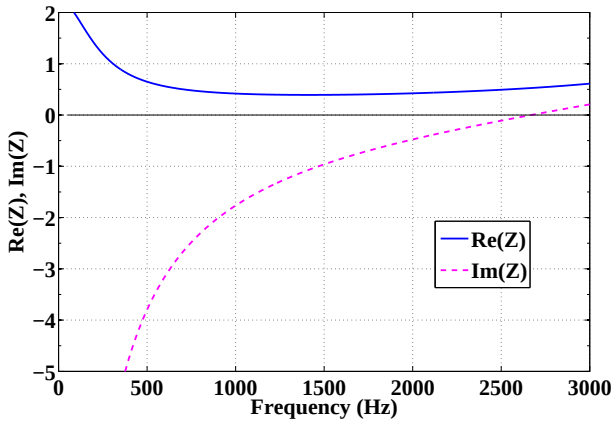

Figure 8.2: Real and imaginary parts of the normal impedance of the porous material (B =25 mm) computed with the fluid equivalent model. The foam parameters are given in the text.

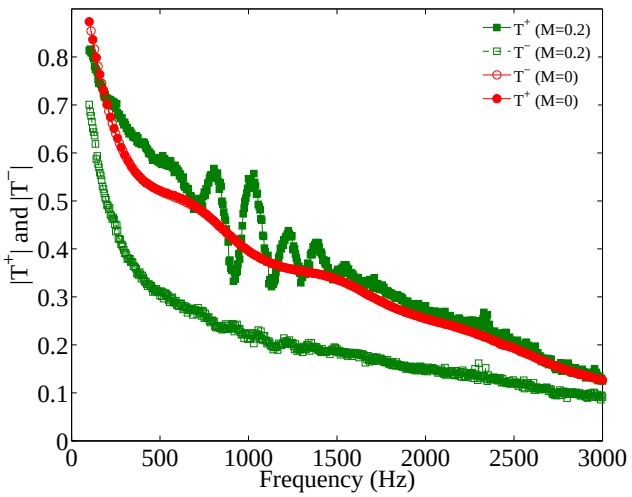

Figure 8.3: Absolute values of the transmission coefficients of the metallic foam sample without flow and for Mach number $M = 0.2$. The source level is 134 dB SPL.

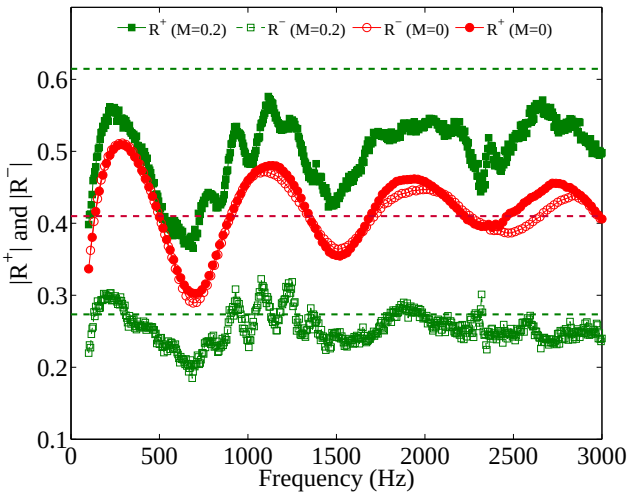

Figure 8.4: Absolute values of the reflection coefficients of the metallic foam sample without flow and for Mach number $M = 0.2$. The dashed lines represent $R_0 = 0.41$, $R_0(1-M)/(1+M)$ and $R_0(1+M)/(1-M)$. The source level is 134 dB SPL.

that exists without flow, the transmission coefficients are equal in both directions. The transmission coefficient for this case without flow decreases smoothly from lowest frequency up to the maximum measured frequency. The reflection coefficient oscillates about a value of $R_0 = 0.41$ which is close to the value $(1-\alpha)/(1+\alpha) = 0.45$, where $\alpha = H/(H+B)$, valid at low frequencies for an area expansion without porous material. The oscillations in the reflection coefficient are linked to the wave reflection at the end of the material ($x = L$).The reflection coefficients without flow are not strictly identical in both direction. The difference (<10%) may be caused by some inhomogeneity of the material proprieties inducing a small breaking of symmetry.

The reflection coefficients for the waves propagating along the flow and against the flow differ significantly. The reflection coefficient against the flow R^- is close to the value $R^- \simeq R_0(1-M)/(1+M)$ where M is the Mach number. The reflection coefficient in the flow direction R^+ is between R_0 and $R_0(1+M)/(1-M)$ (see Fig. 8.4). The transmission coefficients are also different when the direction of wave propagation with respect to direction of flow is changed. Due to convection effects, the wavenumber increases when the wave propagates against the flow and the sound is more attenuated against the flow than in the case without flow. The overall attenuation in the flow direction is of the same order as that in the case without flow. Large oscillations in the frequency range 600-1600 Hz can be observed. It will be shown in the following that these oscillations result from the interference of the acoustic and hydrodynamic waves. The observation of these oscillations is the main result of this chapter and will be studied in detail in the next section.

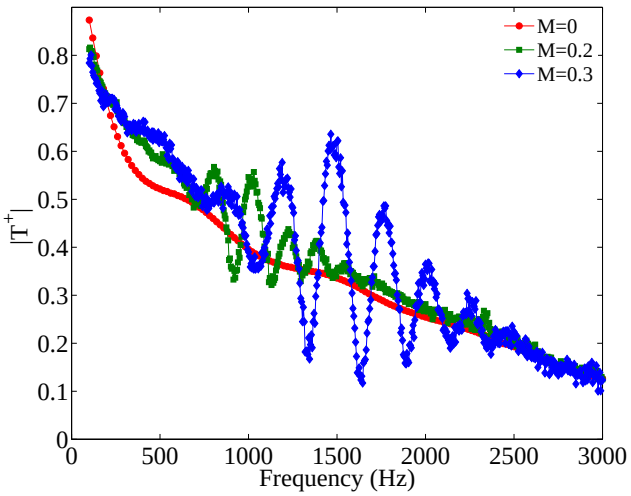

Figure 8.5: Plot of the measured transmission coefficient at different Mach numbers with the source level kept at 134dB SPL.

The measured transmission coefficient T^+ (when the incident sound and the flow are in the same direction) is shown in Fig. 8.5 for two Mach numbers. The amplitude of the oscillations due to the interference of acoustic and hydrodynamic modes is higher for high Mach numbers. It is also interesting to see that the oscillations are prominent only in a certain frequency band which changes depending on the Mach number.

The amplitude of the oscillations changes with the sound source amplitude as well. Shown in Fig. 8.6 is the transmission coefficient T^+ for 3 different upstream source amplitudes keeping the flow Mach number fixed at $M = 0.3$. It can be observed that the amplitude of the oscillations of the absolute value of T^+ increases when the source level decreases. It must be kept in mind that the oscillations in pressure is the product of T^+ and the incident pressure. This value is increasing with the level but a clear saturation of the hydrodynamic effect can be observed.

8.4 Extraction of the hydrodynamic wave characteristics

To fit the transmission coefficient in flow direction T^+, it can be seen as the sum of a contribution due to the "acoustic" transmission T_a^+ and a contribution due to the "hydrodynamic" effects T_h^+. These two contributions propagate at different velocities and the net oscillations in $|T^+|$ can be seen as interference between these two waves. The acoustic contribution is supposed to be smooth and hence, T_a^+ is obtained by a

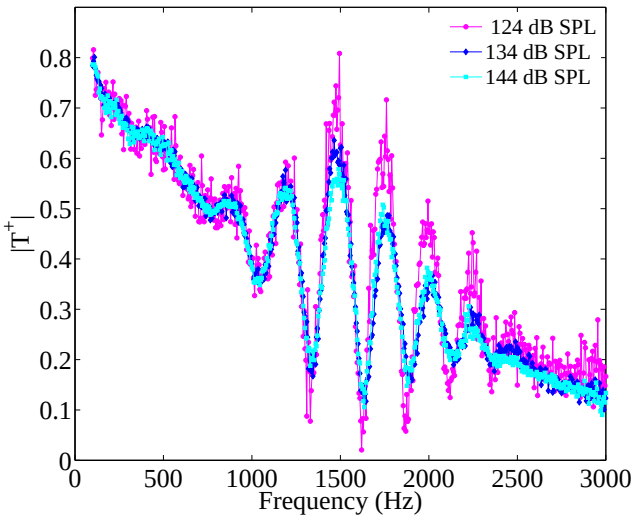

Figure 8.6: Plot of the measured transmission coefficient at different source amplitude with Mach number kept at $M = 0.3$.

fit of T^+ in order to filter the oscillations. To obtain a better fit, T_a^+ is searched under the form $T_a^+ = \mathrm{e}^{-\mathrm{i}k_a L}$ and the value of k_a is approximated by a complex polynomial of degree 7 that fits the data best in a least-square sense. The result of the fit is displayed in 8.7(a). This fit gives good results because the effect of the acoustic wave propagating against the flow is weak. It should be noted that this fit includes all the entrance and exit effects and that k_a is not the wave number of the least attenuated mode for $0 < x < L$. Nevertheless, the real part of k_a is linked to the velocity of the acoustical wave for $0 < x < L$ because the the entrance and exit effects can induce a small phase lag in the transmission coefficient. The equivalent acoustic velocity $c_a = \omega/k_a$ is shown in Fig. 8.7(b). Its value is around the sound velocity in air and takes into account the opposite effects of the convection (increase in the velocity) and of the porous material (slowing of the wave).

The hydrodynamic contribution is obtained by subtracting the acoustic transmission T_a^+ from the total transmission T^+. The amplitude and the phase of the hydrodynamic transmission T_h^+ is given in Fig. 8.8. It can be seen that the hydrodynamic transmission can be sought under the form $T_h^+ = H\mathrm{e}^{-\mathrm{i}(\theta_0+\omega L/c_h)}$ where $\omega = 2\pi f$ is the pulsation, c_h is the velocity of the hydrodynamic wave, θ_0 is the phase lag between the acoustic and the hydrodynamic waves and $H = |T_h^+|$ is the amplitude of the effect of the hydrodynamic wave on the transmission coefficient called for simplicity in the following as "hydrodynamic wave amplitude".

The amplitude of the hydrodynamic transmission $|T_h^+|$ is given in Fig. 8.8(a). It has a significant amplitude value on a limited frequency range (in this case 1000 to 2000

M	0.15	0.2	0.25	0.3
c_h (m/s)	30	35	44	49
f_m (Hz)	770	950	1220	1470
λ_h(mm)	39	37	36	33
f_{PD} (Hz)	1020	1280	1500	1820

Table 8.1: Velocity of the hydrodynamical wave c_h, frequency for maximum amplitude of the hydrodynamic mode f_m, hydrodynamical wave length $\lambda_h = c_h/f_m$ and frequency for maximum increasing of the pressure drop f_{PD} for various Mach numbers.

Hz). A frequency f_m at which the hydrodynamic mode has a maximum amplitude may be identified. This frequency depends on the Mach number but not on the level of the source. Shown in table 8.1 are the obtained values of f_m for different Mach numbers. On the other hand, the amplitude of this maximum depends on the Mach number as well as the source level. Thus, it is linked to the non linear saturation of the hydrodynamic wave.

The angle of the hydrodynamic transmission T_h^+ is given in Fig. 8.8(b). It is supposed that the slope of this angle is directly related to the velocity of the hydrodynamic wave. In Fig. 8.8(b), it can be seen that this velocity can be considered as constant in the frequency range of interest. The angle of T_h^+ is then fitted by a straight line over the frequency range where the amplitude has a significant value. The value of the hydrodynamic wave velocity c_h depends on Mach number but not on the incident sound pressure level (SPL). The value of $M_h = c_h/c_0$, where c_0 is the sound velocity, is given in Fig. 8.9 as a function of the Mach number. It could be seen that the velocity of the hydrodynamic wave is nearly equal to half of the mean flow velocity. It can also be observed that the wavelength of the hydrodynamic perturbation for the maximum amplitude is nearly constant $\lambda_h = c_h/f_m \simeq 35$ mm (see table 8.1). Based on the above results, the following scenario can be imagined to explain the oscillating behavior of the transmission coefficient. An in-

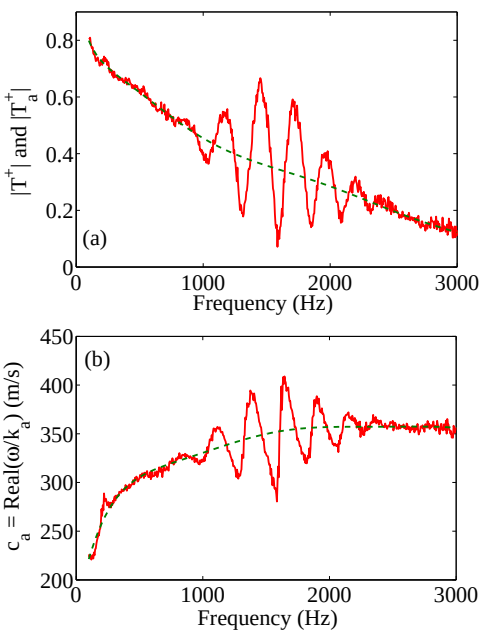

Figure 8.7: (a) Absolute value of T^+ (continuous line) and of the fit T_a^+ (dashed line). (b) Velocity of the acoustic wave computed by $c_a = \mathrm{Re}(\omega/k_a)$ (continuous line) and fit of the velocity (dashed line) ($M = 0.3$ and 134 dB SPL).

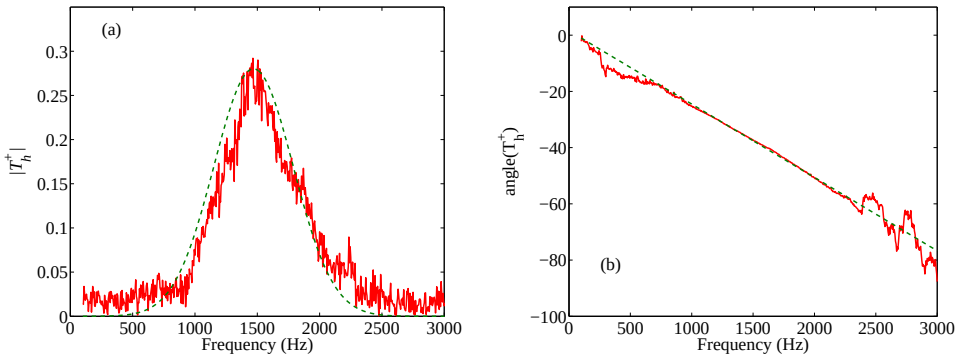

Figure 8.8: (a) absolute value of T_h^+ and (b) angle of T_h^+ (in degrees) as a function of frequency ($M = 0.3$ and 134 dB SPL). The straight line in (b) is the linear approximation used to compute the velocity of the hydrodynamical wave.

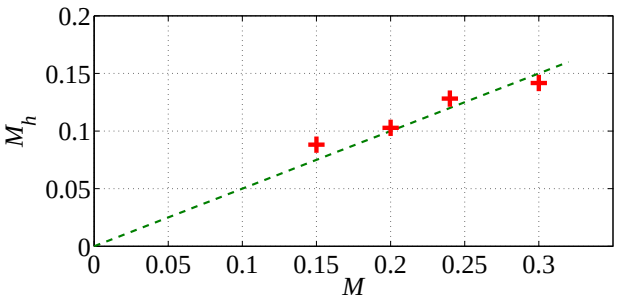

Figure 8.9: Velocity of the hydrodynamical wave $M_h = c_h/c_0$ as a function of flow Mach number M. (134 dB SPL). The straight line corresponds to $M_h = 0.5M_0$

coming acoustic wave from the upstream
side of the porous material triggers a hydrodynamic wave on a limited range of frequencies. The acoustic wave propagates in the flow and in the material while the hydrodynamic wave is convected at half of the flow velocity. During the convection, the hydrodynamic wave is amplified and then its amplitude is saturated by non linear effect. The interference between these two synchronized waves at the downstream side of the porous material induces oscillations in the transmission coefficient.

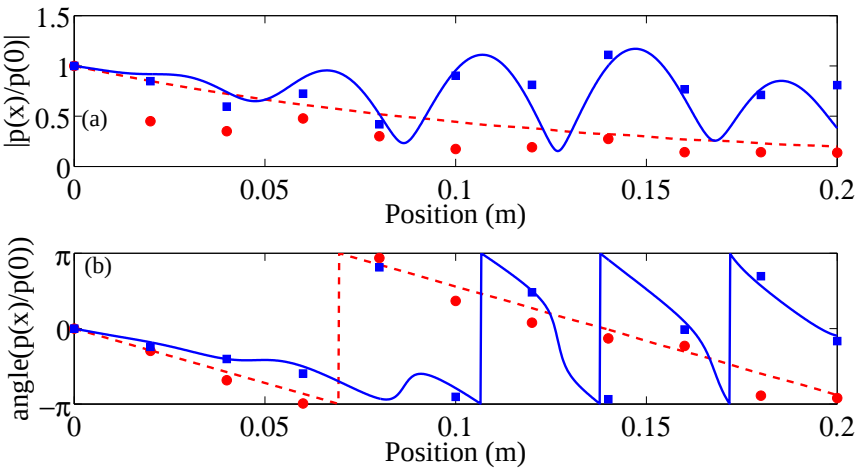

Figure 8.10: Pressure normalized by the pressure at $x = 0$ on the wall opposite to the porous material ($M = 0.3$ and 134dB SPL) given in amplitude (a) and phase (b). $f = 2500$Hz circle: measurements, dashed line: fitted. $f = 1600$Hz, square: measurements, continuous line: fitted.

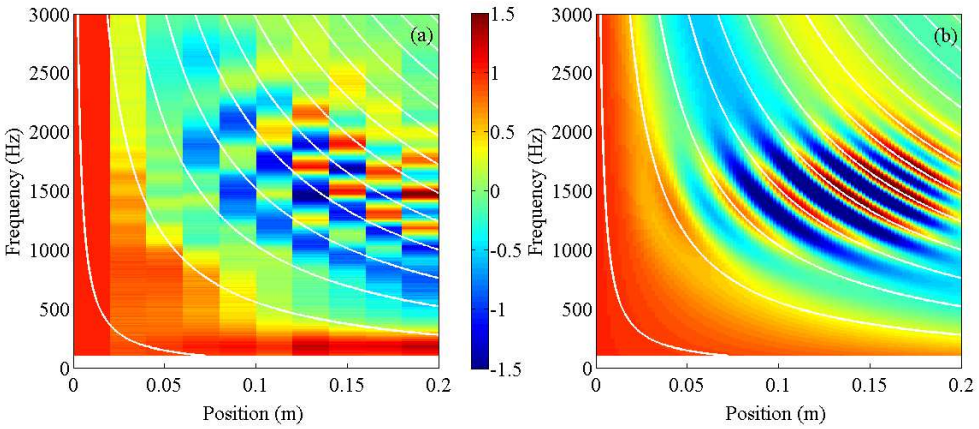

Figure 8.11: Measured (a) and calculated, using the fit (b) pressure in front of the porous material for $M = 0.3$ and 134 dB SPL. The source is located upstream and the effect of the downstream reflection has been removed. The white lines represents the condition: $\omega x/c_h = 2n\pi$.

8.5 Microphone measurements on the wall opposite to the porous material

The transmission coefficient describes in the previous section links the incident plane wave at $x = 0$ to the out-coming plane wave at $x = L$ when the downstream duct is supposed to be anechoic. To gain a deeper insight of what happens between the entrance $x = 0$ and the exit $x = L$ and validate the scenario described previously, the measurements of the array of eleven flush mounted microphones located on the wall opposite to the porous material are used.

Once again, these measurements will be fitted taking into account the above scenario with a minimum of new parameters. The two waves are supposed to travel between $x = 0$ and $x = L$ with a constant velocity. The acoustic velocity is frequency dependent (see Fig. 8.8(b)) and the value used in the following is the previously determined value. To fit the x-dependence of the amplitude of the acoustic wave, it is coherent to use also an exponential behavior $p_a^+(x)/p_1^+ = \mathrm{e}^{-\mathrm{i}k_a x}$. Again, the imaginary part of k_a is the previously determined value. Then the x-dependence of the acoustic part is supposed to be completely determined by the knowledge obtained from the analysis of T^+.

The hydrodynamic part is supposed to have a phase equal to $\theta_0+\omega L/c_h$ where c_h is the velocity of the hydrodynamic wave, previously determined and θ_0 is the phase lag between acoustic and hydrodynamic waves determined by using the value for $f = 0$ in Fig.8.8(b). The value $\theta_0 = -0.3\pi$ will be used in the following. The only quantity that has not been determined previously is the x-dependence of the amplitude of the hydrodynamic wave. This quantity cannot be described by an exponential behavior because of the non linear saturation. A simple polynomial fitting $h(x) = a(X/L)^2 - (a-1)(X/L)^4$, with $a = 30$ is used.

Accordingly the pressure on the $p(x)$ normalized by the pressure at $x = 0$ is written as:

$$\frac{p(x)}{p(0)} = \mathrm{e}^{-\mathrm{i}k_a x} + Hh(x)\mathrm{e}^{-\mathrm{i}(\theta_0+\omega x/c_h)}, \tag{8.1}$$

where H is the amplitude of the hydrodynamic transmission (Fig 8.8(a)). It should be emphasize that the above expression is not a model of the behavior of the porous liner with grazing flow but just a way to fit and understand the measurements.

A comparison between the measured pressure and the values given by (8.1) is plotted in Fig. 8.10. It can be seen that the agreement is reasonable in phase when the hydrodynamic wave is absent ($f = 2500$ Hz, circle) and it can be easily improved by taking into account the entrance and exit effects and the reflected waves on the material zone. When the hydrodynamic wave is present ($f = 1600$ Hz, square), the spacing between the microphones (20 mm) is too large to give a precise outline of the hydrodynamic wave ($\lambda_h \simeq 35$ mm). Again the phase agreement is reasonable. Nevertheless, the 2D plot in Fig. 8.11 depicting the real part of the pressure as a function of the position and frequency shows that the main tendencies are described by the fit. In particular, the isolines in white in Fig. 8.11, representing the condition

$\omega x/c_h = 2n\pi$, confirm that the hydrodynamic wave is convected with velocity c_h. However, the progressive shifting of the experimental maxima relative to the maxima of the fit suggests that the convection velocity of the hydrodynamic wave is not constant along the material.

8.6 Pressure drop along the porous material

It is known that a convected instability can induced an increase of the static pressure drop along the material [18, 96]. This added dissipation is due to an increment of the turbulent wall shear stress induced by the hydrodynamic wave [49, 78]. ΔP_0 is the static pressure difference between the start and the end of the porous material without any acoustic excitation. For this porous material, ΔP_0 increases quadratically as a function of Mach number. ΔP is the same static pressure difference when the sound source is on. Fig. 8.12(a) shows the increment in pressure drop when the acoustic source is turned on. It has been measured that the pressure drop increment is nearly proportional to the incident wave pressure amplitude above a threshold level of 120 dB SPL. The relative increase is of the order of 20% to 40% irrespective of the Mach number for a source level equal to 134 dB SPL. This increment is much smaller than the one observed in locally reacting liners [96].

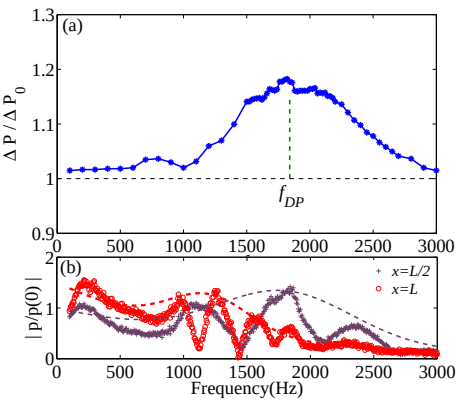

Figure 8.12: (a): Pressure drop with sound ΔP normalized by the pressure drop without sound ΔP_0 as a function of the incident frequency. (b): Absolute value of the normalized pressure on the wall opposite to the porous material for two positions. $M = 0.3$ and 134 dB SPL.

When the pressure drop is plotted against frequency (Fig. 8.12), it is expected that the frequency at which the pressure drop is maximum f_{PD} corresponds to the frequency at which the amplitude of the hydrodynamic wave is maximum f_m. It can be seen in table 8.1 that these frequencies are not equal. A possible explanation of this phenomena is that the frequency range where the the hydrodynamic wave has a large amplitude is bigger for $x \simeq L/2$ than at the end of the material, $x = L$ (see Fig. 8.12(b) and Fig. 8.11(a)). It is unclear, at this point, to decide whether this corresponds to an attenuation of the hydrodynamic wave in the region $L/2 < x < L$ or to a diminution of the pressure induced by the hydrodynamic wave in this region. Further studies with optical measurements (particle image velocimetry or laser Doppler velocimetry) are needed to clarify this point.

It is confirmed by the PIV measurements conducted by [9] that the oscillations of the transmission coefficient are indeed due to the interaction between the instability wave and the acoustic wave at the liner end. The argument that the interaction obeys a wave interference mechanism, quantified by the relative phase of the two waves is also supported.

8.7 Conclusion

The existence of a hydrodynamic wave over a porous material with grazing flow has been demonstrated. Its characteristic properties have been analysed experimentally. This hydrodynamic wave has a significant effect on a limited band of frequencies. When this wave is present, there are large oscillations in the transmission coefficient in the flow direction coming from the interference between the transmitted acoustic wave and this hydrodynamic wave that are propagating at different velocities. The convection velocity of the hydrodynamic wave is close to half of the mean flow speed. It is difficult to claim any firm conclusions about the amplitude of this mode because of the non linear behavior that indicates a saturation of this hydrodynamic wave. The hydrodynamic wave induces an increase of the pressure drop when it is created by an acoustic wave. A peak frequency at which the pressure drop is maximum is identified. Further investigations are needed to model the conditions of appearance, amplification, and saturation of this new kind of hydrodynamic wave.

Chapter 9

Conclusion

In this chapter, we present concluding remarks and formulate some problems that could potentially serve as the beginning of future work.

9.1 Helmholtz resonator type impedance modeling

In Chapter 3, a systematic approximation of the hydrodynamically non linear Helmholtz resonator equation is obtained, including the resulting impedance if the resonator is applied in an acoustic liner. The only unknown parameter that we need to adapt is resistance factor, r, which is $O(1)$. Comparisons with measurements prove that the model predicts the near resonance impedance to a good accuracy. This formulation is useful to predict the impedance of the lining surface accurately, to be used later, in the sound propagation calculations, in numerical simulations. Previous non linear impedance formulations were mainly based upon the CFD calculations and thus, our closed form solution saves plenty of computational time. On the other hand, a closed form solution is useful to understand functional relationship of various parameters that govern the impedance.

The impedance model in Chapter 3 is then refined further, in Chapter 4, to take into account the development of waves inside the resonator cavity that are involved in the damping phenomenon. This way, we capture more physics of the problem and the fidelity of the model is improved. This improvement in the modelling assumptions is clearly reflected by the found impedance formulation. Not only the comparison with measurements improved, but also, the model is able to predict the impedance at higher value of excitation amplitude. Even at 150 dB, the comparison is reasonably accurate. The current and previous (ch. 3) impedance formulations are connected by a low frequency excitation limit and this consistency is reflected in all equations. Apart from this, the current impedance formulation is asymptotically equivalent to the one in Chapter 3 and is more useful than the previous one for more accurate results at higher amplitudes. The N wave problem fits better with the current model because the cavity contains the information about the higher harmonics inside the

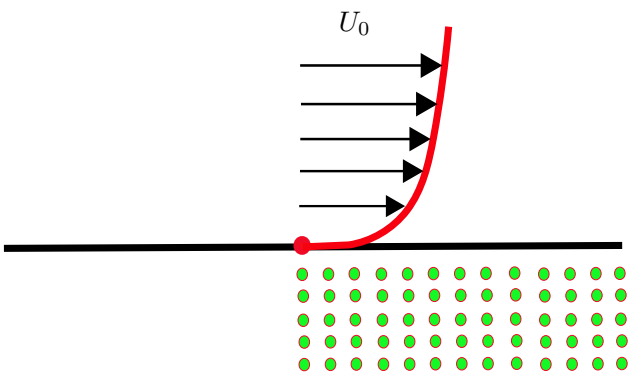

Figure 9.1: Sketch of the problem with a more realistic flow profile

cavity. This could serve as a potential topic for further work.

9.2 Vorticity scattering problem

After studying the Helmholtz resonators in non linear regime, we moved to the study of interaction of vorticity with the lining surface in shear flow, in particular, the interaction at hard wall - soft wall (or vice versa) transition that radiates acoustic waves. This classical problem have been studied previously for uniform flows, in particular, the Wiener Hopf method have been used to get the scattering behaviour in case of bulk absorbing liners under uniform flows [58, 59, 60, 61]. We studied this problem with a linear shear flow profile in incompressible limit and formulated the solution in terms of Fourier integrals. The mathematical complexity of having a shear layer is tackled with the help of the analysis for a pressure release wall, Chapter 5 in case of which, the solution in terms of Fourier integrals is analytically integrable and thus improves the fidelity of involved regularizations. The analysis is further continued to the transitions involving a finite impedance wall, Chapter 6. The solution, although not analytically integrable, allows to obtain the far field limit of the solution integrals. The legitimacy of this limit is verified against the pressure release wall solution and genuine consistency is confirmed. Once the incompressible solution is obtained, we match it with the outer acoustic solution in order to obtain the far field sound.

Based upon the problem parameters ω and σ which represents the frequency of the incoming wake and mean shear rate U', the problem degenerates into mainly two cases. If the mean shear is relatively weak ($\sigma < \omega$), the hydrodynamic far field varies as the inverse square root of the distance from the hard-soft edge. The radiated acoustic power is found to vary with U_0^4 where U_0 is the mean flow velocity at the source position. If the mean shear is relatively strong ($\sigma > \omega$), two features are striking. (i) The hydrodynamic far field tends (in modulus) to a constant, that

implies a strong back reaction to the wall from any uniform or otherwise bounded part of the mean flow, and (ii) the hydrodynamic field can not be matched to an outward radiating acoustic outer field. This impossible matching and the strong back reaction to the wall, leads to the conclusion that the unbounded linear mean shear flow is an inconsistent modeling assumption in the case of high shear. A more realistic flow profile could give further insight in this problem, but this will inevitably rely more on the numerical calculations. Another approach can be based upon using a piecewise linear shear profile if the Wiener-Hopf kernel doesnt become too formidable.

As shown in Fig. 9.1, a more realistic flow profile, something of the type

$$U = U_\infty \tanh(y/L), \qquad U_\infty \ll c_0, \tag{9.1}$$

would connect the edge smoothly to the mean flow velocity U_∞ at a height about $y \sim L$, while $\sigma = U_\infty/L$ and can be superimposed over a vortex sheet at height $y_0 \ll L$. In such modeling, the solution of LEE will not be so straight forward in the closed form, however, the numerical solution can be useful to some extent. This could be a potential point to start investigating the anomalous behavior of the high shear case.

In Chapter 7, we conducted the above analysis for the soft to hard transition of the wall and found that the scattering behavior remains the same. Thus we conclude that the boundary condition reversal does not greatly affect the scattering process. The resulting soundfield for low shear case behaves similar to the previous case and the high shear case still remains inconclusive.

9.3 Experimental observation of hydrodynamic wave over porous surface

In Chapter 8, we studied experimentally, the existence of a hydrodynamic wave over a porous wall with grazing flow at various Mach numbers and extracted some interesting properties of this instability with a crude model. This hydrodynamic wave is found to have a significant effect on a limited range of sound frequencies. When this wave is present, there are large oscillations in the transmission coefficient in the flow direction resulting from the interference between the transmitted acoustic wave and this hydrodynamic wave that are propagating at different velocities. The convection velocity of the hydrodynamic wave is found to be close to half of the mean flow speed.

It is difficult to claim any firm conclusions about the amplitude decay of this mode because of the non linear behavior that indicates a saturation of this hydrodynamic wave. Also this wave induces an increment of the pressure drop when it is created by an acoustic wave. A peak frequency at which the pressure drop is maximum is identified which is not equal to the frequency at which the amplitude of the hydrodynamic wave is maximum. Studies with optical measurements (particle image velocimetry or laser Doppler velocimetry) are needed to clarify this point. Further investigations are

needed to model the conditions of appearance, amplification, and saturation of this wave.

It is confirmed by the PIV measurements conducted by [9] that the oscillations of the transmission coefficient are indeed due to the interaction between the instability wave and the acoustic wave at the liner end. The argument that the interaction obeys a wave interference mechanism, quantified by the relative phase of the two waves is also supported.

Appendix A

Appendix to Chapter 3

A.1 Stability of stationary solution

From the physical origin of the problem, it is very likely that there exists a stable steady solution for a steady external forcing, such that we are not approximating a solution that just would not exist in any realisation. We have checked this mathematically by proving the boundedness of a small perturbation ξ of our solution y in (3.13), satisfying the following equation

$$(y'' + \xi'') + \varepsilon(y' + \xi')|y' + \xi'| + \varepsilon r(y' + \xi') + (y + \xi) = \varepsilon F(\tau). \tag{A.1}$$

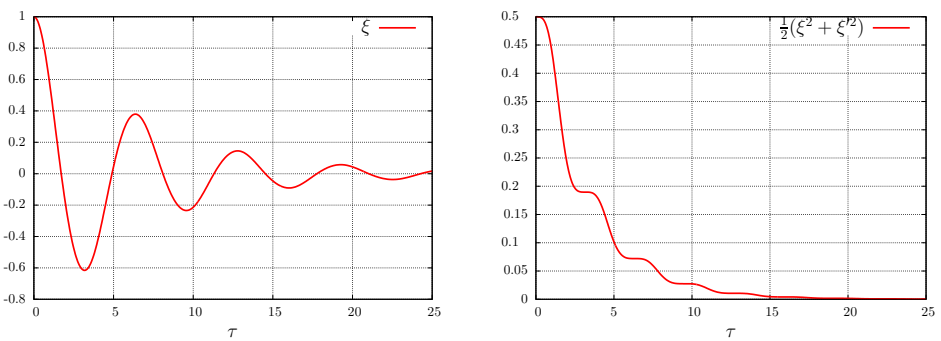

Figure A.1: Amplitude ξ and mechanical energy $\frac{1}{2}(\xi^2 + \xi'^2)$ of a superimposed perturbation when it starts from $\xi(0) = 1 \quad \xi'(0) = 0$. The full solution was approximated by $y = A_0 \cos(\Omega\tau)$ with $\varepsilon = 0.16$, $\Omega = 1$ and $r = 0.2$.

Since, by assumption, y is any solution of the original equation, we have to linear order for small ξ (and a slight error near the zero's of $y' + \xi'$)

$$\xi'' + \phi(\tau)\xi' + \xi = 0 \tag{A.2}$$

where $\phi(\tau) = \varepsilon(r + 2|y'|) \geqslant 0$ (even strictly positive if $r > 0$). We assume an initial condition with $\xi(0)^2 + \xi'(0)^2 = E_0^2$. From (A.2) we have for the mechanical energy $\frac{1}{2}(\xi^2 + \xi'^2)$

$$\frac{\mathrm{d}}{\mathrm{d}\tau}\left(\tfrac{1}{2}(\xi^2 + \xi'^2)\right) = \xi'\xi'' + \xi'\xi = -\phi\xi'^2 \leqslant -\phi(\xi^2 + \xi'^2).$$

It follows that $\frac{\mathrm{d}}{\mathrm{d}\tau}\ln(\xi^2 + \xi'^2) \leqslant -2\phi$. After integration and using the positivity of ϕ we find eventually

$$\xi^2 + \xi'^2 \leqslant E_0^2 \exp\left(-2\int_0^\tau \phi(\tau)\,\mathrm{d}\tau\right).$$

Hence it follows that perturbations are bounded and will decay to zero, confirming the existence of a stable stationary solution. Shown in Fig. A.1 is a plot of ξ and $\frac{1}{2}(\xi^2 + \xi'^2)$.

Appendix B

Appendix to Chapter 4

B.1 Solution of homogeneous problem

Consider the homogeneous equation

$$\begin{aligned} \frac{\mathrm{d}v}{\mathrm{d}\tau} - y &= 0 \\ \phi(\tau - \kappa_0) + \phi(\tau + \kappa_0) &= y(\tau) \\ \phi(\tau - \kappa_0) - \phi(\tau + \kappa_0) &= \tan\kappa_0 v(\tau). \end{aligned} \tag{B.1}$$

Assume for the homogeneous problem the trial solutions

$$y = A\,\mathrm{e}^{\mathrm{i}\lambda\tau}, \quad v = B\,\mathrm{e}^{\mathrm{i}\lambda\tau}, \quad \phi = C\,\mathrm{e}^{\mathrm{i}\lambda\tau}\,. \tag{B.2}$$

Substituting (B.2) back into (B.1), we find

$$2C\cos(\lambda\kappa_0) = A = \mathrm{i}\lambda B, \quad -2\mathrm{i}C\sin(\lambda\kappa_0) = \tan\kappa_0 B, \tag{B.3}$$

leading to

$$\lambda\tan(\lambda\kappa_0) = \tan\kappa_0. \tag{B.4}$$

All solutions of (B.4) come in pairs. If λ is solution then $-\lambda$ is also a solution. However from (4.15), we notice that for a positive ω_0, $\kappa_0 >$ and since product $\kappa_0\tan\kappa_0 = LS_n/\ell S_b$ is a positive constant, $\tan\kappa_0 < 0$ does not occur. For $\tan\kappa_0 > 0$, λ is given as

$$\lambda_1 = 1, \quad \lambda_2, \quad \lambda_3, \ldots. \tag{B.5}$$

For example: if $\kappa_0 = \frac{1}{4}\pi$ and $\tan\kappa_0 = 1$, then

$$\lambda_1 = 1, \quad \lambda_2 = 4.291488, \quad \lambda_3 = 8.1553478 \quad \text{etc.} \tag{B.6}$$

So the general solution for $\tan\kappa_0 > 0$ is [1]

$$y = a_1\cos\tau + b_1\sin\tau + \sum_{n=2}^{\infty} a_n\cos(\lambda_n\tau) + b_n\sin(\lambda_n\tau).$$

B.2 Solution of inhomogeneous problem

Assume for the inhomogeneous problem

$$\begin{aligned} \frac{\mathrm{d}v}{\mathrm{d}\tau} &= y + \mathrm{e}^{\mathrm{i}\Omega\tau} \\ \phi(\tau-\kappa_0) + \phi(\tau+\kappa_0) &= y(\tau) \\ \phi(\tau-\kappa_0) - \phi(\tau+\kappa_0) &= \tan\kappa_0 v(\tau), \end{aligned} \tag{B.7}$$

the trial solution

$$y = A\,\mathrm{e}^{\mathrm{i}\Omega\tau}, \quad v = B\,\mathrm{e}^{\mathrm{i}\Omega\tau}, \quad \phi = C\,\mathrm{e}^{\mathrm{i}\Omega\tau}\,. \tag{B.8}$$

Solving (B.7) with (B.8), we find

$$\begin{aligned} A &= \frac{\tan\kappa_0}{\Omega\tan(\Omega\kappa_0) - \tan\kappa_0}, \\ B &= \frac{-\mathrm{i}\tan(\Omega\kappa_0)}{\Omega\tan(\Omega\kappa_0) - \tan\kappa_0}, \\ C &= \frac{\tan\kappa_0}{2\cos(\Omega\kappa_0)} \cdot \frac{1}{\Omega\tan(\Omega\kappa_0) - \tan\kappa_0}. \end{aligned} \tag{B.9}$$

From here we can construct solutions for inhomogeneous terms $\cos(\Omega\tau)$ and $\sin(\Omega\tau)$ by taking the real or imaginary part of the solution (B.8) respectively. At resonance, when $\Omega\tan(\Omega\kappa_0) - \tan\kappa_0 = 0$, we take the trial solution

$$\begin{gathered} y = A\tau\,\mathrm{e}^{\mathrm{i}\Omega\tau}, \quad v = B\tau\,\mathrm{e}^{\mathrm{i}\Omega\tau}, \quad \phi = C\tau\,\mathrm{e}^{\mathrm{i}\Omega\tau} \\ \text{hence} \quad A = \frac{1}{\mathrm{i}\Omega}, \quad B = 1, \quad C = \frac{1}{\mathrm{i}\Omega\cos(\Omega\kappa_0)}. \end{gathered} \tag{B.10}$$

[1] Although it is not relevant here, if $\tan\kappa_0 < 0$, λ is given by

$$\lambda_0 = \mathrm{i}\mu_0, \quad \mu_0\tanh(\mu_0\kappa_0) = -\tan\kappa_0, \quad \lambda_1 = 1, \quad \lambda_2, \ldots.$$

For example, if $\kappa_0 = \frac{3}{4}\pi$ and $\tan\kappa_0 = -1$,

$$\lambda_0 = \mathrm{i}1.016743, \quad \lambda_1 = 1, \quad \lambda_2 = 2.505496, \quad \lambda_3 = 3.893295, \quad \lambda_4 = 5.253502 \ \text{ etc.}$$

So for $\tan\kappa_0 < 0$, with the presence of diverging exponential terms,

$$y = a_0\,\mathrm{e}^{\mu_0\tau} + b_0\,\mathrm{e}^{-\mu_0\tau} + a_1\cos\tau + b_1\sin\tau + \sum_{n=2}^{\infty} a_n\cos(\lambda_n\tau) + b_n\sin(\lambda_n\tau).$$

The diverging exponential terms in the solution (1) corresponds to the instability of mass - spring system when the mass is negative so that at an applied (or no) force, there is infinite displacement.

From (B.10), we see that the solution grows with time and secular terms appear.

B.3 Order ε^2 equation

Using (4.33), (4.34), (4.38), (4.39) and (4.40) with (4.42), we obtain

$$
\begin{aligned}
&\frac{1}{\tan\kappa_0}\left[\tilde{\phi}_2'(\tilde{\tau}-\kappa_0)-\tilde{\phi}_2'(\tilde{\tau}+\kappa_0)\right]-\left[\tilde{\phi}_2(\tilde{\tau}-\kappa_0)+\tilde{\phi}_2(\tilde{\tau}+\kappa_0)\right]= \\
&\quad -\frac{(\sigma\kappa_0)^2}{2}A_0\cos\kappa_0\cos\tilde{\tau}+\frac{(\sigma\kappa_0)^2}{2\tan\kappa_0}A_0\sin\kappa_0\cos\tilde{\tau} \\
&\qquad -\sigma\kappa_0 A_1\sin\kappa_0\cos\tilde{\tau}-\sigma\kappa_0 B_1\sin\kappa_0\sin\tilde{\tau} \\
&\quad -\sigma\kappa_0\frac{A_0^2\cos^2\kappa_0\tan\kappa_0}{2\pi}\times \\
&\qquad \sum_{n=1}^{\infty}\frac{2(2n+1)\sin(2n+1)\kappa_0\sin(2n+1)\tilde{\tau}}{\cos((2n+1)\kappa_0)\left[(2n+1)\tan(2n+1)\kappa_0-\tan\kappa_0\right](n^2-\frac{1}{4})(n+\frac{3}{2})} \\
&\quad -\frac{\sigma\kappa_0}{\tan\kappa_0}A_1\cos\kappa_0\cos\tilde{\tau}-\frac{\sigma\kappa_0}{\tan\kappa_0}B_1\cos\kappa_0\sin\tilde{\tau} \\
&\quad -\sigma\kappa_0\frac{A_0^2\cos^2\kappa_0}{2\pi}\times \\
&\qquad \sum_{n=1}^{\infty}\frac{2(2n+1)^2\cos(2n+1)\kappa_0\sin(2n+1)\tilde{\tau}}{\cos(2n+1)\kappa_0\left[(2n+1)\tan(2n+1)\kappa_0-\tan\kappa_0\right](n^2-\frac{1}{4})(n+\frac{3}{2})} \\
&\quad -rA_1\cos\kappa_0\sin\tilde{\tau}+rB_1\cos\kappa_0\cos\tilde{\tau}-r\sigma\kappa_0 A_0\frac{\cos\kappa_0}{\tan\kappa_0}\sin\tilde{\tau} \\
&\qquad\qquad +r\frac{A_0^2\cos^2\kappa_0}{\pi}\sum_{n=1}^{\infty}\frac{\cos(2n+1)\tilde{\tau}}{\left[(2n+1)-\frac{\tan\kappa_0}{\tan(2n+1)\kappa_0}\right](n^2-\frac{1}{4})(n+\frac{3}{2})} \\
&-\sigma A_1\cos\kappa_0\cos\tilde{\tau}-\sigma B_1\cos\kappa_0\sin\tilde{\tau}-\sigma^2\kappa_0 A_0\frac{\cos\kappa_0}{\tan\kappa_0}\cos\tilde{\tau} \\
&\qquad\qquad -\sigma\frac{A_0^2\cos^2\kappa_0}{\pi}\sum_{n=1}^{\infty}\frac{(2n+1)\sin(2n+1)\tilde{\tau}}{\left[(2n+1)-\frac{\tan\kappa_0}{\tan(2n+1)\kappa_0}\right](n^2-\frac{1}{4})(n+\frac{3}{2})} \\
&+\left[-A_1\cos\kappa_0\sin\tilde{\tau}+B_1\cos\kappa_0\cos\tilde{\tau}-\sigma\kappa_0 A_0\frac{\cos\kappa_0}{\tan\kappa_0}\sin\tilde{\tau}\right]2A_0\cos\kappa_0|\sin\tilde{\tau}| \\
&+\frac{A_0^2\cos^2\kappa_0}{\pi}\sum_{n=1}^{\infty}\frac{\cos(2n+1)\tilde{\tau}}{\left[(2n+1)-\frac{\tan\kappa_0}{\tan(2n+1)\kappa_0}\right](n^2-\frac{1}{4})(n+\frac{3}{2})}2A_0\cos\kappa_0|\sin\tilde{\tau}| \\
&\qquad\qquad +\theta_1\sin\tilde{\tau}\cos\theta_0+\theta_1\cos\tilde{\tau}\sin\theta_0.
\end{aligned}
$$

Appendix C

Appendix to Chapter 5

C.1 Properties of half range Fourier transforms

Wiener-Hopf method is based upon the properties of half range Fourier transforms. A process $p(t)$ that starts at a finite point $t = 0$ and vanishes for $t < 0$ has interesting property [81] that the corresponding Fourier transform

$$\hat{p}(\omega) = \frac{1}{2\pi} \int_0^\infty p(t)\, \mathrm{e}^{-\mathrm{i}\omega t}\, \mathrm{d}t, \tag{C.1}$$

is analytic in the lower half of the complex plane $\mathrm{Im}(\omega) < 0$. This analytic behaviour of $\hat{p}(\omega)$ in the lower half complex plane is a necessary condition on $\hat{p}(\omega)$ for $p(t) = 0$, for all $t < 0$. A sufficient condition can be found in [66]. In order to exemplify above, consider the following Fourier transforms

$$\frac{1}{2\pi} \int_{-\infty}^\infty H(t)\, \mathrm{e}^{-\alpha t}\, \mathrm{e}^{-\mathrm{i}\omega t}\, \mathrm{d}t = \frac{1}{2\pi(\alpha + \mathrm{i}\omega)}, \tag{C.2}$$

$$\frac{1}{2\pi} \int_{-\infty}^\infty \frac{H(t)}{\sqrt{t}}\, \mathrm{e}^{-\alpha t}\, \mathrm{e}^{-\mathrm{i}\omega t}\, \mathrm{d}t = \frac{1}{2\sqrt{\pi}\sqrt{\alpha + \mathrm{i}\omega}}. \tag{C.3}$$

The transformed functions are analytic only in the lower half of the complex plane because of the existence of the pole $\omega = \mathrm{i}\alpha$ and branch cut from $\mathrm{i}\alpha$ upto ∞ that breaks the analyticity of (C.2) and (C.3) respectively in the upper half of the complex plane as shown in Fig. C.1. Conversely, if we inverse Fourier transform, for example (C.2), the term $\mathrm{e}^{\mathrm{i}\omega t}$ vanishes at infinity for $t > 0$ and ω in upper half of the complex plane. This way, the contour can be closed at infinity, taking the contribution of the pole $\mathrm{i}\alpha$, as shown in Fig. C.2. However, for $t < 0$, we have to close the contour from the lower half of the complex plane, as shown in Fig. C.2, and that results with a zero, because

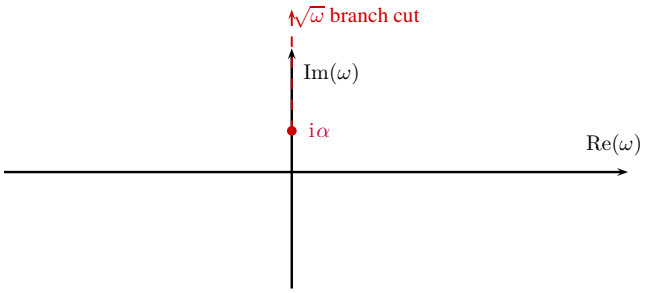

Figure C.1: The pole and branch cut of transformed function in (C.2) and (C.3) respectively.

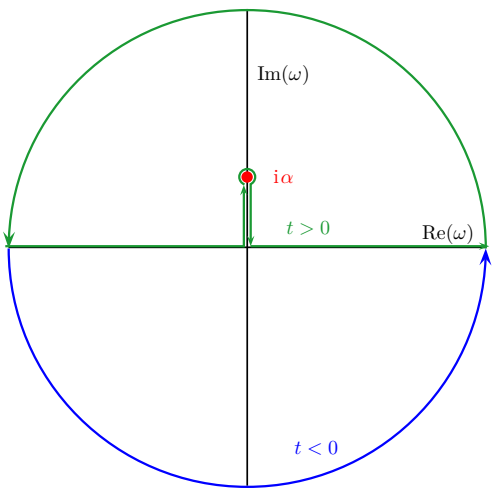

Figure C.2: Closure of the contour for inverse Fourier transform in (C.4).

the function is analytic there.

$$\int_{-\infty}^{\infty} \frac{\mathrm{e}^{\mathrm{i}\omega t}}{2\pi(\alpha + \mathrm{i}\omega)}\,\mathrm{d}\omega = \begin{cases} (t > 0): & \mathrm{e}^{-\alpha t}, \\ (t < 0): & 0. \end{cases} \tag{C.4}$$

This way, we verify that a function which is analytic in the lower half of the complex plane could vanish for $t < 0$.

So, if we have 2 function $F(t)$ and $G(t)$ that vanish for $t < 0$ and $t > 0$ respectively, their corresponding half range Fourier transforms are analytic in the lower and upper half of the complex ω plane respectively. If we define a finite strip about $Re(\omega)$ axis where both the function are same, then they are each other's analytic continuation and form an entire function.

C.2 Behaviour near the edge

In this section, we study the behaviour of the flow variables (u, v, p) close to the edge $z = 0$ in order to understand the difference in the high shear and low shear cases. The only solutions of the form $r^\alpha f(\theta)$, and the behaviour near the edge of our solution, is

$$\begin{aligned}
u(x,y) &= Az^{\alpha-1} + Bz^{*\beta-1} = Ar^{\alpha-1}\,\mathrm{e}^{\mathrm{i}(\alpha-1)\theta} + Br^{\beta-1}\,\mathrm{e}^{-\mathrm{i}(\beta-1)\theta}\\
v(x,y) &= \mathrm{i}Az^{\alpha-1} - \mathrm{i}Bz^{*\beta-1} = \mathrm{i}Ar^{\alpha-1}\,\mathrm{e}^{\mathrm{i}(\alpha-1)\theta} - \mathrm{i}Br^{\beta-1}\,\mathrm{e}^{-\mathrm{i}(\beta-1)\theta}\\
p(x,y) &= -\mathrm{i}\rho_0\left[\frac{\omega+\sigma}{\alpha}Az^\alpha + \frac{\omega-\sigma}{\beta}Bz^{*\beta} - \mathrm{i}\sigma y\big(Az^{\alpha-1} + Bz^{*\beta-1}\big)\right]\\
&= -\mathrm{i}\rho_0\left[Ar^\alpha\,\mathrm{e}^{\mathrm{i}\alpha\theta}\Big(\frac{\omega+\sigma}{\alpha} - \tfrac{1}{2}\sigma + \tfrac{1}{2}\sigma\,\mathrm{e}^{-2\mathrm{i}\theta}\Big)\right.\\
&\qquad\left. + Br^\beta\,\mathrm{e}^{-\mathrm{i}\beta\theta}\Big(\frac{\omega-\sigma}{\beta} + \tfrac{1}{2}\sigma - \tfrac{1}{2}\sigma\,\mathrm{e}^{2\mathrm{i}\theta}\Big)\right].
\end{aligned}$$

In order to satisfy the boundary conditions we choose $\alpha = \beta$. We have the following behaviour for $y = 0$, $x < 0$, *i.e.* $\theta = \pi$

$$\begin{aligned}
u(x,0) &= -r^{\alpha-1}(A\,\mathrm{e}^{\mathrm{i}\alpha\pi} + B\,\mathrm{e}^{-\mathrm{i}\alpha\pi})\\
v(x,0) &= -\mathrm{i}r^{\alpha-1}(A\,\mathrm{e}^{\mathrm{i}\alpha\pi} - B\,\mathrm{e}^{-\mathrm{i}\alpha\pi})\\
p(x,0) &= -\mathrm{i}\frac{\rho_0}{\alpha}r^\alpha\big[(\omega+\sigma)A\,\mathrm{e}^{\mathrm{i}\alpha\pi} + (\omega-\sigma)B\,\mathrm{e}^{-\mathrm{i}\alpha\pi}\big].
\end{aligned}$$

In order to have $v(x,0) = 0$ for $x < 0$ we choose

$$A = A_0\,\mathrm{e}^{-\mathrm{i}\alpha\pi}, \qquad B = A_0\,\mathrm{e}^{\mathrm{i}\alpha\pi}$$

and obtain following behaviour for $y = 0$, $x > 0$, *i.e.* $\theta = 0$

$$\begin{aligned}
u(x,0) &= A_0 r^{\alpha-1}(\mathrm{e}^{-\mathrm{i}\alpha\pi} + \mathrm{e}^{\mathrm{i}\alpha\pi})\\
v(x,0) &= \mathrm{i}A_0 r^{\alpha-1}(\mathrm{e}^{-\mathrm{i}\alpha\pi} - \mathrm{e}^{\mathrm{i}\alpha\pi})\\
p(x,0) &= -\mathrm{i}\frac{\rho_0}{\alpha}A_0 r^\alpha\big[(\omega+\sigma)\,\mathrm{e}^{-\mathrm{i}\alpha\pi} + (\omega-\sigma)\,\mathrm{e}^{\mathrm{i}\alpha\pi}\big].
\end{aligned}$$

To have $p(x,0) = 0$ for $x > 0$ requires

$$(\omega+\sigma)\,\mathrm{e}^{-\mathrm{i}\alpha\pi} + (\omega-\sigma)\,\mathrm{e}^{\mathrm{i}\alpha\pi} = 0.$$

This amounts to

$$\mathrm{e}^{2\pi\mathrm{i}\alpha} = \mathrm{e}^{\pi\mathrm{i}}\,\frac{\omega+\sigma}{\omega-\sigma} = \mathrm{e}^{\pi\mathrm{i}+2\pi\delta}\ \text{(low shear)} \quad \text{or} \quad \mathrm{e}^{2\pi\mathrm{i}\alpha} = \frac{\sigma+\omega}{\sigma-\omega} = \mathrm{e}^{2\pi\delta}\ \text{(high shear)},$$

if we define

$$\delta = \frac{1}{2\pi}\log\Big|\frac{\omega+\sigma}{\omega-\sigma}\Big|.$$

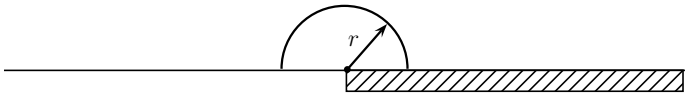

Figure C.3: Energy flux across a small semi-circle of radius r around the singularity.

With low shear we have the following possible solutions for α

$$\alpha = n + \tfrac{1}{2} - \mathrm{i}\delta, \quad n \in \mathbb{Z},$$

and with high shear we have

$$\alpha = n + 1 - \mathrm{i}\delta$$

(where we write $n+1$ instead of n for convenience later). Finally, not any n is possible. Because of a vanishing power output from the edge (also known as the *Bouwkamp-Meixner edge condition* [16, 53])

$$\sim \int_0^\pi \mathrm{Re}(p\ w^*) r \,\mathrm{d}\theta \sim \int_0^\pi r^\alpha r^{(\alpha-1)^*} r \,\mathrm{d}\theta \sim r^{2\,\mathrm{Re}(\alpha)} \to 0 \quad (r \to 0) \tag{C.5}$$

with radial velocity $w = u\cos\theta + v\sin\theta$, we have $\mathrm{Re}(\alpha) > 0$ and so $n \geqslant 0$.

We see that the difference in low and high shear cases arises essentially due to the boundary conditions in relation to the behaviour near the edge.

C.3 Evaluation of the entire function E

Using Liouville's theorem, entire function E can be determined from its behaviour for $k \to \infty$. For this we need the asymptotic behaviour of K_+, $k \to \infty$. From (C.9) and (C.10), we have

$$\lim_{k\to\infty} K_+(k) = 0 \quad \text{or} \quad \text{bounded}. \tag{C.6}$$

The asymptotic behaviour of $G_+(k)$ in the limit $k \to \infty$ is found from the analysis for $r \to 0$ given in Appendix C.2. A pressure distribution p at a small distance r from the discontinuity at $r = 0$ behaves like a power of r, say $p = O(r^\alpha)$. The velocity is then $O(r^{\alpha-1})$. From (C.5) we know that $\mathrm{Re}(\alpha) > 0$. The function $G_+(k)$ from (5.16) is therefore

$$G_+(k \to \infty) \sim \int_0^\infty x^{\alpha-1}\,\mathrm{e}^{\mathrm{i}kx}\,\mathrm{d}x \sim k^{-\alpha}. \tag{C.7}$$

From (5.25), (C.6) and (C.7), we have

$$E(k) = \mathrm{i}\rho_0 G_+(k) K_+(k) + O(1/k) \lesssim k^{-\alpha} + O(1/k) \to 0 \quad (k \to \infty). \tag{C.8}$$

So the function $E(k)$ vanishes at $k \to \infty$. Since it is an entire function, it should vanish everywhere, in other words $E(k) = 0$.

C.4 Evaluation of the split functions

We introduce two complex power functions, one analytic in the upper and the other analytic in the lower half plane, They are defined with branch cuts along the negative, respectively positive, imaginary axis, and equal to its principal branch at the right complex half plane. In order to be as explicit as possible we define the functions via principal value logarithms $\log(\,\cdot\,)$ as follows.

$$(z)_+^a \stackrel{\text{def}}{=} \mathrm{e}^{a\log(-\mathrm{i}z)+\frac{1}{2}\pi\mathrm{i}a}$$
$$(z)_-^a \stackrel{\text{def}}{=} \mathrm{e}^{a\log(\mathrm{i}z)-\frac{1}{2}\pi\mathrm{i}a}$$

This amounts to

$$(z)_+^a = \begin{cases} z^a & \text{if} \quad \operatorname{Re} z > 0, \\ (-z)^a\,\mathrm{e}^{\pi\mathrm{i}a} & \text{if} \quad \operatorname{Re} z < 0, \end{cases}$$
$$(z)_-^a = \begin{cases} z^a & \text{if} \quad \operatorname{Re} z > 0, \\ (-z)^a\,\mathrm{e}^{-\pi\mathrm{i}a} & \text{if} \quad \operatorname{Re} z < 0. \end{cases}$$

Note that we can create a function, discontinuous across the imaginary axis, by the quotient

$$\frac{(z)_+^a}{(z)_-^a} = \begin{cases} 1 & \text{if} \quad \operatorname{Re} z > 0, \\ \mathrm{e}^{2\pi\mathrm{i}a} & \text{if} \quad \operatorname{Re} z < 0. \end{cases}.$$

and

$$\frac{(z)_+^{\frac{1}{2}+a}}{(z)_-^{\frac{1}{2}+a}} = \begin{cases} 1 & \text{if} \quad \operatorname{Re} z > 0, \\ -\,\mathrm{e}^{2\pi\mathrm{i}a} & \text{if} \quad \operatorname{Re} z < 0. \end{cases}.$$

C.4.1 Low-shear case $\sigma < \omega$

Now we rewrite

$$L(k) = \frac{\omega\mu - \sigma k}{k^2+\varepsilon^2} = \mathcal{L}(k,\varepsilon)(\omega-\sigma)(k+\mathrm{i}\varepsilon)_+^{-\frac{1}{2}-\mathrm{i}\delta}(k-\mathrm{i}\varepsilon)_-^{-\frac{1}{2}+\mathrm{i}\delta},$$

where

$$\delta = \frac{1}{2\pi}\log\Big|\frac{\omega+\sigma}{\omega-\sigma}\Big|,$$

Hence we have

$$\mathcal{L}(k,\varepsilon) = \frac{\omega\mu-\sigma k}{\omega-\sigma}(k+\mathrm{i}\varepsilon)_+^{\mathrm{i}\delta-\frac{1}{2}}(k-\mathrm{i}\varepsilon)_-^{-\mathrm{i}\delta-\frac{1}{2}}.$$

It is convenient later to write this in the scaled variable $t = k/\varepsilon$ by $\mathcal{G}(t) = \mathcal{L}(\varepsilon t, \varepsilon)$, such that parameter ε divides out into

$$\mathcal{G}(t) = \frac{\omega\sqrt{t^2+1}-\sigma t}{\omega-\sigma}(t+\mathrm{i})_+^{\mathrm{i}\delta-\frac{1}{2}}(t-\mathrm{i})_-^{-\mathrm{i}\delta-\frac{1}{2}},$$

and G is independent of ε. Note that $\mathcal{G}(t) \to 1$ for $t \to \pm\infty$. More in particular

$$\log \mathcal{G}(t) = \log\Big(1 - \frac{2\delta}{t} + \ldots\Big) = -\frac{2\delta}{t} + \ldots, \qquad t \to \pm\infty.$$

As a result we have (assume $\operatorname{Im} z > 0$) for a $\mathcal{L}_+$ function

$$2\pi\mathrm{i} \log \mathcal{L}_+(z,\varepsilon) = \int_{-\infty}^{\infty} \frac{\log \mathcal{L}(x,\varepsilon)}{x - z}\,\mathrm{d}x = \int_{-\infty}^{\infty} \frac{\log \mathcal{G}(t)}{t - z/\varepsilon}\,\mathrm{d}t$$

For the limit of $\varepsilon \to 0$ we split the integral into

$$\begin{aligned}
&\int_{-\infty}^{-1/\sqrt{\varepsilon}} + \int_{-1/\sqrt{\varepsilon}}^{1/\sqrt{\varepsilon}} + \int_{1/\sqrt{\varepsilon}}^{\infty} \frac{\log \mathcal{G}(t)}{t - z/\varepsilon}\,\mathrm{d}t \simeq \\
&\qquad \int_{-\infty}^{-1/\sqrt{\varepsilon}} \frac{-2\delta}{t(t - z/\varepsilon)}\,\mathrm{d}t + \int_{1/\sqrt{\varepsilon}}^{\infty} \frac{-2\delta}{t(t - z/\varepsilon)}\,\mathrm{d}t - \frac{\varepsilon}{z}\int_{-1/\sqrt{\varepsilon}}^{1/\sqrt{\varepsilon}} \log \mathcal{G}(t)\,\mathrm{d}t \simeq \\
&\qquad\qquad - 4\delta\varepsilon \int_0^{\infty} \frac{1}{x^2 - z^2}\,\mathrm{d}x - \frac{\varepsilon}{z}\int_{-1/\sqrt{\varepsilon}}^{1/\sqrt{\varepsilon}} \log \mathcal{G}(t)\,\mathrm{d}t \to 0
\end{aligned}$$

Since the integral tends to zero we have to conclude that

$$\mathcal{L}_+(z,0) = 1 \quad \text{and} \quad \mathcal{L}_-(z,0) = 1.$$

As a result we have thus for $K = K_+/K_-$ (the limit $\varepsilon \to 0$ of L)

$$K_+(k) = (\omega - \sigma)(k)_+^{-\frac{1}{2} - \mathrm{i}\delta}, \qquad K_-(k) = (k)_-^{\frac{1}{2} - \mathrm{i}\delta}. \tag{C.9}$$

C.4.2 High-shear case $\sigma > \omega$

Now we rewrite

$$L(k) = -\frac{\sigma k - \omega\mu}{k^2 + \varepsilon^2} = -(\sigma - \omega)\mathcal{L}(k,\varepsilon)(k - k_h)(k + \mathrm{i}\varepsilon)_+^{-1-\mathrm{i}\delta}(k - \mathrm{i}\varepsilon)_-^{-1+\mathrm{i}\delta},$$

where $(k - k_h)$ divides out the real zero of L in the strip:

$$k_h = \varepsilon t_0, \quad t_0 = \frac{\omega}{\sqrt{\sigma^2 - \omega^2}}.$$

Hence we have

$$\mathcal{L}(k,\varepsilon) = \frac{\sigma k - \omega\mu}{(\sigma - \omega)(k - k_h)}(k + \mathrm{i}\varepsilon)_+^{\mathrm{i}\delta}(k - \mathrm{i}\varepsilon)_-^{-\mathrm{i}\delta}.$$

It is convenient later to write this in the scaled variable $t = k/\varepsilon$ by $\mathcal{G}(t) = \mathcal{L}(\varepsilon t, \varepsilon)$, such that parameter ε divides out into

$$\mathcal{G}(t) = \frac{\sigma t - \omega\sqrt{t^2+1}}{(\sigma-\omega)(t-t_0)}(t+\mathrm{i})_+^{\mathrm{i}\delta}(t-\mathrm{i})_-^{-\mathrm{i}\delta},$$

and $\mathcal{G}$ is independent of ε. Note that

$$\mathcal{G}(t) \to 1 \qquad \text{for} \quad t \to \pm\infty$$

More in particular we have

$$\log \mathcal{G}(t) = \log\Big(1 + \frac{t_0 - 2\delta}{t} + \dots\Big) = \frac{t_0 - 2\delta}{t} + \dots, \qquad t \to \pm\infty$$

An interesting property is

$$\mathcal{G}(-t) = \frac{1}{\mathcal{G}(t)}.$$

As a result we have (assume $\operatorname{Im} z > 0$) for a $\mathcal{L}_+$ function

$$\begin{aligned}
2\pi\mathrm{i}\log\mathcal{L}_+(z,\varepsilon) &= \int_{-\infty}^{\infty} \frac{\log\mathcal{L}(x,\varepsilon)}{x-z}\,\mathrm{d}x \\
&= \int_{-\infty}^{0} \frac{-\log\mathcal{L}(-x,\varepsilon)}{x-z}\,\mathrm{d}x + \int_0^{\infty} \frac{\log\mathcal{L}(x,\varepsilon)}{x-z}\,\mathrm{d}x \\
&= \int_0^{\infty} \log\mathcal{L}(x,\varepsilon)\Big(\frac{1}{x-z} + \frac{1}{x+z}\Big)\,\mathrm{d}x \\
&= \int_0^{\infty} \log\mathcal{L}(x,\varepsilon)\frac{2x}{x^2-z^2}\,\mathrm{d}x = \int_0^{\infty} \log\mathcal{G}(t)\frac{2t}{t^2-(z/\varepsilon)^2}\,\mathrm{d}t.
\end{aligned}$$

For the limit of $\varepsilon \to 0$ we split the integral into

$$\begin{aligned}
&\int_0^{1/\sqrt{\varepsilon}} \log\mathcal{G}(t)\frac{2t}{t^2-(z/\varepsilon)^2}\,\mathrm{d}t + \int_{1/\sqrt{\varepsilon}}^{\infty} \log\mathcal{G}(t)\frac{2t}{t^2-(z/\varepsilon)^2}\,\mathrm{d}t \simeq \\
&\qquad - \frac{2\varepsilon^2}{z^2}\int_0^{1/\sqrt{\varepsilon}} t\log\mathcal{G}(t)\,\mathrm{d}t + 2(t_0-2\delta)\int_{1/\sqrt{\varepsilon}}^{\infty} \frac{1}{t^2-(z/\varepsilon)^2}\,\mathrm{d}t
\end{aligned}$$

From noting that $t\log\mathcal{G}(t)$ tends to a constant so the first integral is $O(\varepsilon\sqrt{\varepsilon})$, which is smaller than the second of $O(\varepsilon)$, we have

$$\simeq 2(t_0-2\delta)\int_{1/\sqrt{\varepsilon}}^{\infty} \frac{1}{t^2-(z/\varepsilon)^2}\,\mathrm{d}t \simeq 2(t_0-2\delta)\varepsilon\int_0^{\infty} \frac{1}{x^2-z^2}\,\mathrm{d}x = (t_0-2\delta)\varepsilon\frac{\pi\mathrm{i}}{|z|} \to 0.$$

We have to conclude that

$$\mathcal{L}_+(z,0) = 1.$$

This leads to also

$$\mathcal{L}_-(z,0) = 1.$$

As a result we have thus for $K = K_+/K_-$ (the limit $\varepsilon \to 0$ of L)

$$K_+(k) = (\omega-\sigma)k(k)_+^{-1-\mathrm{i}\delta} = (\omega-\sigma)(k)_+^{-\mathrm{i}\delta}, \qquad K_-(k) = (k)_-^{1-\mathrm{i}\delta} \tag{C.10}$$

where the factor $k - k_h$ is thus absorbed by K_+. Note that this is subtle. The factor corresponds to a zero in the strip and therefore does not intervene with the argument of analytic continuation across the strip later. This is different for the scattering at a soft-hard transition where the kernel is reciprocal $1/K(k)$ of our kernel $K(k)$. In this case the factor $k - k_h$ is a **pole**, which does affect analyticity. Therefore, it cannot be left in the equation and has to be multiplied away, effectively by absorbing it in K_-.

As a result we would expect for $K = K_+/K_-$ (the limit $\varepsilon \to 0$ of L)

$$K_+(k) = (\omega-\sigma)(k)_+^{-1-\mathrm{i}\delta}, \qquad K_-(k) = (k)_-^{-\mathrm{i}\delta}. \tag{C.11}$$

C.5 Contour integrals

The integration contour in (5.28) and (5.29) is along the real k axis. For $x > 0$ it can be folded down around the lower branch cut, Fig. 5.4 (the negative imaginary axis) including the contribution of the real pole in $k = k_0$. We have already transformed the variable $k = k_0\kappa$ to obtain the integrals in the form shown in (5.30) and (5.31). Next, we need the following identities (C.12) for $\kappa = -\mathrm{i}t \pm 0$ ($t > 0$ real) assuming $\omega \gtrless \sigma$ as relevant

$$\begin{aligned}
&|-\mathrm{i}t \pm 0| = \mp\mathrm{i}t,\\
&(-\mathrm{i}t+0)_+^{\frac{1}{2}+\mathrm{i}\delta} = \mathrm{e}^{-\frac{1}{4}\pi\mathrm{i}}\Big(\frac{\omega-\sigma}{\omega+\sigma}\Big)^{-\frac{1}{4}} t^{\frac{1}{2}+\mathrm{i}\delta}, \quad (-\mathrm{i}t-0)_+^{\frac{1}{2}+\mathrm{i}\delta} = \mathrm{e}^{\frac{3}{4}\pi\mathrm{i}}\Big(\frac{\omega-\sigma}{\omega+\sigma}\Big)^{\frac{3}{4}} t^{\frac{1}{2}+\mathrm{i}\delta},\\
&(-\mathrm{i}t+0)_+^{\mathrm{i}\delta} = \Big(\frac{\sigma-\omega}{\sigma+\omega}\Big)^{-\frac{1}{4}} t^{\mathrm{i}\delta}, \qquad (-\mathrm{i}t-0)_+^{\mathrm{i}\delta} = \Big(\frac{\sigma-\omega}{\sigma+\omega}\Big)^{\frac{3}{4}} t^{\mathrm{i}\delta}.
\end{aligned} \tag{C.12}$$

For $x < 0$ the integration contour can be folded up around the upper branch cut (the positive imaginary axis) Fig. 5.4 , using the following identities (C.13) for $\kappa = \mathrm{i}t \pm 0$ ($t > 0$ real) and assuming $\omega \gtrless \sigma$ as relevant.

$$|\mathrm{i}t \pm 0| = \pm\mathrm{i}t, \quad (\mathrm{i}t \pm 0)_+^{\frac{1}{2}+\mathrm{i}\delta} = \mathrm{e}^{\frac{1}{4}\pi\mathrm{i}}\Big(\frac{\omega-\sigma}{\omega+\sigma}\Big)^{\frac{1}{4}} t^{\frac{1}{2}+\mathrm{i}\delta}, \quad (\mathrm{i}t \pm 0)_+^{\mathrm{i}\delta} = \Big(\frac{\sigma-\omega}{\sigma+\omega}\Big)^{\frac{1}{4}} t^{\mathrm{i}\delta}. \tag{C.13}$$

Thus, for the low shear case and $x > 0$ with $\kappa = -\mathrm{i}t \pm 0$ ($t > 0$ real), from (5.30),

$$\begin{aligned}
\overline{u} =& \frac{U_0}{\pi}\,\mathrm{e}^{-k_0 y_0}\,\mathrm{e}^{\frac{1}{4}\pi\mathrm{i}}\Big(\frac{\omega+\sigma}{\omega-\sigma}\Big)^{\frac{1}{4}}\bigg[\frac{\omega}{\omega+\sigma}\int_0^\infty \frac{t^{\frac{1}{2}+\mathrm{i}\delta}}{t-\mathrm{i}}\,\mathrm{e}^{-tk_0 z}\,\mathrm{d}t \\
&\qquad - \frac{\omega}{\omega-\sigma}\int_0^\infty \frac{t^{\frac{1}{2}+\mathrm{i}\delta}}{t-\mathrm{i}}\,\mathrm{e}^{-tk_0 z^*}\,\mathrm{d}t\bigg] - 2U_0\frac{\omega}{\omega-\sigma}\,\mathrm{e}^{-k_0 y_0 - \mathrm{i}k_0 z^*} \\
\overline{v} =& \mathrm{i}\frac{U_0}{\pi}\,\mathrm{e}^{-k_0 y_0}\,\mathrm{e}^{\frac{1}{4}\pi\mathrm{i}}\Big(\frac{\omega+\sigma}{\omega-\sigma}\Big)^{\frac{1}{4}}\bigg[\frac{\omega}{\omega+\sigma}\int_0^\infty \frac{t^{\frac{1}{2}+\mathrm{i}\delta}}{t-\mathrm{i}}\,\mathrm{e}^{-tk_0 z}\,\mathrm{d}t \\
&\qquad + \frac{\omega}{\omega-\sigma}\int_0^\infty \frac{t^{\frac{1}{2}+\mathrm{i}\delta}}{t-\mathrm{i}}\,\mathrm{e}^{-tk_0 z^*}\,\mathrm{d}t\bigg] + 2\mathrm{i}U_0\frac{\omega}{\omega-\sigma}\,\mathrm{e}^{-k_0 y_0 - \mathrm{i}k_0 z^*} \\
\overline{p} =& -\frac{\rho_0 U_0^2}{\pi}\,\mathrm{e}^{-k_0 y_0}\,\mathrm{e}^{\frac{1}{4}\pi\mathrm{i}}\Big(\frac{\omega+\sigma}{\omega-\sigma}\Big)^{\frac{1}{4}}\bigg[\int_0^\infty t^{-\frac{1}{2}+\mathrm{i}\delta}\,\mathrm{e}^{-tk_0 z}\,\mathrm{d}t - \int_0^\infty t^{-\frac{1}{2}+\mathrm{i}\delta}\,\mathrm{e}^{-tk_0 z^*}\,\mathrm{d}t \\
&\qquad - \Big(1-\frac{k_0\sigma y}{\omega+\sigma}\Big)\int_0^\infty \frac{t^{\frac{1}{2}+\mathrm{i}\delta}}{t-\mathrm{i}}\,\mathrm{e}^{-tk_0 z}\,\mathrm{d}t + \Big(1-\frac{k_0\sigma y}{\omega-\sigma}\Big)\int_0^\infty \frac{t^{\frac{1}{2}+\mathrm{i}\delta}}{t-\mathrm{i}}\,\mathrm{e}^{-tk_0 z^*}\,\mathrm{d}t\bigg] \\
&\qquad - 2\rho_0 U_0^2\Big(1-\frac{k_0\sigma y}{\omega-\sigma}\Big)\,\mathrm{e}^{-k_0 y_0 - \mathrm{i}k_0 z^*}
\end{aligned} \tag{C.14}$$

For the low shear case and $x < 0$ with $\kappa = \mathrm{i}t \pm 0$ ($t > 0$ real), from (5.30)

$$\begin{aligned}
\overline{u} =& \frac{U_0}{\pi}\,\mathrm{e}^{-k_0 y_0}\,\mathrm{e}^{-\frac{1}{4}\pi\mathrm{i}}\Big(\frac{\omega+\sigma}{\omega-\sigma}\Big)^{-\frac{1}{4}}\frac{\omega}{\omega-\sigma}\int_0^\infty \frac{t^{\frac{1}{2}+\mathrm{i}\delta}}{t+\mathrm{i}}\big(\mathrm{e}^{tk_0 z} + \mathrm{e}^{tk_0 z^*}\big)\,\mathrm{d}t \\
\overline{v} =& \frac{U_0}{\pi}\,\mathrm{e}^{-k_0 y_0}\,\mathrm{e}^{\frac{1}{4}\pi\mathrm{i}}\Big(\frac{\omega+\sigma}{\omega-\sigma}\Big)^{-\frac{1}{4}}\frac{\omega}{\omega-\sigma}\int_0^\infty \frac{t^{\frac{1}{2}+\mathrm{i}\delta}}{t+\mathrm{i}}\big(\mathrm{e}^{tk_0 z} - \mathrm{e}^{tk_0 z^*}\big)\mathrm{d}t \\
\overline{p} =& \frac{\rho_0 U_0^2}{\pi}\,\mathrm{e}^{-k_0 y_0}\,\mathrm{e}^{\frac{3}{4}\pi\mathrm{i}}\Big(\frac{\omega+\sigma}{\omega-\sigma}\Big)^{\frac{3}{4}}\bigg[\int_0^\infty t^{-\frac{1}{2}+\mathrm{i}\delta}\,\mathrm{e}^{tk_0 z}\,\mathrm{d}t + \frac{\omega-\sigma}{\omega+\sigma}\int_0^\infty t^{-\frac{1}{2}+\mathrm{i}\delta}\,\mathrm{e}^{tk_0 z^*}\,\mathrm{d}t \\
&\qquad - \Big(1-\frac{k_0\sigma y}{\omega+\sigma}\Big)\int_0^\infty \frac{t^{\frac{1}{2}+\mathrm{i}\delta}}{t+\mathrm{i}}\,\mathrm{e}^{tk_0 z}\,\mathrm{d}t - \Big(\frac{\omega-\sigma}{\omega+\sigma} - \frac{k_0\sigma y}{\omega+\sigma}\Big)\int_0^\infty \frac{t^{\frac{1}{2}+\mathrm{i}\delta}}{t+\mathrm{i}}\,\mathrm{e}^{tk_0 z^*}\,\mathrm{d}t\bigg].
\end{aligned} \tag{C.15}$$

For the high shear case and $x > 0$ with $\kappa = -\mathrm{i}t \pm 0$ ($t > 0$ real), from (5.31)

$$\begin{aligned}
\overline{u} = \;& \mathrm{i}\frac{U_0}{\pi}\,\mathrm{e}^{-k_0 y_0}\Big(\frac{\sigma+\omega}{\sigma-\omega}\Big)^{\frac{1}{4}}\Big[\frac{\omega}{\sigma+\omega}\int_0^\infty \frac{t^{\mathrm{i}\delta}}{t-\mathrm{i}}\,\mathrm{e}^{-tk_0 z}\,\mathrm{d}t \\
& \qquad + \frac{\omega}{\sigma-\omega}\int_0^\infty \frac{t^{\mathrm{i}\delta}}{t-\mathrm{i}}\,\mathrm{e}^{-tk_0 z^*}\,\mathrm{d}t\Big] + 2U_0\frac{\omega}{\sigma-\omega}\,\mathrm{e}^{-k_0 y_0 - \mathrm{i}k_0 z^*} \\
\overline{v} = & -\frac{U_0}{\pi}\,\mathrm{e}^{-k_0 y_0}\Big(\frac{\sigma+\omega}{\sigma-\omega}\Big)^{\frac{1}{4}}\Big[\frac{\omega}{\sigma+\omega}\int_0^\infty \frac{t^{\mathrm{i}\delta}}{t-\mathrm{i}}\,\mathrm{e}^{-tk_0 z}\,\mathrm{d}t \\
& \qquad - \frac{\omega}{\sigma-\omega}\int_0^\infty \frac{t^{\mathrm{i}\delta}}{t-\mathrm{i}}\,\mathrm{e}^{-tk_0 z^*}\,\mathrm{d}t\Big] - 2\mathrm{i}U_0\frac{\omega}{\sigma-\omega}\,\mathrm{e}^{-k_0 y_0 - \mathrm{i}k_0 z^*} \\
\overline{p} = & -\mathrm{i}\frac{\rho_0 U_0^2}{\pi}\,\mathrm{e}^{-k_0 y_0}\Big(\frac{\sigma+\omega}{\sigma-\omega}\Big)^{\frac{1}{4}}\Big[\int_0^\infty t^{-1+\mathrm{i}\delta}\,\mathrm{e}^{-tk_0 z}\,\mathrm{d}t - \int_0^\infty t^{-1+\mathrm{i}\delta}\,\mathrm{e}^{-tk_0 z^*}\,\mathrm{d}t \\
& - \Big(1-\frac{k_0\sigma y}{\sigma+\omega}\Big)\int_0^\infty \frac{t^{\mathrm{i}\delta}}{t-\mathrm{i}}\,\mathrm{e}^{-tk_0 z}\,\mathrm{d}t + \Big(1+\frac{k_0\sigma y}{\sigma-\omega}\Big)\int_0^\infty \frac{t^{\mathrm{i}\delta}}{t-\mathrm{i}}\,\mathrm{e}^{-tk_0 z^*}\,\mathrm{d}t\Big] \\
& \qquad - 2\rho_0 U_0^2\Big(1+\frac{k_0\sigma y}{\sigma-\omega}\Big)\,\mathrm{e}^{-k_0 y_0 - \mathrm{i}k_0 z^*}\,.
\end{aligned} \tag{C.16}$$

For the high shear case and $x < 0$ with $\kappa = \mathrm{i}t \pm 0$ ($t > 0$ real), from (5.31)

$$\begin{aligned}
\overline{u} = \;& \mathrm{i}\frac{U_0}{\pi}\,\mathrm{e}^{-k_0 y_0}\Big(\frac{\sigma+\omega}{\sigma-\omega}\Big)^{-\frac{1}{4}}\frac{\omega}{\sigma-\omega}\int_0^\infty \frac{t^{\mathrm{i}\delta}}{t+\mathrm{i}}\big(\mathrm{e}^{tk_0 z} + \mathrm{e}^{tk_0 z^*}\big)\,\mathrm{d}t \\
\overline{v} = & -\frac{U_0}{\pi}\,\mathrm{e}^{-k_0 y_0}\Big(\frac{\sigma+\omega}{\sigma-\omega}\Big)^{-\frac{1}{4}}\frac{\omega}{\sigma-\omega}\int_0^\infty \frac{t^{\mathrm{i}\delta}}{t+\mathrm{i}}\big(\mathrm{e}^{tk_0 z} - \mathrm{e}^{tk_0 z^*}\big)\mathrm{d}t \\
\overline{p} = & -\mathrm{i}\frac{\rho_0 U_0^2}{\pi}\,\mathrm{e}^{-k_0 y_0}\Big(\frac{\sigma+\omega}{\sigma-\omega}\Big)^{-\frac{1}{4}}\Big[\frac{\sigma+\omega}{\sigma-\omega}\int_0^\infty t^{-1+\mathrm{i}\delta}\,\mathrm{e}^{tk_0 z}\,\mathrm{d}t - \int_0^\infty t^{-1+\mathrm{i}\delta}\,\mathrm{e}^{tk_0 z^*}\,\mathrm{d}t \\
& - \Big(\frac{\sigma+\omega}{\sigma-\omega} - \frac{k_0\sigma y}{\sigma-\omega}\Big)\int_0^\infty \frac{t^{\mathrm{i}\delta}}{t+\mathrm{i}}\,\mathrm{e}^{tk_0 z}\,\mathrm{d}t + \Big(1+\frac{k_0\sigma y}{\sigma-\omega}\Big)\int_0^\infty \frac{t^{\mathrm{i}\delta}}{t+\mathrm{i}}\,\mathrm{e}^{tk_0 z^*}\,\mathrm{d}t\Big].
\end{aligned} \tag{C.17}$$

C.6 Incomplete Γ function

For $\mathrm{Re}(a) > 0$ the Gamma and incomplete Gamma functions are given by

$$\Gamma(a) = \int_0^\infty t^{a-1}\,\mathrm{e}^{-t}\,\mathrm{d}t, \qquad \Gamma(a,z) = \int_z^\infty t^{a-1}\,\mathrm{e}^{-t}\,\mathrm{d}t.$$

Note the recurrence relations

$$\Gamma(a+1) = a\Gamma(a) \quad \text{and} \quad \Gamma(a+1,z) = a\Gamma(a,z) + z^a\,\mathrm{e}^{-z}\,.$$

The power series expansion of $\Gamma(a,z)$ in z is

$$\Gamma(a,z)=\Gamma(a)-\sum_{n=0}^{\infty}\frac{(-1)^n z^{a+n}}{n!(a+n)}=\Gamma(a)-\frac{z^a}{a}+O(z^{a+1})=\Gamma(a)+z^a\cdot(\text{entire function}).$$

$\Gamma(a,z)$ has a branch cut along negative real axis. Across the branch cut is

$$\mathrm{e}^{\pi\mathrm{i}a}\,\Gamma(a,-y-\mathrm{i}0)-\mathrm{e}^{-\pi\mathrm{i}a}\,\Gamma(a,-y+\mathrm{i}0)=\frac{2\pi\mathrm{i}}{\Gamma(1-a)}.$$

By transforming $t=z\tau$ with $\mathrm{Re}(z)>0$ and relocating the integration contour we obtain

$$\int_0^\infty \tau^{a-1}\,\mathrm{e}^{-z\tau}\,\mathrm{d}\tau=z^{-a}\Gamma(a),\quad\text{resp.}\quad\int_0^\infty \tau^{a-1}\,\mathrm{e}^{-z^*\tau}\,\mathrm{d}\tau=z^{*\,-a}\Gamma(a).$$

If $\mathrm{Re}(z)<0$ we transform $t=-z\tau$ and (noting that $y>0$) we obtain

$$\int_0^\infty \tau^{a-1}\,\mathrm{e}^{z\tau}\,\mathrm{d}\tau=z^{-a}\,\mathrm{e}^{a\pi\mathrm{i}}\,\Gamma(a),\quad\text{resp.}\quad\int_0^\infty \tau^{a-1}\,\mathrm{e}^{z^*\tau}\,\mathrm{d}\tau=z^{*\,-a}\,\mathrm{e}^{-a\pi\mathrm{i}}\,\Gamma(a).$$

(This remains the same if $a=\mathrm{i}\delta$.) Furthermore, we have from [63, eq. 8.6.4]

$$\int_0^\infty \frac{t^a\,\mathrm{e}^{-t}}{t+b}\,\mathrm{d}t=\mathrm{e}^b\,b^a\Gamma(a+1)\Gamma(-a,b),\qquad(|\arg(b)|<\pi,\quad\mathrm{Re}(a)>-1).$$

Now replace b by $-\mathrm{i}z$ with $\mathrm{Re}(z)>0$ such that $\arg(-\mathrm{i}z)=\arg(z)-\frac{1}{2}\pi$, $|\arg(-\mathrm{i}z)|<\pi$, and $(-\mathrm{i}z)^a=\mathrm{e}^{-\frac{1}{2}\pi a\mathrm{i}}\,z^a$. Then by transforming $t=z\tau$ and relocating the integration contour we obtain

$$\int_0^\infty \frac{\tau^a\,\mathrm{e}^{-z\tau}}{\tau-\mathrm{i}}\,\mathrm{d}\tau=\mathrm{e}^{-\frac{1}{2}\pi a\mathrm{i}}\,\Gamma(a+1)\,\mathrm{e}^{-\mathrm{i}z}\,\Gamma(-a,-\mathrm{i}z).\tag{C.18}$$

In the same way we can replace $b=\mathrm{i}(-z)$ and $t=(-z)\tau$ with $\mathrm{Re}(z)<0$ leading to

$$\int_0^\infty \frac{\tau^a\,\mathrm{e}^{z\tau}}{\tau+\mathrm{i}}\,\mathrm{d}\tau=\mathrm{e}^{\frac{1}{2}\pi a\mathrm{i}}\,\Gamma(a+1)\,\mathrm{e}^{-\mathrm{i}z}\,\Gamma(-a,-\mathrm{i}z).\tag{C.19}$$

The above remains the same for z replaced by z^*. Finally we note that for $|z|\to\infty$ we use [63, eq. 8.11.2]

$$\Gamma(-a,z)=z^{-a-1}\,\mathrm{e}^{-z}\big(1+O(1/z)\big)$$

This leads for both $x>0$ and $x<0$, and $y\geqslant 0$, to

$$\mathrm{e}^{-\mathrm{i}z}\,\Gamma(-a,-\mathrm{i}z)\sim(-\mathrm{i}z)^{-a-1}=\mathrm{i}\,\mathrm{e}^{\frac{1}{2}\pi a\mathrm{i}}\,z^{-a-1}\tag{C.20}$$

However, for z replaced by z^* we have

$$\mathrm{e}^{-\mathrm{i}z^*}\,\Gamma(-a,-\mathrm{i}z^*)\sim(-\mathrm{i}z^*)^{-a-1}=\begin{cases}\mathrm{i}\,\mathrm{e}^{-\frac{3}{2}\pi a\mathrm{i}}\,z^{*\,-a-1} & \text{if}\quad x<0\quad\text{and}\quad y>0\\ \mathrm{i}\,\mathrm{e}^{\frac{1}{2}\pi a\mathrm{i}}\,z^{*\,-a-1} & \text{if}\quad x>0\quad\text{or}\quad\ \ y=0.\end{cases}\tag{C.21}$$

Appendix D

Appendix to Chapter 6

D.1 Regularising Wiener-Hopf kernel K

The singularity at $k = 0$ of the Wiener-hopf kernel (6.11)

$$K(k) = 1 + \frac{a}{k} - \frac{b}{\sqrt{k^2}}$$

is regularised by assuming a small $\varepsilon > 0$ with (6.12)

$$K(k) = 1 + \frac{a}{k - \mathrm{i}\varepsilon} - \frac{b}{\sqrt{k^2 + \varepsilon^2}}$$

with in either case the principal value square root assumed. There is a certain amount of arbitrariness in the way we push the pole at $k = 0$ down (to $k+\mathrm{i}\varepsilon$) or up (to $k-\mathrm{i}\varepsilon$), since the singularity encountered in $\log K(k)$ is a logarithmic one and hence integrable in (6.16). Whatever we choose, pushing the pole up or downwards, the logarithm has to be defined such that $\log(1) = 0$ and that none of the branch cuts, emanating from the zeros and poles of K, cross the real axis. This is not easy to achieve in general. However, it appears that if we choose for the pole being pushed upwards, $K(k)$ for $k \in \mathbb{R}$ always, *i.e.* for all 4 cases of table 6.2, avoids the negative real axis (see Fig. D.1), so the standard principal value logarithm is sufficient to take, in which

case	σ	ω	ζ	$\sigma - \omega$	$\mathrm{Re}(\zeta)$
1	15	2	$1 + \mathrm{i}$	$+$	$+$
2	15	2	$1 - \mathrm{i}$	$+$	$-$
3	4	10	$1 + 10\mathrm{i}$	$-$	$+$
4	4	10	$1 - 10\mathrm{i}$	$-$	$-$

Table D.1: 4 cases considered

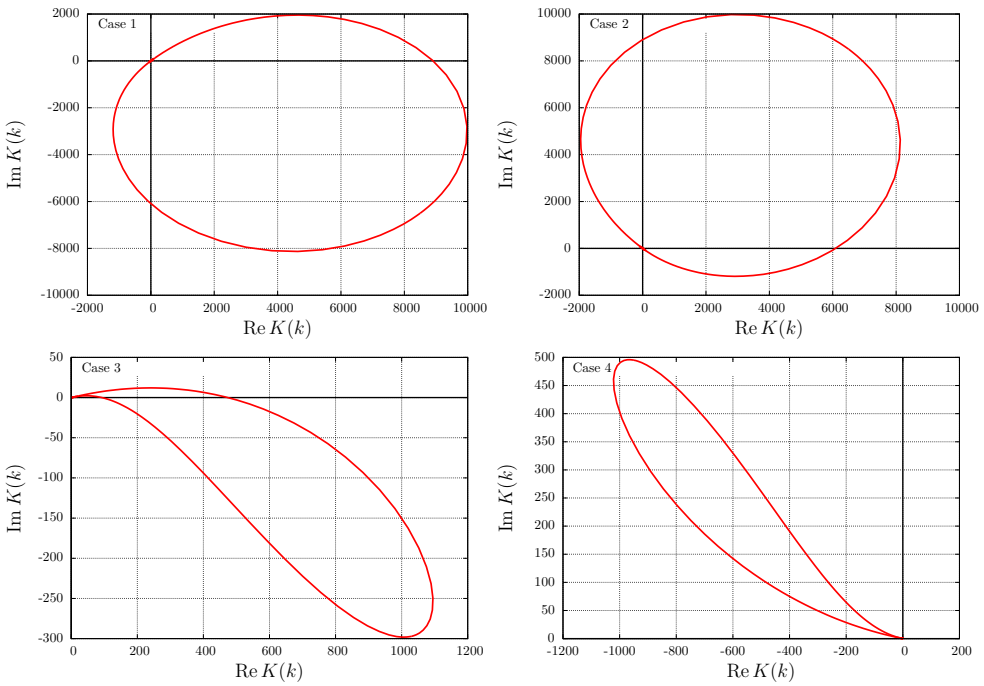

Figure D.1: Trace of $K(k)$, $k \in \mathbb{R}$, for all cases of table D.1 when the pole at $k = 0$ is regularized with $k = k - \mathrm{i}\varepsilon$. $|k| = \sqrt{k^2 + \varepsilon^2}$, $\varepsilon = 10^{-3}$

case we have an analytically exact expression (D.3) for the $\varepsilon = 0$ limit. This is fully confirmed by numerically obtained K_+-integrals for small ε approximating correctly the analytical expression.

It is worth noting that the same happens in case 3 with the pole pushed *down* (*i.e.* with $k + \mathrm{i}\varepsilon$ taken). Also here the trace of K avoids the negative real axis, the principal value log can be taken, and the result approximates the exact expression (D.3). In conclusion: whenever the principal value log can be taken, there is no difference between the pole being pushed up or downwards.

Consider representative examples of the 4 cases as given in table D.1 and graphically displayed in Fig. D.1, where the trace of $K(k)$ is shown for $k \in \mathbb{R}$.

D.2 Analytical evaluation of the split integral

For $\mathrm{Im}(k) > 0$, the principal value logarithm, and $\varepsilon \to 0$ we have

$$2\pi\mathrm{i} \log K_+(k) = I = \int_{-\infty}^{\infty} \frac{f(x)}{x - k}\,\mathrm{d}x, \quad f(x) = \log\left(1 + \frac{a}{x} - \frac{b}{|x|}\right), \quad a = \frac{\sigma}{\mathrm{i}\zeta},\ b = \frac{\omega}{\mathrm{i}\zeta}.$$

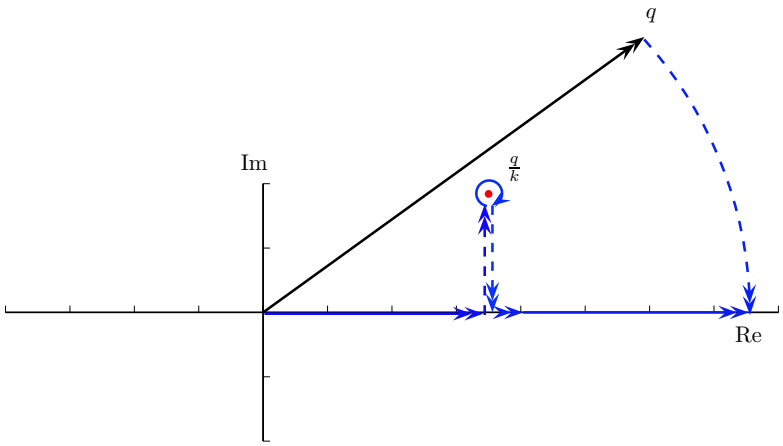

Figure D.2: Closure of the integral contour

We distinguish

$$\int_{-\infty}^{\infty} \frac{\log(1+a/x-b/|x|)}{x-k}\,\mathrm{d}x$$
$$= \int_0^{\infty} \frac{\log(1+(a-b)/x)}{x-k}\,\mathrm{d}x - \int_0^{\infty} \frac{\log(1-(a+b)/x)}{x+k}\,\mathrm{d}x,$$

here referred to as I_1 and I_2 respectively. Consider the first integral

$$I_1 = \int_0^{\infty} \frac{\log(1+q/x)}{x-k}\,\mathrm{d}x$$

where $k, q \in \mathbb{C}$. We transform $x \to 1/x$ and then $qx = y$, to have

$$I_1 = \int_0^{\infty} \frac{\log(1+qx)}{x(1-kx)}\,\mathrm{d}x = \int_0^{q\cdot\infty} \frac{\log(1+y)}{y(1-ky/q)}\,\mathrm{d}y$$
$$= \int_0^{q\cdot\infty} \log(1+y)\left(\frac{1}{y} - \frac{1}{y-q/k}\right)\,\mathrm{d}y$$

We close the contour (Fig. D.2) from $y = q\cdot\infty$ to the real axis at $y = \infty$. Denote $\alpha = q/k$ and $\beta = 1 + q/k$. By defining

$$\begin{aligned} C(k,q) &= -1 \quad \text{if} \quad 0 < \arg(q/k) < \arg q, \\ C(k,q) &= 1 \quad \text{if} \quad \arg q < \arg(q/k) < 0, \\ C(k,q) &= 0 \quad \text{otherwise}, \end{aligned}$$

we indicate the captured pole in $y = \alpha$. In particular for k is real in the limit from

$\mathbb{C}^+$:

$$\begin{aligned} k \in (0,\infty) \;\;\&\;\; \operatorname{Im} q > 0 \quad &\Rightarrow \quad C = -1, \\ k \in (-\infty,0) \;\;\vee\;\; \operatorname{Im} q < 0 \quad &\Rightarrow \quad C = \;\; 0. \end{aligned}$$

We thus find

$$I_1 = \int_0^\infty \log(1+y) \left(\frac{1}{y} + \frac{1}{\alpha - y} \right) \mathrm{d}y - 2\pi \mathrm{i} C(k,q) \log \beta.$$

With the use of the following definition of the dilogarithm [63] (with a branch cut along the negative real axis), related to the polylogarithm of order 2,

$$\operatorname{dilog}(z) = \int_1^z \frac{\log t}{1-t} \, \mathrm{d}t = \operatorname{Li}_2(1-z),$$

we write our integral as a limit

$$I_1 = \lim_{N\to\infty} \int_0^N \log(1+y) \left(\frac{1}{y} + \frac{1}{\alpha - y} \right) \mathrm{d}y \tag{D.1}$$

$$= \lim_{N\to\infty} \int_0^N \frac{\log(1+y)}{y} \, \mathrm{d}y + \lim_{N\to\infty} \int_0^N \frac{\log(1+y)}{\alpha - y} \, \mathrm{d}y. \tag{D.2}$$

The first integral in (D.1) is therefore

$$\int_0^N \frac{\log(1+y)}{y} \, \mathrm{d}y = - \int_1^{N+1} \frac{\log z}{1-z} \, \mathrm{d}z = - \operatorname{dilog}(N+1).$$

The second integral is

$$\int_0^N \frac{\log(1+y)}{\alpha - y} \, \mathrm{d}y = \int_1^{N+1} \frac{\log z}{\beta - z} \, \mathrm{d}z = \int_{\beta^{-1}}^{(N+1)\beta^{-1}} \frac{\log t + \log \beta}{1-t} \, \mathrm{d}t =$$
$$\operatorname{dilog}((N+1)\beta^{-1}) - \operatorname{dilog}(\beta^{-1}) - \log\beta \log((N+1)\beta^{-1} - 1) + \log\beta \log(\beta^{-1} - 1).$$

Altogether, and using the asymptotic behaviour $\operatorname{dilog}(z) \sim -\frac{1}{2}(\log z)^2 + \ldots$ for $z \to \infty$, we have

$$\begin{aligned} I_1 = \int_0^\infty \frac{\log(1+q/x)}{x-k} \, \mathrm{d}x = \lim_{N\to\infty} \Big[&- \operatorname{dilog}(N+1) + \operatorname{dilog}((N+1)\beta^{-1}) - \operatorname{dilog}(\beta^{-1}) \\ &- \log\beta \log((N+1)\beta^{-1} - 1) + \log\beta \log(\beta^{-1} - 1) \Big] - 2\pi\mathrm{i} C(k,q) \log\beta = \\ &- \operatorname{dilog}(\beta^{-1}) + \tfrac{1}{2} \log^2(\beta) + \log\beta \log(\beta^{-1} - 1) - 2\pi\mathrm{i} C(k,q) \log\beta. \end{aligned}$$

The second integral I_2 can be performed in the same fashion to obtain the overall

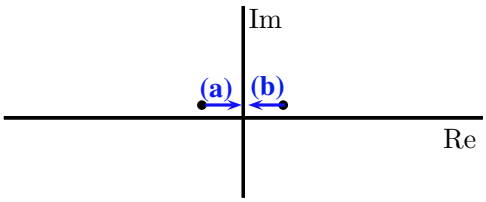

Figure D.3: Path of $k \uparrow 0$ and $k \downarrow 0$, with $\operatorname{Im} k = +0$.

expression of $\log K_+$ for $k \in \mathbb{C}^+$ and $\varepsilon \to 0$ as

$$\begin{aligned} 2\pi\mathrm{i} \log K_+(k) = I = &- \operatorname{dilog}\Big(\frac{k}{k+a-b}\Big) + \operatorname{dilog}\Big(\frac{k}{k+a+b}\Big) \\ &+ \tfrac{1}{2}\log^2\Big(\frac{k+a-b}{k}\Big) - \tfrac{1}{2}\log^2\Big(\frac{k+a+b}{k}\Big) \\ &+ \log\Big(\frac{k+a-b}{k}\Big)\log\Big(\frac{b-a}{k+a-b}\Big) - \log\Big(\frac{k+a+b}{k}\Big)\log\Big(\frac{-b-a}{k+a+b}\Big) \\ &- 2\pi\mathrm{i}C_1 \log\Big(\frac{k+a-b}{k}\Big) + 2\pi\mathrm{i}C_2 \log\Big(\frac{k+a+b}{k}\Big), \end{aligned} \tag{D.3}$$

where $C_1 = C(k, a-b)$ and $C_2 = C(-k, -a-b)$. If required, $\log K_-(k)$ with $k \in \mathbb{C}^-$ is similar.

D.3 Asymptotic analysis of the split integral I for k near 0

The behaviour for $k \to 0$ of the integral $I(k)$ and hence $K_+(k)$ is distinct for high shear ($\sigma > \omega$) or low shear ($\sigma < \omega$). In particular, we will show that $K_+ \sim k^{-\mathrm{i}\delta}$ and $K_+ \sim k^{-\frac{1}{2}-\mathrm{i}\delta}$, respectively. Hence we break this analysis into 2 parts. Also, we will assume the natural condition $\operatorname{Re}(\zeta) > 0$. The limit $k \to 0$ is taken from below and from above, along but just above the real axis, as shown in Fig. D.3. In all cases we use the fact that [63]

$$\operatorname{dilog}(z) = \tfrac{1}{6}\pi^2 + O(z \log z) \quad \text{for} \quad z \to 0,$$

making in general the dilog-parts unimportant to leading orders.

D.3.1 High shear case

This analysis for $k \to 0$ and $\operatorname{Im} k = +0$ relates to the high shear ($\sigma > \omega$) cases 1 and 2 in table 6.2. There is no contribution of the pole q/k, whether we approach from left or right, hence $C_1 = C_2 = 0$.

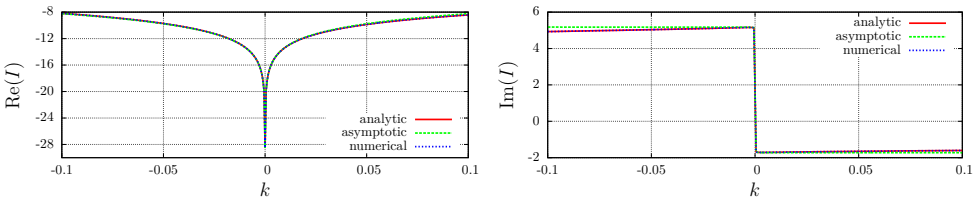

Figure D.4: Comparison of the I calculated from analytical, asymptotic and numerical methods for $\sigma = 5 > \omega = 4$ and $\zeta = \frac{1}{2}(1 + \mathrm{i})$.

Case (a): $k \uparrow 0$

With the principal value logarithm and $k \uparrow 0$, we have

$$\log\Big(\frac{k+a+b}{k}\Big) \simeq \log(a+b) - \log(k) + 2\pi\mathrm{i}, \quad \log\Big(\frac{-b-a}{k+a+b}\Big) \simeq -\pi\mathrm{i}.$$
$$\log\Big(\frac{k+a-b}{k}\Big) \simeq \log(a-b) - \log(k) + 2\pi\mathrm{i}, \quad \log\Big(\frac{b-a}{k+a-b}\Big) \simeq -\pi\mathrm{i}.$$

From (D.3) we have then

$$I \sim \log(k)\log\Big|\frac{a+b}{a-b}\Big| + \tfrac{1}{2}\log^2(a-b) - \tfrac{1}{2}\log^2(a+b) + \pi\mathrm{i}\log\Big(\frac{a-b}{a+b}\Big).$$

Case (b): $k \downarrow 0$

For $k \downarrow 0$, we have

$$\log\Big(\frac{k+a+b}{k}\Big) \simeq \log(a+b) - \log(k), \quad \log\Big(\frac{-b-a}{k+a+b}\Big) \simeq \pi\mathrm{i},$$
$$\log\Big(\frac{k+a-b}{k}\Big) \simeq \log(a-b) - \log(k), \quad \log\Big(\frac{b-a}{k+a-b}\Big) \simeq \pi\mathrm{i}.$$

From D.3, we have

$$I \sim \log(k)\log\Big|\frac{a+b}{a-b}\Big| + \tfrac{1}{2}\log^2(a-b) - \tfrac{1}{2}\log^2(a+b) + \pi\mathrm{i}\log\Big(\frac{a-b}{a+b}\Big).$$

We see that the limits from left and right come down to the same expression. As a result, the asymptotic behaviour of K_+ becomes

$$K_+ \sim c_1 k^{-\mathrm{i}\delta}, \quad \delta = \frac{1}{2\pi}\log\Big|\frac{\sigma+\omega}{\sigma-\omega}\Big|, \tag{D.4}$$

where δ is real positive and c_1 is a complex constant given by

$$c_1 = \mathrm{e}^{\frac{1}{2\pi\mathrm{i}}\left[\frac{1}{2}\log^2(a-b) - \frac{1}{2}\log^2(a+b) + \pi\mathrm{i}\log\left(\frac{a-b}{a+b}\right)\right]} \tag{D.5}$$

For illustration, Fig. D.4 shows a comparison of a numerically, analytically and asymp-

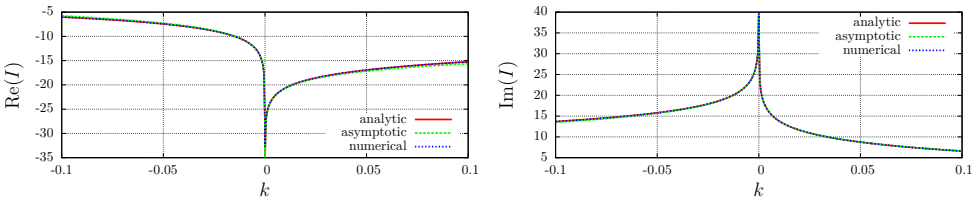

Figure D.5: Comparison of I calculated numerically, analytically, and asymptotically for $\sigma = 4 < \omega = 5$ and $\zeta = \frac{1}{2}(1 + \mathrm{i})$.

totically obtained I.

D.3.2 Low shear case

The asymptotic analysis of (D.3) for $k \to 0$ and $\mathrm{Im}(k) = +0$ considers the low shear ($\sigma < \omega$) cases 3 and 4 of table 6.2. Here, we have a contribution of the q/k-pole when we approach from the right.

Case (a): $k \uparrow 0$

With the principal value logarithm and $k \uparrow 0$, the following hold:

$$\log\Big(\frac{k+a+b}{k}\Big) \simeq \log(a+b) - \log(k) + 2\pi\mathrm{i}, \quad \log\Big(\frac{-b-a}{k+a+b}\Big) \simeq -\pi\mathrm{i},$$
$$\log\Big(\frac{k+a-b}{k}\Big) \simeq \log(a-b) - \log(k), \quad \log\Big(\frac{b-a}{k+a-b}\Big) \simeq \pi\mathrm{i}.$$

From (D.3), we have with $C_1 = C_2 = 0$

$$I \sim \log(k)\left[\log\Big|\frac{a+b}{a-b}\Big| - \pi\mathrm{i}\right] + \tfrac{1}{2}\log^2(a-b) - \tfrac{1}{2}\log^2(a+b) + \pi\mathrm{i}\log\Big(\frac{a-b}{a+b}\Big).$$

Case (b): $k \downarrow 0$

We have

$$\log\Big(\frac{k+a+b}{k}\Big) \simeq \log(a+b) - \log(k), \quad \log\Big(\frac{-b-a}{k+a+b}\Big) \simeq \pi\mathrm{i},$$
$$\log\Big(\frac{k+a-b}{k}\Big) \simeq \log(a-b) - \log(k), \quad \log\Big(\frac{b-a}{k+a-b}\Big) \simeq -\pi\mathrm{i}.$$

Because of the q/k-pole contribution we have $C_1 = -1$ and $C_2 = 0$. From (D.3), we have

$$I \sim \log(k)\Big[\log\Big|\frac{a+b}{a-b}\Big| - \pi\mathrm{i}\Big] + \tfrac{1}{2}\left(\log^2(a-b) - \log^2(a+b)\right) + \pi\mathrm{i}\log\Big(\frac{a-b}{a+b}\Big).$$

We see that the limiting behaviours from the left and from the right are the same.

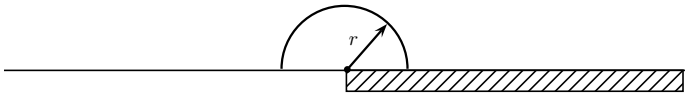

Figure D.6: Energy flux across a small semi-circle of radius r around the singularity.

The asymptotic expression for K_+ is then

$$K_+ \sim c_1 k^{-\frac{1}{2}-\mathrm{i}\delta}, \quad \delta = \frac{1}{2\pi}\log\Big|\frac{\sigma+\omega}{\sigma-\omega}\Big|. \tag{D.6}$$

where (the same as before) δ is real positive and c_1 is a complex constant given by

$$c_1 = \mathrm{e}^{\frac{1}{2\pi\mathrm{i}}\left[\frac{1}{2}\left(\log^2(a-b)-\log^2(a+b)\right)+\pi\mathrm{i}\log\left(\frac{a-b}{a+b}\right)\right]} \tag{D.7}$$

For illustration, Fig. D.5 shows a comparison between numerically, analytically and asymptotically obtained I.

D.3.3 Asymptotic analysis for k large

The analysis for $k \to \infty$ is useful to derive the edge condition in the next section. Again, we consider $\mathrm{Im}(k) = +0$. Noting that for $z \to 0$ we have $\mathrm{dilog}(1-z) \simeq z + O(z^2)$ and $\log(1+z) = z + O(z^2)$, we may obtain for $k \to \infty$

$$I \simeq \frac{2b}{k}\log k + \frac{a-b}{k}\big(\log(b-a) - 2\pi\mathrm{i}C_1\big) - \frac{a+b}{k}\big(\log(-b-a) - 2\pi\mathrm{i}C_2\big).$$

Overall, the dominating term is $\frac{2b}{k}\log k$.

D.4 Evaluation of the entire function E

E can be determined from the condition at infinity. In order to obtain $E(k)$ for $k \to \infty$, we need the asymptotic behaviour of K_+, $k \to \infty$. From D.3.3, we have

$$\lim_{k\to\infty} \log K_+(k) = \lim_{k\to\infty} \frac{2b}{2\pi\mathrm{i}k}\log k = 0 \tag{D.8}$$

so $K_+(k) \to 1$.

The asymptotic behaviour of $G_+(k)$ in the limit $k \to \infty$ is found from the so-called edge condition for $r \to 0$ where r is the distance from the edge. Consider a pressure distribution p at a small distance r from the discontinuity at $r = 0$, such that p is dominated by some power of r, say $p = O(r^\alpha)$. From the momentum equation it follows that the (radial) velocity, say w, should be $w = O(r^{\alpha-1})$. The outward energy flux $\Phi(r)$ across a small circular arc, centred at the edge at radius r (see Fig. D.6) is

then given by

$$\Phi(r) \sim \int_0^\pi pwr \,\mathrm{d}\theta \sim \pi r^\alpha r^{\alpha-1} r \sim r^{2\alpha}. \tag{D.9}$$

In the absence of a physical source at $r = 0$, the energy flux should vanish for $r \downarrow 0$. Hence we must have $\alpha > 0$.

The function $G_+(k)$ from (6.8) is therefore

$$G_+(k \to \infty) \sim \int_0^\infty x^{\alpha-1} \,\mathrm{e}^{\mathrm{i}kx} \,\mathrm{d}x = k^{-\alpha}\Gamma(\alpha)\,\mathrm{e}^{\frac{1}{2}\pi\mathrm{i}\alpha} \tag{D.10}$$

From (6.19), (D.8) and (D.10), we have

$$E(k) = \rho_0 \zeta G_+(k) K_+(k) + O(1/k) \sim k^{-\alpha} \cdot 1 \to 0 \quad (k \to \infty). \tag{D.11}$$

Thus the function $E(k)$ vanishes at $k \to \infty$ and since it is an entire function, it should vanish everywhere, *i.e.* $E(k) = 0$.

D.5 Regularisation of the diverging integral

We want to assign a meaning to

$$\psi(x, y) = \int_0^\infty \frac{1}{k^{1-\mathrm{i}\delta}} \,\mathrm{e}^{\mathrm{i}kz} \,\mathrm{d}k$$

where $z = x + \mathrm{i}y$ with $y > 0$ and δ is real and nonzero. The integral converges for $k \to \infty$ but not for $k = 0$. Following Lighthill - Jones [31, 47], we define the function $H(k)k^{-1+\mathrm{i}\delta}$ as the generalised derivative

$$\frac{H(k)}{k^{1-\mathrm{i}\delta}} \stackrel{\text{def}}{=} \frac{\mathrm{d}}{\mathrm{d}k}\left(\frac{H(k)}{\mathrm{i}\delta k^{-\mathrm{i}\delta}}\right)$$

and the integral

$$\psi(x, y) = \int_{-\infty}^\infty \frac{\mathrm{d}}{\mathrm{d}k}\left(\frac{H(k)}{\mathrm{i}\delta k^{-\mathrm{i}\delta}}\right) \mathrm{e}^{\mathrm{i}kz} \,\mathrm{d}k = -\int_{-\infty}^\infty \frac{zH(k)}{\delta k^{-\mathrm{i}\delta}} \,\mathrm{e}^{\mathrm{i}kz} \,\mathrm{d}k =$$
$$- z\delta^{-1} \int_0^\infty k^{\mathrm{i}\delta} \,\mathrm{e}^{\mathrm{i}kz} \,\mathrm{d}k = -\mathrm{i}\delta^{-1}\Gamma(1 + \mathrm{i}\delta)(-\mathrm{i}z)^{-\mathrm{i}\delta} = \Gamma(\mathrm{i}\delta)(-\mathrm{i}z)^{-\mathrm{i}\delta}.$$

This result is unique and independent of scaling.

Appendix E

Appendix to Chapter 7

E.1 Wiener-Hopf formulation of pressure release wall

Introduce the half-range Fourier transforms

$$F_-(k) = \int_{-\infty}^{0} \overline{v}(x,0)\,\mathrm{e}^{\mathrm{i}kx}\,\mathrm{d}x, \quad G_+(k) = \int_{0}^{\infty} \overline{p}(x,0)\,\mathrm{e}^{\mathrm{i}kx}\,\mathrm{d}x \tag{E.1}$$

that are analytic in $\mathrm{Im}(k) < \varepsilon$ and $\mathrm{Im}(k) > -\varepsilon$ and assumed to be analytic in $\mathbb{C}^+$ and $\mathbb{C}^-$ respectively. We have

$$F_-(k) = -\mathrm{i}|k|A(k) + (\lambda+1)U_0\frac{\mathrm{e}^{-k_0 y_0}}{(k-k_0)}.$$

Furthermore, we have

$$G_+(k) = \int_{0}^{\infty} \overline{p}(x,0)\,\mathrm{e}^{\mathrm{i}kx}\,\mathrm{d}x = \int_{-\infty}^{\infty} \overline{p}(x,0)\,\mathrm{e}^{\mathrm{i}kx}\,\mathrm{d}x = \rho_0 A(k)\mu K(k) \tag{E.2}$$

with Wiener-Hopf kernel

$$K(k) = \frac{\omega\mu - \sigma k}{k^2+\varepsilon^2}, \tag{E.3}$$

where $\mu = |k|$. With $\varepsilon = 0$ and $\omega \neq \sigma$, $K(k)$ is free from zeros however, for $\varepsilon > 0$ there are zero's as shown in Fig. 5.3, namely

$$\begin{aligned} k_l^{\pm} &= +0 \pm \mathrm{i}\varepsilon\frac{\omega}{\sqrt{\omega^2-\sigma^2}} \qquad \text{if} \quad \sigma < \omega, \\ k_h &= \varepsilon\frac{\omega}{\sqrt{\sigma^2-\omega^2}} \qquad\qquad\quad \text{if} \quad \sigma > \omega. \end{aligned}$$

In the low-shear case $\sigma < \omega$, $|k_h^{\pm}| > \varepsilon$, so the zeros are imaginary, outside S and located on the right side of the branchcuts of μ. In the high-shear case $\sigma > \omega$,

however, there is only one zero, which is real and therefore always inside the strip and is needed to be cancelled out as shown in Appendix C.4.2. From (E.2), we arrive at the Wiener-Hopf equation

$$F_-(k) = -\mathrm{i}\frac{G_+(k)}{\rho_0}\frac{1}{K(k)} + (\lambda+1)U_0\frac{\mathrm{e}^{-k_0 y_0}}{(k-k_0)} \tag{E.4}$$

which is to be solved in the standard way [14] by writing

$$K(k) = \frac{K_+(k)}{K_-(k)}, \tag{E.5}$$

where splitfunction K_+ is analytic and nonzero in $\mathbb{C}^+$ and K_- is analytic and nonzero in $\mathbb{C}^-$. We notice from (E.4) that the new kernel is inverse of the previous one (5.20). As a result, from (C.9) and (C.11), we have the following split functions

$$\begin{aligned} K_+(k) &= (\omega-\sigma)(k)_+^{-\frac{1}{2}-\mathrm{i}\delta}, \qquad K_-(k) = (k)_-^{\frac{1}{2}-\mathrm{i}\delta} \qquad (\sigma<\omega) \\ K_+(k) &= (\omega-\sigma)(k)_+^{-1-\mathrm{i}\delta}, \qquad K_-(k) \;\; = (k)_-^{-\mathrm{i}\delta} \qquad (\sigma>\omega). \end{aligned} \tag{E.6}$$

The subtlety for high shear case can be easily overlooked in the case of finite impedance kernel because of the complexity of the regularizations. That is why, the pressure release wall limit analysis has been conducted here.

E.2 Analytic split functions and their asymptotic behaviour

The analytic evaluation of the integral I is performed in D.2. The asymptotic behaviour of the split functions K_+ and K_- is presented here.

E.2.1 Asymptotic behaviour of the split functions for k near 0

The behaviour of the integral $I(k)$ and $K_+(k)$ in the limit $k \to 0$ is different for high shear ($\sigma > \omega$) and low shear ($\sigma < \omega$) cases. hence, they are presented in separate sections.

E.2.2 High shear case

The asymptotic analysis of (D.3) for $k \to 0$ and $\operatorname{Im} k = +0$ relates to the high shear ($\sigma > \omega$) cases 1 and 2 in table 6.2. The following asymptotic behaviour is confirmed by D.4,

$$K_+(k) \sim c_1 k^{-\mathrm{i}\delta} \quad \text{and} \quad K_-(k) \sim \frac{c_1}{(a-\operatorname{sign}(\operatorname{Re} k)b)} k^{1-\mathrm{i}\delta} \tag{E.7}$$

where δ is real positive constant and and c_1 is a complex constant given by

$$\delta = \frac{1}{2\pi}\log\Big|\frac{\sigma+\omega}{\sigma-\omega}\Big|, \quad c_1 = \mathrm{e}^{\frac{1}{2\pi\mathrm{i}}\left[\frac{1}{2}\log^2(a-b)-\frac{1}{2}\log^2(a+b)+\pi\mathrm{i}\log\left(\frac{a-b}{a+b}\right)\right]}. \tag{E.8}$$

We immediately notice that the expression in (E.7) is not analogous to (E.6). This situation arises because the zero k_h at $k = 0$ in (C.4.2) is contained by K_+ rather than K_- because $k = 0$ was a zero in the H-S kernel rather than a pole and hence, was regularized to stay within the numerator. However, since our kernel is inverse of the previous kernel, the zero at $k = 0$ becomes the pole and should be cancelled by multiplying it with K_- to have the strip S free from poles in order to have the analytic continuation of our split functions. We see from (C.4.2) that this pole must be associated with K_- to obtain

$$K_+(k) \sim c_1 k^{-1-\mathrm{i}\delta} \quad \text{and} \quad K_-(k) \sim \frac{c_1}{(a-\operatorname{sign}(\operatorname{Re} k)b)}k^{-\mathrm{i}\delta}. \tag{E.9}$$

E.2.3 Low shear case

The asymptotic analysis of (D.3) for $k \to 0$ and $\operatorname{Im}(k) = +0$ considers the low shear ($\sigma < \omega$) cases 3 and 4 of table 6.2. The following asymptotic behavior is confirmed by D.6

$$K_+(k) \sim c_1 k^{-\frac{1}{2}-\mathrm{i}\delta} \quad \text{and} \quad K_-(k) \sim \frac{c_1}{(a-\operatorname{sign}(\operatorname{Re} k)b)}k^{\frac{1}{2}-\mathrm{i}\delta}. \tag{E.10}$$

where (same as before) δ is real positive and c_1 is a complex constant given by

$$\delta = \frac{1}{2\pi}\log\Big|\frac{\sigma+\omega}{\sigma-\omega}\Big|, \quad c_1 = \mathrm{e}^{\frac{1}{2\pi\mathrm{i}}\left[\frac{1}{2}\left(\log^2(a-b)-\log^2(a+b)\right)+\pi\mathrm{i}\log\left(\frac{a-b}{a+b}\right)\right]}. \tag{E.11}$$

In this case, all the zeros and poles are out of the strip S and that justifies that the expression in (E.10) is analogous to (C.9).

E.3 Evaluation of the entire function E

E can be determined from the condition at infinity. In order to obtain $E(k)$ for $k \to \infty$, we need the asymptotic behaviour of K_+, $k \to \infty$. From D.3.3, we have

$$\lim_{k\to\infty}\log K_+(k) = \lim_{k\to\infty}\frac{2b}{2\pi\mathrm{i}k}\log k = 0 \tag{E.12}$$

so $K_+(k) \to 1$.

The asymptotic behaviour of $G_+(k)$ in the limit $k \to \infty$ is found from the so-called edge condition for $r \to 0$ where r is the distance from the edge. Consider a pressure distribution p at a small distance r from the discontinuity at $r = 0$, such that p is dominated by some power of r, say $p = O(r^\alpha)$. From the momentum equation it

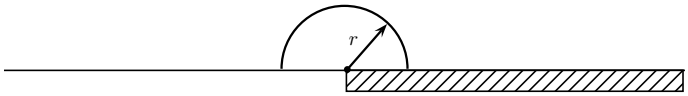

Figure E.1: Energy flux across a small semi-circle of radius r around the singularity.

follows that the (radial) velocity, say w, should be $w = O(r^{\alpha-1})$. The outward energy flux $\Phi(r)$ across a small circular arc, centred at the edge at radius r (see Fig. E.1) is then given by

$$\Phi(r) \sim \int_0^\pi pwr \,\mathrm{d}\theta \sim \pi r^\alpha r^{\alpha-1} r \sim r^{2\alpha}. \tag{E.13}$$

In the absence of a physical source at $r = 0$, the energy flux should vanish for $r \downarrow 0$. Hence we must have $\alpha > 0$.

The function $G_+(k)$ from (7.10) is therefore

$$G_+(k \to \infty) \sim \int_0^\infty (x^\alpha + Zx^{\alpha-1})\,\mathrm{e}^{\mathrm{i}kx}\,\mathrm{d}x = k^{-1-\alpha}\Gamma(1+\alpha)\,\mathrm{e}^{\frac{1}{2}\pi\mathrm{i}(\alpha+1)} + k^{-\alpha}\Gamma(\alpha)\,\mathrm{e}^{\frac{1}{2}\pi\mathrm{i}\alpha} \tag{E.14}$$

From (7.19), (E.12) and (E.14), we have

$$E(k) = \frac{G_+(k)}{\rho_0 \zeta K(k)} + O(1/k) \sim k^{-\alpha} \to 0 \quad (k \to \infty). \tag{E.15}$$

Thus the function $E(k)$ vanishes at $k \to \infty$ and since it is an entire function, it should vanish everywhere, *i.e.* $E(k) = 0$.

E.4 Regularisation of the diverging integral

We want to assign a meaning to

$$\psi(x, y) = \int_0^\infty \frac{1}{k^{1+\mathrm{i}\delta}}\,\mathrm{e}^{\mathrm{i}kz}\,\mathrm{d}k$$

where $z = x + \mathrm{i}y$ with $y > 0$ and δ is real and nonzero. The integral converges for $k \to \infty$ but not for $k = 0$. Following Lighthill-Jones [31, 47], we define the function $H(k)k^{-1-\mathrm{i}\delta}$ as the generalised derivative

$$\frac{H(k)}{k^{1+\mathrm{i}\delta}} \stackrel{\text{def}}{=} \frac{\mathrm{d}}{\mathrm{d}k}\left(\frac{H(k)}{-\mathrm{i}\delta k^{\mathrm{i}\delta}}\right)$$

and the integral

$$\psi(x,y) = \int_{-\infty}^{\infty} \frac{\mathrm{d}}{\mathrm{d}k}\left(\frac{H(k)}{-\mathrm{i}\delta k^{\mathrm{i}\delta}}\right) \mathrm{e}^{\mathrm{i}kz}\ \mathrm{d}k = \int_{-\infty}^{\infty} \frac{zH(k)}{\delta k^{\mathrm{i}\delta}}\, \mathrm{e}^{\mathrm{i}kz}\ \mathrm{d}k =$$
$$z\delta^{-1}\int_{0}^{\infty} k^{-\mathrm{i}\delta}\, \mathrm{e}^{\mathrm{i}kz}\ \mathrm{d}k = \mathrm{i}\delta^{-1}\Gamma(1-\mathrm{i}\delta)(-\mathrm{i}z)^{\mathrm{i}\delta} = \Gamma(-\mathrm{i}\delta)(-\mathrm{i}z)^{\mathrm{i}\delta}.$$

Summary

In this thesis, ideas from applied mathematics are used to model system of equations governing the sound and flow under certain circumstances. In particular, asymptotic methods and complex analysis are used as tools to model the interaction of sound and vorticity.

In Chapter 3, a systematic approximation of the hydrodynamically non linear Helmholtz resonator equation is obtained, including the resulting impedance if the resonator is applied in an acoustic liner. The only unknown parameter that we need to adapt is resistance factor, r, which is $O(1)$. Comparisons with measurements prove that the model predicts the near resonance impedance to a good accuracy. This formulation is useful to predict the impedance of the lining surface accurately, to be used later, in the sound propagation calculations, in numerical simulations. Previous non linear impedance formulations were mainly based upon the LES calculations and thus, our closed form solution saves plenty of computational time. On the other hand, a closed form solution is useful to understand functional relationship of various parameters that govern the impedance.

The impedance model in Chapter 3 is then refined further, in Chapter 4, to take into account the development of waves inside the resonator cavity that are involved in the damping phenomenon. This way, we capture more physics of the problem and the fidelity of the model is improved. This improvement in the modelling assumptions is clearly reflected by the found impedance formulation. Not only the comparison with measurements improved, but also, the model is able to predict the impedance at higher value of excitation amplitude. Even at 150 dB, the comparison is accurate. The current and previous (ch. 3) impedance formulations are connected by a low frequency excitation limit and this consistency is reflected in all equations. Apart from this, the current impedance formulation is asymptotically equivalent to the one in Chapter 3 and is more useful than the previous one for more accurate results at higher amplitudes. The N wave problem fits better with the current model because the cavity contains the information about the higher harmonics inside the cavity. This could serve as a potential topic for further work.

After studying the Helmholtz resonators in non linear regime, we moved to the study of interaction of vorticity with the lining surface in shear flow, in particular, the interaction at hard wall - soft wall transition that radiates acoustic waves. This classical problem have been studied previously for uniform flows, in particular, the

Wiener Hopf method have been used to get the scattering behaviour in case of bulk absorbing liners under uniform flows. We studied this problem with a linear shear flow profile in incompressible limit and formulated the solution in terms of Fourier integrals. The mathematical complexity of having a shear layer is tackled with the help of the analysis for a pressure release wall, Chapter 5 in case of which, the solution in terms of Fourier integrals is analytically integrable and thus improves the fidelity of involved regularizations. The analysis is further continued to the transitions involving a finite impedance wall, Chapter 6. The solution, although not analytically integrable, allows to obtain the far field limit of the solution integrals. The legitimacy of this limit is verified against the pressure release wall solution and genuine consistency is confirmed. Once the incompressible solution is obtained, we match it with the outer acoustic solution in order to obtain the far field sound.

Based upon the problem parameters ω and σ which represents the frequency of the incoming wake and mean shear rate U', the problem degenerates into mainly two cases. If the mean shear is relatively weak ($\sigma < \omega$), the hydrodynamic far field varies as the inverse square root of the distance from the hard-soft edge. The radiated acoustic power is found to vary with U_0^4 where U_0 is the mean flow velocity at the source position. If the mean shear is relatively strong ($\sigma > \omega$), two features are striking. (i) The hydrodynamic far field tends (in modulus) to a constant, that implies a strong back reaction to the wall from any uniform or otherwise bounded part of the mean flow, and (ii) the hydrodynamic field can not be matched to an outward radiating acoustic outer field. This impossible matching and the strong back reaction to the wall, leads to the conclusion that the unbounded linear mean shear flow is an inconsistent modeling assumption in the case of high shear. A more realistic flow profile could give further insight in this problem, but this will inevitably rely more on the numerical calculations. Another approach can be based upon using a piecewise linear shear profile if the Wiener-Hopf kernel doesnt become too formidable.

In Chapter 7, we conducted the above analysis for the soft to hard transition of the wall and found that the scattering behavior remains the same. Thus we conclude that the boundary condition reversal does not greatly affect the scattering process. The resulting soundfield for low shear case behaves similar to the previous case and the high shear case still remains inconclusive.

In Chapter 8, we studied experimentally, the existence of a hydrodynamic wave over a porous wall with grazing flow at various Mach numbers and extracted some interesting properties of this instability with a crude model. This hydrodynamic wave is found to have a significant effect on a limited range of sound frequencies. When this wave is present, there are large oscillations in the transmission coefficient in the flow direction resulting from the interference between the transmitted acoustic wave and this hydrodynamic wave that are propagating at different velocities. The convection velocity of the hydrodynamic wave is found to be close to half of the mean flow speed.

It is difficult to claim any firm conclusions about the amplitude decay of this mode because of the non linear behavior that indicates a saturation of this hydrodynamic wave. Also this wave induces an increment of the pressure drop when it is created

by an acoustic wave. A peak frequency at which the pressure drop is maximum is identified. Further investigations are needed to model the conditions of appearance, amplification, and saturation of this wave.

Curriculum Vitae

Deepesh Kumar Singh was born on April 2, 1986 in village Komari, district Hathras, Utter Pradesh, India. After finishing his school at JNV Agsauli, Hathras, he completed his bachelor's and master's degree in technology from the Department of Aerospace Engineering, Indian Institute of Technology, Kharagpur, India in 2010. He worked within the Fan Noise Group at Rolls Royce Plc. for 2 years at Derby, UK and Bangalore, India and joined the Department of Mathematics and Computer Science of the Technical University Eindhoven (TU/e), the Netherlands, as a doctoral candidate in 2012. The research conducted in his doctoral studies was funded by European Union project *FlowAirS* and the daily work took place at the Centre for Analysis, Scientific computing and Applications (CASA) of TU/e. The results of his research are presented in this thesis.

Acknowledgments

I started my PhD on 15th August 2012, with a motivation to learn the mathematics involving fluids and sound phenomenon and their modeling techniques.

In the beginning, I faced many problems while trying to understand the mathematical intricacies involved in acoustic modeling. I sincerely thank my supervisor Sjoerd Rienstra and promoter Han Slot for their patience while teaching me applied mathematics. I also thank my committee members for going through my thesis and suggesting useful corrections.

I am thankful to Yves Aurégan for exposing me to experimental acoustics and coordinating the *FlowAirS* project in an excellent manner, making the work very exciting with involvement of many experts from different countries in the process. Furthermore, I want to thank European Commission for funding this project and all the members of *FlowAirS*.

I am thankful to all the current and previous CASA members for providing outstanding research environment within the office. In particular, I want to thank Marése, Floor and Enna for managing finance and administration related issues in the most efficient manner.

I thank my school teacher R. P. Upman for inspiring me to learn physics. I also want to thank my mentors from industry, Jeremy Astley, Rie Sugimoto, John Coupland, Peter Schwaller and Nick Humphreys from UK for exposing me to this wonderful research topic on industrial scale and supporting me all the way from 2009 to 2012.

In the end, I would like to thank my mother, Rambeti Devi, my father Rajpal Singh and my brother Arvind for their unconditional support throughout my life. I thank my fiancée Khushboo Rajput for helping me while I was writing this thesis. I would also like to thank all the residents and visitors of Kabelstraat 1, 5612NL, in last 3 years for making my life joyous. Apart from the professional side, I developed a great hobby of electronic music production in the last four years. Living and interacting with many international people enriched me as a person and improved my confidence.

Netherlands is a great country with an embracing outlook that unites the world irrespective of boundaries, religion and race to promote a truly international atmosphere. I became a part of this during my journey and it is to this *international culture*, I dedicate my thesis.

Bibliography

[1] Noise standards: Aircraft type certification. *Fed. Regist*, 34(221):321–351, 1969.

[2] A. Cummings and W. Eversman. High amplitude acoustic transmission through duct terminations: Theory. *Journal of Sound and Vibration*, 91(4):503–518, 1983.

[3] A. McAlpine, M. J. Fisher, and B. J. Tester. "buzz-saw" noise: A comparison of modal measurements with an improved prediction method. *Journal of Sound and Vibration*, 306(3-5):419–443, 2007.

[4] A. Powell. Aerodynamic noise and the plane boundary. *The Journal of the Acoustical Society of America*, 32(8):982–990, 1960.

[5] A. S. Hersh, B. E. Walker, and J. W. Celano. Helmholtz resonator impedance model, part 1: Nonlinear behavior. *AIAA Journal*, 41(5):795–808, 2003.

[6] A. W. Guess. Calculation of perforated plate liner parameters from specified acoustic resistance and reactance. *Journal of Sound and Vibration*, 40(1):119 – 137, 1975.

[7] J. F. Allard and N. Atalla. *Sound propagation in porous materials having a rigid frame*. John Wiley and Sons, Ltd., 2009.

[8] J. F. Allard, D. Lafarge, P. Lemarinier, and V. Tarnow. Dynamic compressibility of air in porous structures at audible frequencies. *Journal of Acoustic Society of America*, 102(4):1995–2006, 1995.

[9] Antoni Alomar and Yves Aurégan. PIV measurement of a porous liner in a duct with flow. *22nd AIAA/CEAS Aeroacoustics Conference, 30 May - 01 June 2016, Lyon, France*, 2016. AIAA Paper 2016-2854.

[10] R. Astley, Vincent Hii, and Gwenael Gabard. A computational mode matching approach for propagation in three-dimensional ducts with flow. American Institute of Aeronautics and Astronautics conference, May 2006.

[11] Y. Aurégan and M. Leroux. Experimental evidence of an instability over an impedance wall in a duct with flow. *Journal of Sound and Vibration*, 317(3-5):432 – 439, 2008.

[12] Y. Aurégan, R. Starobinski, and V. Pagneux. Influence of grazing flow and dissipation effects on the acoustic boundary conditions at a lined wall. *The Journal of the Acoustical Society of America*, 109(1):59–64, 2001.

[13] Yves Aurégan and D. K. Singh. Experimental observation of a hydrodynamic mode in a flow duct with a porous material. *The Journal of the Acoustical Society of America*, 136(2):567–572, 2014.

[14] B. Noble. *Methods Based on the Wiener-Hopf Technique*. Chelsea, 1958.

[15] B. T. Zinn. A theoretical study of non-linear damping by Helmholtz Resonators. *Journal of Sound and Vibration*, 3:347–356, 1970.

[16] C. J. Bouwkamp. A note on singularities occurring at sharp edges in electromagnetic diffraction theory. *Physica*, 12(7):467–474, 1946.

[17] E. J. Brambley and N. Peake. Classification of aeroacoustically relevant surface modes in cylindrical lined ducts. *Wave Motion*, 43:301–310, 2006.

[18] M. Brandes and D. Ronneberger. Sound amplification in flow ducts lined with a periodic sequence of resonators. In *1th AIAA/CEAS Aeroacoustics Conference*, pages 893–901, 1995.

[19] C. Bréard, A. Sayma, M. Imregun, A. G. Wilson, and B. J. Tester. A CFD-based non-linear model for the prediction of tone noise in lined ducts. In *7th AIAA/CEAS Aeroacoustics Conference*, 2001. AIAA-2001-2176.

[20] C. K. W. Tam, H. Ju, M. G. Jones, and T. L. Parrott. A computational and experimental study of slit resonators. *Journal of Sound and Vibration*, 284:947–984, 2005.

[21] C. K. W. Tam, H. Ju, M. G. Jones, W. R. Watson, and T. L. Parrott. A computational and experimental study of resonators in three dimensions. In *15th AIAA/CEAS Aeroacoustics Conference*, 2009. AIAA Paper 2009-3173.

[22] C. K. W. Tam and K. A. Kurbatskii. Microfluid dynamics and acoustics of resonant liners. *AIAA Journal*, 38(8):1331–1339, 2000.

[23] C. K. W. Tam, K. A. Kurbatskii, K. K. Ahuja, and Jr. R. J. Gaeta. A numerical and experimental investigation of the dissipation mechanisms of resonant acoustic liners. *Journal of Sound and Vibration*, 245(3):545–557, 2001.

[24] D. G. Crighton. Radiation from vortex filament motion near a half plane. *Journal of Fluid Mechanics*, 51:357–362, 1 1972.

[25] D. G. Crighton. *Introduction to Wiener-Hopf Methods in Acoustics and Vibration*. Defense Technical Information Center, 1977.

[26] N. Curle. The influence of solid boundaries upon aerodynamic sound. *Proceedings of the Royal Society of London A: Mathematical, Physical and Engineering Sciences*, 231(1187):505–514, 1955.

[27] D. G. Crighton. Radiation from turbulence near a composite flexible boundary. *Proceedings of the Royal Society of London. A. Mathematical and Physical Sciences*, 314(1517):153–173, 1970.

[28] D. G. Crighton, A.P. Dowling, J.E. Ffowcs Williams, M. Heckl, and F.G. Leppington. *Modern methods in analytical acoustics: lecture notes*. Springer, 1992.

[29] D. Innes and D. G. Crighton. On a non-linear differential equation modelling Helmholtz resonator response. *Journal of Sound and Vibration*, 131(2):323–330, 1989.

[30] D. K. Singh. Non-linear N wave source impedance model. In *EURONOISE, 31 May-3 June, 2015, Maastricht, The Netherlands*, 2015.

[31] D. S. Jones. *The Theory of Generalised Functions*. Cambridge University Press, 1982.

[32] NIST Digital Library of Mathematical Functions. http://dlmf.nist.gov/, Release 1.0.10 of 2015-08-07, 2010. Online companion to [63].

[33] E. J. Brambley, M. Darau, and S.W. Rienstra. The critical layer in linear-shear boundary layers over acoustic linings. *Journal of Fluid Mechanics*, 710:545–568, 11 2012.

[34] J. E. Ffowcs Williams and L. H. Hall. Aerodynamic sound generation by turbulent flow in the vicinity of a scattering half plane. *Journal of Fluid Mechanics*, 40(04):657–670, 1970.

[35] H. H. Hubbard, editor. *Aeroacoustics of Flight Vehicles: Noise sources*. Aeroacoustics of Flight Vehicles: Theory and Practice. Volume 1 Noise Sources; Volume 2 Noise Control. Published for the Acoustical Society of America through the American Institute of Physics, 1991.

[36] A. S. Hersh and B. Walker. Effect of grazing flow on the acoustic impedance of helmholtz resonators consisting of single and clustered orifices. "NASA Contractor Report 3177", 1979.

[37] H. H. Hubbard, editor. *Aeroacoustics of Flight Vehicles, Theory and Practice: Noise control*. Number v. 2 in NASA reference publication. National Aeronautics and Space Administration, Office of Management, Scientific and Technical Information Program, 1991.

[38] J. E. Ffowcs Williams. Sound radiation from turbulent boundary layers formed on compliant surfaces. *Journal of Fluid Mechanics*, 22(2):347–358, 1965.

[39] J. H. M. Disselhorst and L. van Wijngaarden. Flow in the exit of open pipes during acoustic resonance. *Journal of Fluid Mechanics*, 99(2):293–319, 1980.

[40] J. M. Roche, L. Leylekian, G. Delattre, and F. Vuillot. Aircraft fan noise absorption: DNS of the acoustic dissipation of resonant liners. In *15th AIAA/CEAS Aeroacoustics Conference*, 2009. AIAA Paper 2009-3146.

[41] D. S. Jones. A simplifying technique in the solution of a class of diffraction problems. *The Quarterly Journal of Mathematics*, 3(1):189–196, 1952.

[42] Phillip Joseph and Anthony Parry. Rotor/wall boundary-layer interaction broadband noise in turbofan engines. 7th AIAA/CEAS Aeroacoustic conference, Maastricht, Netherlands, May 2001. AIAA Paper 2001-2244.

[43] J. Koplik, D. L. Johnson, and R. Dashen. Theory of dynamic permeability and tortuosity in fluid-satured porous media. *J. Fluid. Mech.*, 176:379–402, 1987.

[44] M. J. Lighthill. On sound generated aerodynamically. i. general theory. *Proceedings of the Royal Society of London A: Mathematical, Physical and Engineering Sciences*, 211(1107):564–587, 1952.

[45] Lord Rayleigh. *Theory of Sound: Volume 2*. Dover, 1945.

[46] M. B. Lesser and D. G. Crighton. Physical Acoustics and the Method of Matched Asymptotic Expansions. In W. P. Mason and R. N. Thurston, editors, *Physical Acoustics Principles and Methods*, volume 11 of *Physical Acoustics*, pages 69 – 149. Academic Press, 1975.

[47] M. J. Lighthill. *Introduction to Fourier Analysis and Generalised Functions*. Cambridge University Press, 1958.

[48] M. K. Myers. An exact energy corollary for homentropic flow. *Journal of Sound and Vibration*, 109:277–284, 1986.

[49] D. Marx, Y. Aurégan, H Bailliet, and J. C. Valiere. Piv and ldv evidence of hydrodynamic instability over a liner in a duct with flow. *Journal of Sound and Vibration*, 329(18):3798–3812, 2010.

[50] A. McAlpine and M. J. Fisher. On the prediction of buzz-saw noise in acoustically lined aero-engine inlet ducts. *Journal of Sound and Vibration*, 265(1):175 – 200, 2003.

[51] A. McAlpine, P. J. G. Schwaller, M. J. Fisher, and B. J. Tester. Buzz-saw noise: Prediction of the rotor-alone pressure field. *Journal of Sound and Vibration*, 331(22):4901 – 4918, 2012.

[52] Alan McAlpine, Matthew Wright, Herve Batard, and Sylvain Thezelais. Finite/boundary element assessment of a turbofan spliced intake liner at supersonic fan operating conditions. American Institute of Aeronautics and Astronautics Conference, May 2003. AIAA 2003 - 3305.

[53] J. Meixner. Die Kantenbedingung in der Theorie der Beugung elektromagnetischer Wellen an volkommen leitenden ebenen Schirmen. *Annalen der Physik*, 441(1):1–9, 1950.

[54] M. Myers. *Generalization and extension of the law of acoustic energy conservation in a nonuniform flow.* Aerospace Sciences Meetings. American Institute of Aeronautics and Astronautics, Jan 1986. 1986-471.

[55] M. K. Myers. On the acoustic boundary condition in the presence of flow. *Journal of Sound and Vibration*, 71(3):429 – 434, 1980.

[56] M. K. Myers. Transport of energy by disturbances in arbitrary steady flows. *Journal of Fluid Mechanics*, 226:383–400, 5 1991.

[57] N. Wiener and E. Hopf. Über eine Klasse singuläre Integralgleichungen. *S.B. Preuss. Akad. Wiss.*, pages 696–706, 1931.

[58] Börje Nilsson and Olle Brander. The propagation of sound in cylindrical ducts with mean flow and bulk-reacting lining i. modes in an infinite duct. *IMA Journal of Applied Mathematics*, 26(3):269–298, 1980.

[59] Börje Nilsson and Olle Brander. The propagation of sound in cylindrical ducts with mean flow and bulk-reacting lining ii. bifurcated ducts. *IMA Journal of Applied Mathematics*, 26(4):381–410, 1980.

[60] Börje Nilsson and Olle Brander. The propagation of sound in cylindrical ducts with mean flow and bulk-reacting lining: Iii. step discontinuities. *IMA Journal of Applied Mathematics*, 27(1):105–132, 1981.

[61] Börje Nilsson and Olle Brander. The propagation of sound in cylindrical ducts with mean flow and bulk-reacting lining iv. several interacting discontinuities. *IMA Journal of Applied Mathematics*, 27(3):263–290, 1981.

[62] United States Department of Labour. Occupational safety and health standards. 1991.

[63] F. W. J. Olver, D. W. Lozier, R. F. Boisvert, and C. W. Clark, editors. *NIST Handbook of Mathematical Functions.* Cambridge University Press, New York, NY, 2010. Print companion to [32].

[64] International Civil Aviation Organisation. Annex 16 - environmental protection. *Fed. Regist*, 1981.

[65] P. G. Drazin and W. H. Reid. *Hydrodynamic Stability.* Cambridge University Press, 2004.

[66] A. Papoulis. *The Fourier integral and its applications.* McGraw-Hill electronic sciences series. McGraw-Hill, 1962.

[67] A. D. Pierce. *Acoustics: An Introduction to Its Physical Principles and Applications*. Acoustical Society of America, 1989.

[68] Q. Zhang and D. J. Bodony. Numerical simulation of two-dimensional acoustic liners with high speed grazing flow. *AIAA Journal*, 49(2):365–382, 2011.

[69] R. E. Mickens. *An Introduction to Nonlinear Oscillations*. Cambridge University Press, 1981.

[70] R. M. M. Mattheij, S. W. Rienstra, and J. H. M. ten Thije Boonkkamp. *Partial Differential Equations: Modeling, Analysis, Computation*. Society for Industrial and Applied Mathematics, 2005.

[71] Y. Renou and Y. Aurégan. Failure of the Ingard - Myers boundary condition for a lined duct: An experimental investigation. *J. Acoust. Soc. Am.*, 130(1):52–60, 2011.

[72] S. W. Rienstra. Contributions to the theory of sound propagation in ducts with bulkâĂŘreacting lining lining. *The Journal of the Acoustical Society of America*, 77(5):1681–1685, 1985.

[73] S. W. Rienstra. A classification of duct modes based on surface waves. *Wave Motion*, 37(2):119 – 135, 2003.

[74] S. W. Rienstra. Acoustic scattering at a hard–soft lining transition in a flow duct. *Journal of Engineering Mathematics*, 59(4):451–475, 2007.

[75] S. W. Rienstra and Mirela Darau. Boundary-layer thickness effects of the hydrodynamic instability along an impedance wall. *Journal of Fluid Mechanics*, 671:559–573, 3 2011.

[76] S. W. Rienstra and D. K. Singh. Hard wall–soft wall–vorticity scattering in shear flow. *20th AIAA/CEAS Aeroacoustics Conference, 16-20 June 2014, Atlanta, Georgia, USA*, 2014. AIAA Paper 2014-3350.

[77] S. W. Rienstra and D. K. Singh. Vortical perturbations in shear flow, scattered at a hard wall - pressure release wall transition. *22nd International Congress on Sound and Vibration ICSV22, 12-16 July 2015, Florence, Italy*, 2015.

[78] D. Ronneberger and M. Jüschke. *Oscillations, Waves and Interactions: Sixty Years Drittes Physikalisches Institut; a Festschrift*. Universitätsverlag Göttingen, Göttingen, 2007.

[79] S. A. Orszag and S. C. Crow. Instability of a vortex sheet leaving a semi-infinite plate. *Studies in Applied Mathematics*, 49(2):167–181, 1970.

[80] S. W. Rienstra. Impedance models in time domain, including the extended helmholtz resonator model. In *12th AIAA/CEAS Aeroacoustics Conference, Cambridge, MA, USA*, 2006. AIAA Paper 2006-2686.

[81] S. W. Rienstra and A. Hirschberg. An Introduction to Acoustics. Technical report, Technische Universiteit Eindhoven, 2012. revised and updated version of IWDE 92-06, http://www.win.tue.nl/ sjoerdr/papers/boek.pdf.

[82] D. K. Singh. Vorticity scattering in shear flows at soft wall - hard wall transition. *22nd AIAA/CEAS Aeroacoustics Conference, 30 May - 01 June 2016, Lyon, France*, 2016. AIAA Paper 2016-2703.

[83] D. K. Singh and S. W. Rienstra. A systematic impedance model for non-linear Helmholtz resonator liner. *19th AIAA/CEAS Aeroacoustics Conference, 27-29 May 2013, Berlin, Germany*, 2013. AIAA Paper 2013-2223.

[84] D. K. Singh and S. W. Rienstra. Nonlinear asymptotic impedance model for a Helmholtz resonator liner. *Journal of Sound and Vibration*, 333(15):3536 – 3549, 2014.

[85] D. K. Singh and S. W Rienstra. A systematic impedance model for nonlinear extended Helmholtz resonator liner. *22nd AIAA/CEAS Aeroacoustics Conference, 30 May - 01 June 2016, Lyon, France*, 2016. AIAA Paper 2016-2887.

[86] S.W. Rienstra, M. Darau, and E.J. Brambley. The trailing vorticity field behind a line source in two-dimensional incompressible linear shear flow. *Journal of Fluid Mechanics*, 720:618–636, 4 2013.

[87] T. H. Melling. The acoustic impendance of perforates at medium and high sound pressure levels. *Journal of Sound and Vibration*, 29(1):1 – 65, 1973.

[88] M. A. Temiz, J. Tournadre, I. L. Arteaga, and A. Hirschberg. Non-linear acoustic transfer impedance of micro-perforated plates with circular orifices. *Journal of Sound and Vibration*, 366:418 – 428, 2016.

[89] J. M. Tyler and T. J. Sofrin. Axial flow compressor noise studies. *Transactions of the Society of Automotive Engineers*, 70:309–339, 1962.

[90] U. Ingard. On the Theory and Design of Acoustic Resonators. *Journal of The Acoustical Society of America*, 25, 1953.

[91] U. Ingard and H. Ising. Acoustic nonlinearity of an orifice. *The Journal of the Acoustical Society of America*, 42(1):6–17, 1967.

[92] U. Ingard and S. Labate. Acoustic circulation effects and the nonlinear impedance of orifices. *Journal of Acoustic Society of America*, 22:211–219, 1950.

[93] W. G. Vincenti and C. H. Kruger. *Introduction to physical gas dynamics*. Krieger, The University of Michigan, 1967.

[94] Xuesong Wu. Generation of sound and instability waves due to unsteady suction and injection. *Journal of Fluid Mechanics*, 453:289–313, 2 2002.

[95] Y. Aurégan and D. Marx. Comparison of experiments with stability analysis predictions in a lined flow duct. In *16th AIAA/CEAS Aeroacoustics Conference*, 2010. AIAA Paper 2010-3946.

[96] Y. Aurégan and M. Leroux. Experimental evidence of an instability over an impedance wall in a duct with flow. *Journal of Sound and Vibration*, 317(3–5):432–439, 2008.

[97] Qidou Zhou and Phillip Joseph. A frequency domain numerical method for airfoil broadband self-noise prediction. *Journal of Sound and Vibration*, 299(3):504 – 519, 2007.